frontiers | Research Topics

Frontiers in marine sciences, social sciences and engineering research related to marine (renewable) energy development

Edited by
Zhen Guo, Zhenkui Wang, Shengjie Rui, Zefeng Zhou, Guanqiong Ye and Dongfang Ma

Published in
Frontiers in Marine Science

ISSN 1664-8714
ISBN 978-2-8325-5153-0
DOI 10.3389/978-2-8325-5153-0

About Frontiers

Frontiers is more than just an open access publisher of scholarly articles: it is a pioneering approach to the world of academia, radically improving the way scholarly research is managed. The grand vision of Frontiers is a world where all people have an equal opportunity to seek, share and generate knowledge. Frontiers provides immediate and permanent online open access to all its publications, but this alone is not enough to realize our grand goals.

Frontiers journal series

The Frontiers journal series is a multi-tier and interdisciplinary set of open-access, online journals, promising a paradigm shift from the current review, selection and dissemination processes in academic publishing. All Frontiers journals are driven by researchers for researchers; therefore, they constitute a service to the scholarly community. At the same time, the *Frontiers journal series* operates on a revolutionary invention, the tiered publishing system, initially addressing specific communities of scholars, and gradually climbing up to broader public understanding, thus serving the interests of the lay society, too.

Dedication to quality

Each Frontiers article is a landmark of the highest quality, thanks to genuinely collaborative interactions between authors and review editors, who include some of the world's best academicians. Research must be certified by peers before entering a stream of knowledge that may eventually reach the public - and shape society; therefore, Frontiers only applies the most rigorous and unbiased reviews. Frontiers revolutionizes research publishing by freely delivering the most outstanding research, evaluated with no bias from both the academic and social point of view. By applying the most advanced information technologies, Frontiers is catapulting scholarly publishing into a new generation.

What are Frontiers Research Topics?

Frontiers Research Topics are very popular trademarks of the *Frontiers journals series*: they are collections of at least ten articles, all centered on a particular subject. With their unique mix of varied contributions from Original Research to Review Articles, Frontiers Research Topics unify the most influential researchers, the latest key findings and historical advances in a hot research area.

Find out more on how to host your own Frontiers Research Topic or contribute to one as an author by contacting the Frontiers editorial office: frontiersin.org/about/contact

Frontiers in marine sciences, social sciences and engineering research related to marine (renewable) energy development

Topic editors

Zhen Guo — Zhejiang University, China
Zhenkui Wang — Zhejiang University, China
Shengjie Rui — Norwegian Geotechnical Institute (NGI), Norway
Zefeng Zhou — Norwegian Geotechnical Institute (NGI), Norway
Guanqiong Ye — Zhejiang University, China
Dongfang Ma — Zhejiang University, China

Citation

Guo, Z., Wang, Z., Rui, S., Zhou, Z., Ye, G., Ma, D., eds. (2024). *Frontiers in marine sciences, social sciences and engineering research related to marine (renewable) energy development*. Lausanne: Frontiers Media SA. doi: 10.3389/978-2-8325-5153-0

Table of contents

frontiers | Frontiers in Marine Science

TYPE Editorial
PUBLISHED 01 July 2024
DOI 10.3389/fmars.2024.1421628

OPEN ACCESS

EDITED AND REVIEWED BY
Wei Shi,
Dalian University of Technology, China

*CORRESPONDENCE
Zhen Guo
nehzoug@163.com

RECEIVED 22 April 2024
ACCEPTED 20 June 2024
PUBLISHED 01 July 2024

CITATION
Rui S, Guo Z, Zhou Z, Wang Z, Ye G and Ma D (2024) Editorial: Frontiers in marine sciences, social sciences and engineering research related to marine (renewable) energy development.
Front. Mar. Sci. 11:1421628.
doi: 10.3389/fmars.2024.1421628

Editorial: Frontiers in marine sciences, social sciences and engineering research related to marine (renewable) energy development

Shengjie Rui[1,2], Zhen Guo[1,2]*, Zefeng Zhou[2], Zhenkui Wang[3], Guanqiong Ye[3] and Dongfang Ma[3]

[1]Key Laboratory of Offshore Geotechnics and Material Engineering of Zhejiang Province, College of Civil Engineering and Architecture, Zhejiang University, Hangzhou, Zhejiang, China, [2]Offshore Energy Department, Norwegian Geotechnical Institute, Oslo, Norway, [3]Ocean College, Zhejiang University, Zhoushan, Zhejiang, China

KEYWORDS

marine sciences, marine social sciences, marine engineering, marine energy, renewable energy

Editorial on the Research Topic

Frontiers in marine sciences, social sciences and engineering research related to marine (renewable) energy development

Developing renewable energy to address the relationship between economic development and climate change is one of the most important tasks for many countries (Xu et al., 2024). The ocean contains a variety of energy sources, such as wind energy, solar energy, and wave energy (Rui et al., 2024). In the exploitation of ocean energy, various marine structures, including bottom- fixed and floating structures, are employed to promote the development of oil and gas production platforms, offshore wind turbines, wave energy generation devices, etc (Page et al., 2021; Li et al., 2023). The safety of the structures and their foundations is important for ocean energy utilization (Wang et al., 2020; Jostad et al., 2023). Meanwhile, marine energy development involves multiple disciplines, such as marine biology, chemistry, ecology, and the environment. In addition, human activities (e.g., the construction and installation of offshore structures) affect the exploitation of marine energy (Zhou et al., 2021; Wang et al., 2024). This "Frontiers in Marine Sciences, Social Sciences and Engineering Research Related to Marine (Renewable) Energy Development" Research Topic highlights recent developments in the field of marine (renewable) energy development. This Research Topic publishes 10 peer-reviewed articles, which are briefly summarized below.

Seabed flow involves multi-process, multi-physics, and multi-scale processes, all of which are complex natural phenomena. Zhu et al. summarized the basic information on seabed fluid flow in the China Seas to analyze these features, and then the processes and their implications were investigated. The results emphasize the importance of studying how seabed fluids form and migrate to understand their behavior. In addition to seabed flow, seabed properties are also important for offshore construction, such as foundation design

and installation. Amjadian et al. collected 36 sediment samples in a region of the Irish Sea. Particle size analysis was adopted to calculate the properties of the seabed sediments and to acquire more information about the seabed properties,. Seabed soil liquefaction due to cyclic loading results in an obvious decrease in stiffness and strength, which may contribute to the failure of offshore structures. Li et al. proposed a shear wave velocity threshold as a method to assess the liquefaction of unconsolidated soils, and the soil liquefaction potential was evaluated based on one-dimensional and two-dimensional shear wave velocity profiles. In addition, landslides also influence the soil's long-term stability. Zhang et al. comprehensively considered the spatial variability and multiple factors of the landslide to investigate the development of landslides with weak layers. Then, the influences of dry-wet cycles on reservoir landslides and the sensitivity analysis of the random field parameters were assessed.

The above investigations mainly focus on the marine environment, and the stability and safety in offshore structures are also of great significance. Zhu et al. studied the vibration influence on the Qiantang River seawall based on the measurements of the forced vibrations and pulsations of the seawall under various conditions. The acquired data were analyzed in both time and frequency domains, revealing the time-dependent vibration features of such seawall structures. Lu et al. conducted the analysis of cavity expansion during the piezocone penetration using the hardening soil model with small strain stiffness, and considered deformation analysis of underwater tunnels, which is vital for safe construction. Vacuum preloading was used to improve the properties of the dredged slurry. Cai et al. conducted two vacuum preloading model tests and employed particle image velocimetry to capture soil strain paths and displacements. Vortex-induced vibration may cause fatigue in offshore structures. Gao et al. investigated the potential for vortex-induced vibration when the flow interacts with a bluff body, causing oscillations in the wake. Feng et al. conducted model tests for risers under regular waves with different scales to study the scale effect in wave-structure interactions. The riser model is a novel structural design that can be considered a beam. Tidal turbines are one way of exploiting ocean tidal energy, but the exploitation of tidal power is influenced by the effects of fish-turbine interactions. Peraza et al. combined empirical acoustic density measurements and investigated probabilities in a probability model that considers the interaction between fish and tidal turbines, including fish collisions with stationary turbine components, blade strikes by rotating blades, and/or a collision followed by a blade strike.

In summary, this Research Topic published ten papers on marine sciences and engineering related to marine energy. Some papers focus on the marine environment, while others investigate marine structures. Addressing the problems of marine (renewable) energy can build a better world.

Author contributions

SR: Data curation, Investigation, Validation, Writing – original draft. ZG: Project administration, Resources, Writing – review & editing. ZZ: Conceptualization, Data curation, Formal analysis, Writing – review & editing. ZW: Formal analysis, Resources, Writing – review & editing. GY: Conceptualization, Methodology, Writing – review & editing. DM: Validation, Visualization, Writing – review & editing.

Conflict of interest

The authors declare that the research was conducted in the absence of any commercial or financial relationships that could be construed as a potential conflict of interest.

Publisher's note

References

Jostad, H. P., Liu, H., Sivasithamparam, N., and Ragni, R. (2023). Cyclic capacity of monopiles in sand under Partially drained conditions: a numerical approach. *J. Geotechnical Geoenvironmental Eng.* 149, 04022129. doi: 10.1061/JGGEFK.GTENG-10435

Li, H., Gao, Z., Bachynski-Polić, E. E., Zhao, Y., and Fiskvik, S. (2023). Effect of floater flexibility on global dynamic responses of a 15-MW semi-submersible floating wind turbine. *Ocean Eng.* 286, 115584. doi: 10.1016/j.oceaneng.2023.115584

Page, A. M., Klinkvort, R. T., Bayton, S., Zhang, Y., and Jostad, H. P. (2021). A procedure for predicting the permanent rotation of monopiles in sand supporting offshore wind turbines. *Mar. Structures* 75, 102813. doi: 10.1016/j.marstruc.2020.102813

Rui, S., Zhang, H., Xu, H., Zha, X., Xu, M., and Shen, K. (2024). Seabed structures and foundations related to deep-sea resource development: A review based on design and research. *Deep Undergr. Sci. Eng.* 3:131–148. doi: 10.1002/dug2.12042

Wang, L., Rui, S., Guo, Z., Gao, Y., Zhou, W., and Liu, Z. (2020). Seabed trenching near the mooring anchor: History cases and numerical studies. *Ocean Eng.* 218, 108233. doi: 10.1016/j.oceaneng.2020.108233

Wang, Y., O'Loughlin, C. D., Zhou, Z., and Gaudin, C. (2024). A two-dimensional effective stress framework for modelling whole-life soil strength changes due to pore pressure generation and dissipation, Part 2: Applications. *Can. Geotech. J.* 00: 1–26 . doi: 10.1139/cgj-2022-0332

Xu, H., Rui, S., Shen, K., Jiang, L., Zhang, H., and Teng, L. (2024). Shared mooring systems for offshore floating wind farms: A review. *Energy Rev.* 3, 100063. doi: 10.1016/j.enrev.2023.100063

Zhou, W., Guo, Z., Wang, L., Li, J., and Rui, S. (2021). Effect of cyclic jacking on sand-pile interface shear behaviour. *Soil Dynamics Earthquake Eng.* 141, 106479. doi: 10.1016/j.soildyn.2020.106479

frontiers | Frontiers in Marine Science

TYPE Original Research
PUBLISHED 20 March 2023
DOI 10.3389/fmars.2023.1161366

OPEN ACCESS

EDITED BY
Shengjie Rui,
Norwegian Geotechnical Institute (NGI), Norway

REVIEWED BY
Jiewei Zhan,
Chang'an University, China
Lulu Liu,
China University of Mining and Technology, China

*CORRESPONDENCE
Luqi Wang
wlq93@cqu.edu.cn

SPECIALTY SECTION
This article was submitted to Ocean Solutions, a section of the journal Frontiers in Marine Science

RECEIVED 08 February 2023
ACCEPTED 07 March 2023
PUBLISHED 20 March 2023

CITATION
Zhang W, Meng X, Wang L, Meng F, Wang Y and Liu P (2023) Reliability evaluation of reservoir bank slopes with weak interlayers considering spatial variability.
Front. Mar. Sci. 10:1161366.
doi: 10.3389/fmars.2023.1161366

Reliability evaluation of reservoir bank slopes with weak interlayers considering spatial variability

Wengang Zhang[1,2], Xuanyu Meng[1,2], Luqi Wang[1,2]*, Fansheng Meng[1,2], Yankun Wang[3] and Pengfei Liu[4]

[1]School of Civil Engineering, Chongqing University, Chongqing, China, [2]National Joint Engineering Research Center of Geohazards Prevention in the Reservoir Areas, Chongqing University, Chongqing, China, [3]School of Geosciences, Yangtze University, Wuhan, China, [4]Chongqing Institute of Geological Environment Monitoring, Chongqing, China

Reservoir bank slopes with weak interlayers are common in the Three Gorges Reservoir area. Their stabilities are affected by multi-coupled factors (e.g., reservoir water fluctuations, rainfall, and earthquakes in the reservoir area). Meanwhile, the differences in mechanical parameters of reservoir banks make it more difficult to determine the dynamic stability of bank slopes under complex mechanical environments. In this paper, the multiple disaster-causing factors and spatial variability of the landslide were comprehensively considered to study the long-term evolution trend of the bank slopes with weak interlayers. Specifically, the limit equilibrium method combined with the random field was performed to calculate the reliability. Furthermore, the long-term effects of dry-wet cycles on reservoir bank landslides and the sensitivity analysis of the statistical parameters of the random field were discussed. The results show that the earthquake action had the most significant impact on the failure probability of the landslide. The failure probability was more significantly affected by the vertical fluctuation range of the parameters and the coefficient of variation of the internal friction angle. The increase in failure probability under the action of dry-wet cycles was mainly caused by the reduction of the parameters of the weak interlayer. The reliability evaluation method of reservoir bank slopes can be applied to predict the long-term stability of the coastal banks.

KEYWORDS

slope stability, random fields, failure probability, spatial variability, multiple factors

1 Introduction

Coastal engineering (e.g., the building of sea walls, dykes, and embankments) requires high manufacturing and maintenance costs (Temmerman et al., 2013; Firth et al., 2014; Malone and Newton, 2020; Wang et al., 2020). The rise and fall of sea levels can threaten the long-term operation of coastal engineering; thus, it is necessary to analyze the effect of the changing sea levels on the coastal banks. Similar to the periodically changing reservoir

water levels (Bromhead and Ibsen, 2004; Zhan et al., 2019; Rui et al., 2020), the evaluation method of the stability of the reservoir bank can be applied to coastal engineering to some extent. There are many landslides in the Three Gorges Reservoir area, and the mechanical of the landslide with weak interlayer is complicated. Specifically, many factors induce landslides on reservoir banks, involving reservoir water level, rainfall, and seismic (Wang et al., 2021; Wang et al., 2023). Numerous researchers have studied the causes of landslide failures and concluded that rainwater infiltration is the most important triggering factor in the instability of landslides (e.g., Rahimi et al., 2011; Huang et al., 2016; Wang et al., 2019a; Zhang et al., 2020). The influencing factors of rainfall infiltration slope stability can be summarized as followings: the rainfall intensity, rainfall duration, rainfall before instability and the initial state of soil (Ng and Pang, 2000). Instability mechanism of slope under earthquake action is the key to evaluating and control slope stability under earthquake conditions. At present, there are many methods of slope stability analysis under earthquake conditions, such as the pseudo-static method, the Newmark slider analysis method, and the numerical simulation method (Shukha and Baker, 2008; Zhang and Cao, 2013; Yang et al., 2014; Yeznabad et al., 2021). Based on the quasi-static method, Biondi et al. (2002) put forward the calculation formula of pore water pressure and slope stability by studying the stability of non-cohesive soil slopes during and after earthquakes. The analysis method of the influencing factors of slope stability usually only considers the change of one factor. Notably, in the earthquake zone, the area of landslides induced by rainstorms is three times that of the landslides directly induced by earthquakes (Lin et al., 2006; Chai et al., 2013). It can be found that the rainfall in the strong earthquake area will induce a wider range of landslide disasters.

Slope stability analysis is a popular field of geotechnical engineering for the application of probabilistic methods (Xie et al., 2020). There are differences and correlations in the properties of rock and soil parameters in different spatial locations. Random field theory can better characterize this spatial variability (Wang et al., 2017; Hu and Huang, 2019; Wang et al., 2020). The use of spatially variable analysis has been shown to affect the calculated failure probability of the slope models. For example, it has been shown that for slope models with a mean factor of safety greater than 1, accounting for spatial variability of material properties (e.g., cohesion and unit weight) results in a lower failure probability, compared to the same analysis without using spatial variability (Griffiths and Fenton, 2004; Cho, 2010; Javankhoshdel et al., 2017). A probabilistic analysis that does not consider spatial variability has been shown to result in unrealistic and overly conservative failure probabilities.

In this paper, the influence of spatial variability of geotechnical parameters on actual landslide deformation and stability cannot be considered by traditional methods (Zhang et al., 2023). Thus, the effect of spatial variability of geotechnical materials on landslide stability was studied using the random field. Then, based on the actual reservoir water level fluctuation, rainfall, and regional seismic intensity in 2017, the reliability of the Zhaoshuling landslide within one year was evaluated. Moreover, the effect of dry-wet cycles on failure probability was discussed to determine the long-term evolution trend of the Zhaoshuling landslide.

2 Study area

The Zhaoshuling landslide is situated in Badong County, Hubei Province, adjacent to the Yangtze River in the north and 74 km from the Three Gorges Dam in the east (Figure 1). It is a large reservoir bank bedding landslide. The trailing edge of the Zhaoshuling landslide is about 500 m, and the leading edge is about 100 m. The main strata of the landslide were the second and third sections of the Triassic Badong Formation (T_2b^2 and T_2b^3).

FIGURE 1
Location of the Zhaoshuling landslide.

The stratum of the Zhaoshuling landslide can be divided into three parts from top to bottom: sliding mass, sliding zone, and bedrock (Zhan et al., 2022; Zhang et al., 2022a; Yang et al., 2023). Sliding mass includes sliding rock mass, gravel soil, and the main component of the sliding zone is gravel sandy clay.

The reservoir water level fluctuated between 145~175 m every year (Figure 2A); thus, there was a dry-wet cycles area with 30 m on the bank slope. In addition, there was concentrated rainfall in Badong County (Figure 2B), and the peak acceleration of ground motion was 0.05 g.

The parameters of each layer of the Zhaoshuling landslide are shown in Table 1. Notably, the dry-wet cycles area was the reduced value after 10 dry-wet cycles. And the relevant parameters were obtained from the statistics of the existing papers (Chen et al., 2011; Li et al., 2016; Salimi et al., 2021; Zhang et al., 2022a).

3 Methodology

3.1 Morgenstern-price method

Landslide stability problems are commonly analyzed by using LEMs of slices, and the approach presented here adopts the Morgenstern-Price method. The Morgenstern-Price method assumes that the relationship between the vertical force and the lateral force is $Y = \lambda f(x)X$, The FOS of the slip surface can be obtained by iterative calculation of the balance equation, and the expression is as follows:

$$FS = \frac{\sum (c\Delta LR + RN\tan\varphi)}{\sum WL_W - \sum NL_N} \tag{1}$$

$$FS = \frac{\sum (c\Delta LR\cos\alpha + RN\tan\varphi\cos\alpha)}{\sum N\sin\alpha} \tag{2}$$

$$N = \frac{W + \lambda f(x)(\frac{c\Delta L\cos\alpha}{FS}) - \frac{c\Delta L\sin\alpha}{FS}}{(\cos\alpha + \frac{\sin\alpha\tan\varphi}{FS}) - \lambda f(x)(\frac{\cos\alpha\tan\varphi}{FS} - \sin\alpha)} \tag{3}$$

Where λ is the coefficient of variation of the force between the soil strips; $f(x)$ is the change function of the force between the soil strips; ΔL is the length of the soil strip on the sliding surface; L_W is the length of the lever arm from the centroid of the soil bar to the center of the sliding surface; L_N is the distance from the midpoint of the soil strip at the sliding surface to the corresponding normal; α is the angle between the tangent of the soil strip and the horizontal plane; N is the normal force of the sliding face to the soil strip.

3.2 Random field theory

The random field uses easily available and physically meaningful parameters to characterize random phenomena at different spatial scales.

A random field $\xi(z)$ can be expressed as a trend component $t(z)$ and a volatility component $\omega(z)$. The trend component $t(z)$ is related to the absolute position in space. In addition, the trend component $t(z)$ can be regarded as the mean value μ when it is considered as a constant. If the correlation of the fluctuation component $\omega(z)$ is only related to the relative distance, the fluctuation component $\omega(z)$ can be considered as statistically uniform.

$$\xi(z) = t(z) + \omega(z) \tag{4}$$

Where z represents the spatial position.

There is an autocorrelation between the parameters of the rock and soil mass in the spatial range, which needs to be described by the autocorrelation function. The mean and variance of the random field of parameter ξ can be defined as follows:

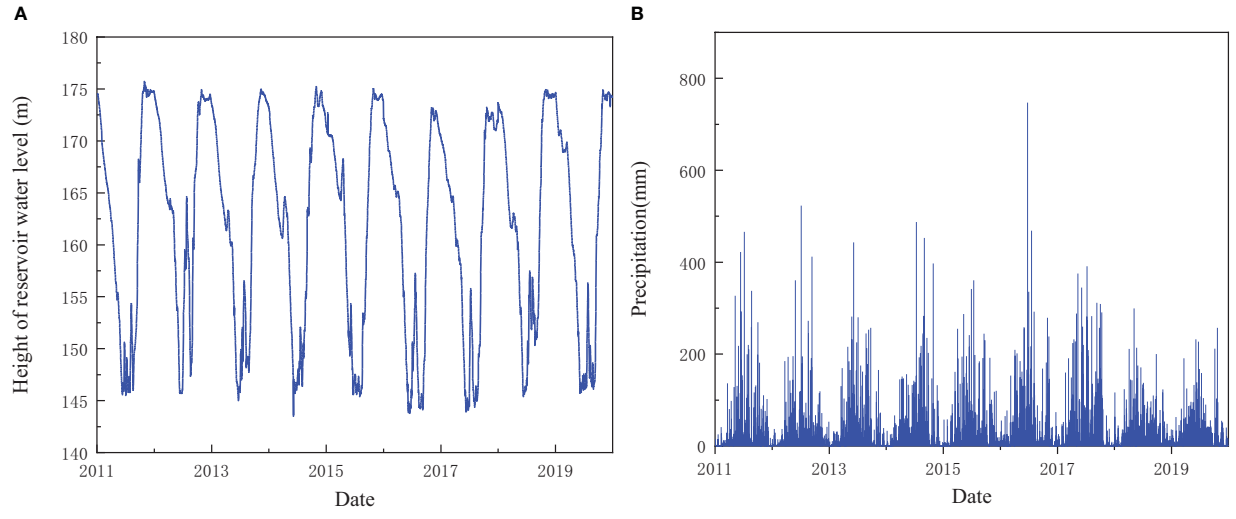

FIGURE 2
The factors affecting the seepage field of the bank landslide. **(A)** The reservoir water level of Three Gorges Reservoir; **(B)** Daily precipitation of Badong County.

TABLE 1 Parameters of rock and soil mass of Zhaoshuling landslide.

Parameter	Sliding Mass	Weak Interlayer	Silty Mudstone	Argillaceous Siltstone	Limestone
Natural unit gravity (kN/m^3)	20	21	23	25.5	25.8
Saturated unit weight (kN/m^3)	22	23	25.9	26.9	26.8
Cohesion (kPa)	130	12	120	200	350
The cohesion of dry-wet cycles zone (kPa)	117.42	6.9	/	/	/
Friction angle (°)	22	18	21	30	32
Friction angle of dry-wet cycles zone (°)	21.6	5.92	/	/	/
Tensile strength (kPa)	1	1	30	100	150
Saturated permeability coefficient (m/s)	1.157E-4	3.472E-5	5.787E-6	5.785E-5	/
Saturated volumetric water content	0.25	0.35	0.25	0.35	/
Residual volumetric water content	0.09	0.05	0.12	0.12	/

"/" indicates parameters that are not used.

$$E(\xi(z)) = \mu \tag{5}$$

$$Var(\xi(z)) = \sigma^2 \tag{6}$$

The covariance function of $\xi(z_j)$ can be expressed as follows:

$$Cov[\xi(z_i), \xi(z_j)] = E[(X(z_i) - \mu(z_i)) \cdot (X(z_j) - \mu(z_j))] \tag{7}$$

During the random field generation using the Local Average Subdivision method, the Markovian covariance functions are used to calculate the covariance value between cells in the field.

$$\rho(\tau_x, \tau_y) = exp[-\sqrt{(\frac{2\tau_x}{\delta_h})^2 + (\frac{2\tau_y}{\delta_v})^2}] \tag{8}$$

Where τ_x and τ_y represent the horizontal relative distance and vertical relative distance between any two points in space, respectively; δ_h and δ_v represent the horizontal and vertical fluctuation ranges, respectively.

3.3 Monte Carlo simulation

The method is generating a random variable sample that conforms to a certain distribution by sampling. And the set of random sample can be used in the performance function. Then, the probability of failure (P_f) is obtained by counting the proportion of failure samples:

$$F = \{F_s(x) < f_s\} \tag{9}$$

$$P_f = \int_F f(x)dx \tag{10}$$

where $f(x)$ = probability density function of random variable x ; F = failure samples;

If there are N trials in calculating FOS, and M times where FOS, the P_f can be defined as follows:

$$P_f = P(<1.2) = \frac{M}{N} \tag{11}$$

The coefficient of variation of the failure probability can be expressed as:

$$\mathrm{COV} = \sqrt{\frac{1 - P_f}{NP_f}} \tag{12}$$

3.4 Latin hypercube sampling

Latin hypercube sampling will be used in Monte Carlo simulations, it is a multidimensional stratified sampling method. The random variable is divided into N groups equally, then building a matrix P of $N \times K$, its column elements are random integers between 1-N and vary. Correspondingly, building a matrix R of $N \times K$, its column elements are random rational numbers between 1-N and vary.

$$\mathbf{S} = \frac{1}{N}(\mathbf{P} - \mathbf{R}) \tag{13}$$

$$x_{ij} = F_{x_j}^{-1}(s_{ij}) \tag{14}$$

where s_{ij} represents the element in the i row and j column of matrix $\mathbf{S}$; x_{ij} means the j variable of the i group of samples; F_{x_j} represents the distribution function of the j variable; x means sample variable.

Latin hypercube sampling avoids repeated sampling by Monte Carlo method and improves computational efficiency

3.5 Computational model of the Zhaoshuling landslide

The two-dimensional saturated-unsaturated seepage slope stability model was established in SLIDE2 (Figure 3). The length of the landslide is 1200 m, and the height of the trailing edge is

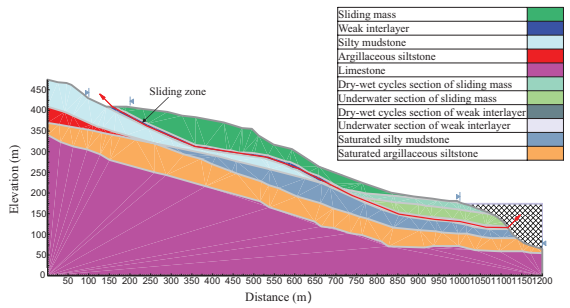

FIGURE 3
Model of the Zhaoshuling landslide.

475 m. Considering that the overall stability of the Zhaoshuling landslide was controlled by the weak interlayer, the weak interlayer was the sliding zone. The changing reservoir water levels are set at the leading edge, the other parts of the landslide are set as rainfall boundaries, and the bottom of the model is set as a waterproof boundary (Zhan et al., 2018; Rui et al., 2021).

The cohesion and friction angle of the sliding mass and the weak interlayer are respectively assigned to the spatial variability, the statistical parameters are obtained with reference to literatures (Suchomel and Masin, 2010; Jiang et al., 2015; Lü et al., 2018; Hu et al., 2020), as shown in Tables 2, 3 respectively.

3.6 Operating conditions

To facilitate the understanding of the proposed multi-factor calculation, a flow chart of failure probability assessment of the Zhaoshuling landslide is shown in Figure 4.

The reliability analysis of the Zhaoshuling landslide in a one-year period considering the spatial variability of parameters would be carried out. The pseudo-static method was used to analyze the reliability of seismic landslide when the annual failure probability was the highest. In order to study the critical instability of landslides under earthquake conditions, the horizontal seismic coefficients were calculated as 0.028, 0.05, 0.1, 0.15, and 0.224, respectively. In addition, the horizontal seismic coefficient was regarded as a random variable conforming to the log-normal distribution, and the COV of the seismic coefficient was 0.3 (Zhang et al., 2021).

The landslide reliability calculation of 30 dry-wet cycles would be carried out when the failure probability was the highest under the combined action of reservoir water level and rainfall. At the same time, the simultaneous reduction and separate reduction of the parameters of the sliding mass and the weak interlayer in the dry-wet cycles would be considered, and the influence of the dry-wet cycles on the failure probability of the landslide could be explored. Correspondingly, the parameters of the dry-wet cycles referred to the published papers (Table 4; Wang et al., 2020; He, 2020; Zhang et al., 2022a; Zhang et al., 2022b).

The random fields of cohesion and internal friction angle generated in one sampling are shown in Figures 5A, B. The mean and standard deviation of the FOS gradually converge with the increase of the number of simulations, when the number of simulations is 5000 times, $COV_{P_f} < 0.1$ (Liu et al., 2019), the calculation results reached convergence in all cases (Figure 6).

4 Result

4.1 Reliability analysis of landslide under reservoir water level and rainfall

4.1.1 January 1st ~ March 20th

In the first stage, the reservoir water level dropped slowly and there was less rainfall. The landslide failure probability was the highest at 0.76% and the lowest at 0.54%, which was always kept at a low level. The seepage pressure generated by the water level difference has little effect on the stability of the landslide. Correspondingly, there is no significant change in failure probability.

4.1.2 March 21th~ June 10th

In the second stage, the failure probability increased rapidly, from 0.54% to 6.62%. The water level difference inside and outside the landslide will generate seepage pressure pointing to the outside of the landslide. In this case, the stability of the landslide will be reduced, and the failure probability will significantly increase. Theoretically, when the reservoir water level drops rapidly to the lowest point, the seepage pressure will increase to a maximum, and the stability of the landslide is the worst at this time. With the decline of the reservoir water, the landslide stability also gradually decreased. Therefore, the landslide stability was mainly affected by the change of reservoir water level.

TABLE 2 Statistical mechanical parameters of sliding mass.

Parameters	Mean	COV	Distribution	Scale of fluctuation	Correlation coefficient
Cohesion (kPa)	130	0.3	Lognormal	$\delta_h = 40m$ $\delta_v = 4m$	-0.5
Cohesion of dry-wet cycles zone (kPa)	117.42	0.3	Lognormal	$\delta_h = 40m$ $\delta_v = 4m$	
Friction angle (°)	22	0.2	Lognormal	$\delta_h = 40m$ $\delta_v = 4m$	-0.5
Friction angle of dry - wet cycles zone (°)	21.6	0.2	Lognormal	$\delta_h = 40m$ $\delta_v = 4m$	

TABLE 3 Statistical mechanical parameters of weak interlayer.

Parameters	Mean	COV	Distribution	Scale of fluctuation	Correlation coefficient
Cohesion (kPa)	12	0.3	Lognormal	$\delta_h = 20m$ $\delta_v = 2m$	-0.5
Cohesion of dry-wet cycles zone (kPa)	6.9	0.3	Lognormal	$\delta_h = 20m$ $\delta_v = 2m$	
Friction angl (°)	18	0.2	Lognormal	$\delta_h = 20m$ $\delta_v = 2m$	-0.5
Friction angle of dry- wet cycles zone (°)	5.92	0.2	Lognormal	$\delta_h = 20m$ $\delta_v = 2m$	

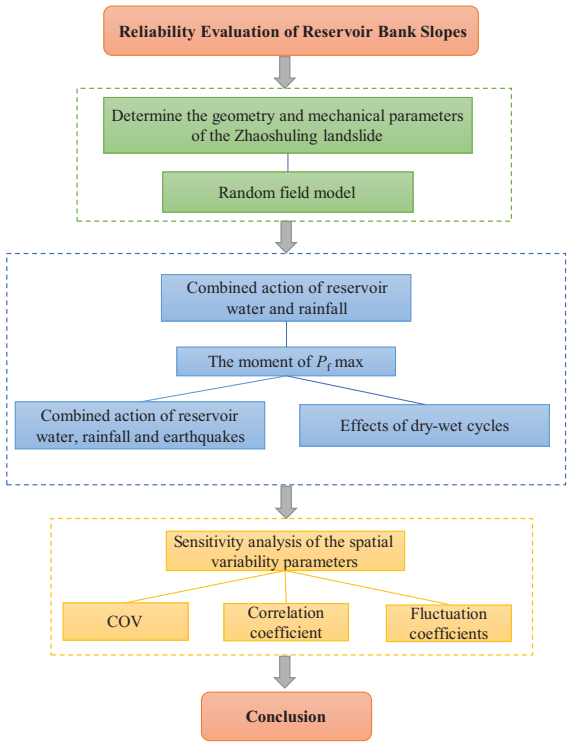

FIGURE 4
Flow chart for probability analysis of the landslide stability.

4.1.3 June 11th ~ August 20th

The reservoir water level remained at 145 m between June 11th and July 1st. Nevertheless, the failure probability as a whole showed a downward trend, from 6.04% to 4.58%. It was speculated that the hysteresis of seepage inside the slope caused the groundwater infiltration line to still change. With the gradual decline of the groundwater level in the landslide, the seepage pressure will gradually decrease. Thus, the stability of the landslide is enhanced again, and the failure probability will be reduced. After that, the reservoir water level rose, and the failure probability dropped rapidly to 1.36%. This suggests that the rising process of the reservoir water level was conducive to the stability of the landslide.

4.1.4 August 21st ~ October 20th

The reservoir water level continued to rise, and the failure probability continued to decline, from 4.92% to 0.06%. In the follow-up, even if the slope stability was significantly enhanced, the decline in the failure probability was not large. Thus, it can be found that when the failure probability was small, the stability change of the landslide cannot be well reflected. The water level in the landslide rises slowly, and the seepage pressure will be generated towards the landslide. The stability of the landslide will be enhanced, and the failure probability will be reduced.

4.1.5 October 21st ~ December 31st

At this stage, the change trends of the failure probability curve were first stable, then rising and then stable. It can be found that although

TABLE 4 Mechanical parameters of sliding mass and weak interlayer with different dry-wet cycles.

Numbers of Dry-wet Cycles	Cohesion of Sliding Mass (kPa)	Friction Angle of Sliding Mass (°)	Cohesion of Weak Interlayer (kPa)	Friction Angle of Weak Interlayer(°)
0	130	22	12	18
5	122.27	21.73	6.95	7.16
10	117.42	21.6	6.90	5.92
15	112.59	21.46	6.90	5.92
20	109.50	20.31	6.90	5.92
25	108.13	19.74	6.90	5.92
30	106.78	19.17	6.90	5.92

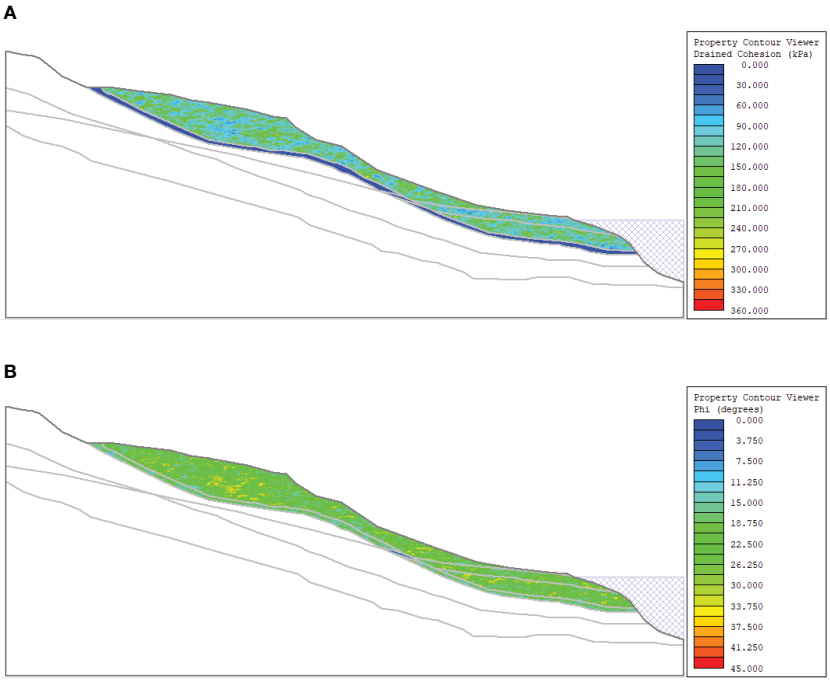

FIGURE 5
Random field model of Zhaoshuling landslide: **(A)** Random field model of cohesion; **(B)** Random field model of internal friction angle.

the reservoir water level and rainfall fluctuated slightly, the landslide stability decreased.

The annual failure probability with reservoir water fluctuation and rainfall changes as shown in Figure 7. The most unstable period of the landslide is in June. The probability of failure increased when the water level decreased, and decreased when the water level increased. Therefore, the failure probability and the water level were basically in the opposite trend. It can be found that the landslide stability was closely related to the fluctuation of the reservoir water level, while the influence of rainfall on the landslide stability was relatively small. In addition, the failure probability at the beginning of the year fluctuated around 0.6%, and the failure probability at the end of the year reached 0.7%. Thus, the landslide stability formed a closed loop after the annual reservoir water level and rainfall experienced a cyclical change.

4.2 Reliability analysis of landslide under combined seismic action of reservoir water level and rainfall

Figure 8 shows results with and without the COV of the seismic coefficient. With the increase of seismic coefficient, the failure probability of the landslide increased significantly. Obviously, the earthquake had a significant effect on the stability of the landslide. In the case of an actual seismic coefficient of 0.05, the failure probability of the landslide reaches about 90%. Notably, failure

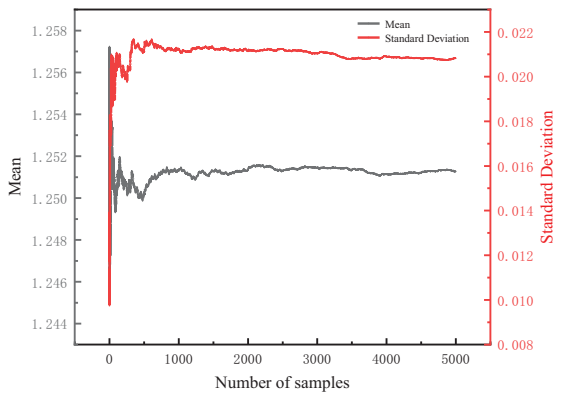

FIGURE 6
Convergence of safety of factor.

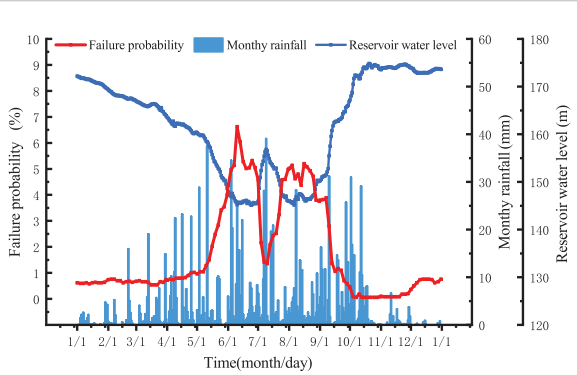

FIGURE 7
Variation of annual failure probability of the Zhaoshuling landslide.

probability decreases when seismic coefficients were regarded as random variables. Thus, the failure probability of landslide will be increased when the seismic coefficients were regarded as constants.

Figure 9A shows the distribution of the FOS was relatively concentrated when the seismic coefficients were small. Conversely, when the seismic coefficient was large, the calculated FOS were more scattered. Notably, Figure 9B shows the probability of FOS less than 1.0 was 46.58% under the horizontal seismic coefficients was 0.224. Similarly, when the horizontal seismic coefficients were 0.224, it can be found that more than half of the cases where the FOS was less than 1.0 (Figure 8A). The Zhaoshuling landslide may be in an unstable state at this time.

4.3 Sensitivity analysis

4.3.1 The effect of the COV

As the COV of cohesion or friction angle increased, the failure probability of landslide increased. Therefore, it can be found the greater the variation of strength parameters, the less conducive to the stability of the landslide. And the degree of variation in the friction angle had a greater impact on the failure probability. Notably, the small mean value of cohesion led to limited variation in the range of cohesion values under the two COV. Thus, the variation degree of cohesion had little influence on the landslide stability.

Figure 10A shows the probability density functions of the FOS. The shape of the probability density function became narrower and the uncertainty in the FOS decreased when the negative value of the COV of the friction angle increased. Similarly, the probability distribution estimated also shows the same trend (Figure 10B). In addition, although when the COV was 0.5 and the FOS was 1.0, the cumulative distribution value was still 0. The landslide will not be completely unstable.

4.3.2 The effect of the correlation coefficient

Figure 11A shows that the probability of failure increased as the correlation coefficient increased. Thus, the stronger the negative correlation between the cohesion and the friction angle, the more conducive to the stability of the slope. But the failure probability did not change much.

Figures 11B, C show that the probability density functions and the probability distribution of the FOS determined from the five correlation coefficients were almost. The reason was that the cohesion had little effect on failure probability.

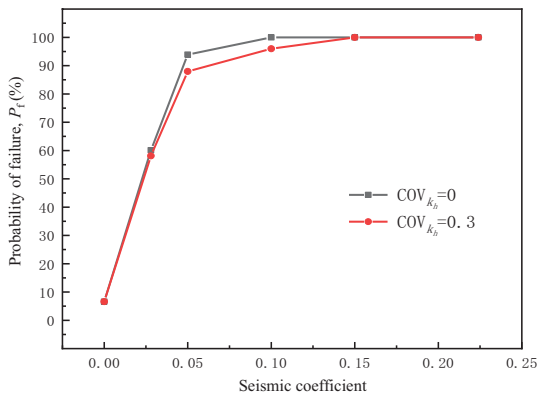

FIGURE 8
Influence of earthquake on failure probability of Zhaoshuling landslide.

4.3.3 The effect of the fluctuation

This section introduces a coefficient to represent the change in the scale of fluctuation, then the fluctuation range of the sliding mass and the weak interlayer is increased or decreased by the same multiple (Table 5). Figure 12A shows the effect of scale of fluctuation on the failure probability. Whether it was the horizontal fluctuation range δ_h or the vertical fluctuation range δ_v, as the fluctuation range increased, the failure probability of landslide increased gradually. Notably, the failure probability was more significantly affected by changes in the vertical fluctuation range.

Figure 12B shows that the probability density function curve had a very obvious change under different vertical fluctuation ranges. As the vertical fluctuation range increased, the peak value of the curve gradually decreased and shifted to the left. Therefore, the distribution of the FOS gradually became scattered and the mean value gradually decreased, and the landslide stability was gradually decreasing. And the curve difference was large when the vertical fluctuation range coefficient was between 0.5 and 2, the probability distribution estimated also shows the same trend (Figure 12C). It can be found that when the vertical fluctuation range exceeded a certain value, the failure probability was not sensitive to its change.

5 Discussion

More than 85% of the slope instability is inseparable from the action of water (Wang et al., 2019b; Yin et al., 2022; Zhang et al., 2022c). The dry-wet cycles effect caused by the rise and fall of the reservoir water level affects the stability of the bank landslide (Rejeb and Bruel, 2001). Lin et al. (2005) studied the microscopic mechanism of water weakening in sandstone, and used dry-wet cycles to simulate leaching effects. The result shows that after 60 dry-wet cycles, the strength loss of sandstone reached 20%, and the porosity showed a nonlinear increase. Under the repeated dry-wet cycles, the surface roughness coefficient, compressive strength and friction angle of the rock mass gradually decrease (Fang et al., 2019). Wang et al. (2019) analyzed the effect of water level rise and fall on the shear strength of sandstone-mudstone, and concluded that the decrease in shear strength was in a logarithmic relationship with the increase in the number of cycles. Therefore, the dry-wet cycles play an important role in the long-term effect of the reservoir bank landslides.

The results of the simulation are summarized in Figures 13, 14. With the increase of the number of dry-wet cycles, the strength of the rock and soil was reduced, and the failure probability of the landslide increased significantly. Obviously, the failure probability basically did not change after 10 dry-wet cycles. So the weakening of

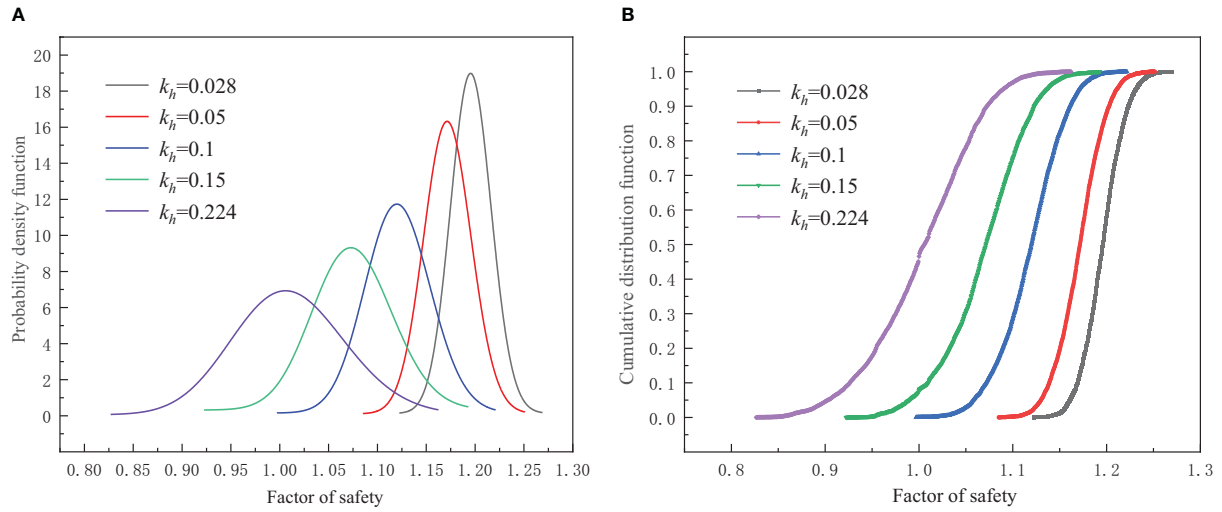

FIGURE 9
Probability density curve and cumulative distribution curve under different seismic coefficients: **(A)** probability density function; **(B)** cumulative distribution function.

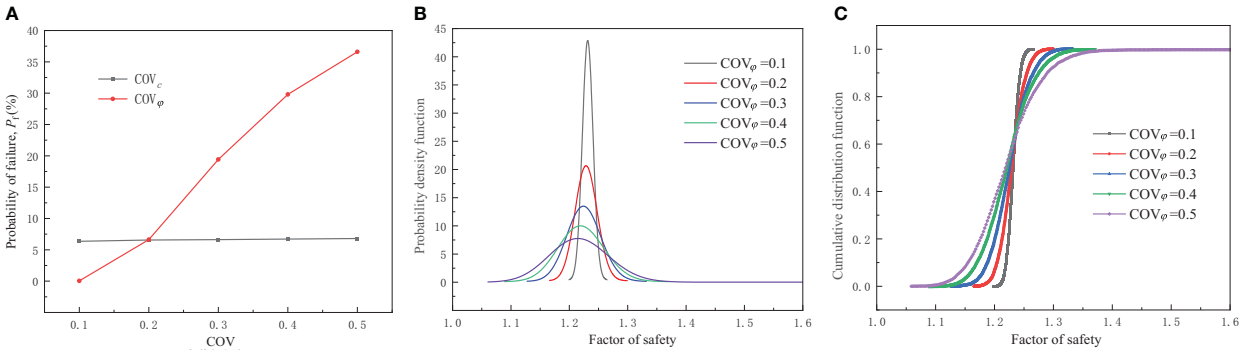

FIGURE 10
The effect of the COV: **(A)** Influence of different COV on failure probability; **(B)** probability density function; **(C)** probability distribution of the FOS.

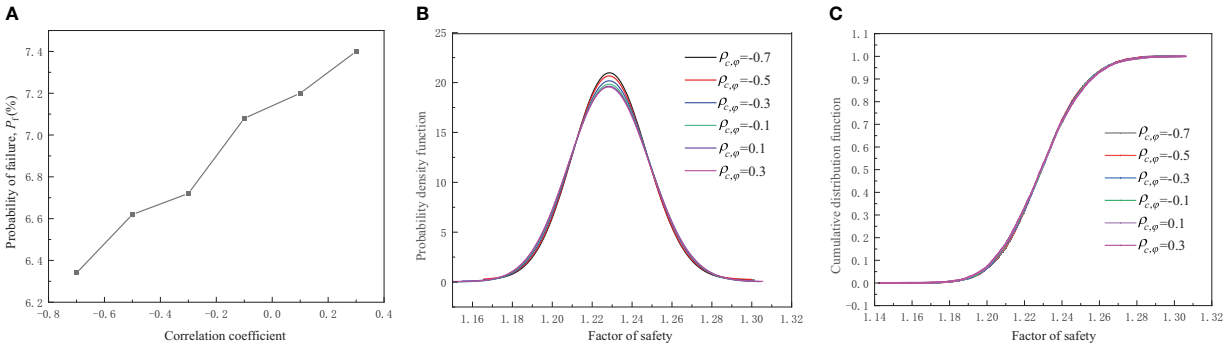

FIGURE 11
The effect of the correlation coefficient: **(A)** Influence of different correlation coefficients on failure probability; **(B)** probability density function; **(C)** probability distribution of the FOS.

TABLE 5 Changes of horizontal and vertical scale of fluctuation.

Coefficient	Stratum	Horizontal fluctuation range	Vertical fluctuation range
0.5	weak interlayer	$\delta_h = 10m$	$\delta_v = 1m$
	sliding mass	$\delta_h = 20m$	$\delta_v = 2m$
1	weak interlayer	$\delta_h = 20m$	$\delta_v = 2m$
	sliding mass	$\delta_h = 40m$	$\delta_v = 4m$
2	weak interlayer	$\delta_h = 40m$	$\delta_v = 4m$
	sliding mass	$\delta_h = 80m$	$\delta_v = 8m$
3	weak interlayer	$\delta_h = 60m$	$\delta_v = 6m$
	sliding mass	$\delta_h = 120m$	$\delta_v = 12m$
4	weak interlayer	$\delta_h = 80m$	$\delta_v = 8m$
	sliding mass	$\delta_h = 160m$	$\delta_v = 16m$

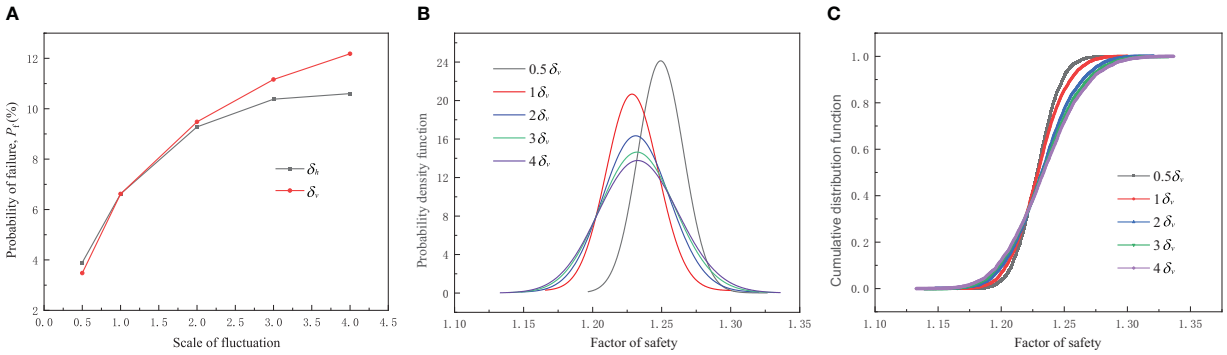

FIGURE 12
The effect of the fluctuation: **(A)** Influence of different fluctuation coefficients on failure probability; **(B)** probability density function; **(C)** probability distribution of the FOS.

the landslide stability by the dry-wet cycle was limited. The reduction of rock and soil strength parameters was also consistent with the failure probability.

Figure 14 shows the change of the failure probability of the landslide was mainly affected by the reduction of the parameters of the weak interlayer. It can be concluded that the weak interlayer played a decisive role in the landslide stability.

The stability of coastal banks is affected by the changing water levels, rainfall, and earthquakes (Sassa and Takagawa, 2019; Liu et al., 2023). The reliability evaluation method of reservoir banks under various disaster-causing factors in this paper can be applied to predict the long-term safety of the coastal banks (Cavanaugh et al., 2019).

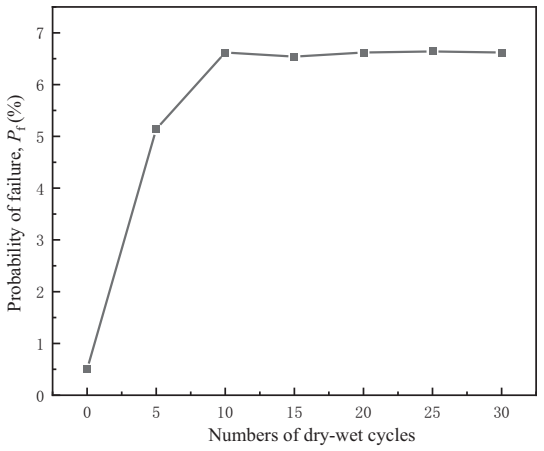

FIGURE 13
Influence of parameters degradation of sliding body and weak interlayer on failure probability under dry-wet cycles.

6 Conclusion

Considering the spatial variability of rock and soil parameters, this paper evaluated the reliability of the Zhaoshuling landslide within one year. Furthermore, the influence of dry-wet cycles on

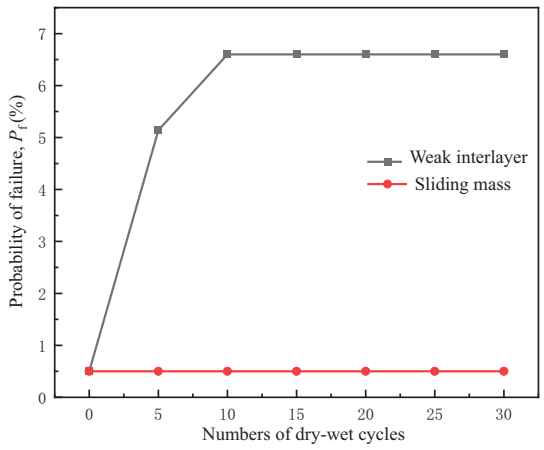

FIGURE 14
Influence of parameters degradation of only sliding mass or weak interlayer on failure probability under dry-wet cycles.

failure probability was discussed, and the sensitivity analysis of random field-related statistical parameters was carried out. Several conclusions can be obtained as followings:

(1) The annual failure probability of the Zhaoshuling landslide varied with reservoir water level and rainfall. When the reservoir water level decreased, the failure probability of the slope increased. Correspondingly, when the reservoir water level increased, the failure probability of the slope decreased. Meanwhile, rainfall had relatively little effect on failure probability. And the June was identified as the most unstable period of the year for the Zhaoshuling landslide.

(2) With the increase of seismic coefficient, the failure probability of landslide increased significantly. Thus, the most important external action affecting the stability of the slope was the earthquake. In addition, the resulting failure probability was slightly reduced when the seismic coefficients were treated as random variables.

(3) Due to the increase in the number of dry-wet cycles, the strength of rock and soil was gradually reduced, and the failure probability of landslide increased significantly. Moreover, the change of the failure probability of the landslide was mainly caused by the reduction of the parameters of the weak interlayer. It was proved that the weak interlayer played a decisive role in the landslide stability.

(4) The spatial variability of rock and soil parameters had a significant impact on the slope stability. The failure probability will increase with the increase of the COV, correlation coefficient, and fluctuation range, respectively. Especially, attention should be paid to the COV of the internal friction angle and the vertical fluctuation range of the parameter when evaluating the reliability of the landslide. The research results can provide important references for the analysis of the formation mechanism of wading landslides, monitoring, and emergency management.

Data availability statement

The raw data supporting the conclusions of this article will be made available by the authors, without undue reservation.

Author contributions

WZ: Supervision, writing- reviewing, and editing. LW: Data curation and writing- original draft preparation. XM and FM: Conceptualization and methodology. YW: Visualization and validation. PL: investigation. All authors contributed to the article and approved the submitted version.

Funding

This study was supported by the National Key R & D Program of China (2019YFC1509605), Cooperation projects between Chongqing University, Chinese Academy of Sciences and other institutes (HZ2021001), Sichuan Transportation Science and Technology Project (2018-ZL-01), China Postdoctoral Science Foundation funded project (2021M700608) and Natural Science Foundation of Chongqing, China (cstc2021jcyj-bsh0047).

Conflict of interest

The authors declare that the research was conducted in the absence of any commercial or financial relationships that could be construed as a potential conflict of interest.

Publisher's note

References

Biondi, G., Cascone, E., and Maugeri, M. (2002). Flow and deformation failure of sandy slopes. *Soil Dynamics Earthquake Eng.* 22 (9-12), 1103–1114. doi: 10.1016/S0267-7261(02)00136-7

Bromhead, E. N., and Ibsen, M. L. (2004). Bedding-controlled coastal landslides in southeast Britain between axmouth and the Thames estuary. *Landslides* 1, 131–141. doi: 10.1007/s10346-004-0015-3

Cavanaugh, K. C., Reed, D. C., Bell, T. W., Castorani, M. C. N., and Beas-Luna, R. (2019). Spatial variability in the resistance and resilience of giant kelp in southern and Baja California to a multiyear heatwave. *Front. Mar. Sci.* 6, 413. doi: 10.3389/fmars.2019.00413

Chai, B., Yin, K. L., Du, J., and Xiao, L. L. (2013). Correlation between incompetent beds and slope deformation at badong town in the three gorges reservoir, China. *Environ. Earth Sci.* 69 (1), 209–223. doi: 10.1007/s12665-012-1948-9

Chen, L. X., Yin, K. L., and Dai, Y. X. (2011). Building vulnerability evaluation in landslide deformation phase. *J. Mountain Sci.* 8 (2), 286–295. doi: 10.1007/s11629-011-2101-z

Cho, S. E. (2010). Probabilistic assessment of slope stability that considers the spatial variability of soil properties. *J. Geotechnical Geoenvironmental Eng.* 136 (7), 975–984. doi: 10.1061/(ASCE)GT.1943-5606.0000309

Fang, J. C., Deng, H. F., Qi, Y., Xiao, Y., Zhang, H. B., and Li, J. L. (2019). Analysis of changes in the micromorphology of sandstone joint surface under dry-wet cycling. *Adv. Materials Sci. Eng.* 11, 8758203. doi: 10.1155/2019/8758203

Firth, L. B., Thompson, R. C., Bohn, K., Abbiati, M., Airoldi, L., Bouma, T. J., et al. (2014). Between a rock and a hard place: Environmental and engineering considerations when designing coastal defence structures. *Coast. Eng.* 87, 122–135. doi: 10.1016/j.coastaleng.2013.10.015

Griffiths, D. V., and Fenton, G. A. (2004). Probabilistic slope stability analysis by finite elements. *J. Geotechnical Geoenvironmental Eng.* 130 (5), 507–518. doi: 10.1061/(ASCE)1090-0241(2004)130:5(507)

He, Q. (2020). *Effect of dry-wet cycle on landslide soil strength and landslide stability analysis in three gorges reservoir area* (Wuhan, China: Wuhan Institute of Technology).

Hu, H. Q., and Huang, Y. (2019). PDEM-based stochastic seismic response analysis of sites with spatially variable soil properties. *Soil Dynamics Earthquake Eng.* 125, 105736. doi: 10.1016/j.soildyn.2019.105736

Hu, H. Q., Huang, Y., and Zhao, L. Y. (2020). Probabilistic seismic-stability analysis of slopes considering the coupling effect of random ground motions and spatially-variable soil properties. *Natural Hazards Rev.* 21 (3), 04020028. doi: 10.1061/(ASCE)NH.1527-6996.0000402

Huang, Q. X., Wang, J. L., and Xue, X. (2016). Interpreting the influence of rainfall and reservoir infilling on a landslide. *Landslides* 13 (5), 1139–1149. doi: 10.1007/s10346-015-0644-8

Javankhoshdel, S., Luo, N., and Bathurst, R. J. (2017). Probabilistic analysis of simple slopes with cohesive soil strength using RLEM and RFEM. *Georisk-Assessment Manage. Risk Engineered Syst. Geohazards* 11 (3), 231–246. doi: 10.1080/17499518.2016.1235712

Jiang, S. H., Li, D. Q., Cao, Z. J., Zhou, C. B., and Phoon, K. K. (2015). Efficient system reliability analysis of slope stability in spatially variable soils using monte carlo simulation. *J. Geotechnical Geoenvironmental Eng.* 141 (2), 04014096. doi: 10.1061/(ASCE)GT.1943-5606.0001227

Li, D. L., Liu, X. R., Li, X. W., and Liu, Y. Q. (2016). The impact of microearthquakes induced by reservoir water level rise on stability of rock slope. *Shock Vibration*, 7583108. doi: 10.1155/2016/7583108

Lin, M. L., Jeng, F. S., Tsai, L. S., and Huang, T. H. (2005). Wetting weakening of tertiary sandstones-microscopic mechanism. *Environ. Geology* 48 (2), 265–275. doi: 10.1007/s00254-005-1318-y

Lin, C. W., Liu, S. H., Lee, S. Y., and Liu, C. C. (2006). Impacts of the chi-chi earthquake on subsequent rainfall-induced landslides in central Taiwan. *Eng. Geology* 86 (2-3), 87–101. doi: 10.1016/j.enggeo.2006.02.010

Liu, X., Wang, Y., and Li, D. Q. (2019). Investigation of slope failure mode evolution during large deformation in spatially variable soils by random limit equilibrium and material point methods. *Comput. Geotechnics* 111, 301–312. doi: 10.1016/j.compgeo.2019.03.022

Liu, S., Wang, L., Zhang, W., He, Y., and Pijush, S. (2023). A comprehensive review of machine learning-based methods in landslide susceptibility mapping. *Geological J.* 1, 19. doi: 10.1002/gj.4666

Lü, Q., Xiao, Z. P., Zheng, J., and Shang, Y. Q. (2018). Probabilistic assessment of tunnel convergence considering spatial variability in rock mass properties using interpolated autocorrelation and response surface method. *Geosci. Front.* 9 (6), 1619–1629. doi: 10.1016/j.gsf.2017.08.007

Malone, T. C., and Newton, A. (2020). The globalization of cultural eutrophication in the coastal ocean: causes and consequences. *Front. Mar. Sci.* 7, 670. doi: 10.3389/fmars.2020.00670

Ng, C. W. W., and Pang, Y. W. (2000). Influence of stress state on soil-water characteristics and slope stability. *J. Geotechnical Geoenvironmental Eng.* 126 (2), 157–166. doi: 10.1061/(ASCE)1090-0241(2000)126:2(157)

Rahimi, A., Rahardjo, H., and Leong, E. C. (2011). Effect of antecedent rainfall patterns on rainfall-induced slope failure. *J. Geotechnical Geoenvironmental Eng.* 137 (5), 483–491. doi: 10.1061/(ASCE)GT.1943-5606.0000451

Rejeb, A., and Bruel, D. (2001). Hydromechanical effects of shaft sinking at the Sellafield site. *Int. J. Rock Mechanics Min. Sci.* 38 (1), 17–29. doi: 10.1016/S1365-1609(00)00061-7

Rui, S. J., Guo, Z., Si, T. L., and Li, Y. J. (2020). Effect of particle shape on the liquefaction resistance of calcareous sands. *Soil Dynamics Earthquake Eng.* 137, 106302. doi: 10.1016/j.soildyn.2020.106302

Rui, S. J., Wang, L. Z., Guo, Z., Cheng, X. M., and Wu, B. (2021). Monotonic behavior of interface shear between carbonate sands and steel. *Acta Geotechnica* 16, 167–187. doi: 10.1007/s11440-020-00987-9

Salimi, K., Cerato, A. B., Vahedifard, F., and Miller, G. A. (2021). General model for the uniaxial tensile strength characteristic curve of unsaturated soils. *J. Geotechnical Geoenvironmental Eng.* 147 (7), 04021051. doi: 10.1061/(ASCE)GT.1943-5606.0002567

Sassa, S., and Takagawa, T. (2019). Liquefied gravity flow-induced tsunami: first evidence and comparison from the 2018 Indonesia sulawesi earthquake and tsunami disasters. *Landslides* 16, 195–200. doi: 10.1007/s10346-018-1114-x

Shukha, R., and Baker, R. (2008). Design implications of the vertical pseudo-static coefficient in slope analysis. *Comput. Geotechnics* 35 (1), 86–96. doi: 10.1016/j.compgeo.2007.01.005

Suchomel, R., and Masin, D. (2010). Comparison of different probabilistic methods for predicting stability of a slope in spatially variable c-phi soil. *Comput. Geotechnics* 37 (1-2), 132–140. doi: 10.1016/j.compgeo.2009.08.005

Temmerman, S., Meire, P., Bouma, T., Herman, P. J., Ysebaert, T., De Vriend, H., et al. (2013). Ecosystem-based coastal defence in the face of global change. *Nature* 504, 79–83. doi: 10.1038/nature12859

Wang, C. F., Chen, Q. S., Shen, M. F., and Juang, H. (2017). On the spatial variability of CPT-based geotechnical parameters for regional liquefaction evaluation. *Soil Dynamics Earthquake Eng.* 95, 153–166. doi: 10.1016/j.soildyn.2017.02.001

Wang, J. J., Liu, M. N., Jian, F. X., and Chai, H. J. (2019). Mechanical behaviors of a sandstone and mudstone under loading and unloading conditions. *Environ Earth Sci* 78, 30. doi: 10.1007/s12665-018-8020-3

Wang, L. Z., Rui, S. J., Guo, Z., Gao, Y. Y., Zhou, W. J., and Liu, Z. Y. (2020). Seabed trenching near the mooring anchor: History cases and numerical studies. *Ocean Eng.* 218, 108233. doi: 10.1016/j.oceaneng.2020.108233

Wang, L., Tang, L., Wang, Z., Liu, H., and Zhang, W. (2020). Probabilistic characterization of the soil-water retention curve and hydraulic conductivity and its application to slope reliability analysis. *Comput. Geotechnics* 121, 103460. doi: 10.1016/j.compgeo.2020.103460

Wang, L. Q., Yin, Y. P., Huang, B. L., and Dai, Z. W. (2020). Damage evolution and stability analysis of the jianchuandong dangerous rock mass in the three gorges reservoir area. *Eng. Geology* 265, 105439. doi: 10.1016/j.enggeo.2019.105439

Wang, L. Q., Yin, Y. P., Huang, B. L., Zhang, Z. H., and Wei, Y. J. (2019a). Formation and characteristics of guang'an village landslide in wuxi, chongqing, China. *Landslides* 16 (1), 127–138. doi: 10.1007/s10346-018-1086-x

Wang, L. Q., Yin, Y. P., Zhang, Z. H., Huang, B. L., Wei, Y. J., Zhao, P., et al. (2019b). Stability analysis of the xinlu village landslide (Chongqing, China) and the influence of rainfall. *Landslides* 16 (10), 1993–2004. doi: 10.1007/s10346-019-01240-5

Wang, L., Zhang, Z., Huang, B., Hu, M., and Zhang, C. (2021). Triggering mechanism and possible evolution process of the ancient qingshi landslide in the three gorges reservoir. *Geomatics Natural Hazards Risk* 12 (1), 3160–3174. doi: 10.1080/19475705.2021.1998230

Wang, L. Q., Xiao, T., Liu, S. L., Zhang, W. G., Yang, B. B., and Chen, L. C. (2023). Quantification of model uncertainty and variability for landslide displacement prediction based on Monte Carlo simulation. *Gondwana Res.* doi: 10.1016/j.gr.2023.03.006

Xie, J., Uchimura, T., Wang, G., Shen, Q., Maqsood, Z., Xie, C. R., et al. (2020). A new prediction method for the occurrence of landslides based on the time history of tilting of the slope surface. *Landslides* 17, 301–312. doi: 10.1007/s10346-019-01283-8

Yang, C. W., Zhang, J. J., Fu, X., Zhu, C. B., and Bi, J. W. (2014). Improvement of pseudo-static method for slope stability analysis. *J. Mountain Sci.* 11 (3), 625–633. doi: 10.1007/s11629-013-2756-8

Yang, H., Song, K., Chen, L., and Qu, L. (2023). Hysteresis effect and seasonal step-like creep deformation of the Jiuxianping landslide in the Three Gorges Reservoir Region. *Eng. Geol.* doi: 10.1016/j.enggeo.2023.107089

Yeznabad, A. F., Molnar, S., and Naggar, H. E. (2021). Probabilistic solution for the seismic sliding displacement of slopes in greater Vancouver. *Soil Dynamics Earthquake Eng.* 140, 106393. doi: 10.1016/j.soildyn.2020.106393

Yin, Y. P., Wang, L. Q., Zhang, W. G., Zhang, Z. H., and Dai, Z. W. (2022). Research on the collapse process of a thick-layer dangerous rock on the reservoir bank. *Bull. Eng. Geology Environ.* 81, 109. doi: 10.1007/s10064-022-02618-x

Zhan, J. W., Wang, Q., Zhang, W., Shangguan, Y., Song, S., and Chen, J. (2019). Soil-engineering properties and failure mechanisms of shallow landslides in soft-rock materials. *Catena* 181, 104093. doi: 10.1016/j.catena.2019.104093

Zhan, J., Yu, Z., Lv, Y., Peng, J., Song, S., and Yao, Z. (2022). Rockfall hazard assessment in the taihang grand canyon scenic area integrating regional-scale identification of potential rockfall sources. *Remote Sens.* 14 (13), 3021. doi: 10.3390/rs14133021

Zhan, J., Zhang, W., Chen, J., Niu, C., Han, X., Sun, X., et al. (2018). Mass movements along the rapidly uplifting river valley, southeast margin of the Tibetan plateau. *Environ. Earth Sci.* 77, 634. doi: 10.1007/s12665-018-7825-4

Zhang, K., and Cao, P. (2013). Slope seismic stability analysis on kinematical element method and its application. *Soil Dynamics Earthquake Eng.* 50, 62–71. doi: 10.1016/j.soildyn.2013.03.002

Zhang, W., He, Y., Wang, L., Liu, S., and Meng, X. (2023). Landslide susceptibility mapping using random forest and extreme gradient boosting: A case study of fengjie, chongqing. *Geological J.* 1–16. doi: 10.1002/gj.4683

Zhang, W., Li, H., Tang, L., Gu, X., Wang, L., and Wang, L. (2022c). Displacement prediction of jiuxianping landslide using gated recurrent unit (GRU) networks. *Acta Geotechnica* 17, 1367–1382. doi: 10.1007/s11440-022-01495-8

Zhang, W. G., Meng, F. S., Chen, F. Y., and Liu, H. L. (2021). Effects of spatial variability of weak layer and seismic randomness on rock slope stability and reliability analysis. *Soil Dynamics Earthquake Eng.* 146, 106735. doi: 10.1016/j.soildyn.2021.106735

Zhang, W. G., Meng, X. Y., Wang, L. Q., and Meng, F. S. (2022a). Stability analysis of the reservoir bank landslide with weak interlayer considering the influence of multiple factors. *Geomatics Natural Hazards Risk* 13 (1), 2911–2924. doi: 10.1080/19475705.2022.2149356

Zhang, W. G., Tang, L. B., Li, H. R., Wang, L., Cheng, L. F., Zhou, T. Q., et al. (2020). Probabilistic stability analysis of bazimen landslide with monitored rainfall data and water level fluctuations in three gorges reservoir, China. *Front. Struct. Civil Eng.* 14 (5), 1247–1261. doi: 10.1007/s11709-020-0655-y

Zhang, K., Wang, L., Dai, Z., Huang, B., and Zhang, Z. (2022b). Evolution trend of the huangyanwo rock mass under the action of reservoir water fluctuation. *Natural Hazards* 113, 1583–1600. doi: 10.1007/s11069-022-05359-y

frontiers | Frontiers in Marine Science

TYPE Review
PUBLISHED 31 March 2023
DOI 10.3389/fmars.2023.1158685

OPEN ACCESS

EDITED BY
Shengjie Rui,
Norwegian Geotechnical Institute (NGI), Norway

REVIEWED BY
Jin Qian,
Institute of Oceanology (CAS), China
Bin Gong,
Shandong University of Science and Technology, China
Jun Liu,
Wenzhou University, China

*CORRESPONDENCE
Jiangxin Chen
jiangxin_chen@sina.com
Yonggang Jia
yonggang@ouc.edu.cn

SPECIALTY SECTION
This article was submitted to Ocean Solutions, a section of the journal Frontiers in Marine Science

RECEIVED 04 February 2023
ACCEPTED 07 March 2023
PUBLISHED 31 March 2023

CITATION
Zhu C, Li Q, Li Z, Duan M, Li S, Zhou Q, Geng M, Chen J and Jia Y (2023) Seabed fluid flow in the China Seas. *Front. Mar. Sci.* 10:1158685. doi: 10.3389/fmars.2023.1158685

Seabed fluid flow in the China Seas

Chaoqi Zhu[1,2,3], Qingping Li[4], Zhenghui Li[1], Minliang Duan[5], Sanzhong Li[3,6], Qingjie Zhou[7], Minghui Geng[8], Jiangxin Chen[9]* and Yonggang Jia[1,2]*

[1]Shandong Provincial Key Laboratory of Marine Environment and Geological Engineering, Ocean University of China, Qingdao, Shandong, China, [2]Laboratory for Marine Geology, Qingdao National Laboratory for Marine Science and Technology, Qingdao, Shandong, China, [3]Key Laboratory of Submarine Geosciences and Prospecting Techniques (MoE), Ocean University of China, Qingdao, Shandong, China, [4]China National Offshore Oil Corporation Research Center, Beijing, China, [5]Hainan Branch of China National Offshore Oil Corporation Limited, Haikou, Hainan, China, [6]Laboratory for Marine Mineral Resources, Qingdao National Laboratory for Marine Science and Technology (Qingdao), Qingdao, Shandong, China, [7]Key Laboratory of Marine Geology and Metallogeny, First Institute of Oceanography, Ministry of Natural Resources, Qingdao, Shandong, China, [8]Key Laboratory of Marine Mineral Resources, Ministry of Natural Resources, Guangzhou Marine Geological Survey, Guangzhou, Guangdong, China, [9]Key Laboratory of Gas Hydrate, Ministry of Natural Resources, Qingdao Institute of Marine Geology, Qingdao, Shandong, China

Seabed fluid flow is a widespread and important natural phenomenon in marine environments, which involves complex multi-physics, multi-process and multi-scale processes. The developments in offshore geophysical technology have facilitated the discovery of the widespread emissions of seabed fluids. For an overview on the state-of-the-art seabed fluid flow research and for obtaining a perspective on future research in the China Seas, we reviewed the data, reports, and publications particularly that associated with cold seeps such as pockmarks, seeps, domes, mud volcanoes, and gas hydrates in the Bohai Sea, the Yellow Sea, the East China Sea, and the South China Sea. This study presents the first report for seabed fluid flow on all China Seas with the basic information required to undertake additional analytical studies of these features. Furthermore, we explore processes responsible for them and their implications. Although the seabed fluid flow is widespread, dynamic, and influential, it is still poorly examined and understood. To understand seabed fluid flow in both time and space, it is important to investigate how and why these seabed fluids form and migrate.

KEYWORDS

China Seas, gas hydrate, methane seep, shallow gas, pockmark, mud volcano, hydrocarbon seepage, marine energy

1 Introduction

Seabed fluid flow encompasses various fluids (liquids and gases) that pass from sediments to seawater (Judd and Hovland, 2009; Zhu et al., 2023). These fluids from dozens of meters to kilometers below the seafloor migrate *via* pathways such as faults, pipes, gas chimneys, and mud diapirs, thus escaping from the seafloor to produce multiple

geomorphic features such as pockmarks and mud volcanoes at different scales (Westbrook et al., 2009; Bünz et al., 2012; Brothers et al., 2013; Andreassen et al., 2017; Serie et al., 2020; Yang et al., 2021). Multi-physics (e.g. solid, liquid, and gas), multi-process (e.g. geological, mechanical, and chemical processes) and multi-scale (e.g. pore-scale and region-scale) processes are involved in the seabed fluid flow (Judd and Hovland, 2009). Seabed fluid exchanges at the seabed-seawater boundary are as important as interactions between oceans and atmosphere (Judd and Hovland, 2009). After seeping into seawater, seabed fluid significantly affects the marine environment such as the physical, chemical, and biological nature of seawater. Furthermore, methane emitted from hydrothermal vents, cold seeps, and mud volcanoes in deep oceans can pass *via* the hydrosphere into the atmosphere. Seabed fluid flow is significant for sub-seabed and seabed geological features, marine biological processes, and composition of oceans, involving geosciences, biosciences, chemical, environmental, and ocean sciences. The presence of seabed fluid flow shows hydrocarbon (gas, oil, gas hydrate) generation, migration, accumulation, and the destabilization of seabed structures, which results in geological hazards such as sedimentary collapse and submarine landslide and poses a potential danger to hydrocarbon exploitation and submarine engineering (Jia et al., 2016; Rui et al., 2020; Wang et al., 2020; Zhu et al., 2020; Zhu et al., 2021).

Multiple developments in offshore geophysical technology (Figure 1) over four decades have allowed marine scientists and engineers to determine and map seabed fluid flow. High-resolution seismic profilers, side-can sonar systems, multibeam echo sounders, remotely operated submersibles (ROVs), and autonomous underwater vehicles (AUVs) have enabled wide, rapid, and detailed surveys from coastal seas to deep oceans. These developments facilitate worldwide discoveries of the widespread emissions of water, petroleum fluids, and hydrothermal fluids. To examine the distribution and nature of the seabed fluid flow, reviewing all data, reports, and publications on seabed fluid flow is necessary. However, offshore geophysical technologies and publications have progressed at an incredible rate that it is impossible to include every example. Therefore, this study is limited to the examples of features associated with seabed fluid flow in the China Seas. The literature on hydrothermal vents is extensive, and therefore we focus on "cold" seeps such as pockmarks, seeps, domes, mud volcanoes, and gas hydrates. This study provides the scientific community with the compendium of seabed fluid flow as the base for additional analytical and profound approaches to subsequent investigations.

2 Geological settings of the China Seas

The China Seas, located in the northwestern Pacific Ocean, consist of four parts, the Bohai Sea, the Yellow Sea, the East China Sea, and the South China Sea (Hu and Wang, 2016). They form an arc from north to south. Figure 2 shows the location map of these China Seas.

The Bohai Sea (Figure 2) is a semi-closed marginal sea in eastern China having a total area of ~77000 km^2 and an average depth of 18 m (Du et al., 2021; Zhang Y et al., 2020; Zhu et al., 2018). Geologically, it belongs to the offshore portion of the Bohai Bay Basin, which is a typical Mesozoic and Cenozoic rifting basin (Hu et al., 2001). Strongly controlled by the Tan-Lu and Zhangjiako-Penglai fault zones (Qi and Yang, 2010; Teng et al., 2010), the Bohai Sea rifts early from the Paleogene and enters the post-rifting thermal subsidence phase from the Neogene with ~7 km of Cenozoic sediments accumulated in sub-basins (Allen et al., 1997; Li et al., 2012; Wang et al., 2014). Neotectonism (tectonic motions after 5.1 Ma) in the Bohai Sea induced multiple faults and traps in the Neogene-Quaternary sequences, thus controlling the tectonic pattern to date (Gong et al., 2010).

The Yellow Sea (Figure 2), embracing an area of ~4.0 × 10^5 km^2, is located on the shallow continental shelf with an average water depth of 44 m (Wang et al., 2014). By a line from the easternmost tip of China's Shandong Peninsula to the western end of North Korea's South Hwanghae Province, the water body is divided into the larger southern and smaller northern yellow seas. The former connects with the Bohai Sea in the Bohai strait and experiences a

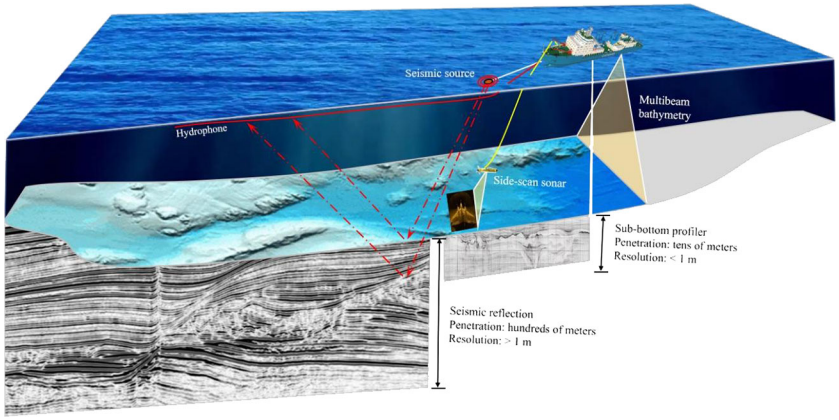

FIGURE 1
Graphic showing geophysical approaches used to identify seabed fluid flows.

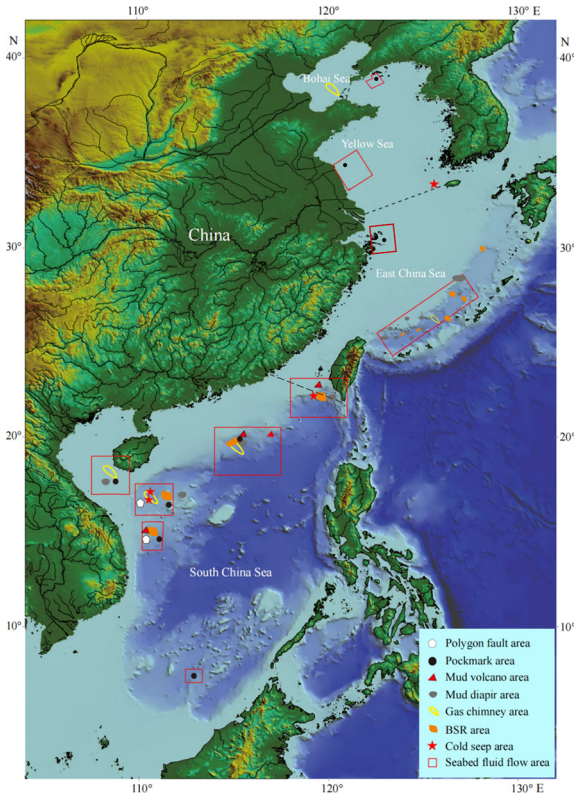

FIGURE 2
Location of these China Seas and the distribution of the fluid escape structures. White pentagon = polygon fault area, black solid circle = pockmark area, red triangle = mud volcano area, gray solid circle = mud diapir area, yellow hollow circle = gas chimney area, orange leaf-shape = bottom-simulating reflector (BSR) area, red star = cold-seep area, and red rectangle = seabed fluid flow area.

major phase of the Paleogene rifting and the initial and Neogene thermal subsidence (He et al., 2007). The latter, however, follows an additional uplift and erosion phase from the late Oligocene to the early Miocene (Yi et al., 2003; Lee, 2010). Here, rifting was confined to localized half-grabens controlled by the Jiaxiang fault with a relatively insignificant thermal subsidence phase (Lee, 2010).

The East China Sea (Figure 2) along the southeastern Chinese continental margin, covering an area of 7.7×10^5 km^2, is composed of the continental shelf with shelf break at water depths of 140–160 m, and the Okinawa trough with an average water depth of 370 m (Wang et al., 2014). The East China Sea continental shelf is featured by NE-striking uplifts and depressions, evolved from the deep Paleogene continental margin rift and has experienced regional open-sea subsidence after the Pliocene (Zhou et al., 1989; Li et al., 2009). However, the Okinawa trough is an active back-arc rifting basin behind the Ryukyu arc, formed by the northwest subduction of the Philippine Sea plate beneath the Eurasian plate (Sibuet et al., 1998). At its early evolution stage, the back-arc rifting is progressive and the syn-rift sedimentation at a rate of 1–2 m/ka has been underway after the late Pleistocene (Tsugaru et al., 1991; Park et al., 1998).

The South China Sea (Figure 2), situated between the western pacific, Eurasian, and Indo-Australian plates, is the largest marginal sea in the western pacific, occupying an area of ~3.5×10^6 km^2 (Wang et al., 2014). The deep-sea basin, continental slope, and continental shelf cover ~15%, 38%, and 47% of the total South China Sea area, respectively; it has an average water depth of 1140 m (Wang et al., 2014). The South China Sea has experienced complex structural and thermal evolution in the Cenozoic (Taylor and Hayes, 1983; Hutchison, 2004). Tectonically, it is characterized by both the northern extensional passive and western strike-slip continental, southern compressive, and eastern active convergent margins (Chen et al., 2015a). Currently, the oceanic crust of the South China Sea is subducting eastward along the Manila trench (Wang et al., 2014).

3 Seabed fluid flow in the Bohai Sea

The highly fluctuating methane in the nearshore areas is attributed to the combined influences of land inputs and *in situ* petroleum contamination. Around the Bohai Sea, the Yellow River water has been reported to contain high methane (Gu et al., 2011). However, the river input of methane is negligible in the central Bohai Sea. Moreover, the tremendous heterogeneity of sea surface methane distributions indicates gas leakage from the seafloor (Zhang et al., 2014a). During the survey periods, the Bohai Sea was a net source of atmospheric methane (Zhang et al., 2014b). The PL19-3 giant oilfield is situated where faulting occurred violently during neotectonism. Oil migrated along the densely distributed

faults and charged the PL19-3 structure rapidly. Fluid/oil migration and accumulation triggered by earthquakes are non-continuous and episodic (Zou et al., 2011). The active faults in the neotectonism became passages for oil to migrate from the Paleogene to Neogene (Gong et al., 2004). Charging the shallow Neogene reservoirs was dynamic, probably ongoing, as a combined result of the existence of active source rocks, development of overpressure, and fault reactivation from 5.1 Ma (Hao et al., 2012). Migration modelling without considering the effect of the densely distributed faults describes a good match between petroleum occurrences and predicted preferential petroleum migration pathways and accumulations, indicating that the densely distributed faults in the Neogene sediments do not influence the petroleum enrichment. If the densely distributed faults in the Neogene sediments act as vertical conduits for petroleum migration, most petroleum would have migrated to Quaternary sediments or the seafloor, causing oil dispersion and degradation (Hao et al., 2007).

Neotectonic controls the late-stage hydrocarbon accumulation and maintains the sustained dynamic equilibrium where the accumulation amount is greater than the diffusion loss in oil and gas. Seismic sections extensively show active fluid escape in the shallow strata *via* faults and gas chimneys in the Bohai Sea such as the PL19-3 oil field (Figure 3, Gong, 2005). High-resolution seismic sections show densely distributed faults before the late Pleistocene and relatively weak fault activities afterward (Wang et al., 2011). Shallow gas occurs at different depths, and the blowouts threaten platforms, causing serious accidents in several drilling operations (Yang and Qi, 2004). The detection of extensive shallow gas by the regional geological survey (Hou et al., 2016) and its accumulation above these faults in the Laizhou Bay (Du et al., 2007) shows the development of widespread fluid flow in the Bohai Sea. However, the distribution, geological controls, and origin of fluids remain unclear following inadequate detailed geophysical investigation and *in situ* measurement and less investigation in methane flux and its environmental effects. Note that the famous Penglai 19-3 oil-spill accident between June 2011 and August 2011 was induced by fluid escape along faults activated by overpressure water injection in the well, indicating that shallow faults can be activated by overpressure fluid flow or geological activities, thereby providing migration and escape pathways for fluids. Recently, we reveal a complex seabed fluid flow system composed of various seafloor expressions (i.e. mounds and pockmarks) and shallow fluid migration pathways in the central-west Bohai Sea based on an integrated study of side-scan sonar, single- and multi-channel seismic data and magnetic data (Duan et al., 2022).

4 Seabed fluid flow in the Yellow Sea

Cold seeps are widespread in the Yellow Sea, as indicated by lots of evidence, including gas seeps, pockmarks, domes, seafloor faults, and micro-ring depressions. Liu et al. (2013) reported certain micro-ring depressions in the north Yellow Sea at a water depth of 50–55 m. These depressions demonstrate circular and irregular ellipse shapes with a major axis of ~2 km and a shallow groove with a width of 200–300 m wide and a depth of 2 m along the edge (Figure 4). These depressions are interpreted as topography features formed by sub-bottom shallow gas leakage and transformed by bottom current and submarine slumping. However, no simultaneous seismic data confirm the above interpretation, and the formation mechanism for this seepage topography remains unclear. Zhao et al. (2009) reported certain seabed pockmarks and domes in the northern depression of the south Yellow Sea basin (location is unknown), related to fault structures as pathways and sources for the seabed hydrocarbon seepages. This indicates the upward migration of pore fluid in the

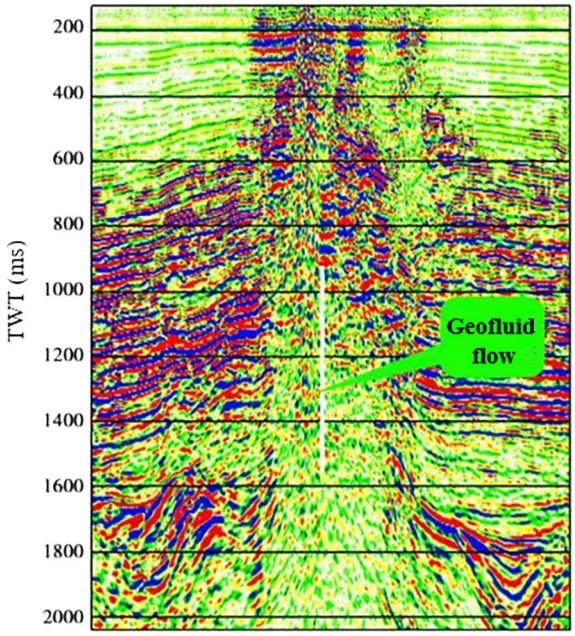

FIGURE 3
PL19-3 oil field in the Bohai bay basin formed in Quaternary and dispersed in the late-stage period of hydrocarbon accumulation (Gong, 2005).

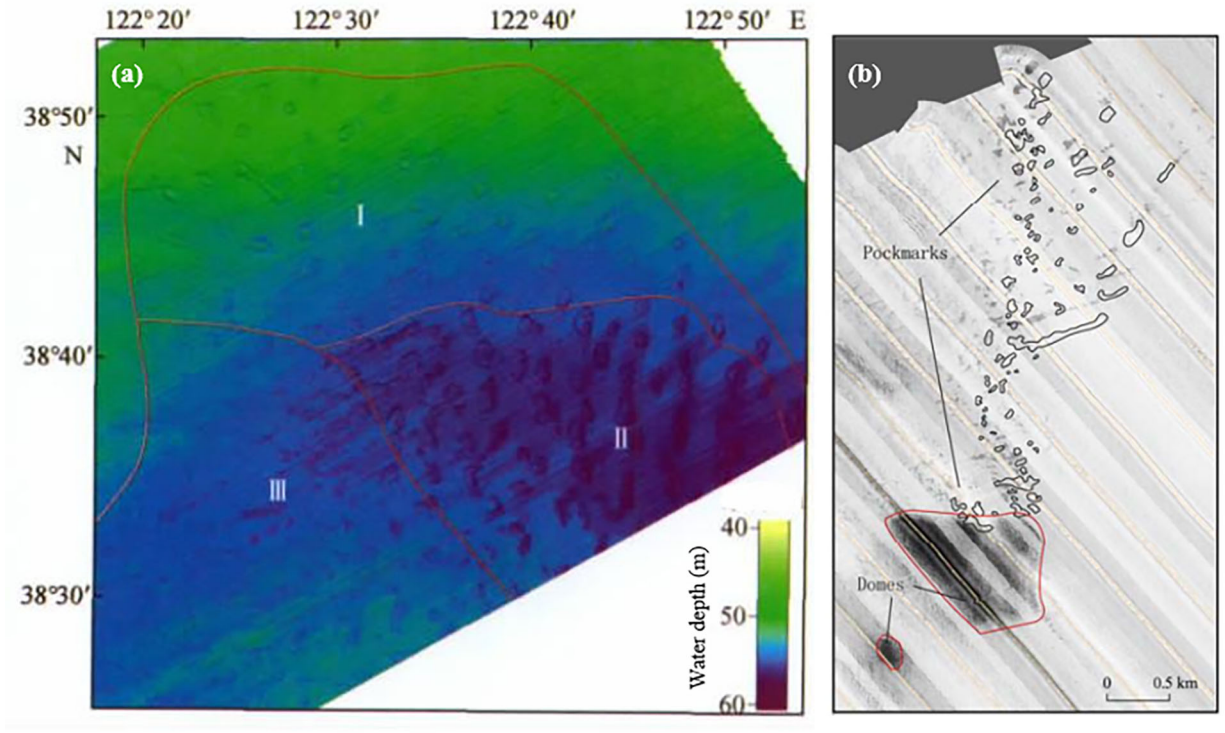

FIGURE 4
Certain geological features on the fluid escape structures in the Yellow Sea. **(A)** Bathymetric map showing the micro-ring depression in the north Yellow Sea (Liu et al., 2013). I) Circular or elliptical micro depressing with a protrusion in the center; II) Elliptical micro depression with depression in the center; III) Curved micro depression. **(B)** Side-scan sonar mosaic image demonstrating domes and pockmarks (Zhao et al., 2009).

deep strata (Figure 4). Jeong et al. (2004) reported a few active gas seepages in the southeastern Yellow Sea. However, geophysical and geochemical observations demonstrate that the gas seepage appears to be explosive to form craters and diapirs, dominant in thermogenic gases, with a smaller amount of biogenic gases. However, seepages in the western Yellow Sea are mostly biogenic with the late Pleistocene peat as the major source. The active cold seeps by acoustic plumes, cloudy turbidity, and point-line-type reflection produce seabed pockmarks and mud domes, as per the occurrence of shallow gas, which is mostly distributed in the buried delta, paleo lacustrine, paleo-fluvial facies, and paleo-tidal channel facies (Gu et al., 2008; Gu et al., 2009; Gu et al., 2006). Kong et al. (2012) compiled a distribution map of marine geohazards with the shallow gas involved as a major factor of marine geohazards. Furthermore, active cold seeps in the central Yellow Sea are speculated to result from fluid escape along faults from the deep. A large collapse crater in the northwestern part of the Subei shoal may be a composite collapse crater resulting from the shallow-faulting-related multipoint eruption of shallow gas, indicating the shallow gas occur in the middle-deep strata (Gu et al., 2009).

5 Seabed fluid flow in the East China Sea

Previous studies demonstrated signs of cold seeps on the continental shelf and slope of the East China Sea. Although shallow gas, pockmarks, small domes, shallow faults, and certain associated gas plumes are extensively reported using geological disaster surveys, the gases are mostly biogenic because of the degradation of organic matter in the shallow sediments of Yangtze Estuary, Hangzhou bay, Xiamen bay, and Zhejiang coast (Jorge et al., 1985; Hu et al., 2012; Liu et al., 2014; Hou et al., 2015; Hu et al., 2016; Figure 5), whereas thermogenic and high pressure as buried several hundreds of meters deep on the vast continental shelf of East China Sea (Yu, 2011; Cui et al., 2013). Previous studies on the Okinawa Trough have demonstrated widespread cold-seep activities. A gas seepage above the acoustic curtain and mud diapir structure (Luan and Qin, 2005; Luan et al., 2008), the authigenic carbonates related to cold seepage (Sun et al., 2015) and intense methane seeps indicated by shallow sulfate-methane interface and abnormal pore water characteristic (Li et al., 2015) show cold seeps are pervasive along the western slope of Okinawa Trough. Roughly circular sediment mounds or mud volcanoes have been mapped for the first time at the shelf edge of the East China Sea. These sediment mounds are associated with large pockmarks. This seepage process is suspected to be very recent, and probably still active (Yin et al., 2003). Then, additional mud volcanoes/diapirs are reported along the western slope of Okinawa Trough. Seismic sections show that gas hydrates, marked by bottom-simulating reflector at the top of mud volcanoes, are observed along with mud diapirs (Xu et al., 2009), fed by the upward fluid along normal faults with a steep dip and slight fault displacement during the formation of mud diapirs (Zhao et al., 2006). Furthermore, bright

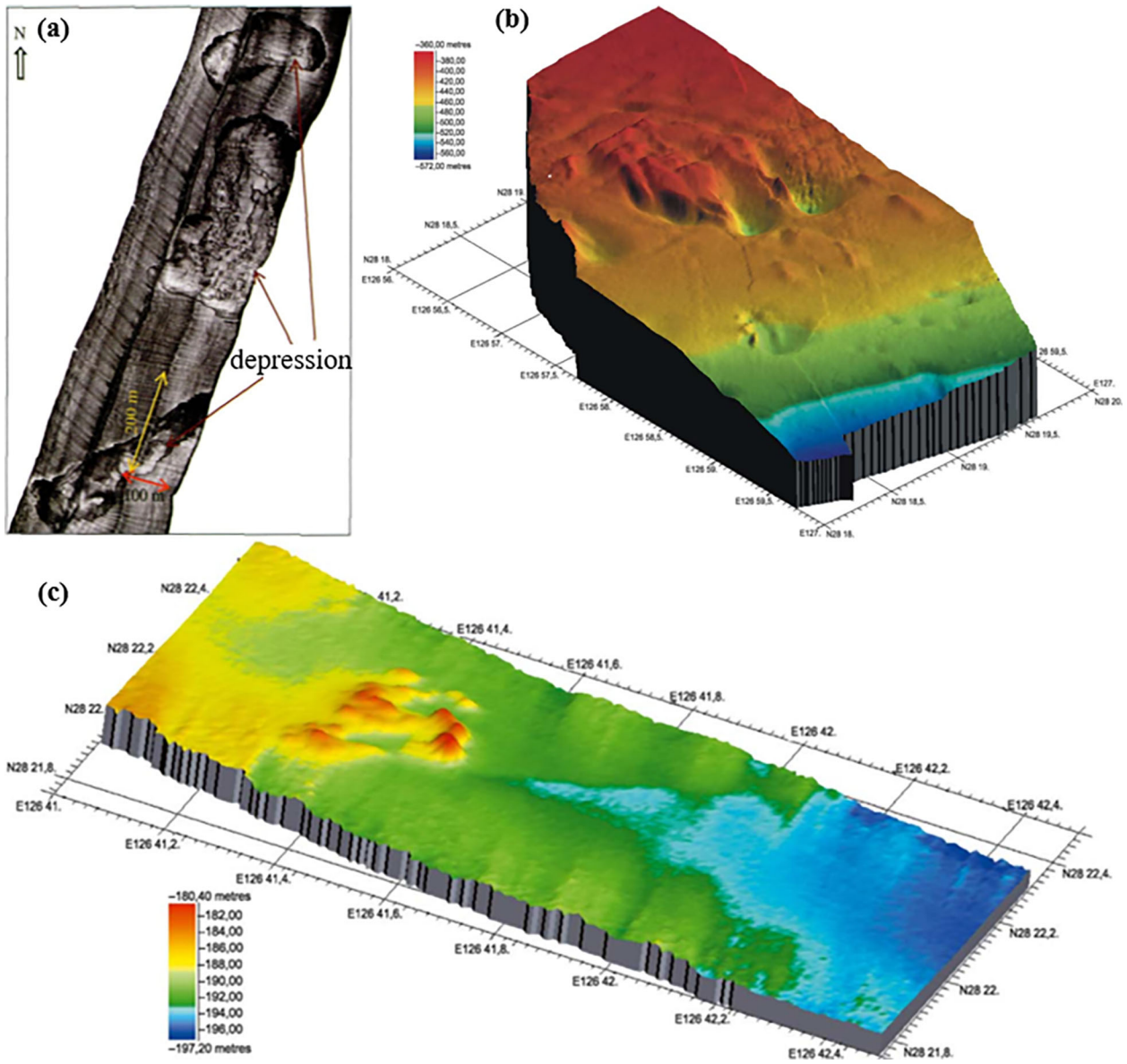

FIGURE 5
Certain geological features on fluid escape structures in the East China Sea. **(A)** Side-scan sonar mosaic image showing the depressions in the Zhoushan area, east of East China Sea (Hou et al., 2015). **(B, C)** Bathymetric map showing sediment depressions and mounds (Yin et al., 2003).

spots, phase reversals, and other acoustic anomalies show that gas and/or fluid escape are important for forming these mud volcanoes (Yin et al., 2003).

Except in mud volcano regions, gas hydrates are widely recognized along the western slope using limited seismic sections (Luan et al., 2006; Luan et al., 2008). In fact, the two regions of methane anomalies in surface sediments reported by Lu et al. (2002) are near two mud volcanoes found four years later. The thermal infrared anomalies before, during, and after earthquakes demonstrate a close relationship with gas hydrate distribution. These indicate that gas hydrates are pervasive in the central and southern Okinawa Troughs (Lu et al., 2002), and cold seeps are closely associated with gas hydrate decomposition. Note that additional investigations demonstrate that cold seeps are extensively spread along the western slope of the Okinawa trough, in the turbidite deposits, which host distinct petrologic composition and sedimentary structures compared with normal marine sediment (Sun et al., 2015). Recently, in a transtensile regime, active gas emissions were reported along the western slope of the mid-Okinawa Trough (Figure 6, Li et al., 2021).

6 Seabed fluid flow in the South China Sea

The South China Sea, one of the largest marginal seas of the west pacific, bears the coldest seeps in China. Tens of possible seep sites have been identified using direct or indirect evidence (Feng D.

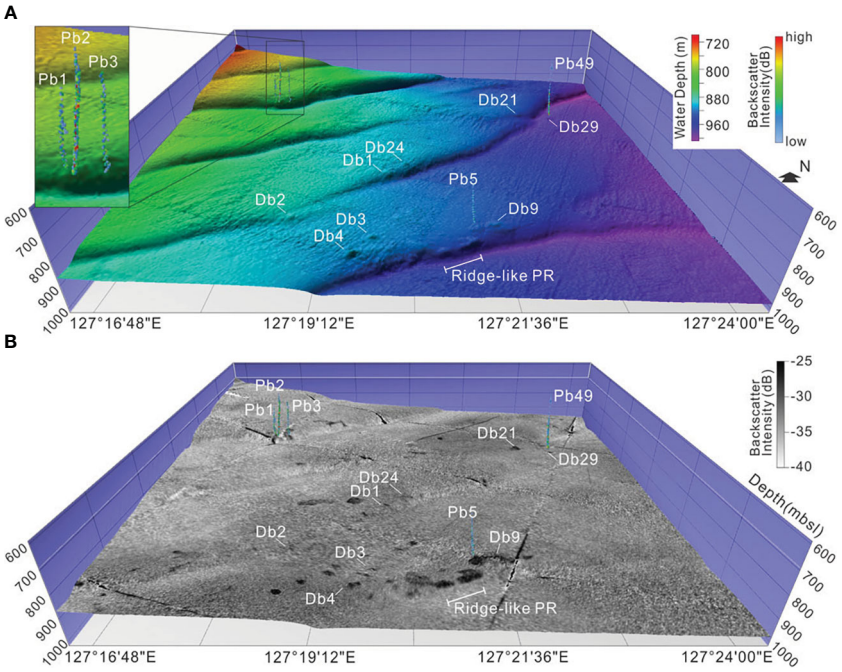

FIGURE 6
(A) 3D view of the bathymetry showing the geometries of positive reliefs and gas plumes. **(B)** 3D view of the map of the backscattering intensities superimposed on the bathymetric one (Li et al., 2021).

et al., 2018). In the South China Sea, focused fluid flows are extremely active. BSRs are reported in Taixinan, Pearl river mouth, and the Qiongdongnan basin, indicating that gas hydrates are extensively distributed in the northern South China Sea (Wang et al., 2018; He et al., 2022; Qian et al., 2022). Moreover, pockmarks have been reported around the South China Sea, including the Pearl river mouth, Qiongdonan, Yinggehai, Zhongjiannan basin, and Nansha region (Chen et al., 2015b; Xiong et al., 2023; Zhang et al., 2020). Furthermore, mud diapirs are reported all over the northern South China Sea and mud volcanoes primarily occur in the Taixinan and Pearl river mouth basins, northeastern South China Sea (Chen et al., 2016; Wan et al., 2019). Except for cold seeps in the Nansha region, others are primarily located on the northern slope of the South China Sea. Active gas seepages are primarily found in the Qiongdongnan basin and Taixinan basin (Wang et al., 2022).

The cold seeps and Jiulong methane reefs were discovered in the South China Sea in 2004 during the Sino-German cooperative investigation in the northeast Dongsha and Taixinan basin (Chen et al., 2005). In the Jiulong methane reef area, the chemoherm edifices and methane-derived carbonates are widespread (Suess, 2005; Han et al., 2008). Field observations and laboratory studies of these carbonates demonstrate multiple microbial structures preserved around and embedded in these carbonates, which supports the anoxic oxidation of methane in their formation (Han et al., 2008; Shi et al., 2014). Other active cold seeps were identified using high-resolution seismic images at the southern summit of the Taiwan ridge, southwest Taiwan in 2008 (Liu et al., 2008; Hsu et al., 2018). ROVs and deep submergence vehicles were used to explore the region in the subsequent years (Feng and Chen, 2015; Feng et al., 2015; Zhang et al., 2017). During the exploration, methane gas hydrates were discovered on the seabed surface of the Taiwan ridge and the exposed hydrates were attached to the inner wall of seeps (Figure 7, Zhang et al., 2017). Multibeam water column data show gas plumes and the possible existence of gas hydrates in the Taixinan basin (Chen et al., 2019). Furthermore, mud volcanoes and authigenic carbonate nodules were discovered in southwest Dongsha (Tong et al., 2013; Yan et al., 2017). Carbonates from southwest Dongsha have relatively high mineral contents and low $^{87}Sr/^{86}Sr$ ratios compared with those from northeast Dongsha, indicating a deeper source of seepage fluids (Tong et al., 2013; Feng D. et al., 2018).

Another important seabed fluid flow region is located in the Shenhu area, which witnessed both China's first gas hydrate drilling in 2007 and offshore gas hydrate production test in 2017. Fluid flow features are widespread; the high-resolution 3D seismic data demonstrate abundant acoustic anomalies, indicating the occurrence of shallow gas. Sun et al. (2012) discovered 45 mud diapirs and 4 isolated mud volcanoes; however, only one mud volcano was exposed on the seafloor with the conduit visible in the seismic profile. Chen et al. (2016) identified 164 gas chimneys, 5 mud diapirs or volcanoes, and 9 pockmarks from the results of high-resolution 3D seismic investigations. Carbonates from the Shenhu area are categorized into two: pipes and crusts; the extremely negative $\delta^{13}C$ value of these carbonates indicates that the primary carbon source in the Shenhu seeps is biogenic methane (Tong et al., 2013). From the results of the multibeam survey, Zhu et al. (2019) reported multiple suspected gas plumes; however, no active cold seeps have been reported with direct and solid evidence in the Shenhu area.

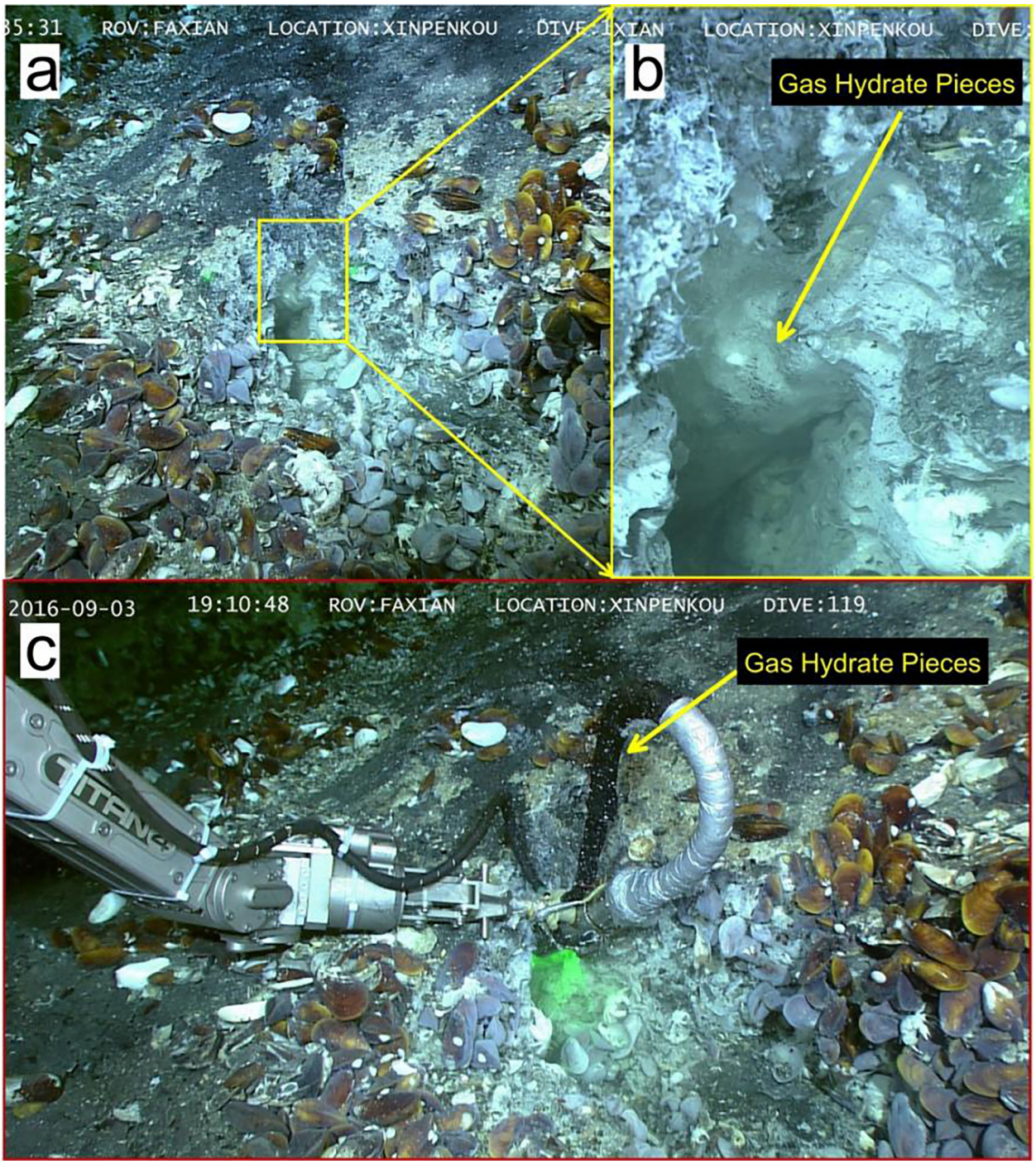

FIGURE 7
Raman observations of gas hydrates exposed on the seafloor. **(A)** The exposed hydrate inside the channel of a cold seep vent surrounded by lush chemosynthetic communities. **(B)** A close-up view of the exposed hydrate attached to the inner wall of the channel. **(C)** The release of small pieces of gas hydrate from the vent (Zhang et al., 2017).

Fluid escape features are developed in Zhongjiannan and adjacent Qiongdongnan basins. Using 2D seismic data and multibeam bathymetry data, Sun et al. (2013) identified three focused fluid escape features, mud volcanoes, pipes, and associated pockmarks, in the Zhongjiannan basin. When fed by gas-rich plumbing systems, mud volcanoes are either isolated or in groups. Chen et al. (2015b) first reported newly discovered crescent pockmarks and pockmark strings in the northern Zhongjiannan basin and discussed the geological and oceanographic controls on these seabed fluid escape structures (Chen et al., 2018). Using the reaction transport model, Luo et al. (2015) suggested that the fluid seepage at the pockmark ceased 39 kyr ago, corresponding to a relative sea-level high-stand and gas hydrate stabilization. Another important progress occurred when active cold and Haima seeps

were discovered using ROV in 2015 and 2016 in the Qiongdongnan basin. Geophysical data were used to outline migration pathways for fluid and gas to the seabed. Furthermore, gas hydrates were recovered in sediments at ~4 m below the seafloor at Haima seep sites (Liang et al., 2017). Recently, a new and active cold seep was reported ~50 km northeast of the Haima cold seeps (Figure 8, Geng et al., 2021). All these prove the ongoing gas seepage activities at this newly discovered cold seep.

From the interpretations of geophysical data, Liu et al. (2021) hypothesized an evolutionary model developing the gas hydrate system and gas seepage at the Haima cold seeps (Figure 9). In addition to these results, thermogenic gas in the Qiongdongnan basin migrating from the deep reservoir through the gas hydrate stability zone along deep faults and gas chimneys forms active cold seeps. The results provide insight in the relationship between seafloor cold seeps and deep hydrocarbon generation and migration. Furthermore, they have important implications for hydrocarbon exploration in the Qiongdongnan basin of the northwestern South China Sea (Geng et al., 2021). Feng D. et al. (2018) quantitated the contribution of cold seep fluids to the bottom-water carbon reservoir of the South China Sea, which help to understand the dynamics and the environmental impact of hydrocarbon seep.

In addition to the northern slope of the South China Sea, a few possible cold seeps are indicated in the southern South China Sea, e.g., methane seepage is inferred from the porewater geochemistry of shallow sediments in the Beikang basin (Feng J. et al., 2018). Zhang K et al. (2020) reported 125 pockmarks close to the Andu seamount in the southern margin of the South China Sea. To date, cold seeps remain poorly investigated in the southern South China Sea.

7 Summaries and conclusions

It is remarkable how common seabed fluid flow is in the China seas, from every seabed environment from coastal waters down to the deep oceans. Given the larger scale and quantity, seabed fluid flows are widespread in the continental margins of the East China Sea (e.g. the Okinawa Trough) and the South China Sea (e.g. the Pearl River Mouth Basin). In the Bohai Sea, seabed fluid flows are also found in the hydrocarbon enrichment basins, such as the Bohai bay basin. In comparison, levels of scale and quantity are low in the Yellow Sea and the East Sea shelf basin.

Previous investigation works on the seabed fluid flow over the last three to four decades have led to significant progresses in our understanding of this geological phenomenon. However, the field investigations on seabed fluid flow are severely insufficient in the Bohai Sea, the Yellow Sea, and the East China Sea shelf basin. In addition, more comprehensive and detailed investigations are required in the Okinawa Trough and the South China Sea for the sake of the gas hydrates and hydrocarbons.

The distribution, feature and origin of the seabed fluid flow are controlled by various geological, biological and oceanographic factors in the China seas. In sedimentary basins the most significant fluids are hydrocarbons, particularly methane, formed by thermogenic or biogenic processes within the sediments. Therefore, seabed fluid escape structures (e.g. pockmarks, seeps, domes, mud diapirs, gas chimneys, and mud volcanoes) are usually associated with deep marine hydrocarbons or shallow gas hydrates. In order to understand the nature of these seabed fluid escape structures in both time and space, it is essential to appreciate how

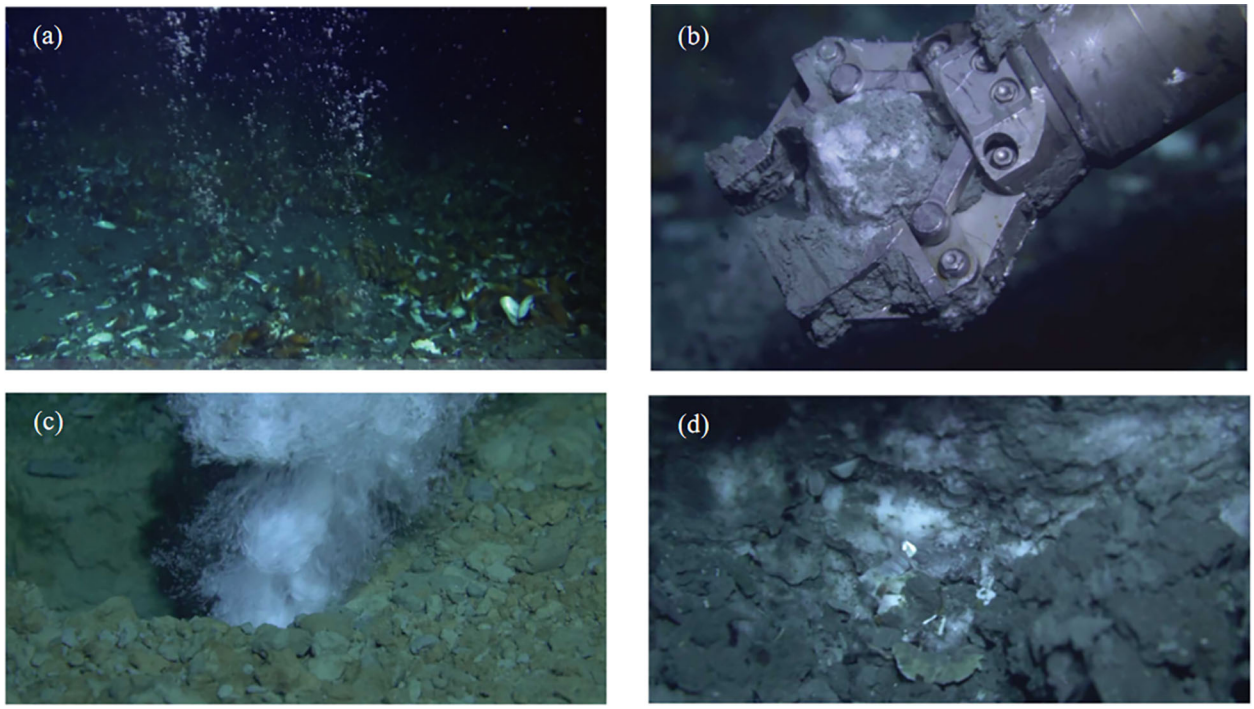

FIGURE 8
Seafloor observations of gas seepages **(A, C)** and near-surface gas hydrates **(B, D)** (Geng et al., 2021).

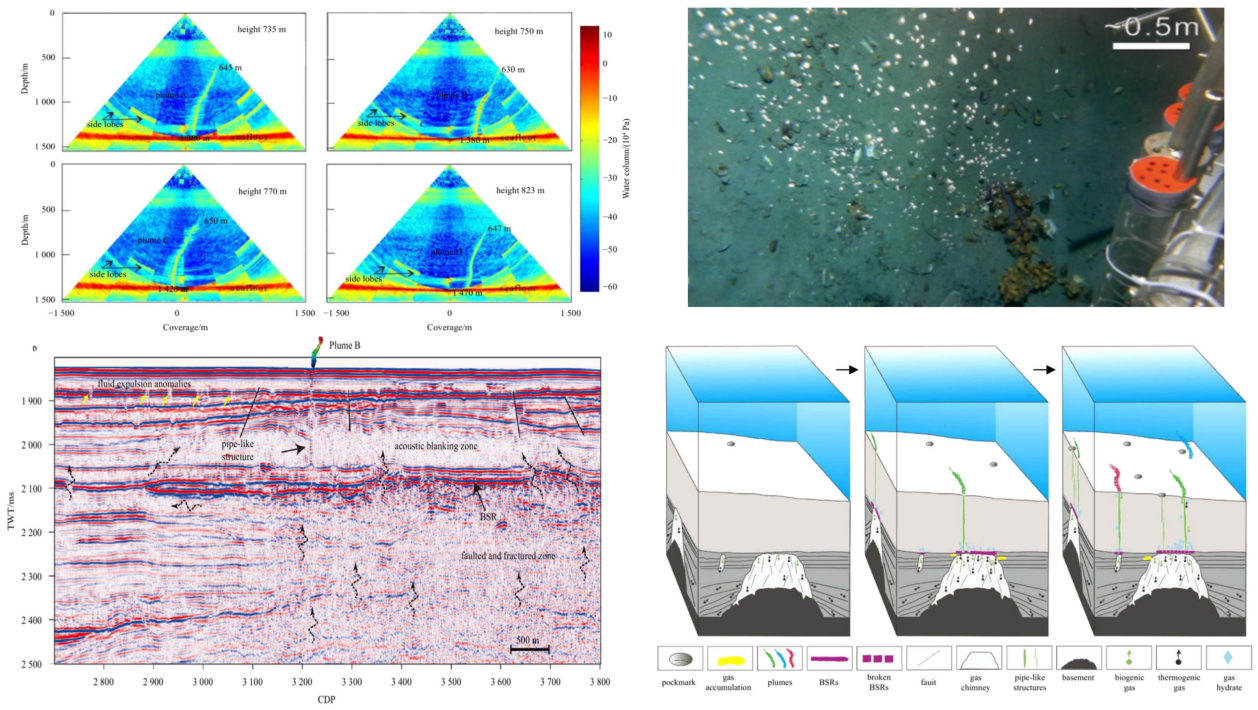

FIGURE 9
Seabed fluid flow at the Haima cold seeps and the evolutionary model associated with the hydrate (Feng et al., 2020; Geng et al., 2021).

and why these seabed fluids form and migrate.Indeed, the seabed fluid flow is clearly a dynamic process and it is determined by a function of endogenic (e.g. seabed hydrocarbon) and exogenous (e.g. marine dynamic conditions) factors.

In essence, seabed fluid flow is a geological process. Further, it may affect marine ecology, ocean biogeochemistry, and even the atmosphere and global carbon cycle. Though these processes may be significant not only to today's climate, but also to global climate change over geological timescales, they are still poorly understood. Considering the widespread, dynamic, and influential feature of seabed fluid flow, more attention should be given to the future study on the seabed fluid flow.

Author contributions

CZ, MD, and JC wrote, edited and revised the text and figures. All authors contributed to the text and figures. All authors contributed to the article and approved the submitted version.

Funding

This research was funded by the National Natural Science Foundation of China [Nos. 42207173, 41831280], the Natural Science Foundation of Shandong Province [Nos. ZR2022QD002, 2022RZB07052], the Shandong Provincial and Qingdao Postdoctoral Foundation [No. SDCX-ZG-202203089], the Key Laboratory of Submarine Geosciences and Prospecting Techniques (MoE) [No. SGPT-2022OF-03], and the Laboratory for Marine Mineral Resources, Qingdao National Laboratory for Marine Science and Technology [Grant No. MMRKF201810]; JC is funded by the Shandong Province "Taishan Scholar" Construction Project. CZ is funded by the Young Elite Scientist Sponsorship Program by CAST.

Acknowledgments

We thank Enago for its linguistic assistance during the preparation of this manuscript and Longyu Lu for his help in the revision..

Conflict of interest

Author MD was employed by Hainan Branch of CNOOC Limited.

The remaining authors declare that the research was conducted in the absence of any commercial or financial relationships that could be construed as a potential conflict of interest.

Publisher's note

References

Allen, M., Macdonald, D., Xun, Z., Vincent, S. J., and Brouet-Menzies, C. (1997). Early Cenozoic two-phase extension and late Cenozoic thermal subsidence and inversion of the bohai basin, northern China. *Mar. Petroleum Geol.* 14, 951–972. doi: 10.1016/S0264-8172(97)00027-5

Andreassen, K., Hubbard, A., Winsborrow, M., Patton, H., Vadakkepuliyambatta, S., Plaza-Faverola, A., et al. (2017). Massive blow-out craters formed by hydrate-controlled methane expulsion from the Arctic seafloor. *Science* 356 (6341), 948–953. doi: 10.1126/science.aal4500

Basins, B. A.. (1991). Report on DELP 1988 cruises in the Okinawa trough: Part 4. preliminary report on the sediment samples. *Bull. Earthquake Res. Institute* 66, 71–89.

Brothers, L. L., Van Dover, C. L., German, C., Kaiser, C. L., Yoerger, D. R., Ruppel, C.D., et al. (2013). Evidence for extensive methane venting on the southeastern US Atlantic margin. *Geology* 41 (7), 807–810. doi: 10.1130/G34217.1

Bünz, S., Polyanov, S., Vadakkepuliyambatta, S., Consolaro, C., and Mienert, J. (2012). Active gas venting through hydrate-bearing sediments on the vestnesa ridge, offshore W-Svalbard. *Mar. Geol.* 332, 189–197. doi: 10.1016/j.margeo.2012.09.012

Chen, Y., Ding, J., Zhang, H., Tang, Q., Zhou, X., Liu, X., et al. (2019). Multibeam water column data research in the taixinan basin: Implications for the potential occurrence of natural gas hydrate. *Acta Oceanol. Sin.* 38 (5), 129–133. doi: 10.1007/s13131-019-1444-0

Chen, J., Guan, Y., Song, H., Yang, S., Geng, M., Bai, Y., et al. (2015a). Distribution characteristics and geological implications of pockmarks and mud volcanoes in the northern and western continental margins of the south China Sea. *Chin. J. Geophys.* 58 (3), 919–938. doi: 10.6038/cjg20150319

Chen, J., Song, H., Guan, Y., Yang, S., Pinheiro, L. M., Bai, Y., et al. (2015b). Morphologies, classification and genesis of pockmarks, mud volcanoes and associated fluid escape features in the northern zhongjiannan basin, south China Sea. *Deep Sea Res. Part II: Topical Stud. Oceanogr.* 122, 106–117. doi: 10.1016/j.dsr2.2015.11.007

Chen, D. F., Huang, Y. Y., Yuan, X. L., and Iii, L.. (2005). Seep carbonates and preserved methane oxidizing archaea and sulfate reducing bacteria fossils suggest recent gas venting on the seafloor in the northeastern south China Sea. *Mar. Petroleum Geol.* 22, 613–621. doi: 10.1016/j.marpetgeo.2005.05.002

Chen, J., Song, H., Guan, Y., Pinheiro, L. M., and Geng, M. (2018). Geological and oceanographic controls on seabed fluid escape structures in the northern zhongjiannan basin, south China Sea. *J. Asian Earth Sci.* 168, 8–47. doi: 10.1016/j.jseaes.2018.04.027

Chen, D., Wang, X., Völker, D., Wu, S, Wang, L, Li, W, et al. (2016). Three dimensional seismic studies of deep-water hazard-related features on the northern slope of south China Sea. *Mar. Petroleum Geol.* 77, 1125–1139. doi: 10.1016/j.marpetgeo.2016.08.012

Cui, Z., Yang, W., Zhang, Y., and Huang, T. (2013). Geo-hazards and their distribution in the middle and south parts of xihu sag, East China Sea. *Mar. Geol. Front.* 29 (7), 36–43. doi: 10.16028/j.1009-2722.2013.07.010

Du, X., Deng, Q., Wang, Z., and Cao, H. (2007). Application of shallow-depth acoustic reflection profiling to the active fault prospecting, in offshore region of Shandong peninsula, China. *Recent Dev. World Seismol.* 11, 1–10. doi: 10.3969/j.issn.0253-4975.2007.11.001

Du, X., Sun, Y., Song, Y., and Zhu, C. (2021). In-situ observation of wave-induced pore water pressure in seabed silt in the yellow river estuary of China. *J. Mar. Environ. Eng.* 10 (4), 305–317.

Duan, M., Tong, S., Chen, J., Azevedo, L., Li, R., and Song, H. (2022). Distribution and geological controls of the seabed fluid flow system, the central-western bohai Sea: A general overview. *Basin Res.* 34 (4), 1440–1464. doi: 10.1111/bre.12666

Fang, H.. (2012). Petroleum charging and leakage in the BZ25-1 field, bohai bay basin. *J. Earth Sci.* 23 (3), 253–267. doi: 10.1007/s12583-012-0251-8

Fang, H., Zou, H., Gong, Z., and Deng, Y. (2007). Petroleum migration and accumulation in the bozhong sub-basin, bohai bay basin, China: Significance of preferential petroleum migration pathways (PPMP) for the formation of large oilfields in lacustrine fault basins. *Mar. Petroleum Geol.* 24 (1), 1–13. doi: 10.1016/j.marpetgeo.2006.10.007

Feng, D., and Chen, D. (2015). Authigenic carbonates from an active cold seep of the northern south China Sea: New insights into fluid sources and past seepage activity. *Deep Sea Res. Part II: Topical Stud. Oceanogr.* 122, 74–83. doi: 10.1016/j.dsr2.2015.02.003

Feng, D., Cheng, M., Kiel, S., Qiu, J. W., Yang, Q., Zhou, H., et al. (2015). Using bathymodiolus tissue stable carbon, nitrogen and sulfur isotopes to infer biogeochemical process at a cold seep in the south China Sea. *Deep Sea Res. Part I: Oceanogr. Res. Pap.* 104, 52–59. doi: 10.1016/j.dsr.2015.06.011

Feng, J., Li, N., Luo, M., Liang, J., and Chen, D. (2020). A quantitative assessment of methane-derived carbon cycling at the cold seeps in the northwestern south China Sea. *Minerals* 10 (3), 256. doi: 10.3390/min10030256

Feng, D., Qiu, J., Hu, Y., Peckmann, J., Guan, H., Tong, H., et al. (2018). Cold seep systems in the south China Sea: An overview. *J. Asian Earth Sci.* 168, 3–16. doi: 10.1016/j.jseaes.2018.09.021

Feng, J., Yang, S., Liang, J., Fang, Y., He, Y., Luo, M., et al. (2018). Methane seepage inferred from the porewater geochemistry of shallow sediments in the beikang basin of the southern south China Sea. *J. Asian Earth Sci.* 168, 77–86. doi: 10.1016/j.jseaes.2018.02.005

Geng, M., Zhang, R., Yang, S., Guo, J., and Chen, Z. (2021). Focused fluid flow, shallow gas hydrate, and cold seep in the qiongdongnan basin, northwestern south China Sea. *Geofluids* 2021, 5594980. doi: 10.1155/2021/5594980

Gong, Z. (2005). Cenozoic China Offshore basins keeping active hydrocarbon accumulation to present. *Acta Petrolei Sin.* 26 (6), 1–6. doi: 10.3321/j.issn:0253-2697.2005.06.001

Gong, Z., Zhang, G., Cai, D., and He, S. (2004). Late-stage hydrocarbon accumulation in the bozhong depression of the bohai bay basin as controlled by neotectonism. *Acta Geol. Sinica-English Ed.* 78 (3), 632–639. doi: 10.1111/j.1755-6724.2004.tb00176.x

Gong, Z., Zhu, W., and Chen, P. (2010). Revitalization of a mature oil-bearing basin by a paradigm shift in the exploration concept. A case history of bohai bay, offshore China. *Mar. Petroleum Geol.* 27, 1011–1027. doi: 10.1016/j.marpetgeo.2009.11.010

Gu, Z., Liu, H., Li, G., and Zhang, Z. (2009). Origin of shallow gas in the western region of the south yellow Sea. *Natural Gas Industry* 29 (1), 26–29. doi: 10.3787/j.issn.1000-0976.2009.01.006

Gu, P., Zhang, G., Li, P., Han, Y., and Zhao, Y. (2011). Effect of the water-sediment regulation on dissolved methane in the lower yellow river estuary and it's adjacent marine area. *China Environ. Sci.* 31 (11), 1821–1828.

Gu, Z., Zhang, Z., and Liu, H. (2006). Seismic features of shallow gas in the western area of the yellow Sea. *Mar. Geol. Quaternary Geol.* 26 (3), 65–74.

Gu, Z., Zhang, Z., Liu, G., and Lan, X. (2008). Shallow geological background of shallow gas in the western south yellow Sea. *Mar. Sci.* 32 (7), 46–51.

Han, X., Suess, E., Huang, Y., Wu, N., and Fang, Y. (2008). jiulong methane reef: microbial mediation of seep carbonates in the south China Sea. *Mar. Geol.* 249 (3-4), 243–256. doi: 10.1016/j.margeo.2007.11.012

He, Y. L., Liang, J. Q., Kuang, Z. G., Deng, W., Ren, J. F., Lai, H. F., et al. (2022). Migration and accumulation characteristics of natural gas hydrates in the uplifts and their slope zones in the qiongdongnan basin, China. *China Geol.* 5 (2), 234–250. doi: 10.31035/cg2022004

He, J., Liang, S., Zhao, Y., Cheng, X., and Li, H. (2007). Characteristics of geologic structures of the north yellow Sea basin: Implications for petroleum explorations. *Mar. Geol. Quaternary Geol.* 27, 101–105.

Hou, F., Wang, B., Sun, J., Li, R., and Wen, Z. (2016). Neotectonic movement across the bohai strait and its engineering geologic significance. *Mar. Geol. Front.* 32 (5), 25–30. doi: 10.16028/j.1009-2722.2016.05004

Hou, Z., Zhang, Y., Cai, C., Liao, L., and Hu, B. (2015). Characteristics of Sea floor shallow gas in the Eastern part of zhoushan dongji island. *Offshore Oil* 35 (3), 27–32. doi: 10.3969/j.issn.1008-2336.2015.03.027

Hsu, H., Liu, C., Morita, S., Tu, S. L., Lin, S., Machiyama, H., et al. (2018). Seismic imaging of the Formosa ridge cold seep site offshore of southwestern Taiwan. *Mar. Geophys. Res.* 39, 523–535. doi: 10.1007/s11001-017-9339-y

Hu, X., Gu, Z., Zhang, X., Zhao, L., and Xing, Z. (2016). Seismic shape features and distribution of shallow gas in the Sea area off the Yangtze river estuary. *Mar. Geol. Quaternary Geol.* 36 (1), 151–157. doi: 10.3724/SP.J.1140.2016.01015

Hu, Y., Li, H., and Xu, J. (2012). Shallow gas accumulation in a small estuary and its implications: A case history from in and around xiamen bay. *Geophys. Res. Lett.* 39 (24), L24605. doi: 10.1029/2012GL054478

Hu, S., O'Sullivan, P., Raza, A., and Kohn, B. (2001). Thermal history and tectonic subsidence of the bohai basin, northern China: A Cenozoic rifted and local pull-apart basin. *Phys. Earth Planetary Interiors* 126, 221–235. doi: 10.1016/S0031-9201(01)00257-6

Hu, J., and Wang, X. H. (2016). Progress on upwelling studies in the China seas. *Rev. Geophys.* 54 (3), 653–673. doi: 10.1002/2015RG000505

Hutchison, C. S. (2004). Marginal basin evolution: The southern south China Sea. *Mar. Petroleum Geol.* 21 (9), 1129–1148. doi: 10.1016/j.marpetgeo.2004.07.002

Jeong, K. S., Cho, J. H., Kim, S. R., Hyun, S., and Tsunogai, U. (2004). Geophysical and geochemical observations on actively seeping hydrocarbon gases on the south-eastern yellow Sea continental shelf. *Geo-Marine Lett.* 24 (1), 53–62. doi: 10.1007/s00367-003-0164-8

Jia, Y., Zhu, C., Liu, L., and Wang, D. (2016). Marine geohazards: Review and future perspective. *Acta Geol. Sin. (English Edition)* 90 (4), 1455–1470. doi: 10.1111/1755-6724.12779

Jorge, B., John, D. M., and Ye, Y. (1985). Geomorphology, shallow structure, and geological hazards in the East China Sea. *Continental Shelf Res.* 4 (1-2), 121–141. doi: 10.1016/0278-4343(85)90025-1

Judd, A., and Hovland, M. (2009). *Seabed fluid flow: the impact on geology, biology and the marine environment* (New York: Cambridge University Press).

Kong, X., Liu, J., Du, Y., Wen, C., and Xu, G. (2012). Characteristics and distribution of geo-hazard factors in the Western south yellow Sea. *Mar. Geol. Quaternary Geol.* 32 (2), 43–52. doi: 10.3724/SP.J.1140.2012.02043

Lee, E. Y. (2010). Subsidence history of the gunsan basin (Cretaceous-Cenozoic) in the yellow Sea, offshore Korea. *Austrian J. Earth Sci.* 103, 111–120.

Li, Q., Cai, F., Liang, J., Shao, H., and Dong, G. (2015). Geochemical constraints on the methane seep activity in western slope of the middle Okinawa trough, the East China Sea. *Sci. China Earth Sci.* 58 (6), 986–995. doi: 10.1007/s11430-014-5034-x

Li, A., Cai, F., Wu, N., Li, Q., and Wang, X. (2021). Gas emissions in a transtensile regime along the Western slope of the mid-Okinawa trough. *Front. Earth Sci.* 9, 557634. doi: 10.3389/feart.2021.557634

Li, S., Zhao, G., Dai, L., Zhou, L., Xin, L., Suo, Y., et al. (2012). Cenozoic Faulting of the bohai bay basin and its bearing on the destruction of the eastern north China craton. *J. Asian Earth Sci.* 47, 80–93. doi: 10.1016/j.jseaes.2011.06.011

Li, C., Zhou, Z., Ge, H., and Mao, Y. (2009). Rifting process of the xihu depression, East China Sea basin. *Tectonophysics* 472, 135–147. doi: 10.1016/j.tecto.2008.04.026

Liang, Q., Hu, Y., Feng, D., Peckmann, J., Chen, L., and Yang, S. (2017). Authigenic carbonates from newly discovered active cold seeps on the northwestern slope of the south China Sea: Constraints on fluid sources, formation environments, and seepage dynamics. *Deep Sea Res. Part I: Oceanogr. Res. Pap.* 124, 31–41. doi: 10.1016/j.dsr.2017.04.015

Liu, X. Y., Chen, Y. L., Lu, B., et al. (2013). Geographic features of the micro ring depreesions to the south of changshan archipelago at the north yellow Sea. *J. Mar. Sci.* 31 (1), 59–65. doi: 10.3969/j.issn.1001-909X.2013.01.007

Liu, B., Chen, J., Yang, L., Duan, M., Liu, S., and Guan, Y. (2021). Multi-beam and seismic investigations of the active haima cold seeps, northwestern south China Sea. *Acta Oceanol. Sin.* 40 (7), 1–15. doi: 10.1007/s13131-021-1721-6

Liu, D., Hu, T., Huang, P., and Ji, Y. (2014). Classification and distribution of marine geohazards factors in zhoushan islands. *Trans. Oceanol. Limnol.* 3, 153–160.

Liu, C., Liao, Y., and Lin, S. (2008). High-resolution seismic images of the Formosa ridge off southwestern Taiwan where "hydrothermal" chemosynthetic community is present at a cold seep site. *Head Neck* 93 (93), 215–219.

Lu, Z., Gong, J., Wu, B., Chen, J., and Deng, J. (2002). Geochemical prospecting for gas hydrate and its perspective prediction in East China Sea. *Miner. Deposits* 21, 184–187. doi: 10.16111/j.0258-7106.2002.s1.009

Luan, X., and Qin, Y. (2005). The discovery of seafloor gas seepage in miyoko section at west trough floor of Okinawa trough. *Sci. Bull.* 50 (8), 802–810. doi: 10.3321/j.issn:0023-074X.2005.08.014

Luan, X., Wang, K., Hyndman, R., and Willoughby, E. (2008). Bottom simulating reflector and gas seepage in Okinawa trough: Evidence of gas hydrate in an active back-arc basin. *J. China Univ. Geosci.* 19 (2), 152–161. doi: 10.1016/S1002-0705(08)60034-5

Luan, X. W., Yue, B. J., and Lu, Y. T. (2006). Seismic characteristics of gas hydrates in the East China Sea. *Mar. Geol. Quaternary Geol.* 26 (5), 91–99.

Luo, M., Dale, A. W., Wallmann, K., Hensen, C., Gieskes, J., Yan, W., et al. (2015). Estimating the time of pockmark formation in the SW xisha uplift (South China Sea) using reaction-transport modeling. *Mar. Geol.* 364, 21–31. doi: 10.1016/j.margeo.2015.03.006

Park, J.-O., Tokuyama, H., Shinohara, M., Suyehiro, K., and Taira, A. (1998). Seismic record of tectonic evolution and backarc rifting in the southern Ryukyu island arc system. *Tectonophysics* 294, 21–42. doi: 10.1016/S0040-1951(98)00150-4

Qi, J., and Yang, Q. (2010). Cenozoic Structural deformation and dynamic processes of the bohai bay basin province, China. *Mar. Petroleum Geol.* 27, 757–771. doi: 10.1016/j.marpetgeo.2009.08.012

Qian, J., Kang, D., Jin, J., Lin, L., Guo, Y., Meng, M., et al. (2022). Quantitative seismic characterization for gas hydrate-and free gas-bearing sediments in the shenhu area, south China sea. *Mar. Petroleum Geol.* 139, 105606. doi: 10.1016/j.marpetgeo.2022.105606

Rui, S., Guo, Z., Si, T., and Li, Y. (2020). Effect of particle shape on the liquefaction resistance of calcareous sands. *Soil Dyn. Earthquake Eng.* 137, 106302. doi: 10.1016/j.soildyn.2020.106302

Serie, C., Huuse, M., and Schodt, N. H. (2020). Gas hydrate pingoes: Deep seafloor evidence of focused fluid flow on continental margins. *Geology* 40 (3), 207–210. doi: 10.1130/G32690.1

Shi, C., Lei, H., Zhao, J., Zhang, J., and Han, C. (2014). Vertical microbial community structure characteristics of sediment in gas hydrate potential area of northern south China Sea jiulong methane reef. *Acta Sedimentol. Sin.* 32 (6), 1072–1082.

Sibuet, J.-C., Deffontaines, B., Hsu, S., Thareau, N., Formal, J. P., and Liu, C. (1998). Okinawa Trough back arc basin: early tectonic and magmatic evolution. *J. Geophys. Res.* 103, 30245–30267. doi: 10.1029/98JB01823

Suess, E. (2005). *RV SONNE cruise report SO 177, sino-German cooperative project, south China Sea continental margin: Geological methane budget and environmental effects of methane emissions and gas hydrates*. IFM-GEOMAR, Kiel. doi: 10.3289/ifm-geomar_rep_4_2005

Sun, Z., Wei, H., Zhang, X., Shang, L., Yin, X., Sun, Y., et al. (2015). A unique fe-rich carbonate chimney associated with cold seeps in the northern Okinawa trough, East China Sea. *Deep Sea Res. Part I: Oceanogr. Res. Pap.* 95, 37–53. doi: 10.1016/j.dsr.2014.10.005

Sun, Q., Wu, S., Cartwright, J., and Dong, D. (2012). Shallow gas and focused fluid flow systems in the pearl river mouth basin, northern south China Sea. *Mar. Geol.* 315-318, 1–14. doi: 10.1016/j.margeo.2012.05.003

Sun, Q., Wu, S., Cartwright, J., Lüdmann, T., and Yao, G. (2013). Focused fluid flow systems of the zhongjiannan basin and guangle uplift, south China Sea. *Basin Res.* 25, 97–111. doi: 10.1111/j.1365-2117.2012.00551.x

Taylor, B., and Hayes, D. E. (1983). Origin and history of the south China Sea basin. *Tectonic Geologic Evol. Southeast Asian Seas Islands: Part 2* 27, 23–56. doi: 10.1029/GM027p0023

Teng, C., Zou, H., and Hao, F. (2010). Control of differential tectonic evolution on petroleum occurrence in bohai bay basin. *Sci. China Earth Sci.* 57, 1117–1128. doi: 10.1007/s11430-013-4771-6

Tong, H., Feng, D., and Cheng, H. (2013). Authigenic carbonates from seeps on the northern continental slope of the south China Sea: New insights into fluid sources and geochronology. *Mar. Petroleum Geol.* 43, 260–271. doi: 10.1016/j.marpetgeo.2013.01.011

Wan, Z., Yao, Y., Chen, K., Zhong, S., Xia, B., and Sun, Y. (2019). Characterization of mud volcanoes in the northern zhongjiannan basin, western south China Sea. *Geol. J.* 54 (1), 177–189. doi: 10.1002/gj.3168

Wang, X., Guan, H., Qiu, J. W., Xu, T., Peckmann, J., Chen, D., et al. (2022). Macro-ecology of cold seeps in the south China Sea. *Geosyst. Geoenviron.*, 100081. doi: 10.1016/j.geogeo.2022.100081

Wang, P., Li, Q., and Li, C. (2014). Geology of the China seas. *Dev. Mar. Geol.* 6, 1–687.

Wang, H., Liu, B., and Li, X. (2011). Activity of the faults in the southern part of bohai Sea since the late pleistocene. *Adv. Earth Sci.* 26 (5), 556–564. doi: 10.11867/j.issn.1001-8166.2011.05.0556

Wang, X., Liu, B., Qian, J., Zhang, X., Guo, Y., Su, P., et al. (2018). Geophysical evidence for gas hydrate accumulation related to methane seepage in the taixinan basin, south China Sea. *J. Asian Earth Sci.* 168, 27–37. doi: 10.1016/j.jseaes.2017.11.011

Wang, L., Rui, S., Guo, Z., Gao, Y., Zhou, W., and Liu, Z. (2020). Seabed trenching near the mooring anchor: History cases and numerical studies. *Ocean Eng.* 218, 108233. doi: 10.1016/j.oceaneng.2020.108233

Westbrook, G. K., Thatcher, K. E., Rohling, E., Piotrowski, A. M., Pälike, H, Osborne, A. H., et al. (2009). Escape of methane gas from the seabed along the West spitsbergen continental margin. *Geophys. Res. Lett.* 36, L15608. doi: 10.1029/2009GL039191

Xiong, P., Cheng, C., Kuang, Z., Ren, J., Liang, J., Lai, H., et al. (2023). Sedimentary characteristics and genetic mechanism of the giant ancient pockmarks in the qiongdongnan basin, northern south China Sea. *Acta Oceanol. Sin.* 42 (2), 1–14. doi: 10.1007/s13131-022-2125-y

Ning, X., Wu, S., Shi, B., Bing, L., Xue, L., Wang, X., et al. (2009). Gas hydrate associated with mud diapirs in southern Okinawa trough. *Mar. Petroleum Geol.* 26 (8), 1413–1418. doi: 10.1016/j.marpetgeo.2008.10.001

Yan, P. A., Wang, Y. A., Liu, J. B., Zhong, G. C., and Liu, X. A. (2017). Discovery of the southwest dongsha island mud volcanoes amid the northern margin of the south China Sea. *Mar. Petroleum Geol.* 88, 858–870. doi: 10.1016/j.marpetgeo.2017.09.021

Yang, J., Lu, M., Yao, Z., Wang, M., Lu, S., Qi, N., et al. (2021). A geophysical review of the seabed methane seepage features and their relationship with gas hydrate systems. *Geofluids* 2021, 1–26. doi: 10.1155/2021/1301044

Yang, H., and Qi, H. (2004). Well blowout precaution and control technology for shallow gas in bohai oilfield. *China offshore Oil* 16 (1), 43–46. doi: 10.3969/j.issn.1673-1506.2004.01.008

Yi, S., Yi, S., Batten, D., Yun, H., and Park, S. J. (2003). Cretaceous And Cenozoic on-marine deposits of the northern south yellow Sea basin, offshore western Korea: Palynostratigraphy and palaeoenvironments, Palaeogeography, palaeoclimatology. *Palaeoecol.* 191 (1), 15–44. doi: 10.1016/S0031-0182(02)00637-5

Yin, P., Berne, S., Vagner, P., Loubrieu, B., and Liu, Z. (2003). Mud volcanoes at the shelf margin of the East China Sea. *Mar. Geol.* 194 (3-4), 135–149. doi: 10.1016/S0025-3227(02)00678-3

Yu, M. (2011). Hazard to water project caused by shallow layered natural gas in the East Sea and control measures. *China Water Resour.* 16, 37–40. doi: 10.3969/j.issn.1000-1123.2011.16.013

Zhang, L., Bai, G., and Zhao, Y. (2014b). Data-processing and recognition of seepage and microseepage anomalies of acid-extractable hydrocarbons in the south slope of the dongying depression, eastern China. *Mar. Petroleum Geol.* 57, 385–402. doi: 10.1016/j.marpetgeo.2014.06.009

Zhang, Y., Chen, B., and Zhai, W. (2020). Exploring sources and biogeochemical dynamics of dissolved methane in the central bohai Sea in summer. *Front. Mar. Sci.* 7. doi: 10.3389/fmars.2020.00079

Zhang, X., Du, Z., Luan, Z., Wang, X., Xi, S., Bing, W., et al. (2017). *In situ* raman detection of gas hydrates exposed on the seafloor of the south China Sea. *Geochem. Geophys. Geosyst.* 18, 3700–3713. doi: 10.1002/2017GC006987

Zhang, K., Guan, Y., Song, H., Fan, W., and Geng, M. (2020). A preliminary study on morphology and genesis of giant and mega pockmarks near andu seamount, nansha region (South China Sea). *Mar. Geophys. Res.* 41 (1), 1–12. doi: 10.1007/s11001-020-09404-y

Zhang, Y., Zhai, W. D., Zang, K. P., and Wang, J. Y. (2014a). Enhanced methane emissions from oil and gas exploration areas to the atmosphere–the central bohai Sea. *Mar. pollut. Bull.* 81 (1), 157–165. doi: 10.1016/j.marpolbul.2014.02.002

Zhao, H., Wu, S., Xu, N., Wang, X., and Zhang, G. (2006). The elementary research of gas hydrate associated with mud diapir structure in the East China Sea. *Geoscience* 20 (1), 115–122. doi: 10.3969/j.issn.1000-8527.2006.01.014

Zhao, T., Zhang, X., Wang, X., and Meng, X. (2009). Acoustic detection of seabed hydrocarbon seepage in the north depression of south yellow Sea basin. *Petroleum Explor. Dev.* 36 (2), 195–199. doi: 10.1016/S1876-3804(09)60119-1

Zhou, Z., Zhao, J., and Yin, P. (1989). "Characteristics and tectonic evolution of the East China Sea," in *Chinese Sedimentary basins. sedimentary basins of the world 1*. Ed. X. Zhu (Amsterdam: Elsevier), 165–179.

Zhu, C., Cheng, S., Zhang, M., Ding, D., Chen, J., Lu, J., et al. (2019). Results from multibeam survey of the gas hydrate reservoir in the zhujiang submarine canyons. *Acta Geol. Sin. (English Edition)* 93, 135–138. doi: 10.1111/1755-6724.14223

Zhu, C., Jiao, X., Cheng, S., et al. (2020). Visualizing fluid migration due to hydrate dissociation: Implications for submarine slides. *Environ. Geotechnics*. doi: 10.1680/jenge.19.00068

Zhu, C., Li, Z., Chen, D., Li, S., Song, X., Shan, H., et al. (2021). Seafloor breathing helping forecast hydrate-related geohazards. *Energy Rep.* 7, 8108–8114. doi: 10.1016/j.egyr.2021.08.187

Zhu, C., Li, S., Chen, J., Wang, D., Song, X., Li, Z., et al. (2023). Nepheloid layer generation by gas eruption: Unexpected experimental results. *J. Oceanol. Limnol.* doi: 10.1007/s00343-022-2108-z

Zhu, C., Liu, X., Shan, H., Zhang, H., Shen, Z., Zhang, B., et al. (2018). Properties of suspended sediment concentrations in the yellow river delta based on observation. *Mar. Geores. Geotechnol.* 36 (1), 139–149. doi: 10.1080/1064119X.2017.1328715

Zou, H. Y., Gong, Z. S., Teng, C. Y., and Zhuang, X.B. (2011). Late-stage rapid accumulation of the PL19-3 giant oilfield in an active fault zone during neotectonism in the bozhong depression, bohai bay. *Sci. China Earth Sci.* 54 (3), 388–398. doi: 10.1007/s11430-010-4144-3

frontiers | Frontiers in Marine Science

TYPE Original Research
PUBLISHED 04 April 2023
DOI 10.3389/fmars.2023.1156486

OPEN ACCESS

EDITED BY
Zefeng Zhou,
Norwegian Geotechnical Institute (NGI), Norway

REVIEWED BY
Yufei Wang,
Norwegian Geotechnical Institute (NGI), Norway
Yubin Ren,
Dalian University of Technology, China

*CORRESPONDENCE
Pegah Amjadian
pgm21ryc@bangor.ac.uk

SPECIALTY SECTION
This article was submitted to Ocean Solutions, a section of the journal Frontiers in Marine Science

RECEIVED 01 February 2023
ACCEPTED 20 March 2023
PUBLISHED 04 April 2023

CITATION
Amjadian P, Neill SP and Martí Barclay V (2023) Characterizing seabed sediments at contrasting offshore renewable energy sites.
Front. Mar. Sci. 10:1156486.
doi: 10.3389/fmars.2023.1156486

Characterizing seabed sediments at contrasting offshore renewable energy sites

Pegah Amjadian*, Simon P. Neill and Vicky Martí Barclay

School of Ocean Sciences, Bangor University, Menai Bridge, United Kingdom

Due to the impacts of climate change, there is an urgent need to scale up existing, and develop novel, renewable energy technologies. Although there are many types of renewable energy technology, ocean renewable energy, including established offshore wind, and novel wave and tidal energy converters, offers many opportunities due to the abundance of the resource, availability of sea space, and (for tidal) predictability. However, the extraction of energy from the ocean environment will influence sediment dynamics and morphodynamics at various temporal and spatial scales. Detailed knowledge of seabed properties is also important for device installation, affecting foundation design and cabling. In this study, 36 seabed sediment samples were collected across a region of the Irish Sea extending from the west of Anglesey into Liverpool Bay up to a maximum distance of around 35 km offshore – a region where there are many existing and planned ocean renewable energy projects. Particle size analysis at quarter phi intervals was used to calculate the statistical properties of the seabed sediment samples, including Mean grain size, Sorting, Skewness and Kurtosis. These properties were compared against the outputs of wave (SWAN) and tidal (TELEMAC) models of the region to investigate the relationship between environmental variables and sediment characteristics, and to determine the impact and challenges of renewable energy technologies deployed in the region. Most of the sediments in the study area are medium sand, polymodal, very poorly sorted, coarse skewed, and very platykurtic. We found that mean water depth and peak current speed have the largest influence on Median grain size, and Sorting can be affected by tidal range, in addition to water depth and peak current speed. Moreover, minimal influence of wave climate was found on the sediments. A thorough discussion based on a literature review of the environmental issues of various energy converters (tidal energy converter (both individual and arrays), tidal barrage/lagoons, and wind turbines) was used to determine how devices in the study region, and at other sites throughout the world, would interact with sediment dynamics. We make recommendations on ways to minimize environmental impacts of ocean energy technologies.

KEYWORDS

sediment dynamics, renewable energy, wind energy, tidal energy, wave energy, Shipek, Irish Sea

1 Introduction

In recent decades, global climate change has become a major concern, applying pressure on many aspects of humankind. The combustion of fossil fuels and emission of greenhouse gases (GHG) such as carbon dioxide (CO_2) are playing a crucial role in the gradual rise in the overall temperature of the atmosphere (Romm, 2022). The consequences of climate change include changes in rainfall patterns, increased flood risk, severe storms, droughts, loss of species, fires, and sea-level rise (De Pryck, 2021). This, in turn, is affecting species distributions, habitats, and processes in the marine environment, leading to serious repercussions (Birchenough et al., 2015). Various methods for reducing or minimizing CO_2 have been suggested (e.g. Hepburn et al. (2019)); however it seems that the most sustainable alternative is taking advantage of renewable energy resources (Newell et al., 2021), hence the demand for renewable energy has grown rapidly as a response to climate change (Dannheim et al., 2020).

Marine energy is the energy that resides in waves, tides, ocean currents, and ocean temperature and salinity gradients, which is available for conversion into electricity (Zabihian and Fung, 2011). In addition, many developments in renewable energy are taking place at sea (e.g. arrays of offshore wind turbines) due to the magnitude of the resource, available sea space, and reduced visual impact (Pelc and Fujita, 2002). However, the presence of marine renewable energy devices can disrupt their environment, from the disturbance of marine mammals during construction (underwater noise) (Madsen et al., 2006) and increased risk of bird collisions (Loss et al., 2013), to changes in hydrodynamics and sediment dynamics. The extraction of energy from the water column could directly impact marine sediment dynamics and affect the stability of morphodynamic features such as offshore sand banks (Neill et al., 2017). The seabed will also be disturbed during the construction and decommissioning of the energy conversion technologies and their associated infrastructure (e.g. foundations and cabling) (Rui et al., 2022). Removal of sediments leads to direct habitat loss, and turbidity will increase because of suspended particle matter (SPM). These resuspended sediments will be transported by the tidal currents, which could represent an additional source of contamination during the construction phase (Gill, 2005).

This study aims to characterize seabed sediments at a range of sites suitable for various offshore renewable energy technologies, relating the sediment properties to environmental variables such as wave height and tidal current speed. The study is based on the processing and analysis of seabed sediment samples collected at sea, compared against environmental data generated by validated wave and tidal models of the region.

2 Study area

The study area is the region of the Irish Sea extending from the west of Anglesey into Liverpool Bay, with 36 seabed sediment samples collected at a maximum distance of around 35 km offshore (Figure 1). The Irish Sea can broadly be regarded as a North-South aligned channel where the semi-diurnal (M2 and S2) tidal constituents dominate the tidal dynamics in the region, and the diurnal tides (K1 and O1) are relatively weak (Coughlan et al., 2021). The combination of relatively shallow water depths and strong currents are responsible for generally high bed shear stress over much of the region (Coughlan et al., 2021).

The tidal wave propagates South to North along the Irish sea, primarily via the St. George channel and the North Channel, which connects the North Atlantic to the Northwest European shelf sea (Coughlan et al., 2021). Moreover, Anglesey and the narrow North Channel, which provide sheltering from the North Atlantic waves, prevent external swells from propagating into the Eastern Irish Sea. Since the Eastern Irish Sea has limited fetch, the waves in this region are often young, but due to shallow depths they can contribute to bed shear stress (Brown and Wolf, 2009).

Seabed sediments throughout the Irish Sea, which was formerly glaciated, are largely composed of reshaped glacial and postglacial material (Dobson et al., 1971; Holmes and Tappin, 2005). These sediments span a wide range of grain-size classes that are capable of being mobilized by waves, and particularly tidal currents (Xu et al., 2017). Moreover, the Central and Southern parts of the Irish Sea are dominated by sediments of sand and gravel grade (Jackson et al., 1995), also an area of muddy sediments called the Western Irish Sea Mud Belt (WISMB) is in the North Irish Sea, West of the Isle of Man. This area experiences seasonal stratification due to the formation of a dome of cold, dense water beneath a strong thermocline (Horsburgh et al., 2000). In this area, seabed sediments are mud to sand and can reach more than 40 m in thickness (Belderson, 1964; Coughlan et al., 2020). Most notably offshore Anglesey and the Southern Irish coast, gravel-grade material is expected to occur closer to the shore and within the Central Western Trough (Coughlan et al., 2021). In addition, sediment transport in the Irish Sea can be determined predominantly by wave action at the inshore waters, while further offshore sediment transport is more dependent on tidal currents (Van Dijk and Kleinhans, 2005; Van Landeghem et al., 2009).

The Irish Sea has considerable potential for renewable energy because of the ideal geographical position for wind generation due to close proximity to the Atlantic (Onoufriou et al., 2021). Considering the frequency and consistency of the wind which areas like Ireland and the United Kingdom experience, can make these regions possible to convert wind energy, especially at large scale (Onoufriou et al., 2021). Due to a large tidal range and strong tidal currents, the region is also host to many planned tidal energy projects, including the multiple tidal ranges schemes in Liverpool Bay (Neill et al., 2018) and the tidal stream array in the Anglesey Skerries (Robins et al., 2014).

3 Methods

36 seabed sediment samples were collected from the RV Prince Madog[1] using a Shipek Sediment Grab Sampler from 3rd – 13th

1 A 34.9 m research vessel with a maximum draft of 3.5 m.

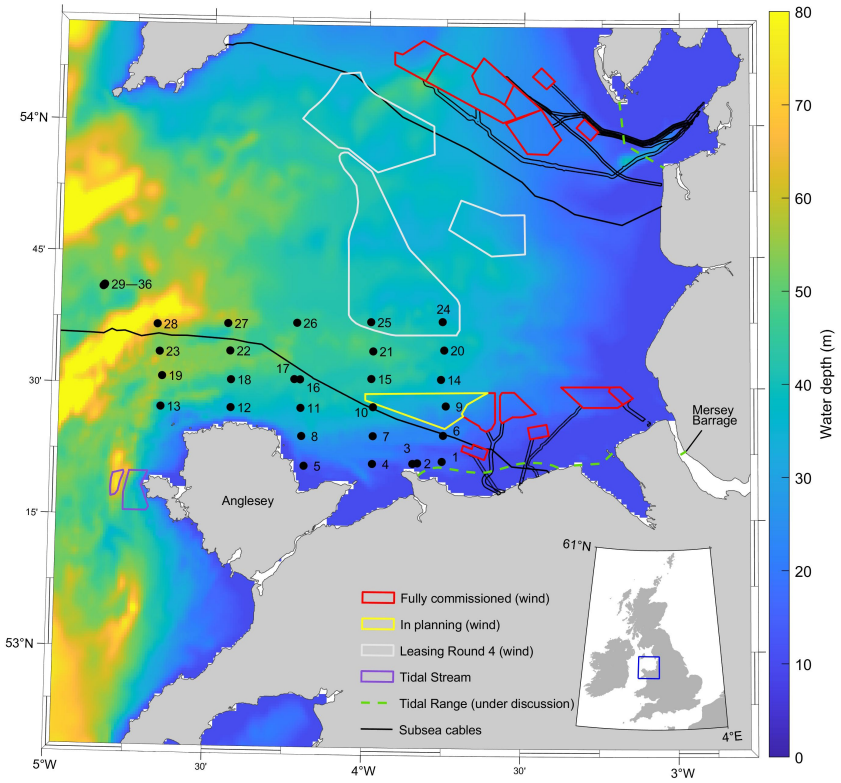

FIGURE 1
Map of sample locations in the Irish Sea and location of existing and proposed wind farms, tidal stream consented sites and tidal range proposed sites. Background color scale is bathymetry (from GEBCO) in meters relative to mean sea level. Wind farm, cables and tidal stream data from The Crown Estate.

June 2021 (Figure 1). The mean water depth at the sampling locations varies from 12 m to 79 m. Four of the locations were sampled twice, i.e. there are 32 unique locations within the 36 samples.

3.1 Laboratory work

We used the dry sieving method for particle size analysis. Each sample was washed (eliminating the salt content) before applying Buchner funnel vacuum filtration, a technique for separating solid products from reaction mixtures. A Buchner funnel was used to pass the mixture through Whatman grade 50 filter papers (nominal particle retention 2.7 m); solids are trapped in the filter while liquids are drawn into the flask under the funnel. A vacuum system was used to speed up the filtration process. When all the water is vacuumed into the flask, the sediment is washed with fresh water, which is retained as it contains the majority of the fine sediments. This retained water was evaporated under a heating lamp to obtain the fine sediment content[2].

Next, the sediment samples were dried in the oven for 24 h at 40°C (grain size is not affected by this temperature as it will only remove unbound water, and the temperature is sufficiently low to prevent baking the clay minerals). Once cooled, the samples were weighed, and if they exceeded 500 g (Krumbein and Pettijohn, 1939) a random bulk splitter was used to divide them into three equal parts, with one portion being used for sieving.

For the mechanical analysis we assembled a 1/4 phi (ϕ) sieve stack increasing from 0.063 mm (4 phi) to 63 mm (-6 phi), where

$$\phi = -\mathrm{Log}_2 d \tag{1}$$

with d the grain diameter in millimeters. The sieve stack was placed on a mechanical shaker for 15 minutes (Ingram, 1971) where the sediment passed through a series of progressively finer meshes. The mass retained on each sieve was recorded (in grams to two decimal places) for subsequent data analysis.

3.2 Data analysis

The samples are characterized using the grain size distribution and statistics package GRADISTAT (Blott and Pye, 2001), which analyzes grain size statistics from any standard measurement technique, including sieving and laser granulometry, by both the method of moments and the Folk and Ward (1957) method (Folk

2 The total fine sediment content is found by adding this component to the mass that remains on the 'pan' after passing through the 63 μm sieve following dry sieving.

and Ward, 1957). The scale is based on the logarithmic Udden-Wentworth size classification, where each size class boundary differs by a factor of two. Additionally, grade scale boundaries are transformed into phi values (ϕ) (Eq. 1) to facilitate the graphical presentation and statistical analysis of grain size frequency data.

The sample statistics used in this study are calculated using the logarithmic graphical method developed by Folk and Ward (1957) for granulometric analysis (Folk and Ward, 1957). Based on this method, there are four parameters that describe the grain size distribution:

1. *Graphical mean* (*Mz*) of sediment size, calculated as follows:

$$Mz = \frac{\phi 16 + \phi 50 + \phi 84}{3} \quad (2)$$

2. where ϕ16, ϕ50, and ϕ 84 are the 16th, 50th, and 84th percentile of the grain size distribution, respectively. *Sorting* (σ_1), which refers to the uniformity of grain size of the sediments, and called the Inclusive Graphic Standard Deviation, found by the formula:

$$\sigma_1 = \frac{\phi 84 - \phi 16}{4} + \frac{\phi 95 - \phi 5}{6.6} \quad (3)$$

3. where ϕ84, ϕ16, ϕ95, ϕ5 represent the values of ϕ at 84, 16, 95, and 5 percentiles. *Skewness* (Sk_1), statistically defined as the degree of asymmetry between grain size distribution. The measure of Inclusive Graphic Skewness is calculated by:

$$Sk_1 = \frac{\phi 16 + \phi 84 - 2\phi 50}{2(\phi 84 - \phi 18)} + \frac{\phi 5 + \phi 95 - 2\phi 50}{2(\phi 95 - \phi 5)} \quad (4)$$

4. *Kurtosis* (K_G), a measure of the ratio of the sorting in the central part of the distribution compared with the distribution at the tails. It is defined as:

$$K_G = \frac{\phi 95 - \phi 5}{2.44(\phi 75 - \phi 25)} \quad (5)$$

The results of the calculation can also be characterized using descriptive expressions for sediment size classification (Table 1). Various sediment types were encompassed by the sample collection, including Clay grain size (< 0.002 mm), Silt (0.002 – 0.063 mm), Sand (0.063 – 2 mm) and Gravel (2 – 64 mm) (Blott and Pye, 2001), also median grain size (*d*50) is the most regular measurement, which is used for grain size, at which 50% of the particles are smaller in mass (Martins, 2003).

3.3 Environmental variables

Time series of depth-averaged current speed and variation in water depths were extracted from a two-dimensional (depth-averaged) tidal model (TELEMAC) (Robins et at., 2019). TELEMAC uses an unstructured-mesh, with the resolution varying from high resolution at the coastline to coarser resolution offshore. The model was run for one month to encompass model spin up and provide a suitable time period to resolve the tidal constituents (Robins et al., 2019). The tidal forcing at the model boundaries consists of 13 diurnal, semi-diurnal and quarter-diurnal harmonic constituents (M2, S2, N2, K2, K1, O1, P1, Q1, M4, MS4, MN4, Mf, and Mm) extracted from the TPXO global tidal database (0.25° resolution) (Egbert et al., 1994).

Wave properties were extracted from a spectral wave model (SWAN) of the study region (Roche et al., 2016). The SWAN model of the Irish Sea is nested within an outer coarser SWAN model of the North Atlantic (Neill and Hashemi, 2013). The model was run for one year (2014) and variables (significant wave height and mean wave period) output 3-hourly at the seabed sediment sample locations. The SWAN model had a spectral resolution of 40 frequencies (from 0.04 to 1.0 Hz) and 45 directions. Wind forcing was from ERA-5 (Soares et al., 2020) which is 3-hourly at a resolution of 0.75 degrees (applied to both inner and outer grids). The full wave energy spectrum is transferred from the outer model to the boundary points of the inner grid, which has a resolution of 500 × 500 m (Roche et al., 2016). Although there will be significant inter-annual variability in the wave climate, the one year selected for the study is sufficient to test whether wave properties were strongly related to the seabed sediment characteristics, particularly as the site is relatively sheltered from swell waves (Section 3). If a relationship is found, this could be the subject of a future, more focused, investigation using a longer time series of wave modelling. By taking advantage of MATLAB and Excel (Regression and Pearson

TABLE 1 Descriptive expressions for different categories of sorting, skewness and kurtosis (Blott and Pye, 2001).

Sorting (σ_1)		Skewness (Sk_1)		Kurtosis (K_G)	
Very well sorted	< 0.35	Very Fine Skewed	+0.3 to +1.0	Very platykurtic	< 0.67
Well sorted	0.35 – 0.50	Fine Skewed	+0.1 to +0.3	Platykurtic	0.67 – 0.90
Moderately well sorted	0.50 – 0.70	Symmetrical	+0.1 to -0.1	Mesokurtic	0.90 – 1.11
Moderately sorted	0.70 – 1.00	Coarse skewed	0.1 to -0.3	Leptokurtic	1.11 – 1.50
Poorly sorted	1.00 – 2.00	Very coarse skewed	-0.3 to -1.0	Leptokurtic	1.50 – 3.00
Very poorly sorted	2.00 – 4.00			Extremely leptokurtic	> 3.00
Extremely poorly sorted	> 4.00				

test) the relationship between seabed sediment properties and environmental characteristics was assessed.

4 Results

4.1 Particle size analysis

Various sediment properties relating to each analyzed Shipek grab sample are presented in Table 2. The raw data is available in the Supplementary Materials. The analysis of grain size distribution spans from Very Fine Sand (0.063 m) to Gravel (63 mm), and is summarized as follows.

The Highest-Class Weight found at each location is given in the second column of Table 2, and the percentage of grain size distribution across the study area summarized in Figure 2. Only 10.2% of the mass of all the collected sediment samples was classified as fine sand. 28% of grain size distribution is medium sand, and can be seen mostly in the stations further offshore. There is 17.8 % coarse sand in the sediment samples across the study region, 8.1 % very coarse sand, and 11.4 % very fine gravel, 6.2 % fine gravel, 5.9 % medium gravel, 8.3 % coarse gravel, 2.5 % and 0.7 % are very coarse gravel and mud clay respectively. Sediments in the western part of the study area are predominantly gravel (Figure 3A). 13/36 (i.e. around 36%) of the samples are sandy gravel, and 16/36 (i.e. around 44%) of the samples are gravelly sand.

The result of sediment analysis in terms of Mode (Unimodal, Bimodal, Trimodal, Polymodal) are given in Table 2 and Figure 4. Most samples are either bimodal (i.e. the majority of samples contain both fine and coarse sediments) or polymodal; consequently this could be considered the reason behind the high percentage of poorly-sorted (39% of samples) grain-size distributions.

An important parameter that should be considered in terms of sediment properties is sorting since, for example, it is difficult to calculate the median grain size for a mixed (poorly sorted) sample of sediment (Folk and Ward, 1957). As can be seen in Table 2 and Figure 4, sorting of each sediment is analyzed and described based on Table 1. Approximately 40% of the samples are very poorly sorted, particularly in the Central-to-Western part of the study area (Figure 3B). The seabed sediments in the Eastern region of the domain are generally moderately to very well sorted, with the exception of two stations in the Southeast (samples 1 and 2) being very poorly sorted. The samples at the most offshore locations (samples 29 to 36) vary from very poorly sorted to moderately well sorted.

Figure 3C indicated that the Northen section (i.e. offshore) the nearshore stations off the North coast of Anglesey are generally platykurtic (i.e. low kurtosis, indicating less kurtosis than normal distribution (less than 3 or negative excess values < 0)). The Southeastern section, towards Colwyn Bay, is more mixed in terms of kurtosis, although 50% of these samples are classified as very leptokurtic. The offshore samples (29 – 36) vary from very leptokurtic (distribution with high kurtosis (numerous outliers)) to very platikurtic (distribution with low kurtosis (infrequent outliers)), and can both impact on normal distribution. In Figure 5, detailed grain size distributions from two contrasting locations were illustrated.

Skewness is one of the most sensitive sediment properties, and deposition conditions have the greatest impact on skewness. Negative skewness indicates that the medium in which the deposit is being made is subject to turbulent energy conditions, and positive skewness indicates that the sedimentation environment is relatively calm and steady (Awasthi, 1970). As can be seen in Figure 3D, near-shore stations are mostly characterized by very fine to fine skewness (positive skewness). Further offshore and towards the eastern region of the study area the samples are mostly on the opposite side of the spectrum, i.e. very coarse and coarse skewed. This is relevant, as the proposed wind farms (Figure 1) would be located in a relatively energetic environment. Regarding the Northwest cluster of stations (29 – 36), they also present a coarse to very coarse skewness.

4.2 Comparison of sediment properties with environmental variables

Significant wave height (H_s) and mean wave period (T_m) were extracted from a SWAN spectral wave model of the study region (Roche et al., 2016). The model output frequency is 3-hourly throughout 2014. Figure 6 shows the variability of H_s and T_m over a year across all of the sample sites. We used these environmental properties to find correlations of waves with sediment properties at the sample locations.

The tidal range across the region was extracted from the TELEMAC model (Robins et al., 2019). As the patterns are similar across the sites, we only plot the sites that experience the largest and smallest tidal range (Figure 7). In general, the tidal range was 8 m (spring), 4 m (neap) and 3.3 m (mean) across the sites. In addition, the tidal elevations are in-phase with one another across the sampling sites, indicative of the standing wave system that is known to occur in the area (Neill et al., 2018). Peak current speed at each location was also extracted from the TELEMAC model, in addition to mean water depths (from the model bathymetry).

The available environmental variables (mean water depth, peak current speed, spring tidal range, significant wave height, and bed shear stress) are plotted against the primary sediment properties (Median Grain Size, Mean, Sorting, Skewness, Kurtosis) on Figures 8–11. The R^2 value and p-values were calculated for each relationship.

Based on Figure 8, water depth and median grain size have a weak negative correlation. Spring tide and grain size have weak positive correlation. Peak velocity and grain size have moderate negative correlation, in addition the p-value of each variable is calculated. Spring tide and grain size positive correlation (negligible correlation). Also, the regression of the D50 and environmental variables are calculated, and R^2 is 51 %, which means that environmental parameters as an independent variable can impact on median grain size as a dependent variable 51 %. Furthermore, the p-value for determining the relationship between mentioned variable is calculated (Figure 12), and the result shows that water depth and peak velocity have relationship with D50.

10.3389/fmars.2023.1156486

TABLE 2 Parameters for describing grain size distribution.

Sample	Highest-Class Weight (mm)	Mode	Mean (M_z)	Sorting (σ_1)	Skewness (Sk_1)	Kurtosis (K_G)
1	11.20	Polymodal	-1.568	2.413	0.274	0.544
2	11.20	Polymodal	-1.518	2.583	0.431	0.523
3	0.25	Bimodal	1.791	0.661	-0.374	1.836
4	0.25	Bimodal	2.078	0.353	0.311	0.858
5	0.30	Bimodal	1.830	0.526	0.475	1.151
6	0.30	Unimodal	1.574	0.216	-0.011	1.726
7	0.30	Trimodal	1.846	0.708	-0.232	2.744
8	11.20	Polymodal	-1.222	2.152	0.350	0.588
9	0.50	Unimodal	1.045	0.460	-0.153	1.971
10	0.30	Polymodal	0.807	1.546	-0.519	1.028
11	0.30	Trimodal	1.794	0.767	-0.192	2.389
12	0.50	Polymodal	-1.844	2.343	-0.007	0.491
13	22.40	Polymodal	-2.347	1.997	0.259	0.667
14	0.30	Polymodal	1.214	0.866	-0.220	1.543
15	2.00	Bimodal	0.561	1.278	-0.324	0.547
16	31.50	Polymodal	-1.873	2.563	0.229	0.534
17	31.50	Bimodal	-3.027	2.190	0.506	0.711
18	16.00	Unimodal	-1.716	2.194	0.225	0.564
19	16.00	Polymodal	-2.416	2.110	0.365	0.798
20	0.30	Polymodal	0.914	1.284	-0.379	0.800
21	31.50	Polymodal	-2.167	2.641	0.238	0.508
22	0.35	Polymodal	-1.501	2.453	0.138	0.604
23	2.00	Bimodal	0.036	1.082	0.255	0.515
24	0.60	Polymodal	0.743	0.945	-0.061	1.232
25	0.32	Polymodal	0.140	1.854	-0.459	0.798
26	26.50	Polymodal	-0.978	2.560	-0.538	0.762
27	0.30	Polymodal	-0.557	2.075	-0.139	0.646
28	26.50	Polymodal	-2.181	2.753	0.395	0.532
29	2.00	Polymodal	-1.762	2.437	-0.444	1.328
30	0.50	Bimodal	0.500	1.277	-0.208	1.203
31	0.43	Polymodal	-0.443	2.033	-0.486	0.775
32	0.43	Polymodal	-0.556	1.853	-0.437	0.689
33	2.00	Trimodal	-0.298	0.657	-0.139	0.609
34	2.00	Trimodal	-0.290	0.650	-0.190	0.615
35	0.71	Bimodal	0.373	0.969	-0.163	1.542
36	2.00	Bimodal	0.313	1.095	-0.188	1.354

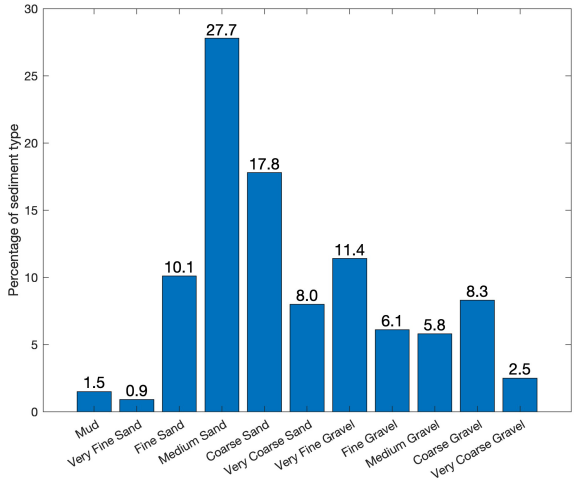

FIGURE 2
Percentage of sediment type across all seabed samples.

Figure 9 indicated the correlation between the sediment properties and environmental variable. R^2 and p-values were calculated for each sediment properties and environmental variable. As can be seen, the trends and relationship were shown on the graph, and all the correlation and relationship were presented on Figure 12.

Also, the bed shear stress (τ_0) at each location was calculated using

$$\tau_0 = \rho u_\star^2 \tag{6}$$

where ρ is the density of the ocean water (taken as 1027 kg/ m^3), and $u_\star$ is shear stress velocity, calculated using

$$u_\star = C_D u|u| \tag{7}$$

where C_D is the drag coefficient (2.5×10^{-3}), and u is the depth-averaged current speed.

The correlation between median grain size and bed shear stress is moderate negative, with a p-value < 0.05 indicating a strong relationship Figure 11. In addition, some samples, for example, sample 13 which in terms of textural can be considered fine gravel has the highest bed shear stress because of high velocity in this region, consequently seabed sediment types can correlate to the bed shear stress (Ward et al., 2015).

Figures 3A–D indicated the distribution of mean, sorting, kurtosis, and skewness across the study area. As can be seen the majority of samples in the eastern part of the study area, are mostly very fine gravel and in the Western part fine coarse sand are more. Moreover, Sample 17 (-3.765 ϕ) has the largest median grain size and sample 4 has the smallest median grain size (1.992 ϕ). The results of linear correlation and regression between environmental variables and sediment properties are shown in Figure 12. When p-value is (< 0.05), it should be considered a statistical significance, in addition the Pearson correlation coefficient (r) of sediment properties and environmental climate were calculated.

D50 has strong relationship with water depth and peak velocity (p-value), and R^2 is 59 % which shows how much the environmental variables can impact on D50 (Figure 12); consequently, 59 % of changes in D50 can be driven by environmental parameters. It is also worth noting that D50 has moderate negative correlation with peak velocity. The result of p-value indicated that peak velocity and water depth have strong relationship with mean, and R^2 is 58%. It shows that independent variables (environmental parameters), 58% can impact on dependent variable (mean). Furthermore, mean and peak velocity have moderate negative correlation. Based on p-value analysis it seems that sorting has strong relationship with peak velocity, water depth, and spring tide.

5 Discussion

The results indicate that the seabed in the eastern part of the study area, a region with much marine renewable energy activity, is comprised mostly of sandy sediments (fine, medium, and coarse sand), whereas the Western region is generally characterized by very fine gravel, and fine gravel. Further, the sediments in the region are generally polymodal, and very poorly sorted. The result of Pearson correlation coefficient indicated that median grain size (D50) and the tidal range have a weak relationship. Velocity can impact on the D50, and they have negative relationship, noting that D50 is in phi values (i.e. -log2 of the grain size in mm). Peak velocity also has an impact on the mean and sorting of the seabed sediments. Bed shear stress, which is a fundamental factor in estimating sediment transport, has moderate negative relationship with D50, with R^2 = 31 %. However, D50 has negligible correlation with tidal range. Significant wave height has negligible correlation with all the sediment properties (D50, Mean, Sorting, Kurtosis, Skewness), so it seems that seabed sediment properties in the study area are dominated by tidal currents. In addition, peak velocity has a moderate negative correlation with mean, and a positive moderate correlation with sorting and D50, so velocity can impact on uniformity of grain size and median grain size. Also, velocity has a negligible correlation with skewness, and weak negative correlation with kurtosis. Overall, it seems that peak current

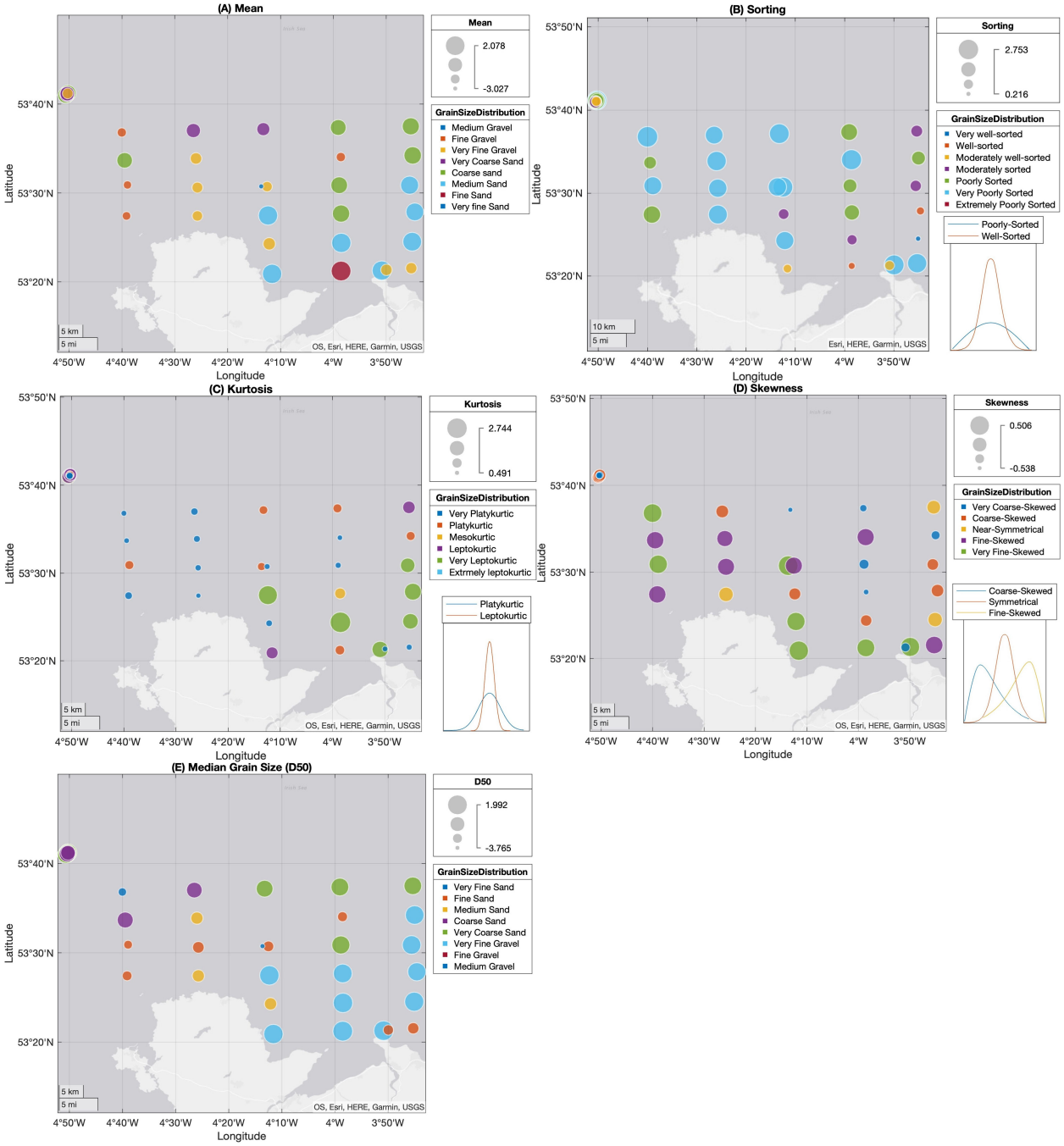

FIGURE 3
Distribution of **(A)** Mean, **(B)** Sorting, **(C)** Kurtosis, **(D)** Skewness, and **(E)** Median grain size across the study area.

speed and water depth have the strongest relationship among all the environmental parameters with sediment properties, consistent with previous studies (e.g. (Ward et al., 2015)).

The marine renewable energy industry is currently exploring coastal regions that are in close proximity to electricity grids for development (Neill et al., 2014). Knowledge of seabed sediment characteristics at a range of sites and across a range of environments that are suitable for a variety of offshore renewable technologies could lead to pairing each location with the most appropriate renewable energy technology. Further, it could be possible to co-locate wind and wave energy (or other renewable energy combinations) at a single location to share infrastructure costs (e.g. cabling) and minimize the variability in power output (Stoutenburg and Jacobson, 2010).

The influence of marine energy converters on hydrodynamic and sediment dynamics is not well known, and primarily theoretical, since collecting samples in these dynamic marine environments is difficult (Auguste et al., 2019), and it is challenging to assess sediment properties pre- and post-construction. To select a suitable site for the installation and

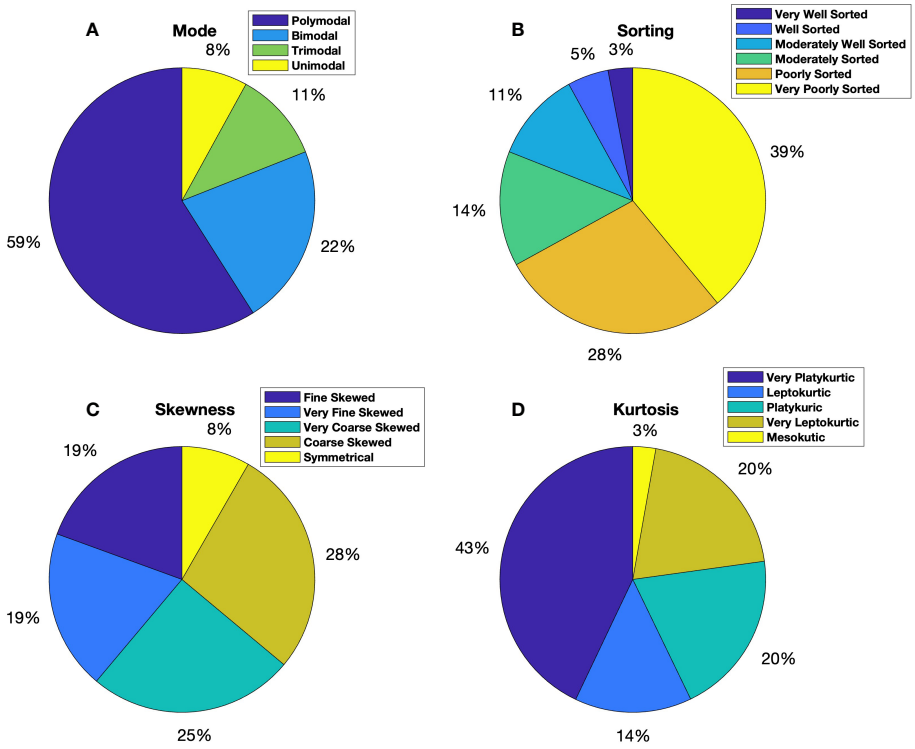

FIGURE 4
The percentage of Grain-Size **(A)** Mode, **(B)** Sorting, **(C)** Skewness and **(D)** Kurtosis across the study area.

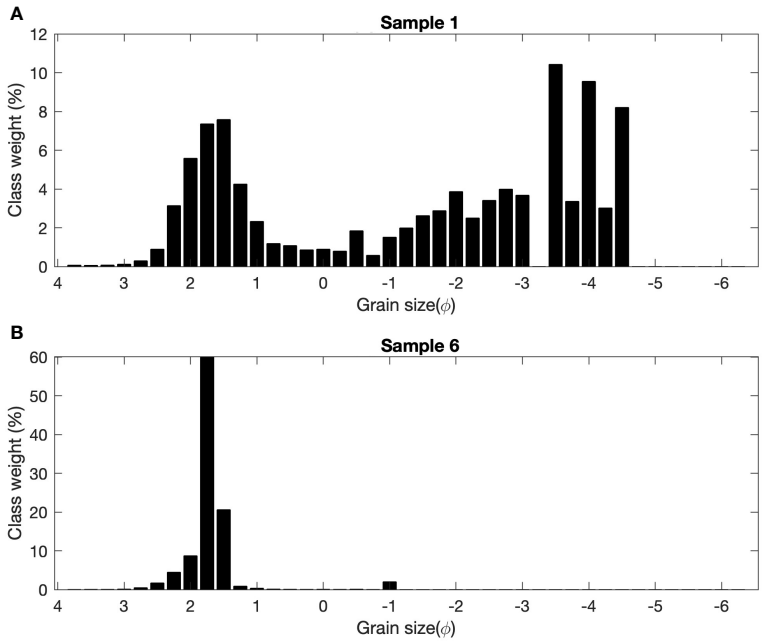

FIGURE 5
Typical sediment grain size distributions shown for two contrasting sites. **(A)** Sample 1 is Sandy Gravel, Polymodal, Very Poorly Sorted, Fine Skewed, Very Platykurtic, and D50 = -2.127 ϕ. **(B)** Sample 6 is Slightly Gravelly Sand, Unimodal, Very Well Sorted, Symmetrical, very Leptokurtic, and D50 = 1.598 ϕ.

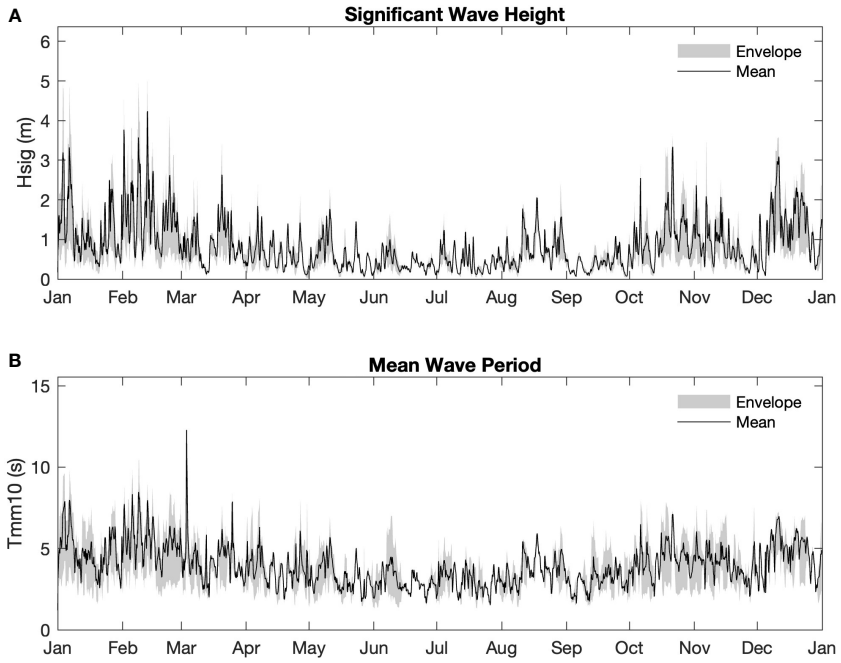

FIGURE 6
Simulated mean, minimum and maximum **(A)** significant wave height (H_s) and **(B)** mean wave period (T_m) across all sample locations during 2014.

operation of a marine energy technology, it will be necessary to understand the hydrography of the area (Bozgeyik, 2019). In most cases, marine renewable energy installations, with the exception of offshore wind, are comprised of a single demonstration device, but the industry is now moving towards demonstration and commercial arrays of at least ten devices, with the final goal of installing large arrays that exceed 100 devices (Shields et al., 2011).

The remainder of the discussion explores various ocean renewable energy technologies and their impact on the hydrodynamic and sediment dynamics, within the context of the analysis of seabed sediments.

5.1 Offshore wind turbines

The selection of an appropriate site for offshore wind farm is a complex process that takes into consideration many factors such as technical/mechanical, environmental, socioeconomic, as well as national legislation and regulations. However, some significant criteria for desirable regions are water depth, wind-energy potential (Vasileiou et al., 2017), and distance-to-shore (Díaz and Soares, 2020).

Water depth has a fundamental role in the installation formula. Present technology enables marine applications to be developed up to a maximum depth of around 60 m (Adelaja et al., 2012; Chaouachi et al., 2017). The water depths at our sampling locations varied from 12 – 79 m, which demonstrates their suitability for various wind turbines technologies.

In the offshore wind industry, there are two primary types of foundations: floating foundations and bottom fixed foundations. It is acceptable for bottom fixed foundations (Figure 13A) to be installed in water depths of up to 60 m. Nevertheless, when water depths exceed 40 m, these structures experience increased hydrodynamic loads, leading to increased cost (Leontaris et al., 2016). The floating concept has been proposed as a solution to this problem (Hernandez C et al., 2021). There are five various types of bottom fixed foundation (Gravity, Monopile, Tripod, Jacket, Tripile foundation) (Hernandez C et al., 2021). Monopiles are the most frequently installed type (81 %), followed by jackets (8 %) (Selot et al., 2019).

There are three types of floating foundation (Figure 13B): semisubmersible foundation, spar foundation, and tension-leg platform (TLP) foundation. Note that floating foundations have only been deployed in a small number of projects (Selot et al., 2019).

The presence of offshore wind turbines presents issues relating to sediment properties. One of the most significant challenges is scouring around the piles of the wind turbines due to interaction with waves and currents (Aminoroayaie Yamini et al., 2018). Waves induce scour of the sediment around the turbine's pile and make it unstable (Aminoroayaie Yamini et al., 2018). Based on laboratory examination it has been observed that maximum scour depth value was reduced by roughly 41 % when the bed particle diameter was increased by 50 %; nevertheless when the particle diameter decreases by 50 %, the maximum scour depth value increases (Aminoroayaie Yamini et al., 2018).

Wakes are considered the other problem of the presence of offshore wind foundations (Vanhellemont and Ruddick, 2014).There can be a wide variety of wake effects depending on the foundation type, due to differences in the diameters of foundation structures and the volumes of impermeable structures in the water column and on the seafloor (Zhang et al., 2020). In contrast to monopile foundations, tripod, tripile, and jack-up

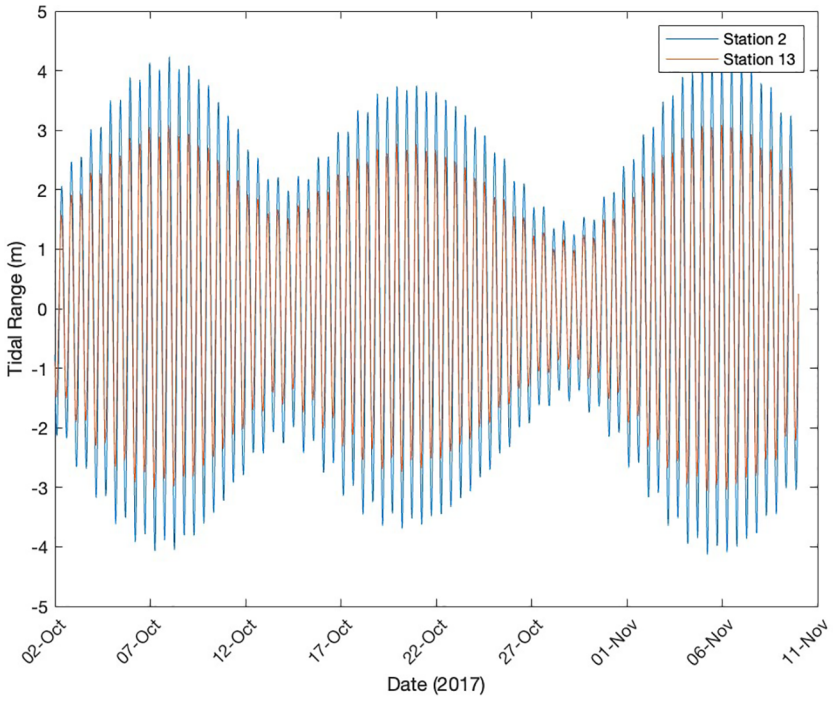

FIGURE 7
Time series of simulated tidal elevations for two contrasting sites across the study region, i.e. the locations that exhibited the highest (sample 2) and lowest (sample 13) tidal range.

foundations are estimated to have reduced wake effects due to smaller diameters (Zhang et al., 2020). However, by taking advantage of jacket foundations, the wake effect could be minimized because of a smaller volume of structure in the water column as well as at floating foundations, where there are weaker currents near the seabed (Zhang et al., 2020). Installation of offshore foundations are primarily responsible for the release of suspended sediment (Zhang et al., 2020), sediment transport and downstream sedimentation (Vanhellemont and Ruddick, 2014). During installation, gravity foundations requiring seabed preparation (e.g. dredging) and monopiles that employ reverse circular drilling will have the greatest impact on sediment (Zhang et al., 2020). Consequently, suspended sediments concentrations will increase in the wake of turbine monopiles within an offshore wind farm (Vanhellemont and Ruddick, 2014).

5.2 Tidal energy

Tidal energy conversion, either by tidal stream (kinetic energy) or tidal range (potential energy) will impact sediment dynamics over various temporal and spatial scales (Shields et al., 2011; Ahmadian et al., 2012).

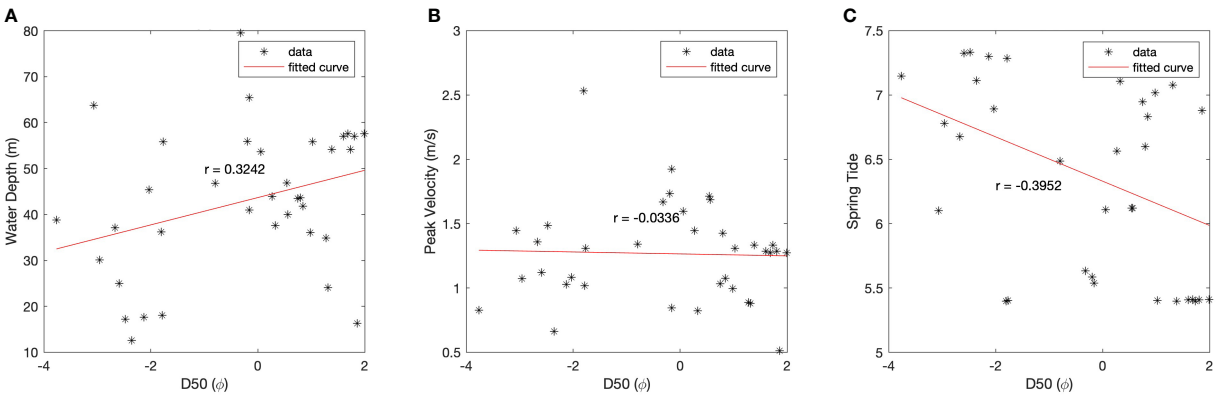

FIGURE 8
Correlation between d_{50} and environmental variables: **(A)** water depth, **(B)** peak tidal velocity **(C)** spring tide.

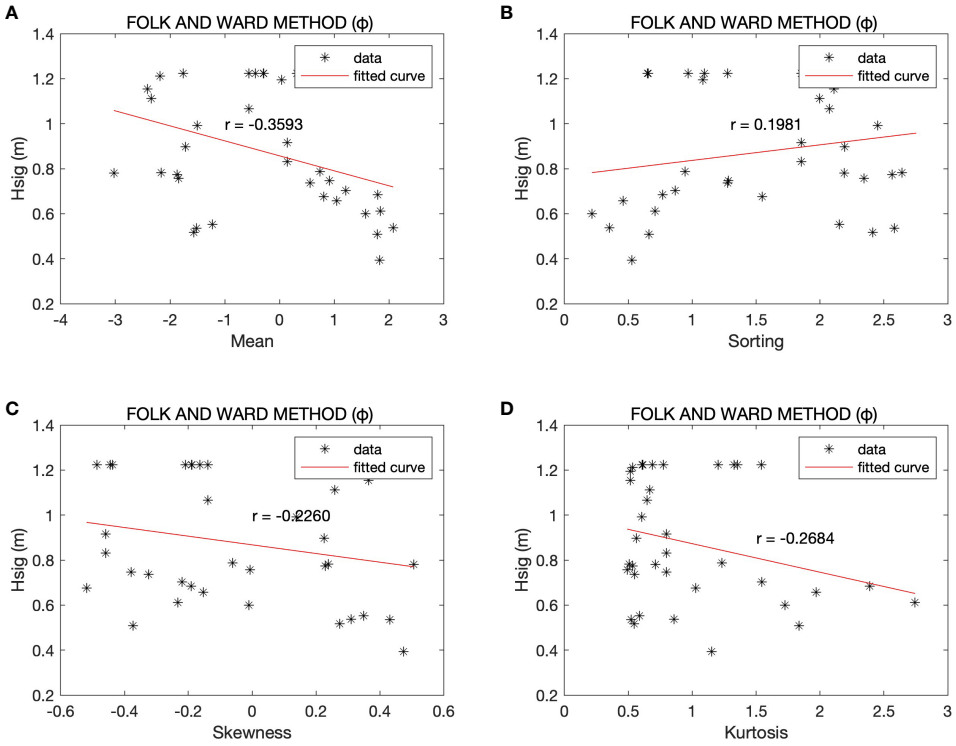

FIGURE 9
Correlation between H_s and sediment properties: **(A)** Mean, **(B)** Sorting, **(C)** Skewness, **(D)** Kurtosis of seabed sediment samples.

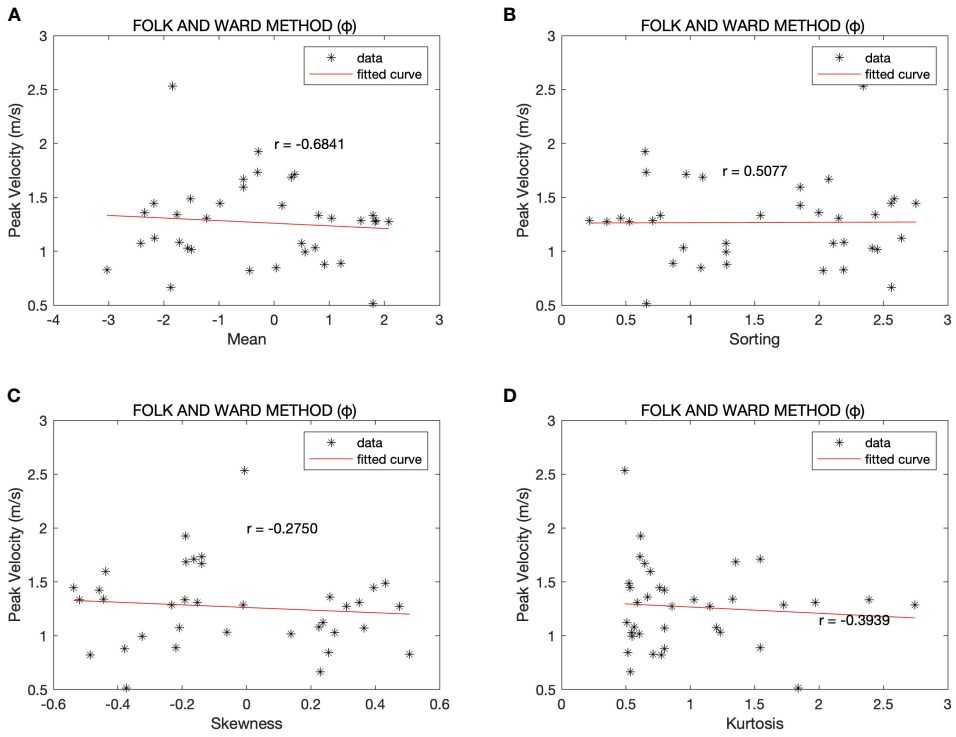

FIGURE 10
Correlation between Peak Velocity and sediment properties: **(A)** Mean, **(B)** Sorting, **(C)** Skewness, **(D)** Kurtosis.

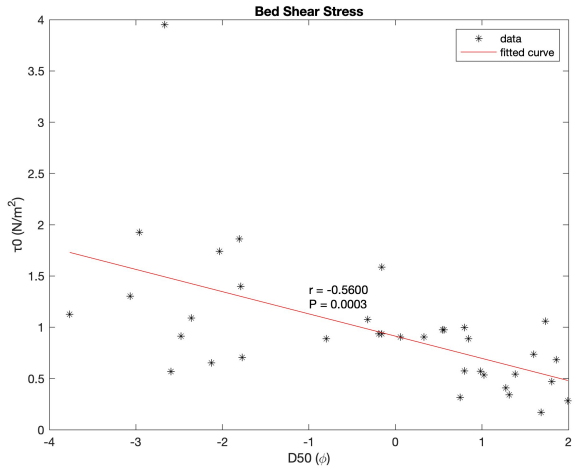

FIGURE 11
The correlation of *D*50 and bed shear stress.

5.2.1 Tidal stream devices

Tidal Energy Converters (TEC) can be installed in locations with ideal flow conditions (i.e., high velocity with low turbulence). They are normally installed close to coastlines, in straits and near headlands, where topography and bathymetry will enhance flow speeds (Shields et al., 2011). The current generation of Tidal Stream Energy devices require flow speeds in excess of 2.5 m/s and water depths between 25 and 50 m (Lewis et al., 2019). Moreover, the seabed at most tidal energy sites will be characterized by medium to coarse sands and gravels, and sediment concentrations are not likely

p-value \ Correlation (r)	D50	Mean(Mz)	Sorting(σI)	Skewness(SKI)	Kurtosis(KG)
Hsig	-0.2264 / 0.589	-0.3593 / 0.6237	0.1981 / 0.7745	-0.226 / 0.4387	-0.2684 / 0.5991
Wave Period	-0.3026 / 0.2152	-0.4146 / 0.3151	0.2121 / 0.46	0.3563 / 0.0376	-0.3588 / 0.4232
Peak velocity	-0.6591 / 0.0006	-0.6966 / 0.0018	0.5067 / 0.0033	0.3574 / 0.0045	-0.3147 / 0.106
Water Depth	-0.3175 / 0.0139	-0.4296 / 0.0614	0.3149 / 0.0300	0.3474 / 0.0004	-0.4218 / 0.0613
Spring Tide	0.2878 / 0.4461	0.3912 / 0.2719	-0.1717 / 0.0367	-0.4289 / 0.0893	0.3659 / 0.8642
bed Shear Stress	-0.5600 / 0.0003	-0.1007 / 0.2092	0.0177 / 0.278	-0.1091 / 0.1833	-0.0826 / 0.6824
R/h	0.2787 / 0.1558	0.4112 / 0.5049	-0.28 / 0.5329	-0.2526 / 0.0002	0.4166 / 0.1339

FIGURE 12
The result of Correlation and Regression analysis (green color indicates p-value < 0.05, and pink shows moderate or strong correlation (*r*)). *R*/*h* is the ratio of spring tidal range (*R*) to water depth (*h*).

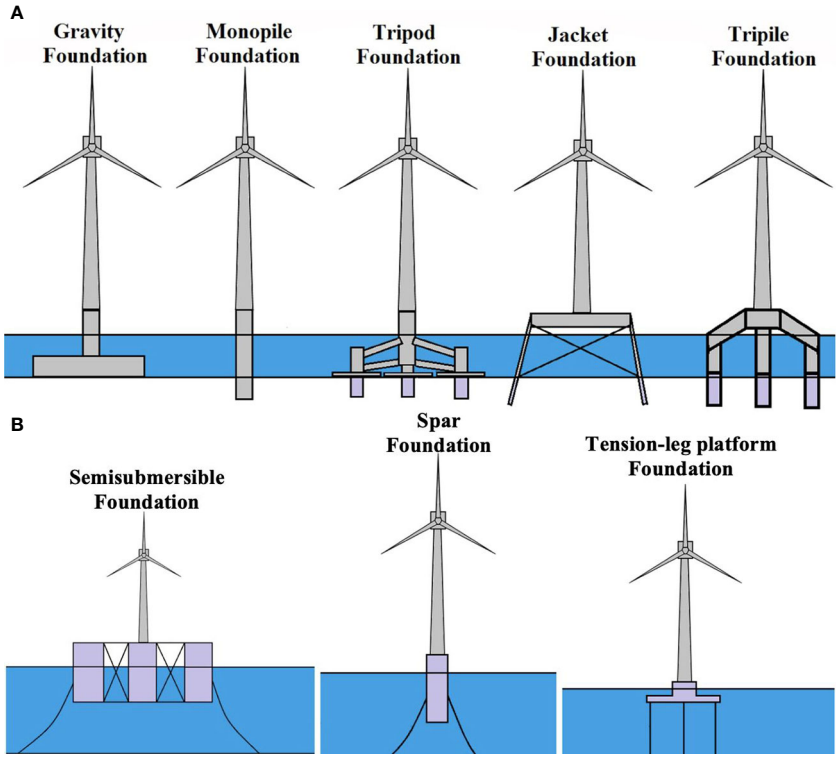

FIGURE 13
(A) Various types of bottom fixed foundation of offshore wind turbines, **(B)** Offshore wind turbine floating foundations (Hernandez C et al., 2021).

to impose significant loadings on turbine blades (Neill et al., 2017). Tidal stream devices can be installed individually or in arrays. An individual tidal energy converter (TEC) consists of a support structure and a rotor, generally in the horizontal axis configuration. It is also worth noting that a wake is generated by both the rotor and the support structure (Neill and Elliott, 2004); consequently sediment dynamics are likely to be altered by turbine operation. Firstly, because of strong tidal flows, localized scouring will occur (Den Boon et al., 2004), and to avoid foundation erosion, developers will have to consider scour protection, such as rock armor, when installing turbines in regions with sufficient sources of mobile sediment. Secondly, wakes cause sediments to be winnowed (Wolanski et al., 1984), in this case, a poorly sorted sediment is dispersed (enhance sorting), consequently, the coarser fraction remains (increase the grain size). It is possible that well-sorted sediment could develop in the wake zone, contributing to further erosion issues (Neill et al., 2017). Moreover, based on the analysis presented here, sorting can be affected by current speed, water depth, and tidal range (Figure 12). Velocity and sorting have weak positive correlation, and with increasing velocity, sediments would become more well-sorted. In contrast, velocity and mean have negative moderate correlation which means with increasing velocity the mean (grain size) is reduced. Consequently, in the presence of a tidal stream device, the risk of erosion is higher in the wake – due to reduced velocity the mean (the average size) of sediments increase, and wake effect can make it intensify (towards well-sorted). Overall, it has been found that even though single turbines will have local impacts (less than 1 km) (Neill et al., 2009; Mekhilef et al., 2012) the development of large TEC arrays will exceed the natural variability of morphodynamic features such as offshore sand banks due to their potential near-field and far-field effects (Neill et al., 2012; Robins et al., 2014).

5.2.2 Tidal range power plants

Tidal barrages and tidal lagoons can generate considerable power when the tidal range is sufficient (Neill et al., 2017). A tidal barrage spans the entire width of a seaway or estuary (Waters and Aggidis, 2016), whereas a tidal lagoon only partly impounds a seaway (Neill et al., 2017). A Tidal range power plant would reduce the magnitude of the tidal currents and thus reduce the suspended sediment load while providing greater bed stability, encouraging the colonization of an otherwise highly suppressed ecosystem (Kirby and Shaw, 2005).As can be seen in Figure 12, based on the analysis of the sediment samples, velocity has negative correlation with median grain size and mean, and by reducing the velocity the median grain size and mean will increase. Also, sorting and velocity are positively correlated, and decreasing the velocity will lead to decreased sorting. Barrages and lagoons are also likely to increase sediment deposition in certain areas, the location and magnitude of which will depend upon specific design and the prevailing source of the sediment (Mekhilef et al., 2012). Moreover, sediments are transported outside the lagoon, and are accumulated inside the lagoon (Neill et al., 2017). In addition, counter-rotating eddies might emerge in the turbine wake because of the focusing of turbines and sluices in particular parts of the lagoon wall (Wang et al., 2009) leading to concentrated sediment resuspension and

scour. Equally spacing turbines around the lagoon (although at likely increased cost) can reduce this impact (Wang et al., 2009).

6 Conclusion

Seabed sediment samples collected across one of the most energetic regions of the Irish Sea were analyzed, and the relationship with environmental characteristics assessed. Most of the sediments within the study area are medium sand, polymodal, very poorly sorted, coarse skewed, and very platykurtic. In addition, environmental parameters such as water depth and current speeds have a strong impact on median and mean grain size. Moreover, water depth, current speed, and tidal range can influence sorting. Skewness (which quantifies the asymmetry of grain size distribution) can be affected by wave period, velocity, water depth and tidal range. Because skewness is affected by a wider range of factors than the other sediment properties, it is the most sensitive statistic. Furthermore, in agreement with previous model studies, bed shear stress and median grain size are strongly related. Since marine renewable energy has received increased attention in recent years, it is essential to investigate the optimal site, foundations, and cable technologies, in addition to environmental impact of the devices. Wakes generated either by offshore wind or tidal stream turbines lead to winnowing of seabed sediments (i.e. removal of the fine content), leading to well sorted sediments which are further susceptible to erosion. In addition, the development of tidal range power plants can alter current speeds, leading to changes in the rate of deposition. Although it is not possible to fully assess the impact such large structures will have on seabed sediment prior to construction, it is possible to minimize such impacts by careful planning, for example equally spacing the turbines around the embankment. The only variables that were both significant and strongly correlated to environmental properties were median grain size (related to peak current speed and bed shear stress) and mean grain size (related to peak current speed). Although sorting and skewness were both found to be significant, the correlations across all environmental variables were low. Our general recommendation is to minimize impacts of marine renewable energy technologies that affect both the mean and median grain size. This relates primarily to tidal energy conversion, both tidal range and tidal stream. We recommend that the scale of such schemes be restricted in high energy regions.

Data availability statement

The original contributions presented in the study are included in the article/Supplementary Material. Further inquiries can be directed to the corresponding author.

Author contributions

PA and SN contributed to the conception and design of the study. PA processed the sea bed sediment samples and performed the statistical analysis SN extracted the environmental variables from the models PA wrote the first draft of the manuscript. SN and VM wrote sections of the manuscript. All authors contributed to the article and approved the submitted version.

Funding

We acknowledge the support of SEEC (Smart Efficient Energy Centre) at Bangor University, part-funded by the European Regional Development Fund (ERDF), administered by the Welsh Government.

Acknowledgments

Many thanks to Guy Walker-Springett for his advice during sediment lab work, and Peter Robins for providing TELEMAC Model output of the study region.

Conflict of interest

The authors declare that the research was conducted in the absence of any commercial or financial relationships that could be construed as a potential conflict of interest.

Publisher's note

Supplementary material

The Supplementary Material for this article can be found online at: https://www.frontiersin.org/articles/10.3389/fmars.2023.1156486/full#supplementary-material

References

Adelaja, A., McKeown, C., Calnin, B., and Hailu, Y. (2012). Assessing offshore wind potential. *Energy Policy* 42, 191–200. doi: 10.1016/j.enpol.2011.11.072

Ahmadian, R., Falconer, R., and Bockelmann-Evans, B. (2012). Far-field modelling of the hydro-environmental impact of tidal stream turbines. *Renewable Energy* 38, 107–116. doi: 10.1016/j.renene.2011.07.005

Aminoroayaie Yamini, O., Mousavi, S. H., Kavianpour, M. R., and Movahedi, A. (2018). Numerical modeling of sediment scouring phenomenon around the offshore wind turbine pile in marine environment. *Environ. Earth Sci.* 77, 1–15. doi: 10.1007/s12665-018-7967-4

Auguste, C., Nader, J.-R., Marsh, P., and Cossu, R. (2019). "Influence of tidal energy converters on sediment dynamics in tidal channel," in *Proc. 13th European Wave and Tidal energy Conf.* 1–6. Available at: https://espace.library.uq.edu.au/view/UQ:5ac15f1.

Awasthi, A. (1970). Skewness as an environmental indicator in the solani river system, roorkee (India). *Sedimentary Geology* 4, 177–183. doi: 10.1016/0037-0738(70)90010-2

Belderson, R. (1964). Holocene Sedimentation in the western half of the Irish Sea. *Mar. Geology* 2, 147–163. doi: 10.1016/0025-3227(64)90032-5

Birchenough, S. N., Reiss, H., Degraer, S., Mieszkowska, N., Borja, Á., Buhl-Mortensen, L., et al. (2015). Climate change and marine benthos: a review of existing research and future directions in the north Atlantic. *Wiley Interdiscip. reviews: Climate Change* 6, 203–223. doi: 10.1002/wcc.330

Blott, S. J., and Pye, K. (2001). GRADISTAT: a grain size distribution and statistics package for the analysis of unconsolidated sediments. *Earth Surface Processes Landforms* 26, 1237–1248. doi: 10.1002/esp.261

Bozgeyik, M. E. (2019). Application of suitability index to Turkish coasts for wave energy site selection (Middle East Technical University).

Brown, J. M., and Wolf, J. (2009). Coupled wave and surge modelling for the eastern Irish Sea and implications for model wind-stress. *Continental Shelf Res.* 29, 1329–1342. doi: 10.1016/j.csr.2009.03.004

Chaouachi, A., Covrig, C. F., and Ardelean, M. (2017). Multi-criteria selection of offshore wind farms: Case study for the Baltic states. *Energy Policy* 103, 179–192. doi: 10.1016/j.enpol.2017.01.018

Coughlan, M., Guerrini, M., Creane, S., O'Shea, M., Ward, S. L., Van Landeghem, K. J., et al. (2021). A new seabed mobility index for the irish sea: Modelling seabed shear stress and classifying sediment mobilisation to help predict erosion, deposition, and sediment distribution. *Continental Shelf Res.* 229, 104574. doi: 10.1016/j.csr.2021.104574

Coughlan, M., Long, M., and Doherty, P. (2020). Geological and geotechnical constraints in the Irish Sea for offshore renewable energy. *J. Maps* 16, 420–431. doi: 10.1080/17445647.2020.1758811

Dannheim, J., Bergström, L., Birchenough, S. N., Brzana, R., Boon, A. R., Coolen, J. W., et al. (2020). Benthic effects of offshore renewables: identification of knowledge gaps and urgently needed research. *ICES J. Mar. Sci.* 77, 1092–1108. doi: 10.1093/icesjms/fsz018

Den Boon, J., Sutherland, J., Whitehouse, R., Soulsby, R., Stam, C., Verhoeven, K., et al. (2004). "Scour behaviour and scour protection for monopile foundations of offshore wind turbines," in *Proceedings of the European Wind Energy Conference*, Vol. 14 (London, UK: EWEC).

De Pryck, K. (2021). Intergovernmental expert consensus in the making: the case of the summary for policy makers of the IPCC 2014 synthesis report. *Global Environ. Politics* 21, 108–129. doi: 10.1162/glep_a_00574

Díaz, H., and Soares, C. G. (2020). Review of the current status, technology and future trends of offshore wind farms. *Ocean Eng.* 209, 107381. doi: 10.1016/j.oceaneng.2020.107381

Dobson, M., Evans, W., and James, K. (1971). The sediment on the floor of the southern Irish Sea. *Mar. Geology* 11, 27–69. doi: 10.1016/0025-3227(71)90083-1

Egbert, G. D., Bennett, A. F., and Foreman, M. G. (1994). TOPEX/POSEIDON tides estimated using a global inverse model. *J. Geophysical Research: Oceans* 99, 24821–24852. doi: 10.1029/94JC01894

Folk, R. L., and Ward, W. C. (1957). Brazos river bar [Texas]; a study in the significance of grain size parameters. *J. Sedimentary Res.* 27, 3–26. doi: 10.1306/74D70646-2B21-11D7-8648000102C1865D

Hernandez, C., Shadman, M., Maali Amiri, M., Silva, C., Segen, F., Estefen, SF., et al. (2021). Environmental impacts of offshore wind installation, operation and maintenance, and decommissioning activities: A case study of Brazil. *Renewable Sustain. Energy Rev.* 144, 110994. doi: 10.1016/j.rser.2021.110994

Gill, A. B. (2005). Offshore renewable energy: ecological implications of generating electricity in the coastal zone. *J. Appl. Ecol.* 42 (4), 605–615. doi: 10.1111/j.1365-2664.2005.01060.x

Hepburn, C., Adlen, E., Beddington, J., Carter, E. A., Fuss, S., Mac Dowell, N., et al. (2019). The technological and economic prospects for CO2 utilization and removal. *Nature* 575, 87–97. doi: 10.1038/s41586-019-1681-6

Holmes, R., and Tappin, D. (2005). *DTI strategic environmental assessment area 6, Irish Sea, seabed and surficial geology and processes*. British Geological Survey Commissioned Report, CR/05/057.

Horsburgh, K., Hill, A., Brown, J., Fernand, L., Garvine, R., and Angelico, M. (2000). Seasonal evolution of the cold pool gyre in the western Irish Sea. *Prog. Oceanogr.* 46, 1–58. doi: 10.1016/S0079-6611(99)00054-3

Ingram, R. L. (1971). Sieve analysis. *Procedures Sedimentary Petrology*, 49–67.

Jackson, D. I., Jackson, A. A., Evans, D., Wingfield, R. T. R., Barnes, R. P., and Arthur, M. J. (1995). JUnited Kingdom offshore regional report: the geology of the Irish Sea. (London: HMSO for the British Geological Survey)

Kirby, R., and Shaw, T. (2005). "Severn Barrage, UK – environmental reappraisal," in *Proceedings of the institution of civil engineers-engineering sustainability* 158 (1), 31–39. doi: 10.1680/ensu.2005.158.1.31

Krumbein, W., and Pettijohn, F. (1939). *Manual of sedimentary petrography*. XIV (New York and London: Taylor & Francis), 225–227. doi: 10.1080/11035893909452786

Leontaris, G., Morales-Nápoles, O., and Wolfert, A. R. (2016). Probabilistic scheduling of offshore operations using copula based environmental time series–an application for cable installation management for offshore wind farms. *Ocean Eng.* 125, 328–341. doi: 10.1016/j.oceaneng.2016.08.029

Lewis, M. J., Palmer, T., Hashemi, R., Robins, P., Saulter, A., Brown, J., et al. (2019). Wave-tide interaction modulates nearshore wave height. *Ocean Dynam.* 69, 367–384. doi: 10.1007/s10236-018-01245-z

Loss, S. R., Will, T., and Marra, P. P. (2013). Estimates of bird collision mortality at wind facilities in the contiguous united states. *Biol. Conserv.* 168, 201–209. doi: 10.1016/j.biocon.2013.10.007

Madsen, P. T., Wahlberg, M., Tougaard, J., Lucke, K., and Tyack, P. (2006). Wind turbine underwater noise and marine mammals: implications of current knowledge and data needs. *Mar. Ecol. Prog. Ser.* 309, 279–295. doi: 10.3354/meps309279

Martins, L. (2003). Recent sediments and grain-size analysis. *Gravel* 1, 90–105.

Mekhilef, S., Saidur, R., and Kamalisarvestani, M. (2012). Effect of dust, humidity and air velocity on efficiency of photovoltaic cells. *Renewable Sustain. Energy Rev.* 16, 2920–2925. doi: 10.1016/j.rser.2012.02.012

Neill, S. P., Angeloudis, A., Robins, P. E., Walkington, I., Ward, S. L., Masters, I., et al. (2018). Tidal range energy resource and optimization–past perspectives and future challenges. *Renewable Energy* 127, 763–778. doi: 10.1016/j.renene.2018.05.007

Neill, S., and Elliott, A. (2004). *In situ* measurements of spring–neap variations to unsteady island wake development in the firth of forth, Scotland. *Estuarine Coast. Shelf Sci.* 60, 229–239. doi: 10.1016/j.ecss.2004.01.001

Neill, S. P., and Hashemi, M. R. (2013). Wave power variability over the northwest European shelf seas. *Appl. Energy* 106, 31–46. doi: 10.1016/j.apenergy.2013.01.026

Neill, S. P., Hashemi, M. R., and Lewis, M. J. (2014). The role of tidal asymmetry in characterizing the tidal energy resource of Orkney. *Renewable Energy* 68, 337–350. doi: 10.1016/j.renene.2014.01.052

Neill, S. P., Jordan, J. R., and Couch, S. J. (2012). Impact of tidal energy converter (TEC) arrays on the dynamics of headland sand banks. *Renewable Energy* 37, 387–397. doi: 10.1016/j.renene.2011.07.003

Neill, S. P., Litt, E. J., Couch, S. J., and Davies, A. G. (2009). The impact of tidal stream turbines on large-scale sediment dynamics. *Renewable Energy* 34, 2803–2812. doi: 10.1016/j.renene.2009.06.015

Neill, S. P., Robins, P. E., and Fairley, I. (2017). "The impact of marine renewable energy extraction on sediment dynamics," in *Marine renewable energy* (Cham: Springer International Publishing), 279–304. doi: 10.1007/978-3-319-53536-4_12

Newell, R., Raimi, D., Villanueva, S., and Prest, B. (2021). Global energy outlook 2021: Pathways from Paris. *Resour. Future* 8.

Onoufriou, J., Russell, D. J., Thompson, D., Moss, S. E., and Hastie, G. D. (2021). Quantifying the effects of tidal turbine array operations on the distribution of marine mammals: Implications for collision risk. *Renewable Energy* 180, 157–165. doi: 10.1016/j.renene.2021.08.052

Pelc, R., and Fujita, R. M. (2002). Renewable energy from the ocean. *Mar. Policy* 26, 471–479. doi: 10.1016/S0308-597X(02)00045-3

Robins, P. E., Cooper, D., Malham, S. K., and Jones, D. L. (2019). Viral dispersal in the coastal zone: A method to quantify water quality risk. *Environ. Int.* 126, 430–442. doi: 10.1016/j.envint.2019.02.042

Robins, P. E., Neill, S. P., and Lewis, M. J. (2014). Impact of tidal-stream arrays in relation to the natural variability of sedimentary processes. *Renewable Energy* 72, 311–321. doi: 10.1016/j.renene.2014.07.037

Roche, R., Walker-Springett, K., Robins, P., Jones, J., Veneruso, G., Whitton, T., et al. (2016). Research priorities for assessing potential impacts of emerging marine renewable energy technologies: Insights from developments in Wales (UK). *Renewable Energy* 99, 1327–1341. doi: 10.1016/j.renene.2016.08.035

Romm, J. (2022). *Climate change: What everyone needs to know* (New York: Oxford University Press).

Rui, S., Guo, Z., Wang, L., Wang, H., and Zhou, W. (2022). Inclined loading capacity of caisson anchor in south china sea carbonate sand considering the seabed soil loss. *Ocean Eng.* 260, 111790. doi: 10.1016/j.oceaneng.2022.111790

Selot, F., Fraile, D., and Brindley, G. (2019). *Offshore wind in Europe-key trends and statistics 2018*. C. Walsh., WindEurope. eds (Brussels: WindEurope).

Shields, M. A., Woolf, D. K., Grist, E. P., Kerr, S. A., Jackson, A. C., Harris, R. E., et al. (2011). Marine renewable energy: The ecological implications of altering the hydrodynamics of the marine environment. *Ocean Coast. Manage.* 54, 2–9. doi: 10.1016/j.ocecoaman.2010.10.036

Soares, P. M., Lima, D. C., and Nogueira, M. (2020). Global offshore wind energy resources using the new ERA-5 reanalysis. *Environ. Res. Lett.* 15, 1040a2. doi: 10.1088/1748-9326/abb10d

Stoutenburg, E., and Jacobson, M. (2010). "Optimizing offshore transmission links for marine renewable energy farms," in *OCEANS 2010 MTS/IEEE SEATTLE*. (Seattle: IEEE), 1–9. doi: 10.1109/OCEANS.2010.5664506

Van Dijk, T. A., and Kleinhans, M. G. (2005). Processes controlling the dynamics of compound sand waves in the north Sea, Netherlands. *J. Geophysical Research: Earth Surface* 110. doi: 10.1029/2004JF000173

Vanhellemont, Q., and Ruddick, K. (2014). Turbid wakes associated with offshore wind turbines observed with landsat 8. *Remote Sens. Environ.* 145, 105–115. doi: 10.1016/j.rse.2014.01.009

Van Landeghem, K. J., Uehara, K., Wheeler, A. J., Mitchell, N. C., and Scourse, J. D. (2009). Post-glacial sediment dynamics in the Irish Sea and sediment wave morphology: Data–model comparisons. *Continental Shelf Res.* 29, 1723–1736. doi: 10.1016/j.csr.2009.05.014

Vasileiou, M., Loukogeorgaki, E., and Vagiona, D. G. (2017). Gis-based multi-criteria decision analysis for site selection of hybrid offshore wind and wave energy systems in Greece. *Renewable Sustain. Energy Rev.* 73, 745–757. doi: 10.1016/j.rser.2017.01.161

Wang, Z., Li, X., Ren, C., Yong, Z., Zhu, J., Luo, W., et al. (2009). Growth of Ag nanocrystals on multiwalled carbon nanotubes and Ag-carbon nanotube interaction. *Sci. China Ser. E: Technol. Sci.* 52, 3215–3218. doi: 10.1007/s11431-009-0278-y

Ward, S. L., Neill, S. P., Van Landeghem, K. J., and Scourse, J. D. (2015). Classifying seabed sediment type using simulated tidal-induced bed shear stress. *Mar. Geology* 367, 94–104. doi: 10.1016/j.margeo.2015.05.010

Waters, S., and Aggidis, G. (2016). Tidal range technologies and state of the art in review. *Renewable Sustain. Energy Rev.* 59, 514–529. doi: 10.1016/j.rser.2015.12.347

Wolanski, E., Imberger, J., and Heron, M. L. (1984). Island wakes in shallow coastal waters. *J. Geophysical Research: Oceans* 89, 10553–10569. doi: 10.1029/JC089iC06p10553

Xu, Y., Ren, Q., Zheng, Z.-J., and He, Y.-L. (2017). Evaluation and optimization of melting performance for a latent heat thermal energy storage unit partially filled with porous media. *Appl. Energy* 193, 84–95. doi: 10.1016/j.apenergy.2017.02.019

Zabihian, F., and Fung, A. S. (2011). Review of marine renewable energies: case study of Iran. *Renewable Sustain. Energy Rev.* 15, 2461–2474. doi: 10.1016/j.rser.2011.02.006

Zhang, F., Cohen, M., and Barr, A. (2020). *Economic impact study of new offshore wind lease auctions by BOEM*. Available at: https://tethys.pnnl.gov/sites/default/files/publications/Offshore-wind-economic-impact-analysis.pdf.

frontiers | Frontiers in Marine Science

TYPE Original Research
PUBLISHED 19 May 2023
DOI 10.3389/fmars.2023.1195496

OPEN ACCESS

EDITED BY
Zefeng Zhou,
Norwegian Geotechnical Institute (NGI), Norway

REVIEWED BY
Yankun Wang,
Yangtze University, China
Luqi Wang,
Chongqing University, China
Lunbo Luo,
China Three Gorges Corporation, China

*CORRESPONDENCE
Yan Zhang
avayan8006@163.com
Tao Liu
ltmilan@ouc.edu.cn

RECEIVED 28 March 2023
ACCEPTED 05 May 2023
PUBLISHED 19 May 2023

CITATION
Lu Y, Yu P, Zhang Y, Chen J, Liu T, Wang H and Liu H (2023) Deformation analysis of underwater shield tunnelling based on HSS model parameter obtained by the Bayesian approach.
Front. Mar. Sci. 10:1195496.
doi: 10.3389/fmars.2023.1195496

Deformation analysis of underwater shield tunnelling based on HSS model parameter obtained by the Bayesian approach

Yao Lu[1], Peng Yu[2], Yan Zhang[3]*, Jian Chen[4], Tao Liu[1,5]*, Han Wang[1] and Hongjun Liu[6]

[1]Shandong Provincial Key Laboratory of Marine Environment and Geological Engineering, Ocean University of China, Qingdao, China, [2]Key Laboratory of Geological Safety of Coastal Urban Underground Space, Ministry of Natural Resources, Qingdao, China, [3]College of Civil Engineering, Anhui Jianzhu University, Hefei, China, [4]China Railway 14th Bureau Group Corporation Limited, China Railway Construction Corporation Limited, Jinan, China, [5]Qingdao National Laboratory of Marine Science and Technology, Ocean University of China, Qingdao, China, [6]College of Environmental Science and Engineering, Ocean University of China, Qingdao, China

Deformation analysis and control of underwater large-diameter shield tunnels is a prerequisite for safe tunnel construction. Reasonable selection of constitutive model and its parameters is the key to accurately predicting the deformation induced by underwater shield tunnelling. In this paper, the finite element analysis of cavity expansion during the piezocone penetration test (CPTU) based on the hardening soil model with small strain stiffness (HSS) model was carried out, and the correlation model of the normalized cone tip resistance Q with the reference secant modulus E_{50}^{ref} and the effective internal friction angle φ was established and verified using mini CPTU chamber test. Then, a Bayesian probability characterization approach for E_{50}^{ref} of silty clay based on CPTU was proposed. Furthermore, the deformation analysis of Jinan Yellow River tunnel crossing the south embankment was carried out to verify the reliability of the proposed approach. The good agreement between the field measurement and numerical simulation confirms that the parameters obtained by the Bayesian approach are reliable. Finally, a sensitivity analysis was performed to study the law of riverbed settlement induced by underwater large-diameter shield tunnelling. The results show that the increasing support pressure could effectively reduce the riverbed settlement, but there is an upper limit. The optimal support pressure of established model is between 0.45 MPa and 0.5 MPa. The uphill section causes greater riverbed settlement than the downhill section. Under the same condition, increasing buried depth and water level will lead to a more significant settlement.

KEYWORDS

underwater large-diameter shield tunnel, HSS model, CPTU, Bayesian inversion, construction deformation analysis

1 Introduction

In recent years, many underwater tunnels have been built worldwide because of their various advantages, such as all-weather operation and not affecting navigation (Huang and Zhan, 2019; Qiu et al., 2019; Tang et al., 2021). By the end of 2020, 245 underwater tunnels have been built in China, mainly in the Huangpu River, the Pearl River and the Yangtze River. There are three main methods of tunnel construction, including drill-and-blast, shield tunnelling and immersed tube methods, among which shield tunnelling is the most widely used one (Lin et al., 2013). With the increasing scale of underwater tunnels, shield diameter and tunnelling distance are constantly refreshed. The most representative underwater large-diameter shield tunnel projects in China include Wuhan Heping Avenue South Extension, Jinan Yellow River Tunnel and Nanjing Yangtze River Tunnel, whose excavation diameters are more than 14 m. Although a wealth of experience has been accumulated in the construction of underwater large-diameter shield tunnels, the disturbance of the surrounding soil caused by shield tunnelling is still unavoidable. Therefore, the core problem of underwater large-diameter shield tunnel construction is how to control the stability of shield tunnelling to minimize the construction deformation, especially under high water pressure and shallow overburden conditions.

Numerical simulation techniques have become a crucial tool for analyzing challenging geotechnical engineering problems due to significant advancements in computer technology. However, the reliability of numerical simulation results mainly depends on the selection of geotechnical constitutive model and its parameters. Many studies (Jardine et al., 1986; Burland, 1989) have already shown that soil strain in most areas around underground structures such as tunnels was within the range of 0.01% - 0.1%, which belongs to the small strains. Meanwhile, numerical simulation studies have shown that the soil deformation and stress distribution of underground structures predicted by the commonly used Mohr-Coulomb model is different from the actual ones and sometimes even greatly overestimated. On the other hand, the model considering the nonlinear small strain stiffness of soil can accurately represent the associated deformation laws (Zhang et al., 2019; Zhou et al., 2020). The hardening soil model with small strain stiffness (HSS) model is widely used to assess the response and control of underground construction under small strain conditions in soils (Likitlersuang et al., 2013; Ng et al., 2020). HSS model contains 13 parameters which are difficult to determine each parameter in the tunnel project through laboratory tests due to the lengthy acquisition cycle. To simplify the application of HSS model, many researchers have summarized the empirical correlations between reference secant modulus E_{50}^{ref}, reference tangent modulus E_{oed}^{ref} and reference unloading/reloading modulus E_{ur}^{ref} through laboratory tests and back analysis (Wang et al., 2012; Huang et al., 2013; Ng et al., 2020). Although there are different empirical correlations between different regions and soils, it is appropriate to set $E_{ur}^{ref} = 3\ E_{50}^{ref} = 3\ E_{oed}^{ref}$ in many practical cases. E_{50}^{ref} denotes the reference secant modulus corresponding to 50% of the failure load of the triaxial consolidation drainage test when the reference stress p^{ref} is 100 kPa, reflecting the shear hardening characteristics of soil. It can be seen that E_{50}^{ref} can be used as a critical parameter to obtain other stiffness parameters.

In-situ testing is preferable for underwater tunnel projects where soil sampling is challenging in submerged locations. Piezocone penetration test (CPTU) is one of the most widely used methods, with the advantages of high repeatability, accuracy and the ability to obtain continuous stratigraphic profiles with different strata in vertical directions (Cai et al., 2017; Mo et al., 2020). These advantages facilitate the fast acquisition of HSS model parameters. However, the geotechnical parameters required for engineering can not be directly given by CPTU, extensive research must be conducted to develop transformation models of CPTU data with geotechnical parameters (Sadrekarimi, 2016). To date, there are still few studies on HSS model parameters obtained by converting CPTU test data. Further work needs to be carried out to establish the connection between the two and obtain geotechnical parameters. And the transformation accuracy also needs to be improved.

In recent years, the Bayesian approach has provided a new way to solve the problem of probabilistic characterization of soil parameters in geotechnical engineering, such as Young's modulus (E_u) (Wang and Cao, 2013), effective friction angle (φ') (Tian et al., 2016), soil behaviour type index I_c (Cao et al., 2019), coefficient of consolidation in the horizontal direction (c_h) (Zhao et al., 2022). Under a Bayesian framework, the engineering experience is quantified as prior knowledge and can subsequently be updated by the likelihood function integrated with test information. Finally, posterior knowledge considering various uncertainties can be obtained (Cao et al., 2016; Wang et al., 2016; Ching and Phoon, 2019). However, the application of the Bayesian approach in probabilistic characterization of E_{50}^{ref} has not been reported.

This paper focuses on the approach of obtaining geotechnical parameters of underwater large-diameter shield tunnel and its construction deformation mechanism and response. The transformation model between the CPTU test data and the reference secant modulus E_{50}^{ref} and effective internal friction angle φ' of the HSS model in the Jinan Yellow River basin silty clay was constructed. A Bayesian probability characterization approach for the HSS model with E_{50}^{ref} of silty clay based on CPTU was proposed, which obtained the most probable values of E_{50}^{ref}. The obtained model parameters were applied to the Yellow River tunnel project to analyze the deformation laws of underwater large-diameter shield construction.

2 Study area

The Jinan Yellow River Tunnel project is located in Tianqiao District, connecting Queshan north and Jiluo road south. With a section length of 2519 m, this tunnel goes underneath the Yellow River. The tunnel adopts a highway and rail transit joint construction scheme with roads arranged on the upper layer and M2 metro sections arranged on the lower layer. The diameter of slurry shield machine is 15.76 m, and the external and internal

radius of the lining is 15.2 m and 13.9 m, respectively. The lining ring consists of 10 segments with a width of 2.0 m and a thickness of 0.6 m. According to the site investigation, the site mainly goes through silt clay containing local calcareous nodules and fine sand, underlying soil is completely weathered gabbro. The tunnel buried depth is 11.2 - 42.3 m, and the maximum water pressure is 0.65 MPa. Figure 1 shows the project overview and a typical geological profile.

3 Methodology

3.1 Transformation model

3.1.1 Cavity expansion model

Following the work of Randolph et al. (1994), the cone tip resistance q_c is related to the limit pressure p_{lim} during the spherical cavity expansion. When using a more practical complex constitutive model, numerical analysis is often required for simplified calculations. A spherical cavity expansion was modelled in the Plaxis 2D to simulate the penetration process, following similar procedures described by Xu and Lehane (2008) and Suryasentana and Lehane (2014). Considering the symmetry of spherical cavity expansion, the model dimension is x = 12 m, y = 24 m. According to the studies of Suzuki (2015) and Xu (2007), there are no boundary effects. The initial radius of the spherical cavity a_0 is 0.1 m. A positive volume strain of 10% is applied to the cavity cluster in multiple stages to simulate the gradual expansion. The construction phase of the model is divided into 21 steps. Before calculation, 7 nodes and 8 stress points around the cavity wall are selected as output. Finally, the selected nodes and stress points data are averaged separately to plot the relationship between the limit pressure p_{lim} and excess pore pressure Δu with the normalized displacement a/a_0. The cone tip resistance q_c is obtained from the following relationship: $q_c = p_{lim} + \sqrt{3}[c' + (p_{lim} - u)]\tan\varphi'$.

3.1.2 Correlations between q_c and E_{50}^{ref}

In order to correct the relationship proposed by Suzuki (2015), Table 1 listed 15 analysis cases to study the influence of model parameters E_{50}^{ref} and φ' on the limit pressure p_{lim} using the HSS model. The influence of the over consolidation ratio is not considered (OCR = 1). The permeability coefficient of soil is 0.02 m/d (2.3×10^{-7} m/s), according to the geological prospecting report.

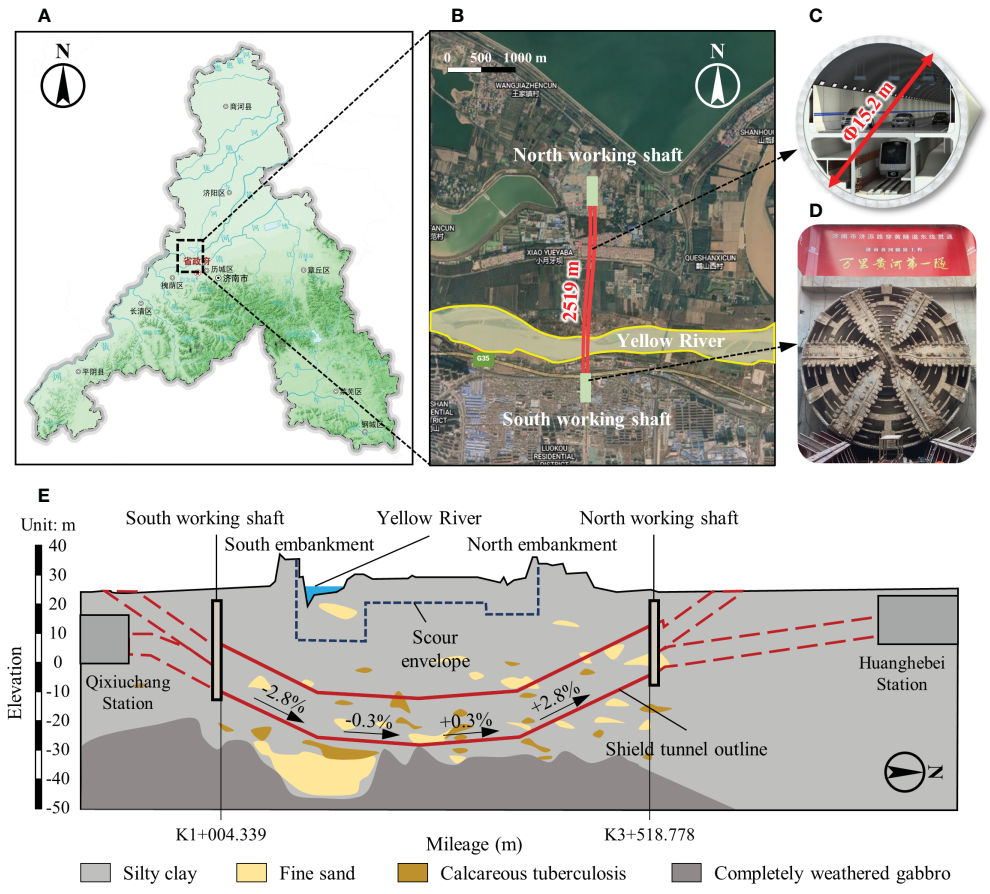

FIGURE 1
Project overview: **(A, B)** Location of the Jinan Yellow River Tunnel project. **(C)** Tunnel structure. **(D)** Shield cutter head. **(E)** Longitudinal section of engineering geology.

TABLE 1 Research scheme of spherical cavity expansion based on the HSS model.

Case	E_{50}^{ref} (MPa)	φ' (°)	$\gamma_{0.7}$ (×10^{-4})	m	K_0^{nc}	$E_{oed}^{ref}/E_{50}^{ref}$	$E_{ur}^{ref}/E_{50}^{ref}$	G_0^{ref}/E_{ur}^{ref}
HSS01	2.0	15.0	2.0	0.7	1-sinφ'	1.0	3.0	3.5
HSS02	5.0							
HSS03	10.0							
HSS04	15.0							
HSS05	20.0							
HSS06	2.0	22.0						
HSS07	5.0							
HSS08	10.0							
HSS09	15.0							
HSS10	20.0							
HSS11	2.0	25.0						
HSS12	5.0							
HSS13	10.0							
HSS14	15.0							
HSS15	20.0							

The cone tip resistance q_c can be obtained by substituting the limit pressure p_{lim} of each group into the formula. Therefore, the normalized cone tip resistance Q, E_{50}^{ref}/p'_0 and φ' are drawn in Figure 2. The relationship between log$Q$ and log(E_{50}^{ref}/p'_0) is almost linear in logarithmic coordinates. According to the results proposed by Suzuki (2015) based on the HS model, the normalized cone tip resistance Q relation based on the HSS model can be obtained as follows:

$$Q = \frac{q_c - \sigma_{v0}}{\sigma'_{v0}} = 1.4\left(\frac{E_{50}^{ref}}{p'_0}\right)^{0.23}(\sin\varphi')^{0.47} \quad (1)$$

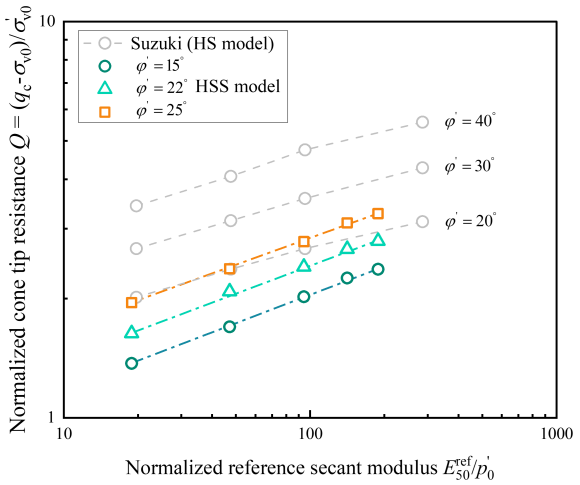

FIGURE 2
Relationship between normalized cone tip resistance Q and reference secant modulus E_{50}^{ref} and effective internal friction angle φ'.

3.2 Calibration chamber test

To verify the applicability of the relationship for Jinan silty clay, a mini CPTU calibration chamber test of remolded soil was conducted. Figure 3 shows the calibration chamber system, including the calibration chamber, loading device, pump and mini CPTU. The chamber contains test soil with a height of 600 mm and a diameter of 525 mm. The chamber wall is 40 mm thick to maintain K_0 consolidation. To ensure that the soil sample height can meet the penetration requirements after consolidation, a 300 mm high ring with the same diameter is added to the upper part of the chamber to accommodate the slurry during consolidation. Vertical stresses can be independently controlled by the pump, providing a maximum vertical load of 200 kPa. The loading plate is equipped with four penetration holes and one spare hole. The diameter of the hole is 16 mm, and the distance between the penetration holes is 10 times the mini CPTU diameter, which can effectively reduce the influence of boundary effects on the test data. The mini CPTU used in the calibration chamber tests has a diameter of 16 mm and a cone angle of 60°. Due to the instability of the sleeve friction test results, the CPTU is not equipped with a sleeve friction sensor, but only with the cone tip resistance and pore pressure sensor. A servo motor controls the CPTU to penetrate the soil from the reserved hole at a constant rate of 20 mm/s.

Remolded specimens of silt clay, taken from about 10 m deep in the north working shaft of the Yellow River Tunnel project, were prepared and tested. The primary property index of soils was obtained by laboratory tests. The water content is 23.0%. Liquid limit and plastic limit are 33.5% and 19.0%, respectively. The initial void ratio is 0.67.

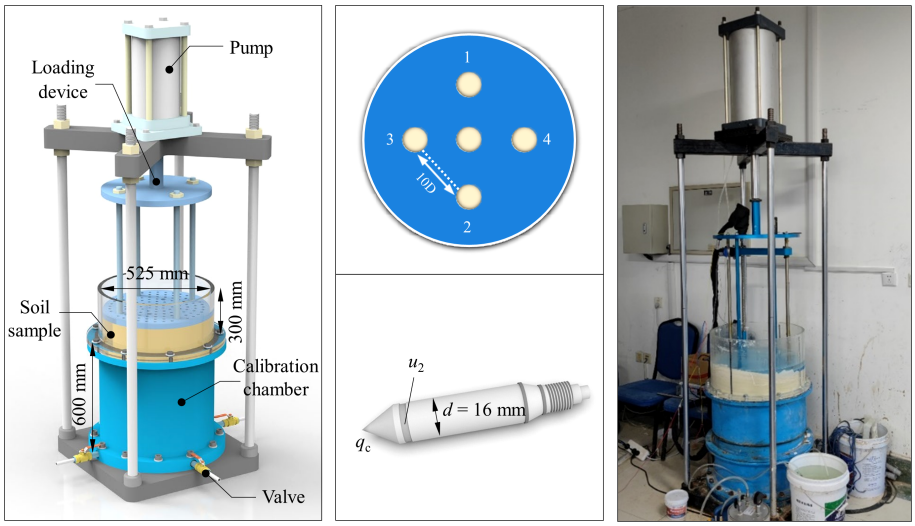

FIGURE 3
Calibration chamber system.

For the calibration chamber test, cylindrical soil samples were prepared using the slurry consolidation method. Then, apply the overburden stress of 100 kPa and measure the vertical deformation twice a day. When the deformation is less than 0.1mm/d, the test can be started. The consolidation time of this experiment is 16 d. After consolidation, the penetration test procedure is as follows: Remove the geotextiles from the surface of the soil sample and connect the saturated mini CPTU with the penetration equipment. Keep the CPTU probe below the chamber's water level before the test begins. Then, click the computer with the data acquisition instrument and start the penetration test. The test was stopped when the CPTU penetration depth reached 300 mm. After the completion of the first test, the geotextile was readjusted and the pressure was reset to 100 kPa. The next set of penetration tests was conducted after consolidation for 1 h. Repeat the above steps for four tests.

Figure 4 shows the results of four repeated tests in saturated remolded specimens. The penetration was performed to a depth of about 300 mm, at which stage the distance to the bottom boundary was about 200 mm (about 12 times the cone diameter). From the results of cone tip resistance q_c, it can be seen that q_c increases rapidly when the CPTU starts to penetrate the shallow surface soil (about 50 mm). The maximum values of the four repeated tests differed greatly, with the maximum reaching about 500 kPa and the minimum about 350 kPa. This phenomenon is mainly caused by surface soil over consolidation. When the CPTU penetration reaches 50 - 150 mm, the q_c fluctuation range decreases significantly. It enters the stable penetration zone until the penetration depth exceeds 150 mm. The cone tip resistance q_c of the four groups of tests is 331.6 kPa, 313.4 kPa, 338.6 kPa, and 324.4 kPa, respectively. Similar to the cone tip resistance, when the CPTU penetrated 150 mm, the gap between the results of the excess pore pressure Δu gradually decreased. The excess pore pressure Δu is 150.3 kPa, 151.2 kPa, 143.2 kPa and 155.7 kPa, respectively.

3.3 Transformation model verification

To verify the applicability of formula (1) in silty clay, the results of cone tip resistance q_c of the CPTU calibration chamber test were substituted into formula (1), and the calculated E_{50}^{ref} was finally obtained, as shown in Figure 5. With the increase of q_c, the E_{50}^{ref} also increases, which is basically linear. At the same time, the E_{50}^{ref} test values of the undisturbed soil and the remolded soil obtained through the triaxial consolidation drainage test are also shown in Figure 5, respectively 6.4 MPa and 5.3 MPa. It can be seen that all the calculated values are located near the test values, and the calculated mean value is 6.1MPa, which is relatively close to the test value of undisturbed soil, with a deviation of 4.9%. The deviation from E_{50}^{ref} test value of remolded soil is 13.1%. Thus, E_{50}^{ref} calculated by the formula (1) is reliable and suitable for CPTU penetration in silty clay.

3.4 Bayesian probability characterization of E_{50}^{ref}

3.4.1 Inherent variability of E_{50}^{ref}

The influence factors such as particle composition and transport process lead to different soil properties. Therefore, there is inherent variability in soil, independent of the knowledge state of geotechnical properties, and will not decrease with the increase of knowledge (Phoon and Kulhawy, 1999; Wang and Cao, 2013; Wang et al., 2023). E_{50}^{ref} is a continuous variable and must be non-negative because of its physical meaning. Therefore, geotechnical parameters are often modeled as logarithmic normal random variables (Wang and Cao, 2013). Assume that E_{50}^{ref} is a lognormal random variable with a mean μ and a standard deviation σ, expressed as

$$\ln E_{50}^{\mathrm{ref}} = \mu_N + \sigma_N z \tag{2}$$

10.3389/fmars.2023.1195496

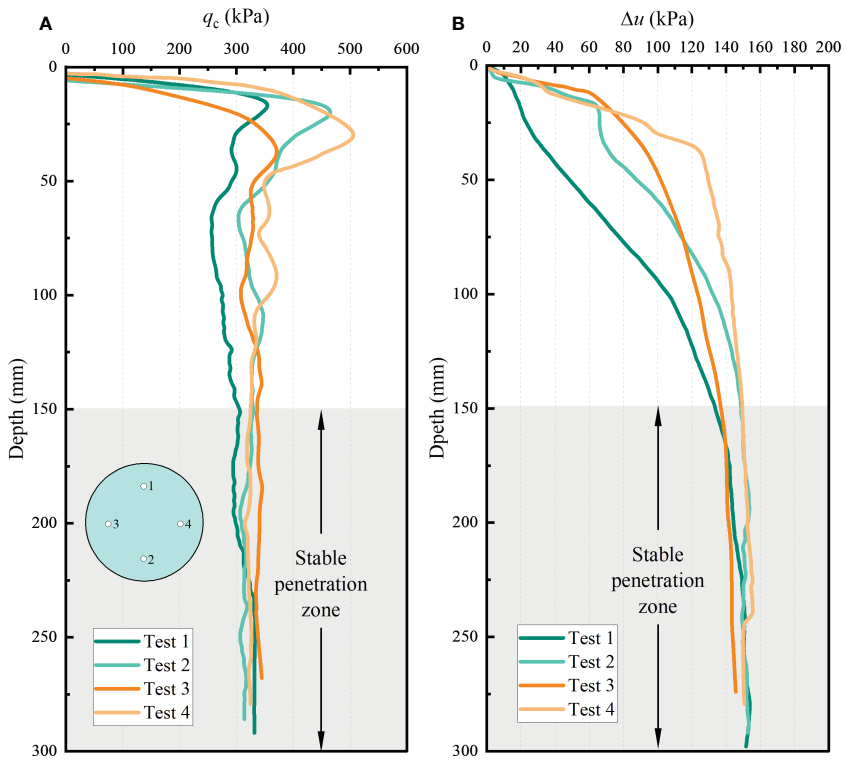

FIGURE 4
Calibration chamber test results: **(A)** Relationship between cone tip resistance q_c and depth h **(B)** Relationship between excess pore pressure Δu and depth h.

in which μ_N and σ_N are the mean and standard deviation of $\ln E_{50}^{ref}$, z is a normal random variable with a mean of 0 and SD of 1.

3.4.2 Transformation uncertainty

Eq. (1) can be rewritten in a log-log scale as:

$$\ln Q = a \ln E_{50}^{ref} + b + \epsilon \quad (3)$$

in which $\ln Q$ is normalized cone tip resistance in a log scale; a, b is the coefficient, ϵ is a Gaussian variable representing the transformation uncertainty.

Combining Eqs. (2) and (3) lead to:

$$\ln Q = (a\mu_N + b) + a\sigma_N z + \epsilon \quad (4)$$

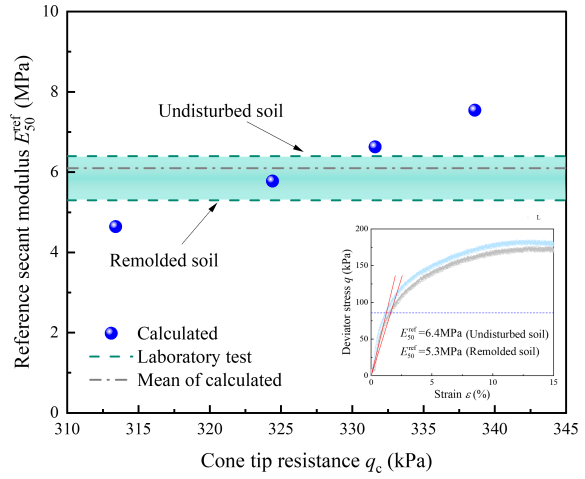

FIGURE 5
Comparison between calculated values and experimental values of E_{50}^{ref}.

3.4.3 Bayesian framework

For the given prior knowledge and CPTU data, the probability density function of E_{50}^{ref} can be expressed as:

$$P(E_{50}^{ref} \mid \text{Data, Prior}) = \int_{\mu,\sigma} P(E_{50}^{ref} \mid \mu, \sigma) P(\mu, \sigma \mid \text{Data, Prior}) d\mu d\sigma \quad (5)$$

in which $P(E_{50}^{ref}|\mu,\sigma)$ is the conditional probability of a given set of μ and σ. Because E_{50}^{ref} is lognormally distributed, it can be expressed as:

$$P(E_{50}^{ref} \mid \mu, \sigma) = \frac{1}{\sqrt{2\pi}\sigma_N E_{50}^{ref}} \exp\left\{-\frac{1}{2}\left[\frac{\ln E_{50}^{ref} - \mu_N}{\sigma_N}\right]^2\right\} \quad (6)$$

Using Bayesian formula, $P(\mu,\sigma|\text{Data, Prior})$ can be expressed as:

$$P(\mu, \sigma|\text{Data, Prior}) = (\mu, \sigma|\text{Data}) = KP(\text{Data} \mid \mu, \sigma) P(\mu, \sigma) \quad (7)$$

in which K is a normalized constant independent of μ and σ; Data = $\{\ln Q_i, i=1, 2, \ldots, n_s\}$ is a set of CPTU test data; $P(\text{Data}|\mu,\sigma)$ is

the likelihood function which is expressed as:

$$P(\text{Data}\,|\,\mu,\sigma) = \prod_{i=1}^{n} \frac{1}{\sqrt{2\pi}\sqrt{(a\sigma_N)^2+\sigma_\varepsilon^2}} exp\left\{-\frac{1}{2}\left[\frac{\ln Q_i-(a\sigma_N+b)}{\sqrt{(a\sigma_N)^2+\sigma_\varepsilon^2}}\right]^2\right\} \quad (8)$$

$P(\mu,\sigma)$ is assumed to be a uniform distribution, expressed as:

$$P(\mu,\sigma) = \frac{1}{\mu_{max}-\mu_{min}} \times \frac{1}{\sigma_{max}-\sigma_{min}}, \mu \in [\mu_{min},\ \mu_{max}], \sigma \in [\sigma_{min}, \sigma_{max}] \quad (9)$$

Substitute Eqs. (6) - (9) into Eqs. (5) to obtain the posterior probability density function of E_{50}^{ref} calculated according to the approach proposed by Wang and Cao (2013).

4 Results and discussion

4.1 Probability distribution of E_{50}^{ref}

Consider a set of prior knowledge, $\mu\in[3.9, 8.0]$, $\sigma\in[0.5, 3.0]$. And using CPTU field test data from the Jinan Yellow River Basin as input data for Bayesian inversion, the scatter diagram of E_{50}^{ref} is shown in Figure 6A. Most samples are between 3.0 and 10.0 MPa. With the increase of the sample value, the scatter gradually becomes sparse, and all the sample values are less than 25 MPa. Further analysis from the statistical histogram (Figure 6B) shows 27367 sample points in 3.0 - 10.0 MPa, accounting for 91.0%. It peaks in the 6.0 - 7.0 MPa interval with a sample size of 6481. Figure 6C is the probability density function of E_{50}^{ref} estimated by Figure 6A, and it also includes the value of E_{50}^{ref} obtained from $E_{50}^{ref} = E_{s1\text{-}2}$. $E_{s1\text{-}2}$ is the compression modulus of undisturbed soil. 93.8% of the undisturbed soil data is within the range of 3.0 - 10.0 MPa, which is consistent with the inversion results. Figure 6D plots the cumulative distribution function of E_{50}^{ref}. The cumulative distribution function of equivalent samples and that obtained from empirical correlation have a good consistency. Such a good agreement demonstrates that the information in the equivalent samples is consistent with the information obtained through empirical correlation. Also, the approach used to estimate the distribution of E_{50}^{ref} is feasible in Jinan silty clay.

The mean and standard deviation estimated from equivalent samples and empirically converted data are 6.9 MPa and 2.1 MPa, 6.7 MPa and 1.9 MPa, respectively. The mean difference between the equivalent samples and converted data is 0.2 MPa, and the standard deviation is 0.2 MPa, with deviations of 3.0% and 10.5%, respectively. The results indicate that E_{50}^{ref} obtained by the two methods are in good agreement, especially the mean value. Suppose the mean value is chosen to be the characteristic value of E_{50}^{ref}. The final characteristic value of E_{50}^{ref} from the Bayesian approach is 6.9 MPa.

4.2 Sensitivity analysis of Bayesian approach

4.2.1 Mean μ

The equivalent samples of E_{50}^{ref} reflect the combined information of a prior knowledge and corresponding test data. Three groups of

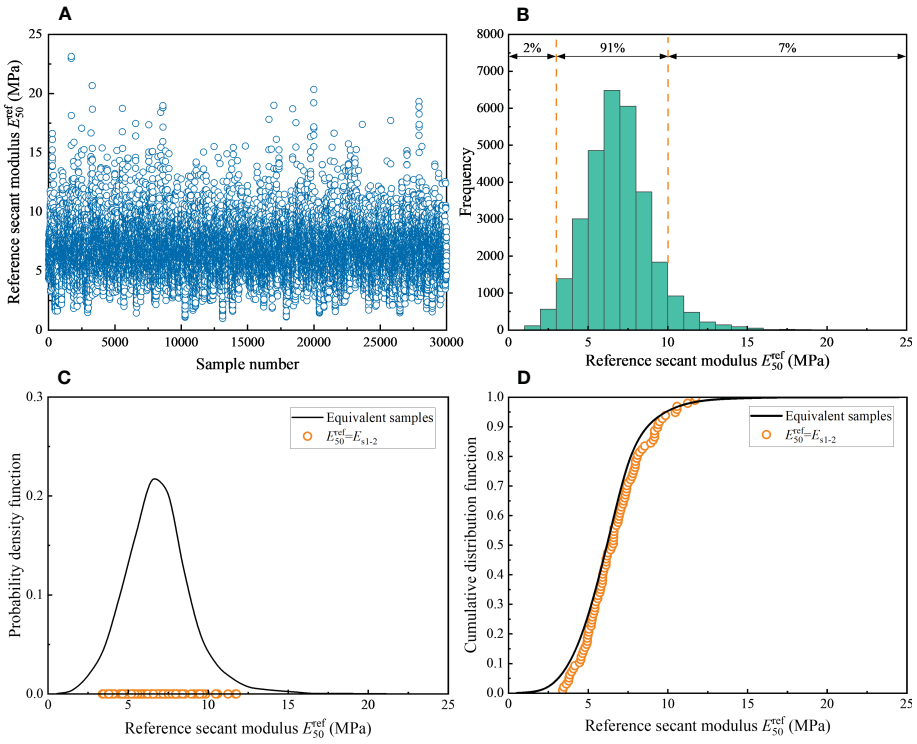

FIGURE 6
Probability distribution of E_{50}^{ref}: **(A)** Scatter plot. **(B)** Histogram. **(C)** Probability density function. **(D)** Cumulative distribution function.

mean shown in Figure 7A are selected to study the influence of mean μ. All of them are uniform distribution, of which the second group has been used in Section 4.1 and will serve as the basis for the research. The Bayesian inversion results are shown in Figure 7B. As seen in the histogram, the final results obtained by $\mu\in[5.0, 7.0]$ and $\mu\in[3.9, 8.0]$ are closer, peaking at 6.5 MPa and 5.5 MPa in the center of the interval, respectively. The results obtained in the maximum interval range $\mu\in[1.6, 15.0]$ differ greatly from the two ranges mentioned above, reaching a peak at 13.5 MPa in the center of the interval. At the same time, the sample distribution ranges of $\mu\in[5.0, 7.0]$ and $\mu\in[3.9, 8.0]$ are consistent. Samples with a smaller prior range $\mu\in[5.0, 7.0]$ are more concentrated, and the sample size at the peak exceeds 7000. The large prior range of the mean value makes the final result deviate greatly from the true value of E_{50}^{ref}.

The samples of sensitivity analysis were also used to estimate the probability density function and cumulative distribution function of E_{50}^{ref}, as shown in Figure 7C, D. The gray dashed line in the figure is the peak value, from which the results are consistent with the above analysis. Through the equivalent samples estimation, the final results of E_{50}^{ref} obtained from $\mu\in[5.0, 7.0]$ and $\mu\in[3.9, 8.0]$ are 6.2 MPa and 6.9 MPa, with a deviation of 3.1% and 7.8% from 6.4 MPa in laboratory test, respectively. However, the results obtained from $\mu\in[1.6, 15.0]$, with a deviation almost doubled, significantly deviating from the acceptable error range of the parameter inversion results. The standard deviation of the three groups is 1.9MPa, 2.1MPa and 2.7MPa, respectively. The range of the mean value of E_{50}^{ref} in this inversion is a relatively subjective judgment obtained by statistical analysis of a small amount of data. Its value range is derived from the statistics of E_{50}^{ref} test values of soils in different regions. Therefore, better inversion results were obtained when the selected test values $\mu\in[3.9, 8.0]$ were chosen for the silty clay in each region. Narrowing this range gives more accurate results, such as $\mu\in[5.0, 7.0]$. And when $\mu\in[1.6, 15.0]$, the increase in scope leads to ambiguity of information, resulting in unreasonable results. Therefore, a reasonable range of prior knowledge of soil parameters must be selected in practical application. Statistics of silty clay values in specific areas will greatly increase the reliability of the inversion results.

4.2.2 Standard deviation σ

Similar to the research of μ, the three groups of standard deviation are selected to explore the influence of σ, as shown in Figure 8A. Compared to the μ, the results of $\sigma\in[0.5, 2.0]$, $\sigma\in[0.5, 3.0]$ and $\sigma\in[0.5, 8.0]$ have little difference in Figure 8B. The peaks are located close to each other, at 7.5 MPa, 6.5 MPa and 6.5 MPa in the center of the interval, respectively. Similarly, as the selected range of σ decreases, the obtained samples become more concentrated and the probability density function becomes steeper, reflecting that the accurate selection of the range of prior knowledge has a greater influence on the posterior distribution.

The equivalent samples are plotted as probability density function and cumulative distribution function, as shown in Figure 8C, D. It can be determined from the peak position that the change of σ range has less effect on the peak of E_{50}^{ref} probability density function than μ. However, the change of σ range has a certain influence on the shape of probability density function, which gradually transitions from normal distribution to lognormal distribution. The estimated E_{50}^{ref} for the three ranges is 6.9 MPa, 6.9 MPa, and 6.8 MPa, with deviations from laboratory test 6.4 MPa of 7.8%, 7.8%, and 6.3%, respectively. The standard deviation of samples estimation is 1.6MPa, 2.1MPa and 4.6MPa, respectively. From another perspective, the larger σ range makes the sample more discrete and changes more significantly than μ.

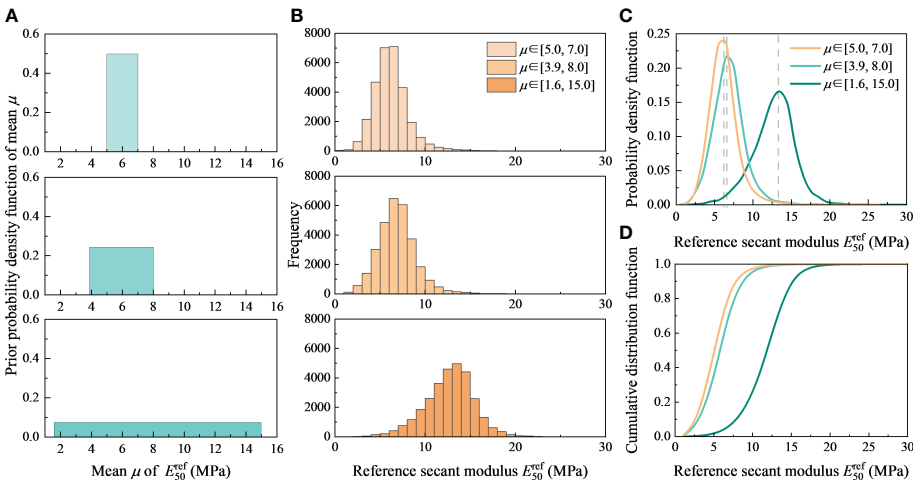

FIGURE 7
Sensitivity analysis of mean μ: **(A)** Three groups of μ. **(B)** Histogram. **(C)** Probability density function. **(D)** Cumulative distribution function.

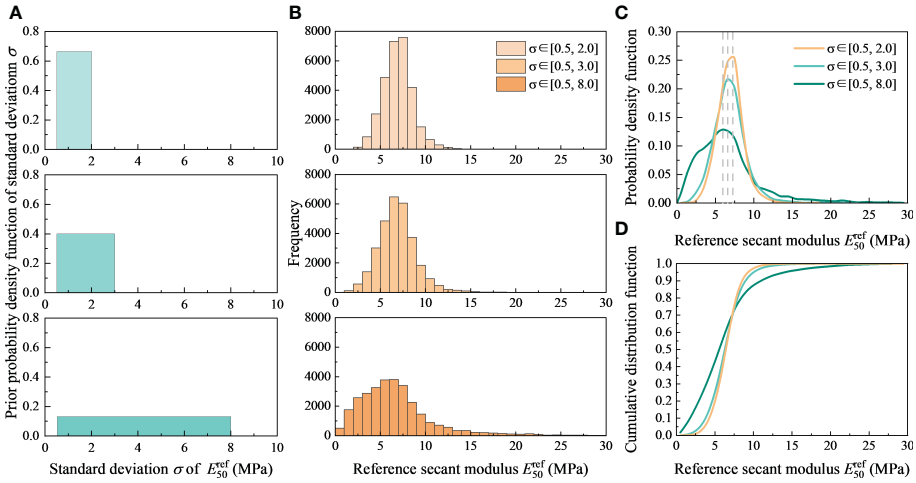

FIGURE 8
Sensitivity analysis of standard deviation σ. **(A)** Three groups of σ. **(B)** Histogram. **(C)** Probability density function. **(D)** Cumulative distribution function.

4.3 Deformation analysis of underwater shield tunnelling

4.3.1 Numerical model

PLAXIS was used to establish the numerical model of the Yellow River tunnel passing through the south embankment in this paper. To simplify the calculation, the following assumptions were made in the modelling process: (1) The silty clay stratum is homogeneous and isotropic; (2) Regardless of the longitudinal slope of the tunnel, the tunnel is laid horizontally; (3) The water level of the Yellow River is constant, and the seepage is neglected.

The model dimension is 360 m×150 m×100 m, the overburden depth of the tunnel is 40 m, and the shallowest section is 30 m below the Yellow River. A support pressure of 0.5 MPa is set in front of the tunnel face and increases with depth by 0.01 MPa/m. The tunnel advances in the Y-direction with every 10 m (5 rings) for a construction stage. The eastern line is constructed before the western line. The numerical model is shown in Figure 9.

The HSS model and elastic model were assumed for soil, shield shell and segment, respectively. Bayesian inversion result was used for the value of E_{50}^{ref}. The value of E_{oed}^{ref} and E_{ur}^{ref} was obtained from the empirical relationships, expressed as $E_{oed}^{ref} = E_{50}^{ref}$, $E_{ur}^{ref} = 3\,E_{50}^{ref}$. And the other parameters were taken from the laboratory test, such as consolidation drainage test, standard consolidation test and resonant column test, or the default values. The Young's Modulus E of segment is decreased to 80% of its initial value of 35.5 GPa, which is based on the tunnelling experience in China, to take into account the impact of joint on the stiffness of tunnel lining (Feng et al., 2011; Xie et al., 2016). The soil parameters are listed in Table 2.

4.3.2 Comparison between numerical simulation and field measurement

To further study the deformation caused by shield tunnelling, three monitoring points, D_1, D_2 and D_3, were set up at the top of the embankment section. Meanwhile, two deep settlement monitoring points, S_1 and S_2, were set at 30 m and 34 m below point D_3. The site monitoring point layout is also shown in Figure 9.

The monitoring and simulation results of the D_1, D_2 are shown in Figure 10A. It can be seen that the embankment settlement can be divided into three stages, which are the initial stage, rapid settlement stage and stable stage. According to the monitoring results, the support pressure applied in front of the tunnel face caused the monitoring sites D_1 and D_2 to heave. Compared with the field measurement, the simulation results of shield tunnelling did not show the phenomenon of surface heave. And the settlement

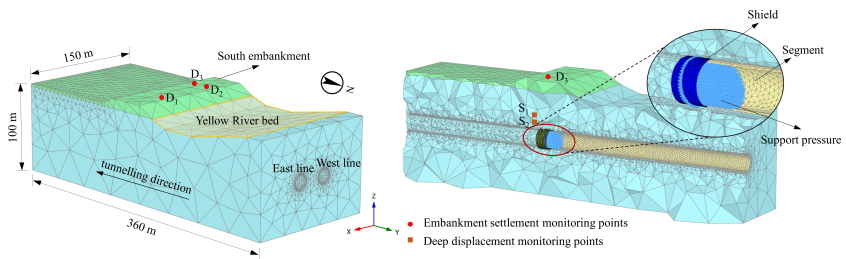

FIGURE 9
3D numerical model of the Yellow River tunnel passing through the south embankment.

TABLE 2 Physical model parameters of soil.

Soil	c' (kPa)	φ' (°)	E_{50}^{ref} (MPa)	E_{ur}^{ref} (MPa)	E_{oed}^{ref} (MPa)	G_0^{ref} (MPa)	$\gamma_{0.7}$ ($\times10^{-4}$)
Embankment	13.0	23.0	15.0	45.0	15.0	100.0	2.0
Silt clay	15.0	22.0	7.0	20.2	6.2	71.4	1.5
Soil	**ψ (°)**	**R_f**	**ν_{ur}**	**p^{ref} (kPa)**	**K_0^{nc}**	**m**	
Embankment	0	0.9	0.2	100	0.61	0.8	
Silt clay	0	0.9	0.2	100	0.63	0.8	

started at the beginning of the tunnelling, but the settlement was almost negligible. When the shield tunnelling reached the vicinity of the monitoring point, both the simulated and monitored embankment settlement rates accelerated significantly and a large embankment settlement appeared. In this stage, the maximum settlement predicted by the monitoring and simulation is 5.5 mm and 6.5 mm, respectively, accounting for 65% and 90% of the total settlement. The difference between the two settlement is small, but the settlement proportion is large. This is because in the field measurement, there is the re-consolidation settlement after soil disturbance, and the settlement of this part is second only to the settlement generated by construction disturbance in the project. The rapid settlement stage (Stage 1) at point D_2 is longer, with a maximum settlement of 12 mm, accounting for more than 90% of the total embankment settlement. This indicates that the advanced construction of the east line greatly influences the stacking of the west line settlement, and the final settlement of the west line is greater than the east line. The settlement rate of monitoring points D_1 and D_2 in the rapid settlement stage is about 0.8 - 1.3 mm/d. Figure 10A also shows the results obtained from the non-inverted model, which can be seen to be larger than the measured and inverted results. It indicates that the non-inverted parameters underestimate the stiffness of the soil, resulting in a certain deviation in the calculation results. One issue should be addressed in Figure 10A. When the east line was excavated, the boundary settlement was about -6 mm. rather than 0 mm, as we find out in most field monitoring. The mesh size and the chosen soil model are both to cause this phenomenon. A smaller mesh size is typically required for the advanced soil model to obtain convergence results. However, a small mesh size will reduce computational efficiency and is unsuitable for large models. It is noted that the total settlement of monitoring point D_2 above the west line was higher than D_1 above the east line. This is because when the axis distance between the two tunnels is relatively close, the soil in the middle area of the two tunnels will be affected by two large-diameter shield construction disturbances. In this model, the results of measured maximum settlement at D_1 and D_2 are 8.5 mm and 13 mm, respectively. The numerical results are 7.3 mm and 10.5 mm, respectively.

The comparison of field measurement between monitoring points D_3, S_1 and S_2 in Figure 10B shows that the settlement trend of D_3 was roughly the same as that of S_1 and S_2. Among them, the settlement of the monitoring point S_2 closer to the tunnel (about 3 m) is more extensive, and the maximum settlement reaches -13.5 mm. The value and settlement rate of this monitoring point is greater than those of the other two. From the simulation results, the settlement changes of S_1 and S_2 are the same at the beginning of the tunnel excavation, and the amount of change is small. The settlement at D_3 is about 2 mm larger than the deep settlement. The settlement of the three monitoring points grows quickly when the tunnel is close to an embankment, and the deep settlement is more noticeable than the surface settlement. The maximum settlement of S_2 is slightly larger than S_1, and the ground settlement is the smallest. In terms of the total settlement of each stage, the measured monitoring point S_1, which is located around 7 m above the tunnel, is close to the monitoring point D_3 at the top of the embankment. The maximum settlement is -10.6 mm and -11.4 mm, respectively.

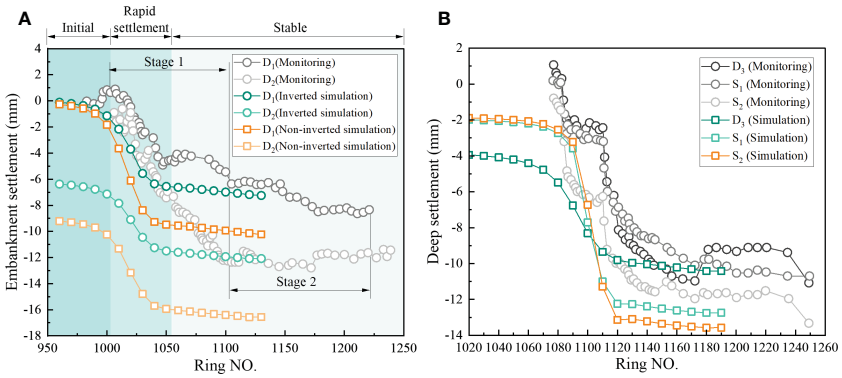

FIGURE 10
Comparison between field measurement and simulated result: **(A)** Embankment settlement of D_1 and D_2. **(B)** Deep settlement of D_3, S_1 and S_2.

At the same time, the simulated settlement curve is about 10 rings ahead of the field measurement. This is because in numerical simulation, considering the horizontal and homogeneous soil layer, the set support pressure is a constant. In actual construction, due to the dynamic adjustment of construction parameters, the displacement near the tunnel surface caused by construction has been well controlled, and the affected range is smaller than the simulation results, resulting in lag in the measured results. The corresponding conclusion can also be drawn from the fact that the final simulation prediction result is larger than the actual measurement. In general, comparing numerical simulation and field measurement, it can be seen that the simulation results agree with the measurements, proving the viability of the method used to obtain the HSS model parameters from the CPTU data.

4.4 Influencing factors of river bed settlement

4.4.1 Support pressure

The soil disturbance caused by tunnel construction can be significantly reduced by using reasonable support pressure, avoiding engineering risks such as splitting and roof falling in shallow underwater soil sections and river water backflow. The actual support pressure set in the Yellow River tunnel project is mostly between 0.3 MPa - 0.6 MPa. Therefore, six analysis cases of 0.3 MPa, 0.35 MPa, 0.4 MPa, 0.45 MPa, 0.5 MPa and 0.55 MPa were selected.

Figure 11 shows the maximum riverbed settlement under different support pressures. When the support pressure is 0.3 MPa, the influence of soil displacement in front of the tunnel face has caused a large riverbed settlement, the maximum settlement is -8.9 mm. When pressure increases to 0.45MPa, the riverbed settlement is well controlled, and the maximum settlement is -2.0mm. Before 0.45MPa, the decrease rate was almost linear, and after 0.45MPa, the decrease rate slowed down. It can be seen that when the support pressure increases to a certain extent, the influence of support pressure on settlement control is limited. For this model, the optimal supporting pressure is between 0.45MPa and 0.5MPa.

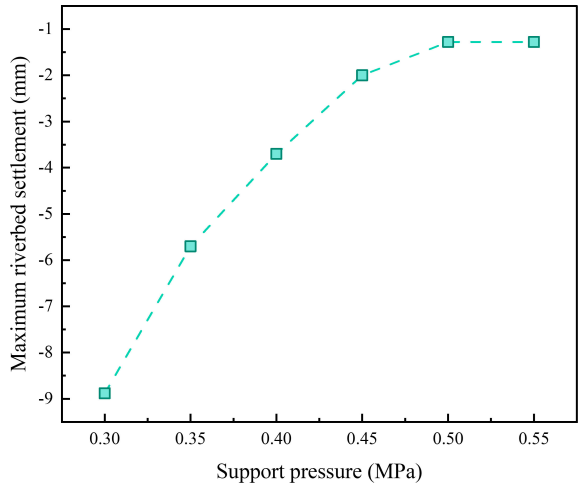

FIGURE 11
Maximum riverbed settlement at different support pressures.

4.4.2 Shield slope

The longitudinal slope of the shield tunnel is mainly controlled within 5° in the design. However, the longitudinal slope may exceed the design value due to the complexity of geological conditions and the uncertainty of shield attitude control. Cheng et al. (2021) designed the longitudinal slope angle as 15° to capture the tunnel failure mode more obviously in the small-size model test and verified it with numerical simulation. In most projects, the maximum longitudinal slope angle in practical application is usually less than 10°. Therefore, +10°, +5°, 0°, -5°, -10° were selected for comparative study.

Figure 12 shows the failure mechanism of the tunnel face at different slopes. When the slope angle of the tunnel is +10°, the soil deformation extends to the ground, resulting in an extensive range of settlement trough. When the slope angle is +5°, the range of settlement trough is smaller. The failure mechanism of a horizontal tunnel is similar to +5°. In all cases of shield downslope, the deformation effects did not reach the surface. This condition is mainly determined by the horizontal projection area of tunnel on the ground. It is generally understood that the larger the projection area is, the larger the impact area of the tunnel excavation on the riverbed, which will lead to increased settlement.

Figure 13A shows the transverse riverbed settlement of different slopes at which the buried depth is 2D. The transverse riverbed settlement of the tunnel reaches its maximum value at the middle line of the tunnel. With the tunnel slope from +10° to -10°, the maximum transverse riverbed settlement is -25.8 mm, -20.8 mm, -17.0 mm, 13.4 mm and -11.1 mm, respectively. It is obvious that the uphill section will cause greater riverbed settlement than the downhill section.

4.4.3 Buried depth

Buried depth affects the tunnel construction deformation. Under the same condition, different buried depths will cause different stratum displacements. Generally, the shallowest buried depth of the tunnel should be greater than 0.7D (D refers to the outside diameter of the tunnel). And the buried depth of the Jinan Yellow River Tunnel is between 11.2 - 42.3m, about 0.7D - 2.8D. Based on this, six working conditions were selected: 0.7D, 1.0D, 1.5D, 2.0D, 2.5D and 3.0D.

Figure 13B shows the transverse riverbed settlement of different buried depths. Under the same conditions, when the buried depth is less than or equal to 2.0D, the riverbed settlement increases with the increase of the buried depth. Under 0.7D, the supporting pressure of 0.3 MPa has exceeded the sum of soil and water pressure. Most areas are uplifted, and the maximum uplifted is about 5.0mm. The transverse riverbed settlement of the tunnel at 1.0D is small, about -1.6mm at most. With the increase of tunnel buried depth, the maximum riverbed settlement reached -8.5mm at 2.0D. It is worth noting that the above phenomenon was studied only by changing the buried depth. In other words, the greater the buried depth, the smaller the support pressure ratio.

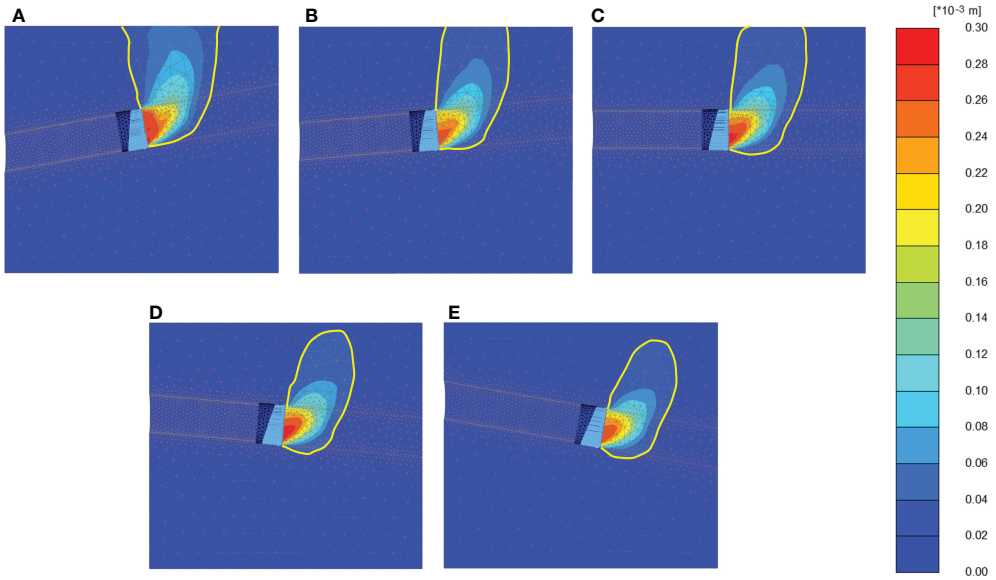

FIGURE 12
Failure mechanism at different slopes: **(A)** +10°. **(B)** +5°. **(C)** 0°. **(D)** -5°. **(E)** -10°.

It can also be seen that when the tunnel buried depth is 2.5D and 3.0D, the maximum riverbed settlement no longer increases with the increase of buried deep, and the law is precisely the opposite. This is because when the buried depth is greater than 2.0D, the soil arch effect is generated in the upper soil, preventing the formation deformation caused by tunnel excavation transmitting to the riverbed, and the riverbed deformation is reduced.

4.4.4 Water level

Construction of underwater tunnels is challenging because they must withstand greater water pressure than conventional tunnels. The level of water not only affects the structural design of segments and waterproofing and plays a crucial role in the selection of construction parameters (Du et al., 2021). The water condition also restricts the implementation of various pretreatment measures. Before the Wuhan Yangtze River Tunnel, the maximum water pressure of the large-diameter shield built on the Huangpu River in Shanghai did not exceed 0.45 MPa. Subsequently, the maximum water pressure is constantly refreshed with the vigorous development of large-diameter shield tunnels.

Combined with the previous research, when the support pressure is 0.3 MPa, the water level of 3 m, 5 m, 7 m, 10 m, 20 m was selected for analysis. The calculation results are shown in Figure 13C. The riverbed settlement increases with the water level rise. This is because the change in water level in the model is equivalent to the uniform load of different sizes applied on the riverbed. In contrast, the high-water level represents that the model receives a greater vertical load, naturally increasing the riverbed settlement. The maximum transverse settlement caused by the 20 m water level is -54.1mm and -54.7mm, respectively. It indicates that the support pressure adopted cannot support the tunnelling, so the results are not shown.

5 Conclusions

In this work, the Bayesian probability characterization approach for the HSS model parameter E_{50}^{ref} of silty clay was

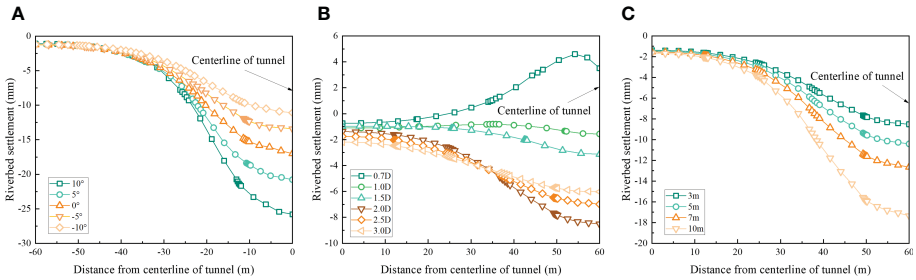

FIGURE 13
Transverse riverbed settlement under different influencing factors: **(A)** Shield slopes. **(B)** Buried depths. **(C)** Water levels.

proposed. Also, deformation analysis induced by the underwater tunnel construction in the Jinan Yellow River Tunnel project has been performed. The analysis results from the numerical simulation are consistent with the monitoring data. In addition, this paper analyses the deformation response of underwater tunnel construction under different support pressures, shield slopes, buried depths and water levels. The following conclusions can be drawn:

(1) Based on the HSS model, the finite element analysis of cavity expansion during CPTU penetration was carried out, and the correlation model of the normalized cone tip resistance Q with the reference tangent modulus E_{50}^{ref} and the effective internal friction angle φ' was established and verified using mini CPTU chamber test. It shows that the results obtained from the correlation model are all located near the test values and are relatively close to the test values of undisturbed soil, with a deviation of 4.9%, which verifies the applicability of the model in the CPTU penetration of silty clay.

(2) A Bayesian inversion approach for calculating the reference secant modulus E_{50}^{ref} of silty clay in Jinan was presented based on the penetration data and the transformation model. The results show that the estimated E_{50}^{ref} obtained by the Bayesian equivalent sample method is 6.9 MPa, which agrees with the laboratory test result of 6.4 MPa. With the decrease of the range selected by the prior information mean μ and standard deviation σ, the obtained samples will become more concentrated, and the probability density function will become steeper.

(3) The good agreement between the measurement and numerical simulation confirms that the parameters obtained by the Bayesian probability characterization approach considering the inherent variability of soil parameters and the uncertainty of the transformation model are reliable. This indicates that the proposed Bayesian probability characterization approach combined with CPTU can be applied to evaluate the law of riverbed settlement induced by underwater tunnelling construction.

(4) With the pressure increase, the maximum riverbed settlement gradually decreases, but there is an upper limit. The optimal support pressure of the established model is between 0.45 MPa and 0.5 MPa. With the tunnelling slope from +10° to -10°, the tunnel construction settlement trough gradually decreases. Under the same condition, before the buried depth is 2D, the riverbed deformation increases with the increase of the buried depth. After the buried depth exceeds 2D, the riverbed settlement decreases due to the soil arching effect. The riverbed settlement increases with the water level rise.

Data availability statement

The raw data supporting the conclusions of this article will be made available by the authors, without undue reservation.

Author contributions

YL: Conceptualization, methodology, software, investigation, data curation, writing – original draft, writing – review & editing. PY: Investigation, writing – review & editing. YZ: Conceptualization, writing – review & editing, funding acquisition. JC: Project administration. TL: Conceptualization, supervision, funding acquisition. HW: Data curation. HL: Supervision, project administration. All authors contributed to the article and approved the submitted version.

Funding

This work presented in this paper was supported by the National Natural Science Foundation of China (U2006213), the National Natural Science Foundation of China (42277139) and the Natural Science Foundation of China (42207172).

Acknowledgments

We appreciate the reviewers for their valuable comments, which are crucial to shaping our manuscript, at the same time, we are also grateful for the financial support provided by the above-mentioned funds.

Conflict of interest

Author JC is employed by China Railway 14th Bureau Group Corporation Limited.

The remaining authors declare that the research was conducted in the absence of any commercial or financial relationships that could be constructed as a potential conflict of interest.

Publisher's note

References

Burland, J. B. (1989). Ninth laurits bjerrum memorial lecture: "small is beautiful-the stiffness of soils at small strains. *Can. Geotech. J.* 26 (4), 499–516. doi: 10.1139/t89-064

Cai, G. J., Zou, H. F., Liu, S. Y., and Puppala, A. J. (2017). Random field characterization of CPTU soil behavior type index of jiangsu quaternary soil deposits. *Bull. Eng. Geol. Environ.* 76 (1), 353–369. doi: 10.1007/s10064-016-0854-x

Cao, Z. J., Wang, Y., and Li, D. Q. (2016). Quantification of prior knowledge in geotechnical site characterization. *Eng. Geol.* 203, 107–116. doi: 10.1016/j.enggeo.2015.08.018

Cao, Z. J., Zheng, S., Li, D. Q., and Phoon, K. K. (2019). Bayesian Identification of soil stratigraphy based on soil behaviour type index. *Can. Geotech. J.* 56 (4), 570–586. doi: 10.1139/cgj-2017-0714

Cheng, C., Jia, P. J., Zhao, W., Ni, P. P., Bai, Q., Wang, Z. J., et al. (2021). Experimental and analytical study of shield tunnel face in dense sand strata considering different longitudinal inclination. *Tunn. Undergr. Space Technol.* 113, 103950. doi: 10.1016/j.tust.2021.103950

Ching, J. Y., and Phoon, K. K. (2019). Constructing site-specific multivariate probability distribution model using Bayesian machine learning. *J. Eng. Mech.* 145 (1). doi: 10.1061/(ASCE)EM.1943-7889.0001537

Du, X., Sun, Y. F., Song, Y. P., and Zhu, C. Q. (2021). In-situ observation of wave-induced pore water pressure in seabed silt in the yellow river estuary of China. *J. Mar. Environ. Eng.* 10 (4), 305–317.

Feng, K., He, C., and Xia, S. (2011). Prototype tests on effective bending rigidity ratios of segmental lining structure for shield tunnel with large cross-section. *Chin. J. Geotech. Eng.* 33 (11), 1750–1758.

Huang, X., Schweiger, H. F., and Huang, H. W. (2013). Influence of deep excavations on nearby existing tunnels. *Int. J. Geomech.* 13 (2), 170–180. doi: 10.1061/(ASCE)GM.1943-5622.0000188

Huang, M., and Zhan, J. W. (2019). Face stability assessment for underwater tunneling across a fault zone. *J. Perform. Constr. Facil.* 33 (3), 04019034. doi: 10.1061/(ASCE)CF.1943-5509.0001296

Jardine, R. J., Potts, D. M., Fourie, A. B., and Burland, J. B. (1986). Studies of the influence of non-linear stress-strain characteristics in soil-structure interaction. *Géotechnique* 36 (3), 377–396. doi: 10.1680/geot.1986.36.3.377

Likitlersuang, S., Surarak, C., Wanatowski, D., Oh, E., and Balasubramaniam, A. (2013). Finite element analysis of a deep excavation: a case study from the Bangkok MRT. *Soils Found.* 53 (5), 756–773. doi: 10.1016/j.sandf.2013.08.013

Lin, C. G., Zhang, Z. M., Wu, S. M., and Yu, F. (2013). Key techniques and important issues for slurry shield under-passing embankments: a case study of hangzhou qiantang river tunnel. *Tunn. Undergr. Space Technol.* 38, 306–325. doi: 10.1016/j.tust.2013.07.004

Mo, P. Q., Gao, X. W., Yang, W. B., and Yu, H. S. (2020). A cavity expansion-based solution for interpretation of CPTu data in soils under partially drained conditions. *Int. J. Numer. Anal. Methods Geomech.* 44 (7), 1053–1076. doi: 10.1002/nag.3050

Ng, C., Zheng, G., Ni, J. J., and Zhou, C. (2020). Use of unsaturated small-strain soil stiffness to the design of wall deflection and ground movement adjacent to deep excavation. *Comput. Geotech.* 119, 103375. doi: 10.1016/j.compgeo.2019.103375

Phoon, K. K., and Kulhawy, F. H. (1999). Characterization of geotechnical variability. *Can. Geotech. J.* 36 (4), 612–624. doi: 10.1139/t99-038

Qiu, D. H., Cui, J. H., Xue, Y. G., Liu, Y., and Fu, K. (2019). Dynamic risk assessment of the subsea tunnel construction process: analytical model. *J. Mar. Environ. Eng.* 10 (3), 195–210.

Randolph, M. F., Dolwin, J., and Beck, R. (1994). Design of driven piles in sand. *Géotechnique* 44 (3), 427–448. doi: 10.1680/geot.1994.44.3.427

Sadrekarimi, A. (2016). Evaluation of cpt-based characterization methods for loose to medium-dense sands. *Soils Found.* 56 (3), 460–472. doi: 10.1016/j.sandf.2016.04.012

Suryasentana, S. K., and Lehane, B. M. (2014). Numerical derivation of cpt-based p-y curves for piles in sand. *Géotechnique* 64 (3), 186–194. doi: 10.1680/geot.13.P.026

Suzuki, Y. (2015). Investigation and interpretation of cone penetration rate effects (The University of Western Australia).

Tang, S. H., Zhang, X. P., Liu, Q. S., Xie, W. Q., Yang, X. M., Chen, P., et al. (2021). Analysis on the excavation management system of slurry shield tbm in permeable sandy ground. *Tunn. Undergr. Space Technol.* 113, 103935. doi: 10.1016/j.tust.2021.103935

Tian, M., Li, D. Q., Cao, Z. J., Phoon, K. K., and Wang, Y. (2016). Bayesian Identification of random field model using indirect test data. *Eng. Geol.* 210, 197–211. doi: 10.1016/j.enggeo.2016.05.013

Wang, Y., and Cao, Z. J. (2013). Probabilistic characterization of young's modulus of soil using equivalent samples. *Eng. Geol.* 159, 106–118. doi: 10.1016/j.enggeo.2013.03.017

Wang, Y., Cao, Z. J., and Li, D. Q. (2016). Bayesian Perspective on geotechnical variability and site characterization. *Eng. Geol.* 203, 117–125. doi: 10.1016/j.enggeo.2015.08.017

Wang, W., Wang, H., and Xu, Z. (2012). Experimental study of parameters of hardening soil model for numerical analysis of excavations of foundation pits. *Yantu Lixue/Rock Soil Mechanics.* 33 (8), 2283–2290. doi: 10.16285/j.rsm.2012.08.006

Wang, L. Q., Xiao, T., Liu, S. L., Zhang, W. G., Yang, B. B., and Chen, L. C. (2023). Quantification of model uncertainty and variability for landslide displacement prediction based on Monte Carlo simulation. *Gondwana Res.* doi: 10.1016/j.gr.2023.03.006

Xie, X. Y., Yang, Y. B., and Ji, M. (2016). Analysis of ground surface settlement induced by the construction of a large-diameter shield-driven tunnel in shanghai, China. *Tunn. Undergr. Space Technol.* 51, 120–132. doi: 10.1016/j.tust.2015.10.008

Xu, X. T. (2007). Investigation of the end bearing performance of displacement piles in sand (The University of Western Australia).

Xu, X. T., and Lehane, B. M. (2008). Pile and penetrometer end bearing resistance in two-layered soil profiles. *Géotechnique* 58 (3), 187–197. doi: 10.1680/geot.2008.58.3.187

Zhang, W. G., Hou, Z. J., Goh, A., and Zhang, R. H. (2019). Estimation of strut forces for braced excavation in granular soils from numerical analysis and case histories. *Comput. Geotech.* 106, 286–295. doi: 10.1016/j.compgeo.2018.11.006

Zhao, Z. N., Congress, S., Cai, G. J., and Duan, W. (2022). Bayesian Probabilistic characterization of consolidation behavior of clays using CPTU data. *Acta Geotech.* 17 (3), 931–948. doi: 10.1007/s11440-021-01277-8

Zhou, H. Z., Zheng, G., He, X. P., Wang, E. Y., Guo, Z. Y., and Nie, D. Q. (2020). Numerical modelling of retaining structure displacements in multi-bench retained excavations. *Acta Geotech.* 15 (9), 2691–2703. doi: 10.1007/s11440-020-00947-3

frontiers | Frontiers in Marine Science

TYPE Original Research
PUBLISHED 19 June 2023
DOI 10.3389/fmars.2023.1211616

OPEN ACCESS

EDITED BY
Shengjie Rui,
Norwegian Geotechnical Institute (NGI), Norway

REVIEWED BY
Lei Guo,
Shandong University, China
Zhenguo Guo,
Tongji University, China

*CORRESPONDENCE
Qingsheng Meng
qingsheng@ouc.edu.cn

RECEIVED 25 April 2023
ACCEPTED 31 May 2023
PUBLISHED 19 June 2023

CITATION
Li Y, Meng Q, Wang S, Wang W and Chen Y (2023) Assessing the liquefaction potential of seabed soils based on ocean ambient noise in the Yellow River Delta. *Front. Mar. Sci.* 10:1211616. doi: 10.3389/fmars.2023.1211616

Assessing the liquefaction potential of seabed soils based on ocean ambient noise in the Yellow River Delta

Yang Li[1], Qingsheng Meng[1,2]*, Shilin Wang[1], Wenjing Wang[1] and Yuhong Chen[1]

[1]College of Environmental Science and Engineering, Ocean University of China, Qingdao, China, [2]Key Laboratory of Marine Environment Science and Ecology, Ministry of Education, Qingdao, China

Seabed soils can undergo liquefaction under cyclic loading, resulting in a rapid decrease in strength and stiffness, which may lead to the destruction of offshore structures. Therefore, the assessment of seabed soil liquefaction will become an important factor in disaster prevention and risk analysis in coastal and offshore engineering construction. In this study, the ocean ambient noise with low-frequency, long-wavelength, and wide-band characteristics was used to conduct and analysis noise based on the horizontal-to-vertical spectral ratio method. The shear wave velocity of the seabed soil was obtained by inverting the ocean ambient noise dataset. Then, we proposed a shear wave velocity threshold that can be used for liquefaction assessment of Holocene unconsolidated fine-grained soils by statistical analysis, and the liquefaction potential of the soils was evaluated according to 1-D shear wave velocity structures and 2-D shear wave velocity profiles. The results showed that the distribution of the shear wave velocity obtained by inverting ocean ambient noise was generally consistent with the measured shear wave velocity in the field, indicating that the inversion results have a certain degree of accuracy. A shear wave velocity threshold of 200 m/s was proposed for liquefaction assessment, determining that the soils within 0-10 m depth in the coastal area of Yellow River Delta have liquefaction potential. This result is in accordance with the assessment based on the critical shear wave velocity, indicating that this threshold is applicable to the assessment of seabed soil liquefaction in the Yellow River Delta. The *in-situ* observations of ocean ambient noise provide a more convenient, economical, and environmentally friendly method, which can help to investigate marine geology disasters and serve marine engineering construction.

KEYWORDS

ocean ambient noise, in-situ observations, shear wave velocity, inversion, liquefaction assessment

1 Introduction

Soil liquefaction is one of the significant factors affecting soil stability, among them, seabed soil liquefaction is a harmful marine geological disaster, which has attracted widespread attention from domestic and foreign geotechnical engineering and coastal engineering communities. Under the continuous erosion and scouring of waves, fine particles on the surface soil of the seabed migrate out and escape along the pores of the coarse particles, thereby forming larger pores in the soil (Dassanayake et al., 2022). This can destroy the structural integrity of the soil, and weaken the hydraulic properties (Jia et al., 2014) and engineering characteristics (Liu et al., 2013) of the soil, which may induce soil liquefaction under cyclic loading (Bachrach et al., 2001), causing damage to offshore structures such as submarine pipelines (Sumer et al., 1999; Zhou et al., 2013), offshore platforms (Sumer, 2014; Zhang et al., 2017), and breakwaters (Jeng, 2001; Zhao and Jeng, 2015). The Yellow River Delta is a typical rapidly deposited delta, and also the place with the densest offshore structures on the south coast of the Bohai Bay. The fine-grained soils such as silt and silty sand are widely developed in the Yellow River Delta, with weaker permeability and poorer water stability, which makes them more prone to unstable failure of soil such as liquefaction (Ren et al., 2020; Wang et al., 2022; Liu et al., 2023; Zhang et al., 2023). For this reason, accurately assessing the seabed liquefaction has become an essential part of disaster prevention and mitigation in the construction of the Yellow River Delta.

At present, there are three primary methods for assessing soil liquefaction: *in-situ* tests (Fergany and Omar, 2017), laboratory tests (Kumar et al., 2020), and numerical simulation (Ye et al., 2016; Zhao et al., 2018). These methods have been maturely applied in the study of liquefaction in sandy soils due to their safety and reliability (Amini and Qi, 2000; Dobry and Abdoun, 2017; Ye et al., 2018). However, for seabed soil, sampling measurements and laboratory tests can only obtain the physical and mechanical properties of shallow soil layers (Meng et al., 2018), and cannot guarantee the natural structure and stress state of seabed soil, resulting in failure to reflect the real dynamic response of soil. Numerical simulation can provide guidance for experimental research and theoretical analysis, but the simplification of boundary conditions and material properties in the numerical simulation process with a certain degree of randomness can lead to affect the reliability of the results. Furthermore, invasive *in-situ* tests such as standard penetration test (SPT) (Seed et al., 1983) and cone penetration test (CPT) (Boumpoulis et al., 2021; Geyin and Maurer, 2021) are complex and expensive, making them unsuitable for large-scale seabed measurements. Submarine acoustic exploration technology uses the acoustic properties of the compression waves (P-waves) and the shear waves (S-waves) to investigate the engineering properties of seabed soils. This method can effectively avoid measuring errors caused by disturbances, which is becoming a prominent means for studying the properties of seabed soils (Gorgas et al., 2002; Hou et al., 2018). Compared with the results of SPT and CPT testing, shear wave velocity (V_s) is closely related to liquefaction resistance, and is influenced by factors such as porosity ratio, stress state, relative density, and soil type (Hardin and Drnevich, 1972; Tokimatsu and Uchida, 1990; Xu et al., 2015). Moreover, V_s is one of the fundamental mechanical properties of soils, which can characterize the shear stiffness under small strain conditions and soil-structure interaction, and has potential application prospects in assessing soil liquefaction (Qin et al., 2020; Lin et al., 2021). Nevertheless, traditional shear wave velocity testing requires placing shear wave sensors in surface or underground boreholes, making it difficult to conduct measurements in the seabed. Moreover, the harsh seafloor environment and complex sediment structure seriously affect the measurement accuracy, and the high cost and limited measurement range restrict the development of submarine acoustic exploration technology.

There exist weak and low-amplitude vibration in the natural environment, known as ambient noise, which are commonly considered as an interference signal in geophysics. Over the past few decades, researchers have gradually discovered that ambient noise can be used to prospect subsurface structures (Aki, 1957; Toksoz, 1964). The composition of different body and surface waves in ambient noise is highly complex (Bonnefoy-Claudet et al., 2006). Nakamura (Nakamura, 1989; Nakamura, 2008; Nakamura, 2009) proposed the horizontal to vertical spectral ratio method (HVSR), which normalizes the amplification effects of the horizontal and vertical components of ambient noise, calculates the Fourier spectrum ratio of the horizontal and vertical components of noise, and evaluates the ground response characteristics of soft sediment caused by multiple reflections of shear waves (Nakamura, 2000; Nakamura, 2019). The HVSR curve is closely related to the properties of the soil (Field et al., 1990; Field and Jacob, 1993) and is considered as a "transfer function" of the vertically incident shear wave in the strata (Nakamura, 1989; Nakamura, 2008). Kawase et al. (2011) proved that the horizontal-to-vertical spectral ratios match the ratios estimated from 1D shear wave velocity model using the simple theory of diffuse field. Therefore, based on the fundamental resonant frequency and spectral amplitude on the HVSR curve, the shear wave velocity can be estimated using an inversion algorithm (forward modeling routine and Monte Carlo method) and an empirical relationship between shear wave velocity and depth, such as the quarter-wavelength theory (Joyner et al., 1981; Boore, 2003; Edwards et al., 2011). The ambient noise on land is mainly caused by industrial machinery, vehicles, and other human activities, which is predominantly composed of high-frequency and short-wavelength noise (Bonnefoy-Claudet et al., 2006). In contrast, ocean ambient noise is mainly caused by the action of waves on the seabed (Hasselmann, 1963; Bromirski et al., 2005), and it is a broad-band vibration with low-frequency and long-wavelength characteristics, which ensures that ocean ambient noise exploration has a greater detection depth and sufficient resolution.yao

The structure of this study is as follows: Firstly, we introduce the feasibility analysis for assessing the liquefaction potential of seabed soils based on shear wave velocities obtained by inverting ocean ambient noise. Secondly, we present the geological overview of the study area (the coastal zone of the Yellow River Delta). Third, we describe the inversion method and strategy of ocean ambient noise. Fourth, we discuss the characteristics of ocean ambient noise and the accuracy of inversion results, respectively. In addition, we propose and validate the shear wave velocity threshold that can

be used for fine-grained soil liquefaction assessment based on statistical analysis. Finally, we conclude this study by discussing and concluding the effectiveness, limitations and potential for assessing the liquefaction of seabed soils by the shear wave velocity obtained by the inversion of ocean ambient noise.

2 Geological overview

The Yellow River Delta is located on the southern coast of Bohai, and the Yellow River Delta Plain is a fluvial plain formed by the long-term siltation and continuous sea reclamation of high-concentration sediment carried by the Yellow River. We selected the northern coastal zone of the Yellow River Delta as our study area (Figure 1), which has an overall flat topography and gentle slope. The thickness of the Quaternary strata is about 26 m, with a horizontal distribution. Due to the special deposition pattern, silty soils are commonly developed in the surface sediments, with predominantly silt, fine sand and small amounts of clay (Zhao et al., 2013), showing the engineering characteristics of a high water content, poor grading, low bearing capacity, and high compressibility. In addition, thin-layered soft soil layers are widely developed in the stratum, with a thickness of about 1-5 m, which are interspersed with the sedimentary layers in a finger-like way. The engineering geological environment of the Yellow River Delta region is controlled by the sedimentary dynamic environment, which is mainly determined by the muddy and sandy nature of the Yellow River and its frequent siltation and migration. Owing to the migration of the Yellow River Estuary, the sediment supply has been interrupted. In the northern coastal zone, under the action of long-term differential hydrodynamic forces, the structural integrity of the surface soil of the tidal flats are destroyed, leading to a decrease in strength and gradual erosion, which has formed a drop of nearly 1 m between the tidal flats and the embankment. Thus, the study of the engineering characteristics of seabed soil under dynamic action would be helpful to maintain the safety of marine buildings.

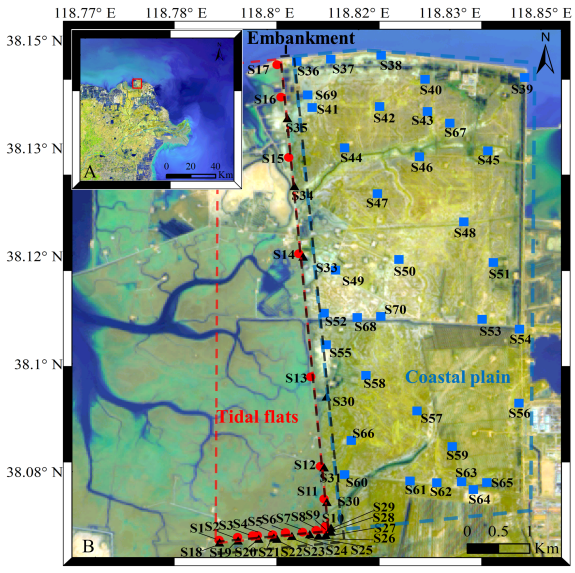

FIGURE 1
Map of the northern coastal areas of the Yellow River Delta. **(A)** The map of the study area (red rectangle). **(B)** The distribution of measurement stations within the study area. The red dashed line represents the tidal flats with the stations in red circles; the black dashed line represents the embankment with the stations in black triangles; the blue dashed line represents the coastal plain with the stations in blue square.

3 Inversion method

In this paper, the OpenHVSR-inversion program (Bignardi et al., 2018) is used to invert the HVSR curves of ocean ambient noise and obtain the shear wave velocity. This program can be used to model and invert HVSR dataset simultaneously, obtaining the distribution of shear wave velocity in different depth layers to construct 2-D or 3-D subsurface models. The forward modeling is based on the method proposed by Tsai and Housner (1970), which calculates the theoretical transfer function of the layered subsurface model. The inversion strategy is based on the Monte Carlo method, where a randomly perturbed version of the best fitting model is generated in each iteration, and used to compute a set of simulated curves for comparison with experimental curves. The generation of many trial models allows exploring the parameters space while searching for a new and better fitting model.

Several *in-situ* ambient noise recordings were carried out in the Yellow River Delta, and the observed distribution of fundamental frequency is shown in Figure 2, which is mainly concentrated in the range of 0.8-9.8 Hz (Meng et al., 2023). As a result, we set the frequency band for inversion from 0.6 to10 Hz. The inversion was divided into three stages. In the first stage, the inversion was started with a simple 4-layer subsurface model (Table 1), limiting the frequency band to 0.6-4 Hz. Successively, when the best-fit model was found, the result was saved as a new project and the subsurface

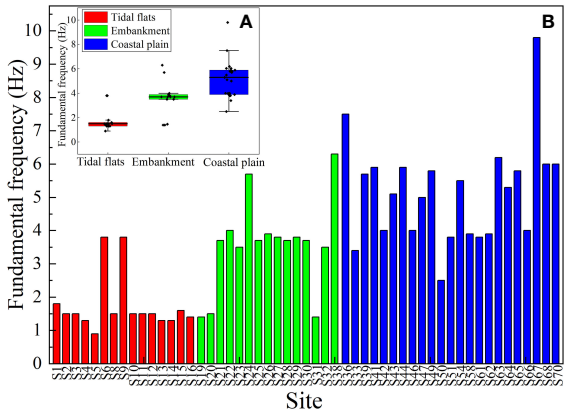

FIGURE 2
Statistics of fundamental frequency in the coastal zone of the Yellow River Delta (modified from Meng et al., 2023). **(A)** The distribution of fundamental frequency for stations in different study areas, where the red represents the tidal flats, the green represents the embankment, and the blue represents the coastal plain. **(B)** The fundamental frequency for all stations.

TABLE 1 Initial subsurface parametric model.

Compressive waves velocity/V_p(m/s)	Shear waves velocity/V_s(m/s)	Density /ρ(K_g/m^3)	Thickness /h(m)	P-waves daming /Q_p	S-waves daming /Q_s
386	192	1.7	30	15	5
620	310	1.8	30	25	10
792	390	1.8	40	30	15
1000	500	1.8	999	999	999

model was edited, dividing the deeper layer in three sublayers, while the total thickness of the layer remains unchanged. Then, set the frequency band for the second stage to 0.6-8 Hz and continue with the next, with the shallower layer dividing in four sublayers, and so on. The frequency band for the third stage was set at 0.6-10 Hz, with a total of 10 layers.

In each stage of the inversion, firstly, the longitudinal wave velocity, shear wave velocity, and thickness were allowed a 5% perturbation for 3000 iterations of global inversion. Secondly, the best-fitting model of the HVSR curve for each station was locally optimized, allowing a 15% perturbation of the parameters for 5000 iterations. Finally, 10000 iterations were performed with 20% lateral constraint perturbations. In order to provide a more intuitive description of the inversion results, an example of the inversion of the ocean ambient noise in the Yellow River Delta is given in Figure 3. Figure 3A illustrates the HVSR curve of the measured noise (black), the standard deviation (gray), the best-fitting curve obtained by Monte Carlo inversion (red), and the fitting curve generated by the last iteration of Monte Carlo inversion (blue). It can be seen that peaks are observed in the HVSR curve at both 1.9 Hz and 10 Hz in Figure 3A. According to the method for identifying the fundamental frequency proposed by Meng et al. (2023), the fundamental frequency of the soil at this station is 1.9 Hz, not 10 Hz, and the peak at 10 Hz was caused by the fundamental Rayleigh waves (Nakamura, 2008). The Figure 3A also shown the good consistency among the best-fit curve and the fitted curve generated by the last iteration with the HVSR curve. Figure 3B represents the shear wave velocity structure of the observation station obtained by inversion of the ocean ambient noise.

To evaluate the accuracy of the inversion, we used two concepts: global misfit and local misfit. Local misfit refers to the normalized misfit between the simulated and experimental curve at each station. For the global misfit, we introduced the objective function (Bignardi et al., 2018):

$$E(m) = aM(m) + bS(m) + \sum_{j=1}^{5} \alpha_j R_j(m)$$

Where $M(m)$ represents the misfit between the simulated and experimental curves; $S(m)$ represents the fitting degree of the simulated and experimental curves at the peaks; and $R_j(m)$ represents the regularization term. The constants a and b in above Equation are used to balance the relative weight of the $M(m)$ and $S(m)$ terms. Based on the objective function, we define the global misfit as $aM(m) + bS(m)$.

Figure 4A shows the global misfit of the inversion results. As can be seen from the figure that the global misfit between the inversion results and experimental data is 0.1, and the fitting degree at the peak of the experimental curve and simulated curve is around 0.9. The normalized misfit between the experimental data and simulated data at each station is shown in Figure 4B, and it can be seen that there are 52 stations with a local misfit of less than 0.1; 6 stations with a local misfit between 0.1 to 0.2; and only 6 stations have a local misfit exceeding 0.2.

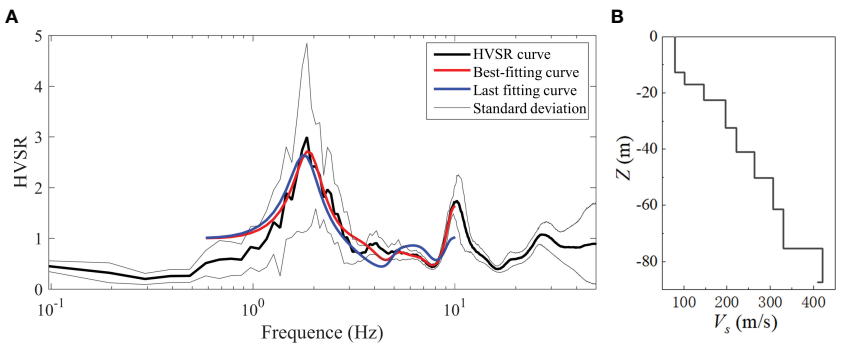

FIGURE 3
Example of inversion of marine ambient noise recording. **(A)** Best-fit model. **(B)** The structure of shear wave velocity corresponding to the best-fit model.

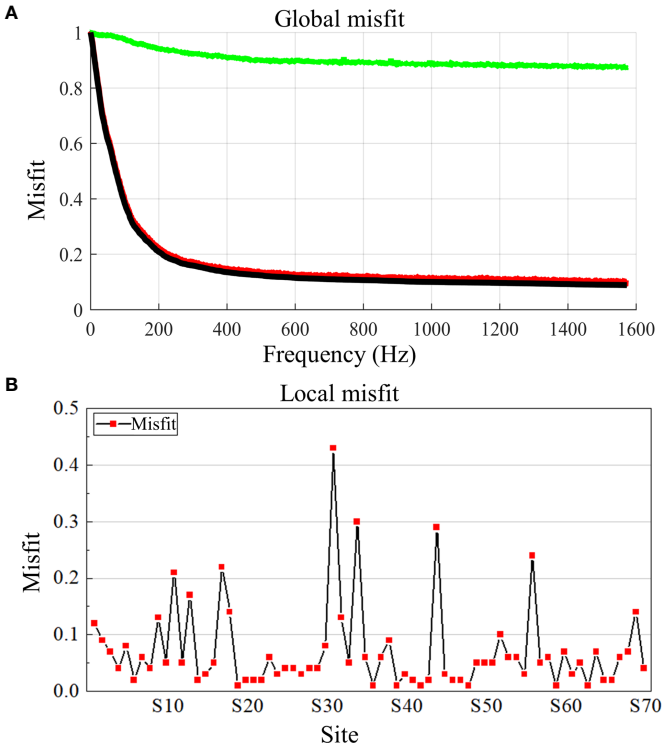

FIGURE 4
Value of the normalized misfit. **(A)** Global misfit, where the black curve represents the misfit of the inversion results (the *aM*(*m*)+*bS*(*m*) in Equation); the red curve is the misfit of the experimental and simulated curves (the *aM*(*m*) in Equation); and the green curve is the fitting degree at the peak of the experimental and simulated curves (the *bS*(*m*) in Equation). **(B)** Normalized misfit for each station at the end of the inversion.

4 Results and discussion

4.1 Characteristics of ocean ambient noise

Ocean ambient noise is a persistent acoustic field in the ocean, and different sources produce noise of different frequencies (Bonnefoy-Claudet et al., 2006). The movement of the Earth's crust is the primary source of ultra-low frequency noise in the ocean, with quasi-periodicity of 1-7 Hz; nonlinear interaction of back-propagating sea surface waves produces random noise with frequencies between 5-10 Hz; sound waves emitted by atmospheric sources (such as lightning) can couple into the underwater sound field, with frequencies also below 10 Hz; ship navigation produces sound waves with frequencies ranging from 5-500 Hz; and deep-sea currents, internal solitary waves, and turbulence caused by fragmentation create a wider frequency range. In the coastal and nearshore noise fields, waves, as the primary source of noise, waves striking along the coasts are the main source of low-frequency noise with a range of 0.5-1.2 Hz (Gutenberg, 1958), and the strong interaction between waves with the seabed can generate noise up to 10 Hz (Olofsson, 2010). In this paper, we concern the ambient noise with frequency below 10 Hz.

We conducted ocean ambient noise recordings using the single-station array and the centerless circular array with a radius of 1 m on the tidal flats in the Yellow River Delta. Figure 5 shows the Fourier spectrum of ocean ambient noise recorded by six stations in the centerless circular array. There is a certain energy of ambient noise in each station from low to high frequencies. The Fourier spectrum shows good amplitude consistency in the low-frequency band (1.9-7.7 Hz) and differentiation in the high-frequency band. Thus, it could be considered that the ocean ambient noise propagates in all directions with almost the same energy in each direction within this band. According to the analysis of the characteristics, the ocean ambient noise recorded on the tidal flats in the Yellow River Delta shows a good consistency in the low-frequency band and relative dispersion in the high-frequency band. We analyze that the factors such as waves, tides, and wind are the main sources of noise on the tidal flats, so the recorded noise mainly presents low-frequency and long-wavelength characteristics, and of course, it also contains some high-frequency and short-wavelength noise generated by the navigation. Compared with land ambient noise, ocean ambient noise dominates in the low-frequency band, which can be used to obtain deeper seabed soil information.

4.2 Inversion results of shear wave velocity

After obtaining the inversion results, the distribution of shear wave velocity within the depth range of 0-100 m was statistically analyzed. The confidence intervals of the shear wave velocity at the confidence levels of 95% and 75% were also calculated, as shown in Table 2. The accuracy and applicability of the inverted shear wave

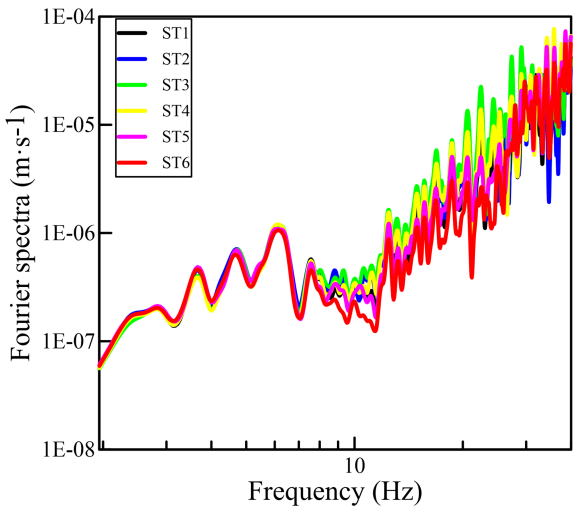

FIGURE 5
Fourier spectrum of ambient noise recorded by six stations in a centerless circular array.

velocity were tested by comparing them with the field measurements (Liu et al., 2015).

From Table 2, it can be found that the average, minimum and maximum values of shear wave velocity obtained by inversion are basically consistent with the field measurements at depths of 10-90 m depth. However, the ranges of shear wave velocities obtained from the inversion are underestimated in the depth of 0-10 m. Among them, the shear wave velocity obtained from the inversion respectively are 83-102 m/s and 87-98 m/s at 90% and 75% confidence intervals, which deviate from the field results of 108-183 m/s and 123-167 m/s. The inversion results are lower compared with the measured results, -which is speculated to be related to the groundwater table. The field measurements of shear wave velocity were carried out at locations far from the sea, while the study area is located in the coastal zone with extremely shallow groundwater table and high soil moisture content, resulting in a lower shear wave velocity. Within the range of 10-90 m, the distribution of the inverted shear wave velocity in the stratum satisfies the results of the field measurements at the 95% and 75% confidence intervals. Nevertheless, in the depth range below 30 m, the maximum value of the shear wave velocity and the lower limit of the 95% confidence interval are both higher than the measured data. Moreover, there exist an abnormally high value for the inverted shear wave velocity at the bottom layer.

Liu et al. (2007) conducted shear wave velocity tests on the northern coastal zone in the Yellow River Delta and obtained measured shear wave velocities of 91-137 m/s within the depth range of 0-10 m (Table 3). Yang et al. (2022) carried out field measurements using the single-hole method on tidal flats in the Yellow River Delta, and the measured shear wave velocities were mainly distributed in a range of 100-250 m/s within the depth range of 0-20 m. The inverted results are in good agreement with the field measurements, which further proves the accuracy of the inversion shear wave velocities.

4.3 Shear wave velocity threshold

Andrus and Stokoe (Andrus and Stokoe, 1999; Andrus and Stokoe, 2000; Andrus et al., 2004) proposed a simplified method for soil liquefaction assessment using shear wave velocity (V_s) and stress-corrected shear wave velocity (V_{s1}) based on a large amount of investigations of earthquake liquefaction occurring in fine-grained soils, such as fine sand, gravel, and silty clay. For Holocene unconsolidated fine-grained soil, Youd and Idriss (2001) established the relationship between V_s and cyclic stress ratio (CSR) for liquefaction and non-liquefaction areas according to

TABLE 2 Distribution of shear wave velocity obtained by HVSR curves inversion and measured field data from Liu et al. (2015).

Depth (m)	Average value (m/s)		Minimum value (m/s)		Maximum value (m/s)		Standard deviation (m/s)		Confidence interval (m/s)			
									Confidence 95%		Confidence 75%	
	A	B	A	B	A	B	A	B	A	B	A	B
1-10	145	93	100	80	233	134	19.1	19.4	108-183	83-102	123-167	87-98
11-20	191	206	130	117	318	297	27.6	43.6	137-245	185-227	159-223	196-218
21-30	245	259	152	166	369	373	31.7	66.5	183-307	227-291	208-281	241-277
31-40	264	266	179	146	377	486	34.4	87.1	196-331	224-308	224-303	242-290
41-50	301	318	202	214	397	423	33.1	53.1	236-366	293-344	263-339	304-333
51-60	328	321	231	222	431	425	31.3	67.0	267-390	288-353	292-364	302-339
61-70	349	359	255	285	446	510	29.3	61.3	291-407	330-389	315-383	342-376
70-80	369	381	260	230	479	490	33.3	83.3	303-434	340-421	330-407	358-403
81-90	390	411	291	286	491	499	32.8	57.4	326-455	384-439	352-428	396-427
91-100	414	443	309	296	501	856	32.4	121.9	350-477	384-501	376-451	410-476

The A stands for inversion results and the B stands for field test data.

TABLE 3 Field measured shear wave velocity and calculated critical shear wave velocity in the Yellow River Delta (modified from Liu et al., 2007).

Depth (m)	shear wave velocity (m/s)	stress-corrected shear wave velocity (m/s)
1	91	136.98
2	115.6	141.47
3	127.4	151.37
4	155.9	150.39
5	150.3	152.59
10	137.7	160.43

a probabilistic statistical method and proposed the upper limit of V_s (180 m/s) as a threshold for liquefaction assessment in engineering practice (Yulianur et al., 2020). However, statistical analysis of the relationship between stress-corrected shear wave velocity and CSR revealed certain limitations of this threshold. To illustrate this viewpoint, we collected the investigation data from over 50 different locations. The liquefaction areas were determined by the observation of liquefaction phenomena and *in-situ* tests (SPT and CPT). The relationship between the cyclic stress ratio (CSR) and shear wave velocity or stress-corrected shear wave velocity is established based on probabilistic statistics of the distribution of shear wave velocity.

Figure 6A shows the relationship between CSR and the measured average V_s in liquefaction and non-liquefaction fields, and Figure 6B presents the relationship between CSR and V_{s1}. The measured V_s of soils in liquefaction area ranged from 79 to 210 m/s, generally lower than 180 m/s, with only four data exceeding this threshold for an error of about 4%. Differently, the distribution of V_{s1} ranged from 104 to 271 m/s, with 15% of the data exceeding 180 m/s. As a result, it may be risky to use the shear wave velocity of 180 m/s as the threshold for soil liquefaction assessment in practical engineering applications. The confidence interval of V_{s1} in 95% confidence is 149.10-160.47 m/s, with 95% of the data below 200 m/s. Accordingly, it is considered that 200 m/s as the threshold for liquefaction assessment of fine-grained soils will be of practical application.

4.4 Soil liquefaction assessment

According to the statistics of the field investigation data for soil liquefaction, wave-induced soil liquefaction generally occurs in shallow surface seabed within a few meters (Hirst and Richards, 1977; Sassa et al., 2006), and depth of the seismic liquefaction may occur up to 20 m below the surface in the gravel, and the depth in silt and silty sand is commonly less than 20 m (Holzer et al., 1999; Bray et al., 2004). Liu et al. (2005) considered that the silt soils in the Yellow River Delta have liquefaction potential under dynamic loads based on the pore-pressure model. As shown in Tables 2, the inverted shear wave velocity is in general agreement with the field measured results within 30 m depth. Consequently, it can be used to evaluate problems such as seabed soil liquefaction.

Figure 7 shows the shear wave velocity structures of three areas on the coastal zone. The red dashed line and solid line represent the dividing lines of shear wave velocity of 180 m/s and 200 m/s, respectively. It can be seen that the vertical distribution of shear wave velocity corresponds roughly to the boundaries of soil indicated by the borehole Yang et al. (2022). Moreover, the shear wave velocity of the soil within a depth of 10 m is generally less than

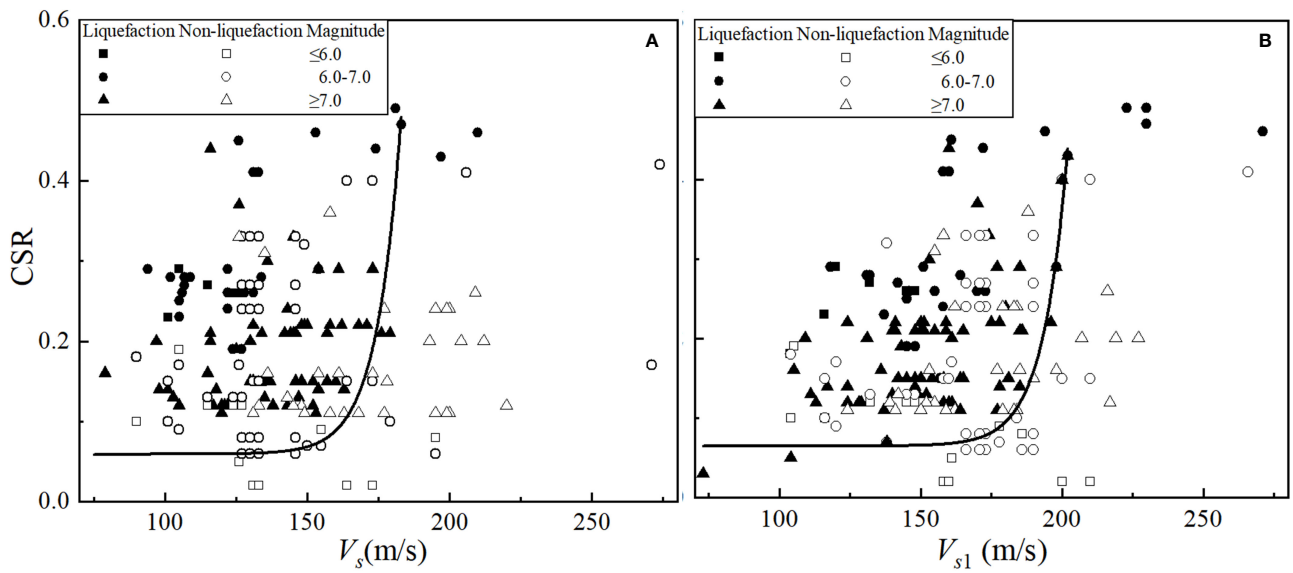

FIGURE 6
V_s -based liquefaction and non-liquefaction for Holocene unconsolidated fine-grained soils. **(A)** The relationship between the measured V_s and cyclic stress ratio (CSR). **(B)** The relationship between V_{s1} and CSR. In the figures, the square, circle and triangle represent respectively shear wave velocities of soils with earthquake magnitudes ≤6.0, 6.0-7.0, ≥7.0; the solid and hollow figures correspond to shear wave velocities liquefaction and non-liquefaction areas respectively.

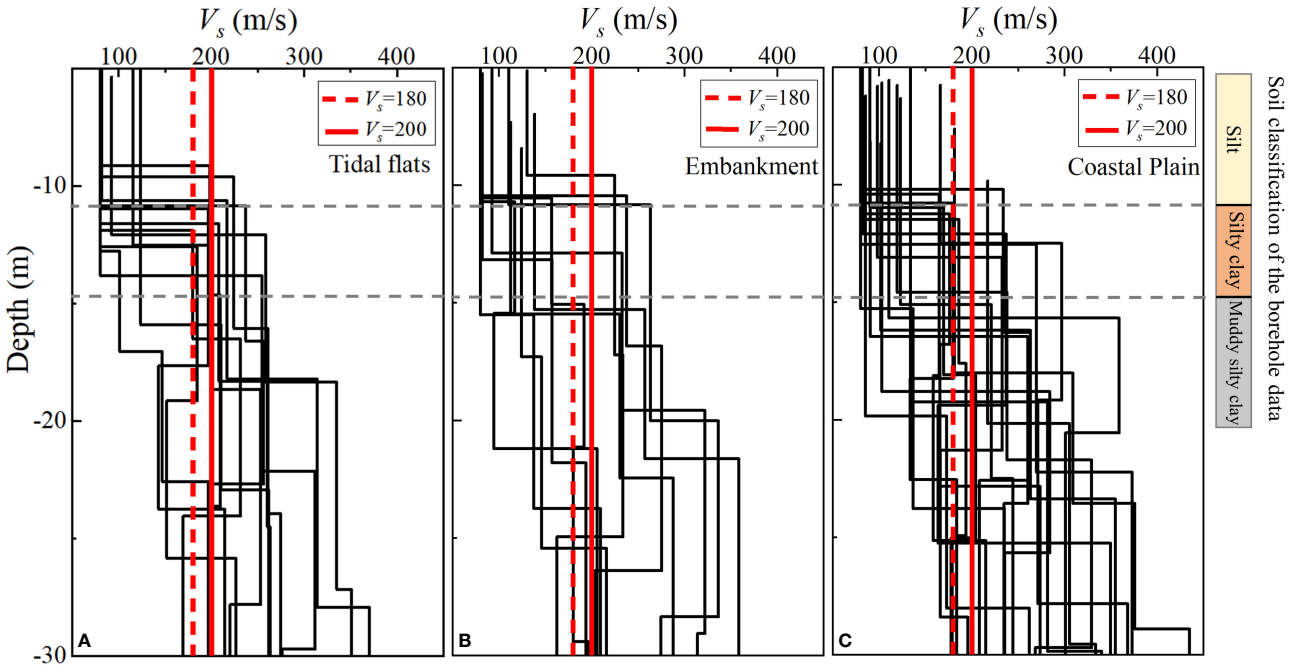

FIGURE 7
1-D shear wave velocity structure within 30 m depth at each station. The Yellow River delta is divided into three study areas, namely **(A)** the tidal flats area in front of the embankment, **(B)** the embankment area, and **(C)** the coastal plain area. The bar in the figure represent the soil layer classification, and the borehole data is cited from Yang et al. (2022).

200 m/s, indicating that the fine-grained soil at this depth has a certain potential for liquefaction. Liu et al. (2007) calculated the critical shear wave velocity within the range of 0-10 m based on the empirical relationship between shear wave velocity and the number of blows of standard penetration, which is found to be from 136 to 160 m/s (Table 3). The inverted shear wave velocity within the depth range of 0-10 m is determined to be between 80-133.87 m/s, which is lower than the critical shear wave velocity for each layer. Therefore, it is determined that the soil within the range of 0-10 m on the tidal flat was judged to be liquefiable. The results of the soil liquefaction assessment based on the shear wave velocity threshold and the critical shear wave velocity were consistent within the depth range of 0-10 m. Meanwhile, it can be observed that there were multiple low-velocity anomalies in the vertical shear wave velocity structure of the strata, and there were significant differences in the shear wave velocity of the soil at the same depth range in the lateral direction. As shown in Figure 7, from the coastal plain to the tidal flat in front of the embankment, the shear wave velocity of the soil follows the trend of gradually decreasing from land to sea. According to geological data in the region, the high-concentration sediment continuously accumulates during the transportation process of the river due to oscillation and diversion of the Yellow River estuary, sea level changes, and the combined effects of waves, tides, and storm surges. The fluvial deposits and coastal deposits in different periods have been superimposed and deposited, forming a sedimentary structure that appears as a finger-like interlocking in the horizontal direction, and the gradually advancing from land to sea in the vertical direction. In different depth ranges, there are marine deposits with high water content and high saturation, as well as soft soil layers with high water content, high porosity ratio, and low shear strength, which are unevenly distributed in the tidal flat. This results in the common presence of low-velocity abnormal segments in the shear wave velocity structure.

A measuring line was set up along the east-west direction on the tidal flat in front of the embankment in the Yellow River Delta. Figure 8 shows the inversion results of seven observation stations on the tidal flat. Figure 8A shows the shear wave velocity profile within a depth range of 30 m. For comparison, we first converted the frequency to "pseudo-depth" using the quarter-wavelength formula ($h=V_s/4f$) to obtain the HVSR curve with depth, then, we plotted the HVSR profiles in Figure 8B with interpolation method based on all curves. The figure shows that the shear wave velocity of the geological layer exhibits a layered distribution, which is consistent with the sedimentary characteristics of the region. Geological layers with a shear wave velocity less than 200 m/s are distributed within a depth range of 10 m, and some stations can reach 20 m. The distribution of the HVSR shows a negative correlation with the magnitude of the shear wave velocity (Figure 8B). The level of the horizontal and vertical spectral ratio of ambient noise reflects the amplification effect of the soil on seismic motion. The looser the soil, the more significant the amplification effect of the seismic wave amplitude is, while the noise spectral ratio is larger. At the same time, soft soil has a lower degree of compaction and a lower shear wave velocity. It can be understood that the shear wave velocity of the surface soil of the tidal flats is low and its engineering properties are poor. Soft surface soil will amplify the amplitude and energy of

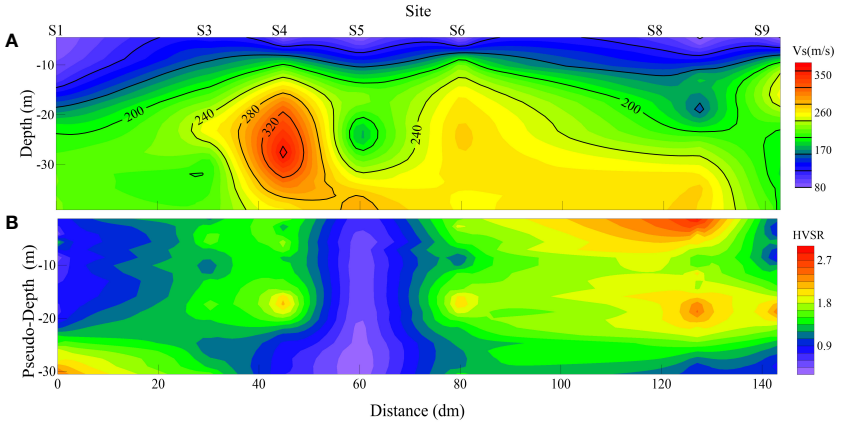

FIGURE 8
Inversion results along the east-west lateral line of 7 observation stations on the tidal flat in the Yellow River Delta. **(A)** 2-D Shear wave velocity profile of the tidal flat. **(B)** For comparison, the HVSR profile is formed by the HVSR curves, and the frequency axis is converted to "pseudo-depth" by the assumption that V_s=350 m/s for soft layers.

seismic waves. If seismic waves in a certain frequency band coincide with the resonance frequency of the overlying soil, the resonance effect will be induced, which will cause unpredictable damage to the overlying buildings.

5 Conclusion

The purpose of this paper is to obtain the shear wave velocity of seabed soils by inversion of ocean ambient noise for rapid assessment of seabed soil liquefaction. *In-situ* noise recording and analysis were performed in the northern coast of the Yellow River Delta using the HVSR method to obtain the shear wave velocity of the seabed soil. Based on statistical analysis of liquefaction investigation data, a shear wave velocity threshold was proposed for assessing the liquefaction potential, and the location of liquefiable soil was identified in the light of 1-D shear wave velocity structure and 2-D shear wave velocity profile. In summary, the following results were obtained:

1. Ocean ambient noise has the characteristics of low-frequency, long-wavelength, and wide bandwidth. Therefore, *in-situ* observations of ocean ambient noise can not only obtain the physical and mechanical properties of the seabed soil in a deeper range depending on the propagation characteristics of noise in the seabed sediment, but also monitor the deformation and stability of the seabed soil, provide the necessary support for the design and construction of marine engineering, and are of great significance for risk assessment and the early warning of marine geology disasters.

2. Shear wave velocities of seabed soils were obtained by inversing the HVSR dataset of oceanic ambient noise. The stratigraphic distribution of the shear wave velocity obtained by inversion is broadly consistent with existing research results, which indicates that the results have a certain degree of accuracy and that the method for inverting ocean ambient noise is quite feasible.

3. The application of a shear wave velocity threshold of 200 m/s in assessing the liquefaction potential of fine-grained soils in the Yellow River Delta yielded consistent results with traditional methods. The assessment showed the liquefaction potential of soil in depths of 0-10 m, and indicated that this threshold is reasonable for liquefaction assessment of seabed soil in the Yellow River Delta. Accordingly, the stability problems of the soil in the tidal flat area should be taken into sufficient consideration during engineering construction. It is necessary to adopt measures such as replacement methods and dynamic consolidation for foundation treatment to ensure the safety of engineering construction and use.

4. The HVSR-based ocean ambient noise prospecting method has the advantages of being convenient, economical, environment-independent, and deeper detection depth. It can provide services for disaster prevention and mitigation of marine engineering construction, and has good practical application. In addition, in the actual application process, combining this method with other geotechnical tests (such as drilling, *in-situ* tests, or laboratory tests, etc.) can more accurately determine the engineering characteristics of soil, and further classify the liquefaction hazard of soil, which is crucial for coastal protection and marine engineering construction.

Data availability statement

The raw data supporting the conclusions of this article will be made available by the authors, without undue reservation.

Author contributions

Conceptualization & methodology, YL, QM and SW. Formal analysis, YL and WW. Data curation, YL and YC. Writing—original draft preparation, YL. Writing—review & editing, YL and QM. Visualization, YC and SW. Project administration, YL and WW.

Funding acquisition, QM. All authors contributed to the article and approved the submitted version.

Funding

The study is supported by the National Natural Science Foundation of China (Nos. 42272327), and the Social and livelihood project of Shandong Province (2021, 202131001).

Acknowledgments

The authors would like to thank Zhiyuan Chen who participated in recording the ambient noise in the field and Yupeng Ren who participated in revising the manuscript.

Conflict of interest

The authors declare that the research was conducted in the absence of any commercial or financial relationships that could be construed as a potential conflict of interest.

Publisher's note

All claims expressed in this article are solely those of the authors and do not necessarily represent those of their affiliated organizations, or those of the publisher, the editors and the reviewers. Any product that may be evaluated in this article, or claim that may be made by its manufacturer, is not guaranteed or endorsed by the publisher.

References

Aki, K. (1957). Space and time spectra of stationary stochastic waves, with special reference to microtremors. *Bull. Earthq. Eng.* 35, 414–456.

Amini, F., and Qi, G. Z. (2000). Liquefaction testing of stratified silty sands. *J. Geotech. Geoenviron. Eng.* 126, 208–217. doi: 10.1061/(ASCE)1090-0241(2000)126:3(208

Andrus, R. D., and Stokoe, K. H. (1999). Liquefaction resistance based on shear wave velocity. *Proceed. NCEER Workshop Eval. Liquefact. Resist. Soils.* 22, 89–128. doi: 10.1186/s40703-020-00132-1

Andrus, R. D., and Stokoe, K. H. (2000). Liquefaction resistance of soils from shear-wave velocity. *J. Geotech. Geoenviron. Eng.* 126, 1015–1025. doi: 10.1061/(ASCE)1090-0241(2000)126:11(1015

Andrus, R. D., Stokoe, K. H., and Hsein Juang, C. (2004). Guide for shear-wave-based liquefaction potential evaluation. *Earthq. Spectra* 20, 285–308. doi: 10.1193/1.1715106

Bachrach, R., Nur, A., and Agnon, A. (2001). Liquefaction and dynamic poroelasticity in soft sediments. *J. Geophys. Res.* 106, 13515–13526. doi: 10.1029/2000JB900474

Bignardi, S., Yezzi, A. J., Fiussello, S., and Comelli, A. (2018). OpenHVSR - processing toolkit: enhanced HVSR processing of distributed microtremor measurements and spatial variation of their informative content. *Comput. Geosci.* 120, 10–20. doi: 10.1016/j.cageo.2018.07.006

Bonnefoy-Claudet, S., Cotton, F., and Bard, P.-Y. (2006). The nature of noise wavefield and its applications for site effects studies: a literature review. *Earth-Sci. Rev.* 79, 205–227. doi: 10.1016/j.earscirev.2006.07.004

Boore, D. M. (2003). Simulation of ground motion using the stochastic method. *Pure Appl. Geophys.* 160, 635–676. doi: 10.1007/PL00012553

Boumpoulis, V., Depountis, N., Pelekis, P., and Sabatakakis, N. (2021). SPT and CPT application for liquefaction evaluation in Greece. *Arab. J. Geosci.* 14, 1631. doi: 10.1007/s12517-021-08103-1

Bray, J. D., Sancio, R. B., Durgunoglu, T., Onalp, A., Youd, T. L., Stewart, J. P., et al. (2004). Subsurface characterization at ground failure sites in adapazari, Turkey. *J. Geotech. Geoenviron. Eng.* 130, 673–685. doi: 10.1061/(ASCE)1090-0241(2004)130:7(673)

Bromirski, P. D., Duennebier, F. K., and Stephen, R. A. (2005). Mid-ocean microseisms. *Geochem. Geophys. Geosyst.* 6 (4), Q04009. doi: 10.1029/2004GC000768

Dassanayake, S. M., Mousa, A. A., Ilankoon, S., and Fowmes, G. J. (2022). Internal instability in soils: a critical review of the fundamentals and ramifications. *Transp. Res. Rec.* 2676, 1–26. doi: 10.1177/03611981211056908

Dobry, R., and Abdoun, T. (2017). Recent findings on liquefaction triggering in clean and silty sands during earthquakes. *J. Geotech. Geoenviron. Eng.* 143, 04017077. doi: 10.1061/(ASCE)GT.1943-5606.0001778

Edwards, B., Poggi, V., and Fah, D. (2011). A predictive equation for the vertical-to-horizontal ratio of ground motion at rock sites based on shear-wave velocity profiles from Japan and Switzerland. *Bull. Seismol. Soc Amer.* 101, 2998–3019. doi: 10.1785/0120110023

Fergany, E., and Omar, K. (2017). Liquefaction potential of Nile delta, Egypt. *NRIAG J. Astron. Geophys.* 6, 60–67. doi: 10.1016/j.nrjag.2017.01.004

Field, E. H., Hough, S. E., and Jacob, K. H. (1990). Using microtremors to assess potential earthquake site response: a case study in flushing meadows, new York city. *Bull. Seismol. Soc Amer.* 80, 1456–1480. doi: 10.1785/BSSA08006A1456

Field, E., and Jacob, K. (1993). The theoretical response of sedimentary layers to ambient seismic noise. *Geophys. Res. Lett.* 20, 2925–2928. doi: 10.1029/93GL03054

Geyin, M., and Maurer, B. W. (2021). Evaluation of a cone penetration test thin-layer correction procedure in the context of global liquefaction model performance. *Eng. Geol.* 291, 106221. doi: 10.1016/j.enggeo.2021.106221

Gorgas, T. J., Wilkens, R. H., Fu, S. S., Frazer, L. N., Richardson, M. D., Briggs, K. B., et al. (2002). *In situ* acoustic and laboratory ultrasonic sound speed and attenuation measured in heterogeneous soft seabed sediments: eel river shelf, California. *Mar. Geol.* 182, 103–119. doi: 10.1016/S0025-3227(01)00230-4

Gutenberg, B. (1958). Microseisms. *Adv. Geophys.* 5, 53–92. doi: 10.1016/S0065-2687(08)60075-8

Hardin, B. O., and Drnevich, V. P. (1972). Shear modulus and damping in soils: design equations and curves. *J. Soil Mech. Found. Eng.* 98, 667–692. doi: 10.1061/JSFEAQ.0001760

Hasselmann, K. (1963). A statistical analysis of the generation of microseisms. *Rev. Geophys.* 1, 177–210. doi: 10.1029/RG001i002p00177

Hirst, T. J., and Richards, A. F. (1977). *In situ* pore-pressure measurement in Mississippi delta front sediments. *Mar. Geotech.* 2, 191–204. doi: 10.1080/10641197709379779

Holzer, T. L., Bennett, M. J., Ponti, D. J., and Tinsley, J. C. (1999). Liquefaction and soil failure during 1994 northridge earthquake. *J. Geotech. Geoenviron. Eng.* 125, 438–452. doi: 10.1061/(ASCE)1090-0241(1999)125:6(438

Hou, Z., Chen, Z., Wang, J., Zheng, X., Yan, W., Tian, Y., et al. (2018). Acoustic characteristics of seafloor sediments in the abyssal areas of the south China Sea. *Ocean Eng.* 156, 93–100. doi: 10.1016/j.oceaneng.2018.03.013

Jeng, D. S. (2001). Mechanism of the wave-induced seabed instability in the vicinity of a breakwater: a review. *Ocean Eng.* 28, 537–570. doi: 10.1016/S0029-8018(00)00013-5

Jia, Y., Zheng, J., Yue, Z., Liu, X., and Shan, H. (2014). Tidal flat erosion of the huanghe river delta due to local changes in hydrodynamic conditions. *Acta Oceanol. Sin.* 33, 116–124. doi: 10.1007/s13131-014-0501-y

Joyner, W. B., Warrick, R. E., and Fumal, T. E. (1981). The effect of quaternary alluvium on strong ground motion in the coyote lake, California, earthquake of 1979. *Bull. Seismol. Soc Amer.* 71, 1333–1349. doi: 10.1785/BSSA0710041333

Kawase, H., Sanchez-Sesma, F., and Matsushima, S. (2011). The optimal use of horizontal-to-vertical spectral ratios of earthquake motions for velocity inversions based on diffuse-field theory for plane waves. *Bull. Seismol. Soc Amer.* 101, 2001–2014. doi: 10.1785/0120100263

Kumar, S. S., Murali Krishna, A., and Dey, A. (2020). Assessment of dynamic response of cohesionless soil using strain-controlled and stress-controlled cyclic triaxial tests. *Geotech. Geol. Eng.* 38, 1431–1450. doi: 10.1007/s10706-019-01100-y

Lin, A., Wotherspoon, L., Bradley, B., and Motha, J. (2021). Evaluation and modification of geospatial liquefaction models using land damage observational data from the 2010–2011 Canterbury earthquake sequence. *Eng. Geol.* 287, 106099. doi: 10.1016/j.enggeo.2021.106099

Liu, X., Jia, Y., Zheng, J., Hou, W., Zhang, L., Zhang, L.-P., et al. (2013). Experimental evidence of wave-induced inhomogeneity in the strength of silty seabed sediments: yellow river delta, China. *Ocean Eng.* 59, 120–128. doi: 10.1016/j.oceaneng.2012.12.003

Liu, X., Liu, H., and Jia, Y. (2007). Investigation on prediction methods and characteristics of earthquake-induced liquefaction of silty soil in the yellow river delta. *Chin. J. Rock Mech. Eng. (in Chinese).* 26, 2981–2987. doi: 10.3321/j.issn:1000-6915.2007.z1.060

Liu, F., Liu, L., and Liu, J. (2015). Characteristic analysis of shear wave velocity of the yellow river delta. *China Eng. Consult. (in Chinese)* 10, 90–93. doi: 10.3969/j.issn.1006-9607.2015.10.017

Liu, H., Wang, X., Jia, Y., Qiao, S., and Zhang, H. (2005). Experimental study on liquefaction properties and pore-water pressure model of saturated silt in yellow river delta. *Rock Soil Mech. (in Chinese).* 26, 83–87. doi: 10.16285/j.rsm.2005.s2.046

Liu, X., Wang, Y., Zhang, H., and Guo, X. (2023). Susceptibility of typical marine geological disasters: an overview. *Geoenviron. Disasters* 10, 10. doi: 10.1186/s40677-023-00237-6

Meng, Q., Li, Y., Wang, W., Chen, Y., and Wang, S. (2023). A case study assessing the liquefaction hazards of silt sediments based on the horizontal-to-vertical spectral ratio method. *J. Mar. Sci. Eng.* 11, 104. doi: 10.3390/jmse11010104

Meng, Q., Liu, S., Jia, Y., Xiao, Z., and Wang, X. (2018). Analysis on acoustic velocity characteristics of sediments in the northern slope of the south China Sea. *Bull. Eng. Geol. Environ.* 77, 923–930. doi: 10.1007/s10064-017-1070-z

Nakamura, Y. (1989). A method for dynamic characteristics estimation of subsurface using microtremor on the ground surface. *Q. Rep. RTRI.* 30 (1), 25–33.

Nakamura, Y. (2000). Clear identification of fundamental idea of nakamura's technique and its applications. *Proc. XII World Conf. Earthquake Eng.* 3, 2656.

Nakamura, Y. (2008). On the H/V spectrum. In The 14th Word Conference on Earthquake Engineering, Beijing, China. 12–17.

Nakamura, Y. (2009). "Basic structure of QTS (HVSR) and examples of applications," in *Increasing seismic safety by combining engineering technologies and seismological data NATO science for peace and security series c: environmental security*. Eds. M. Mucciarelli, M. Herak and J. Cassidy (Dordrecht: Springer Netherlands), 33–51. doi: 10.1007/978-1-4020-9196-4_4

Nakamura, Y. (2019). What is the Nakamura method? *Seismol. Res. Lett.* 90, 1437–1443. doi: 10.1785/0220180376

Olofsson, B. (2010). Marine ambient seismic noise in the frequency range 1-10 Hz. *Lead. Edge* 29, 418–435. doi: 10.1190/1.3378306

Qin, L., Ben-Zion, Y., Bonilla, L. F., and Steidl, J. H. (2020). Imaging and monitoring temporal changes of shallow seismic velocities at the garner valley near anza, California, following the M7.2 2010 El mayor-cucapah earthquake. *J. Geophys. Res. Solid Earth* 125, e2019JB018070. doi: 10.1029/2019JB018070

Ren, Y., Xu, G., Xu, X., Zhao, T., and Wang, X. (2020). The initial wave induced failure of silty seabed: liquefaction or shear failure. *Ocean Eng.* 200, 106990. doi: 10.1016/j.oceaneng.2020.106990

Sassa, S., Takayama, T., Mizutani, M., and Tsujio, D. (2006). Field observations of the build-up and dissipation of residual pore pressures in seabed sands under the passage of storm waves. *J. Coast. Res.* 39, 410–414. doi: 10.1007/s00367-020-00680-6

Seed, H. B., Idriss, I. M., and Arango, I. (1983). Evaluation of liquefaction potential using field performance data. *J. Geotech. Eng.* 109, 458–482. doi: 10.1061/(ASCE)0733-9410(1983)109:3(458

Sumer, B. (2014). Advances in seabed liquefaction and its implications for marine structures. *Geotech. Eng.* 45, 1–14. doi: 10.1007/s40722-014-0005-z

Sumer, B. M., Fredsøe, J., Christensen, S., and Lind, M. T. (1999). Sinking/floatation of pipelines and other objects in liquefied soil under waves. *Coast. Eng.* 38, 53–90. doi: 10.1016/S0378-3839(99)00024-1

Tokimatsu, K., and Uchida, A. (1990). Correlation between liquefaction resistance and shear wave velocity. *Soils Found.* 30, 33–42. doi: 10.3208/sandf1972.30.2_33

Toksoz, M. N. (1964). Microseisms and an attempted application to exploration. *Geophysics* 29, 154–177. doi: 10.1190/1.1439344

Tsai, N. C., and Housner, G. W. (1970). Calculation of surface motions of a layered half-space. *Bull. Seismol. Soc Amer.* 60, 1625–1651. doi: 10.1785/BSSA0600051625

Wang, Y., Cao, T., Gao, Y., and Shao, J. (2022). Experimental study on liquefaction characteristics of saturated yellow river silt under cycles loading. *Soil Dyn. Earthq. Eng.* 163, 107457. doi: 10.1016/j.soildyn.2022.107457

Xu, X., Ling, D., Cheng, Y., and Chen, Y. (2015). Correlation between liquefaction resistance and shear wave velocity of granular soils: a micromechanical perspective. *Géotechnique* 65, 337–348. doi: 10.1680/geot.SIP.15.P.022

Yang, Z., Cui, Y., Guo, L., Liu, X., Jia, C., Shi, W., et al. (2022). Semi-empirical correlation of shear wave velocity prediction in the yellow river delta based on CPT. *Mar. Geores. Geotechnol.* 40, 487–499. doi: 10.1080/1064119X.2021.1913458

Ye, B., Hu, H., Bao, X., and Lu, P. (2018). Reliquefaction behavior of sand and its mesoscopic mechanism. *Soil Dyn. Earthq. Eng.* 114, 12–21. doi: 10.1016/j.soildyn.2018.06.024

Ye, J., Jeng, D., Chan, A., Wang, R., and Zhu, Q. (2016). 3D integrated numerical model for fluid-structures-seabed interaction (FSSI): elastic dense seabed foundation. *Ocean Eng.* 115, 107–122. doi: 10.1016/j.oceaneng.2016.01.003

Youd, T. L., and Idriss, I. M. (2001). Liquefaction resistance of soils: summary report from the 1996 NCEER and 1998 NCEER/NSF workshops on evaluation of liquefaction resistance of soils. *J. Geotech. Geoenviron. Eng.* 127, 297–313. doi: 10.1061/(ASCE)1090-0241(2001)127:4(297

Yulianur, A., Saidi, T., Setiawan, B., Sugianto, S., and Rusdi, M. (2020). Microtremor measurement at liquefaction-induced ground deformation area. *J. Eng. Sci. Technol.* 15, 2871–2889. Available at: https://jestec.taylors.edu.my/Vol%2015%20issue%205%20October%202020/15_5_2.pdf

Zhang, H., Lu, Y., Liu, X., Li, X., Wang, Z., Ji, C., et al. (2023). Morphology and origin of liquefaction-related sediment failures on the yellow river subaqueous delta. *Mar. Pet. Geol.* 153, 106262. doi: 10.1016/j.marpetgeo.2023.106262

Zhang, Q., Zhou, X., Wang, J., and Guo, J. (2017). Wave-induced seabed response around an offshore pile foundation platform. *Ocean Eng.* 130, 567–582. doi: 10.1016/j.oceaneng.2016.12.016

Zhao, H., and Jeng, D. (2015). Numerical study of wave-induced soil response in a sloping seabed in the vicinity of a breakwater. *Appl. Ocean Res.* 51, 204–221. doi: 10.1016/j.apor.2015.04.008

Zhao, H., Jeng, D., Liao, C., Zhang, J., Guo, Z., and Chen, W. (2018). Numerical modelling of liquefaction in loose sand deposits subjected to ocean waves. *Appl. Ocean Res.* 73, 27–41. doi: 10.1016/j.apor.2018.01.011

Zhao, G., Te, Q., Xue, C., Ma, Y., and Ye, S. (2013). Surface sediments, sedimentary subenvironments and shoreline evolution of modern yellow river delta. *Mar. Geol. Quater. Geol. (in Chinese).* 33, 47–52. doi: 10.3724/SP.J.1140.2013.05047

Zhou, X., Jeng, D., Yan, Y., and Wang, J. (2013). Wave-induced multi-layered seabed response around a buried pipeline. *Ocean Eng.* 72, 195–208. doi: 10.1016/j.oceaneng.2013.06.031

frontiers | Frontiers in Marine Science

TYPE Original Research
PUBLISHED 05 July 2023
DOI 10.3389/fmars.2023.1212413

OPEN ACCESS

EDITED BY
Shengjie Rui,
Norwegian Geotechnical Institute (NGI), Norway

REVIEWED BY
Xun Zhang,
Southwest Jiaotong University, China
Yong Rui,
Ningbo University, China
Hang Xu,
Zhejiang University, China

*CORRESPONDENCE
Li Shi
lishi@zjut.edu.cn

RECEIVED 26 April 2023
ACCEPTED 19 June 2023
PUBLISHED 05 July 2023

CITATION
Zhu S, Tu X, Hu M, Shi L and Zhou L (2023) Field investigation on the impact of vehicle traffic on the vibration of ancient seawalls in Qiantang River.
Front. Mar. Sci. 10:1212413.
doi: 10.3389/fmars.2023.1212413

Field investigation on the impact of vehicle traffic on the vibration of ancient seawalls in Qiantang River

Shenming Zhu[1], Xiaobing Tu[2], Min Hu[2], Li Shi[3]* and Lei Zhou[2]

[1]Zhejiang Qiantang River Basin Centre, Hangzhou, Zhejiang, China, [2]Huadong Engineering Corporation Limited, Hangzhou, Zhejiang, China, [3]College of Civil Engineering, Zhejiang University of Technology, Hangzhou, Zhejiang, China

To investigate the vibrational impact of vehicular traffic on the ancient Qiantang River seawall, on-site measurements of the seawall's pulsation and forced vibrations under different vehicle speeds and axle loads were conducted. The acquired data were analyzed in the time domain, frequency domain, and 1/3 octave bands, revealing the time-frequency vibrational characteristics of the ancient seawall structure. The results indicate that the characteristic frequencies of the ancient seawall are 3 Hz and 10 Hz, with the primary frequency band of the structural vibrations induced by vehicular traffic ranging from 0 to 30 Hz. Vehicle traffic primarily caused vertical vibrations in the seawall structure, with along-dike horizontal vibrations being significantly higher than cross-dike vibrations. Based on the measurement results, an empirical relationship between the peak vibration velocity of the ancient seawall and variations in vehicle speed and axle load was established. It was found that, compared to axle load, increased vehicle speed had a more pronounced amplification effect on the structural vibrations of the ancient seawall. To ensure the vibrational safety of the ancient seawall relics, maximum vehicle speeds for different loading conditions of tri-axle trucks were provided based on vibration limits: for an axle load of 10 t, speeds should be below 34 km/h; for 11.52 t, below 24 km/h; for 13.04 t, below 20 km/h; and for 14.56 t, below 15 km/h.

KEYWORDS

vehicle traffic, ancient seawall, vibration, field measurement, time-domain analysis, frequency-domain analysis

1 Introduction

The ancient Qiantang River seawall, located on the northern bank of the Qiantang River estuary, serves as a crucial barrier against natural disasters such as tidal bores, typhoon storm surges, and floods. Initially constructed during the Ming and Qing dynasties, the ancient seawall has been designated as a national cultural relic protection unit and is among the few national relics still in service. Given the exceptional historical

and cultural value of national cultural relics and the difficulty in restoring them when damaged, both domestic and international standards impose strict protection requirements for these relics. For instance, China's "Technical specifications for protection of historic buildings against man-made vibration" (GB/T 50452-2008, 2008) prescribes stringent vibration response limits for cultural relics made of different materials and constructed using various masonry techniques. The ancient Qiantang River seawall essentially comprises a stone retaining wall, with block stones laid in layers using glutinous rice mortar and gradually tapering to form a trapezoidal cross-section. Factors such as the non-uniform cross-sectional shape, the staggered masonry technique, and the differences in the material properties of block stones and mortar render the vibrational response of the ancient seawall structure highly complex.

With rapid urban development, existing cultural relics, such as bell towers, pagodas, and temples made of brick and stone structures, inevitably experience vibrational disturbances from nearby traffic (Vogiatzis, 2000; Ma et al., 2016; Alan and Caliskan, 2017), blasting (Pal Roy et al., 2016; Xiong et al., 2020), and construction (Jiang et al., 2012; Fan et al., 2018). External vibration sources can induce vibrational waves within the structures of cultural relics, with the fundamental cause of material deterioration or even structural damage being dynamic strain (γ_d). However, directly measuring dynamic strain is challenging, and thus current domestic and international cultural relic protection standards often adopt vibration velocity ($[v]$) as an indirect control indicator (an empirical relationship exists between dynamic strain and vibration velocity: $\gamma_d \approx [v]/c$, where c is the vibration wave propagation speed within the cultural relic structure). It is evident that different structural and material types of cultural relics have distinct wave speeds (c), and consequently, different vibration velocity limits ($[v]$).

In light of the complexity of cultural relic structures and materials, it is difficult to predict the vibration levels of these structures using theoretical formulas when external excitation sources, such as construction vibrations and moving vehicles, are present. Existing research predominantly employs numerical simulations (Zhao et al., 2013; Sadeghi and Esmaeili, 2017; Ma et al., 2018) and on-site measurements (Meng et al., 2009; Hinzen, 2014) to analyze the vibrational impacts of subway trains on ancient city towers (Xin et al., 2019), bell towers (De Angelis et al., 2022), and other brick and stone cultural relic structures. Ma et al., 2011 established a train-track coupling model and a 3D coupled finite element model of the tunnel-soil-structure system to analyze the dynamic responses of monuments at different train speeds, finding that vibrations exceeded the limits when train speeds surpassed 58 km/h. Due to the passage of time and long-term weathering, cultural relics exhibit numerous uncertainties in architectural structure and material properties (Gentile and Saisi, 2007). To ensure the accuracy of brick and stone cultural relic numerical models, these models often require comparison and validation against on-site measurement results (Aras et al., 2011). Li et al., 2021 tested the dynamic responses of a pagoda under the influence of moving train loads and used the measured data to verify the accuracy of the finite element model of pagoda. Crispino, 2001 measured the vibration velocities of historical buildings under the influence of different vehicle types and speeds, using the data to validate the feasibility of the empirical prediction model of Watts (Watts, 1992).

In the field of traffic-induced environmental vibration control, existing researches primarily focused on vibration reduction measured along the propagation path, such as filled trenches (Cai et al., 2021), empty trenches (Yang et al., 2018), pile rows (Cheng et al., 2022), and wave barriers (Chen et al., 2022). Wang et al., 2022 optimized the design parameters of pile row vibration barriers using a 3D finite element model and found through field vibration tests that pile rows can reduce vibrations by approximately 30% to 50%. As the ancient seawall is a cultural relic structure, it is infeasible to construct vibration barriers, such as pile rows, between the road behind the seawall and the ancient seawall itself to protect its structural integrity. Instead, it may be worthwhile to consider controlling vehicle speed and axle load from the vibration source perspective to mitigate the vibrational impact on the ancient seawall structure caused by traffic behind the seawall.

With climate warming and sea-level rise, increasingly frequent and intense tidal bores pose a more severe challenge to the ancient seawall at the Qiantang River estuary. Currently, the ancient Qiantang River seawall is undergoing a upgradation to improve its flood protection from a 50-year recurrence interval to a 100-year recurrence interval. During the renovation period, the inevitable passage of construction vehicles behind the seawall will have a vibrational impact on the ancient seawall, posing a threat to the durability of cultural relic materials and structural safety. In response, this study conducts on-site measurements of the pulsation of the ancient seawall and its vibrational response under different construction vehicle speeds and loads. The time-domain extreme values and frequency-domain analyses of the test results are performed to analyze the characteristic frequencies of the ancient seawall. A quantitative relationship between the ancient seawall's time-domain vibration extreme values and axle loads and vehicle speeds is established, providing a scientific basis for proposing speed and axle load limits for construction vehicles traveling behind the seawall.

2 Basic information on the ancient seawall

As shown in Figure 1, the ancient seawall is located on the north bank of the Qiantang River estuary and is constructed as a vertical stone retaining wall. The seawall in the test area has a height of 5.44 m and a bottom width of 3.84 m. The seawall consists of 17 layers of masonry stones, narrowing progressively upward into a trapezoidal shape with a top width of 1.44 m. The seawall is constructed using 0.32 m thick and 0.38 m wide stone blocks arranged in a staggered manner with overlapping joints, as shown in Figures 2 and 3. The stones are bonded with glutinous rice mortar.

The foundation of the ancient seawall is clay, with 11 rows of wooden piles arranged within the foundation to support the seawall body. The area behind the seawall consists of soil backfill, with the top surface of the fill level with the top of the seawall. A concrete road is situated 8 meters behind the seawall and has a width of 4 meters. The road typically serves as a scenic patrol route, during construction, it is used as a construction route mainly for tri-axle

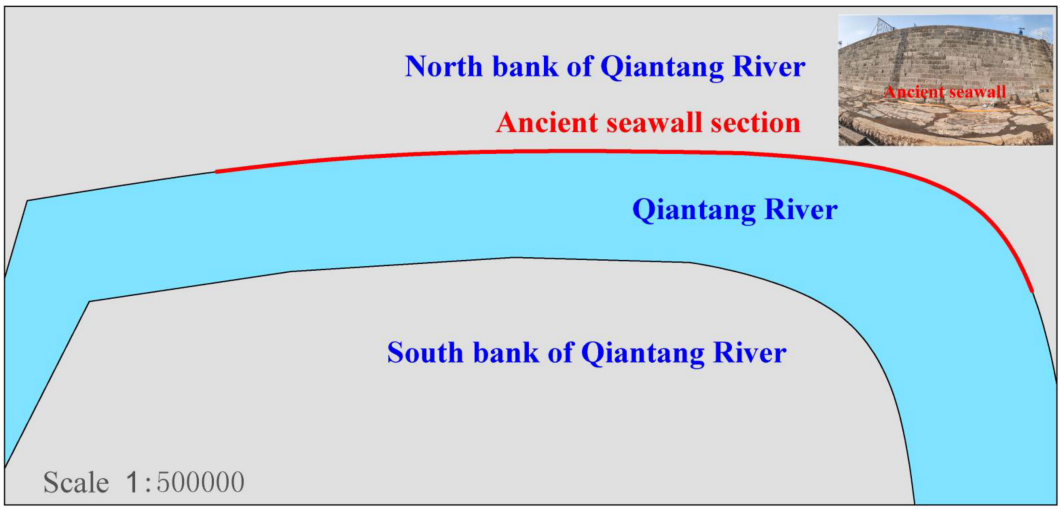

FIGURE 1
Schematic illustration of the ancient seawall cultural relics at the mouth of the Qiantang River and its north bank.

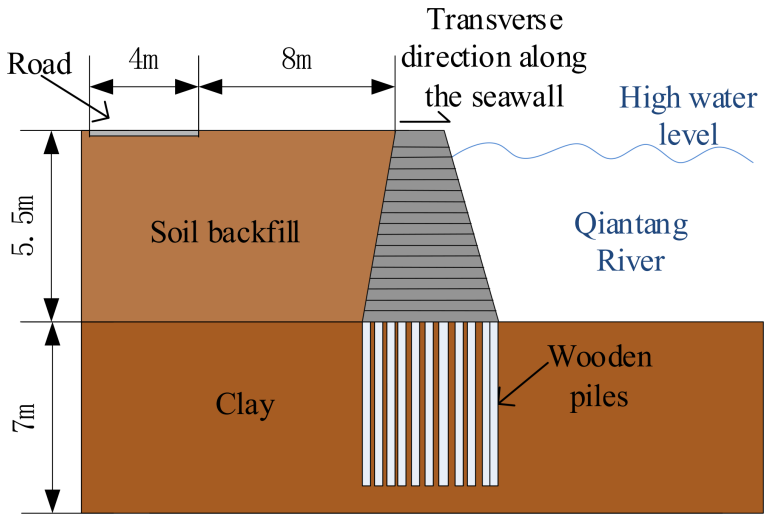

FIGURE 2
Schematic diagram of the ancient seawall at the Qiantang River estuary and nearby roads.

loader trucks and other construction vehicles. The physical and mechanical properties of the various soil layers are presented in Table 1. For the sake of clarity in subsequent descriptions, we define *X* as the transverse direction along the seawall, *Y* as the longitudinal direction along the seawall, and *Z* as the vertical direction.

3 Test plan

On-site vibration velocity measurements were taken using Donghua 2D001-type magneto-electric vibration sensors, with a sensitivity of 20 V·s/m and a frequency range of 1-100 Hz. Data was collected using the Donghua DH5922D dynamic signal test and analysis system (8 channels), with a sampling frequency of 500 Hz.

3.1 Pulsation test

The ambient vibration test of ancient seawall was conducted during construction breaks, with two horizontal and one vertical vibration velocity sensors placed at the top of the seawall. The sensors arrangement is shown in Figures 4 and 5, and the ambient vibration test duration was 10 minutes.

3.2 Vehicle-induced vibration test

A 100-meter test section was set up on the road behind the seawall, with tri-axle loader trucks controlled to travel at constant speed through the test section. Three-direction vibration velocity sensors

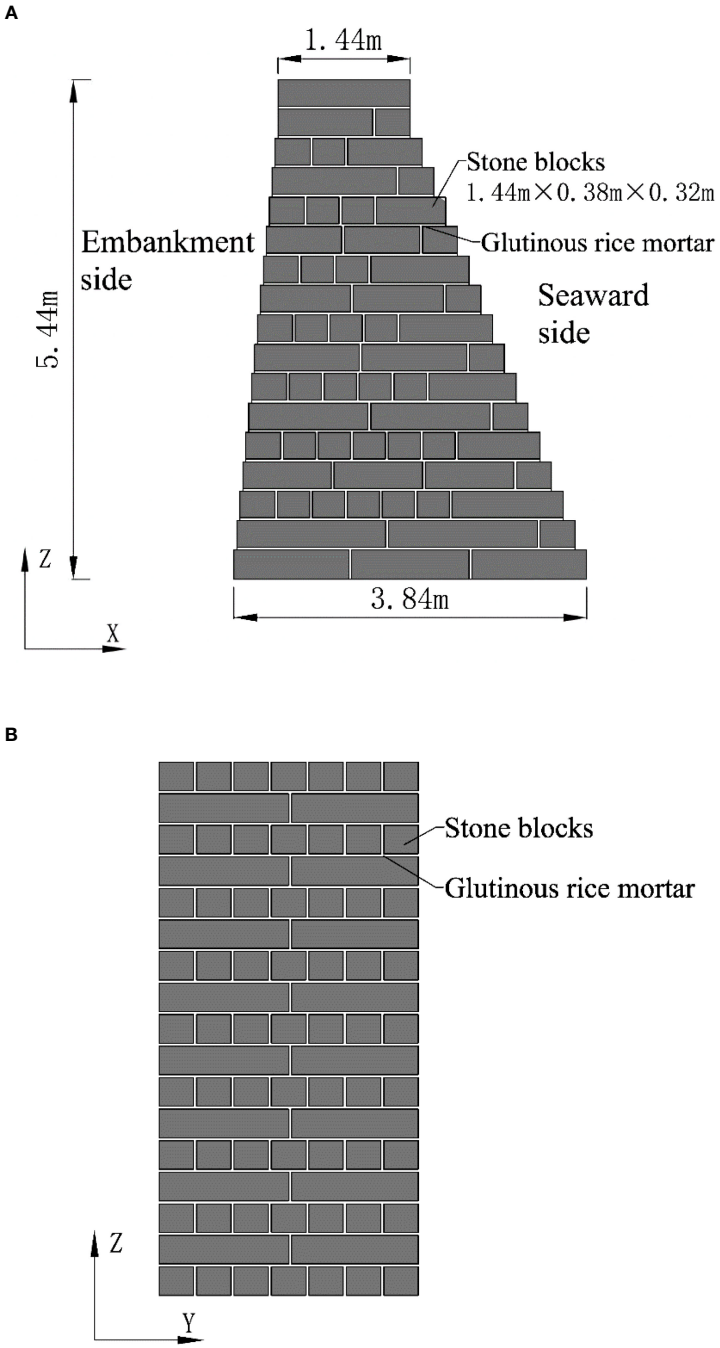

FIGURE 3
Schematic diagram of the ancient seawall masonry structure. **(A)** Cross-sectional view along the seawall. **(B)** Longitudinal sectional view along the seawall.

TABLE 1 Physical and mechanical properties of the soil layers behind the seawall.

Soil layer	Water content(%)	Density (kN/m^3)	Specific Gravity G_s	Void ratio e	Liquid limit W_L	Plastic limit W_P
Backfill soil	26.9	18.8	2.71	0.786	30.6	19.0
Clay	38.4	18.2	2.75	1.054	42.4	23.7

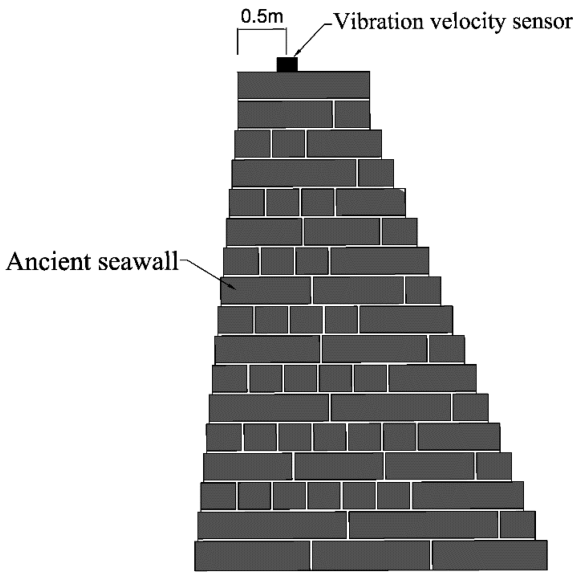

FIGURE 4
Schematic diagram of pulsation test vibration sensor arrangement.

were arranged at the midpoint of the road surface and at the top of the seawall, as shown in Figures 6 and 7. Field tests were mainly conducted under two conditions: axle load and vehicle speed.

3.2.1 Different axle load conditions

The main vehicle type traveling on the road behind the seawall is a tri-axle loader truck transporting concrete sheet piles, each weighing approximately 3.8 t. Considering three different conditions: empty vehicle, transporting 1 sheet pile, and transporting 3 sheet piles, the distribution of total vehicle weight and axle load for each condition is shown in Figures 8–10. The vehicle speed was controlled at 20 km/h and the travel route followed the centerline of the road.

3.2.2 Different vehicle speed conditions

An empty tri-axle loader truck was selected, with a total vehicle weight of 25 t and an axle load of 10 t. Vehicle speeds were controlled at 20 km/h, 40 km/h, and 60 km/h, with the travel route of vehicle following the centerline of the road.

4 Test results and analysis

4.1 Time-domain results

4.1.1 Pulsation

The three-directional ambient vibration time history curve of the ancient seawall structure under natural vibration conditions is shown in Figure 11. As seen in the figure, the overall changes in the three-directional vibration velocity of the ancient seawall are relatively stable. The peak values of the three-directional ambient vibration of the ancient seawall structure are shown in Table 2, indicating that the vertical vibration is the most significant, with a peak value of 0.0237 mm/s, which is 1.58 and 1.29 times the horizontal *X* and *Y* directions, respectively.

4.1.2 Different axle load conditions

The time history curves of vertical vibration velocity (*Z*) and horizontal vibration velocity (*X*, *Y*) of the ancient seawall under different axle load conditions are shown in Figure 12. The overall forced vibration changes of the ancient seawall structure caused by the vehicles are consistent, and the three-directional vibration velocity of the ancient seawall structure increases as the vehicle approaches, with the vertical direction showing the most significant increase. As the axle load of the vehicle increases, the three-directional vibration velocity of the ancient seawall structure also increases. The peak values of the three-directional vibration velocity of the ancient seawall structure under different axle load conditions are shown in Table 3. As can be seen from the table, the vertical direction is the dominant direction of vehicle-induced vibration for the ancient seawall, with the peak vibration velocity reaching 7.02 and 2.79 times the horizontal *X* (cross-dike direction) and *Y* directions (along-dike direction), respectively.

As shown in Figure 13, the peak values of the three-directional vibration velocity of the ancient seawall structure basically increase

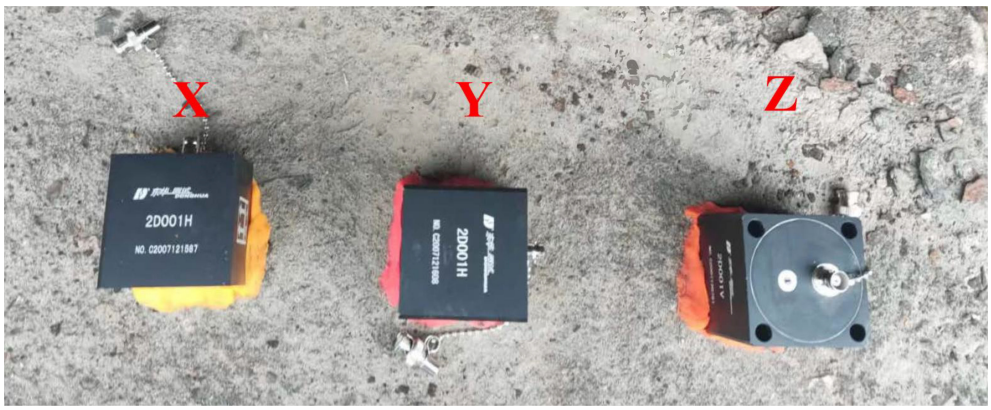

FIGURE 5
Physical layout of pulsation test vibration sensors.

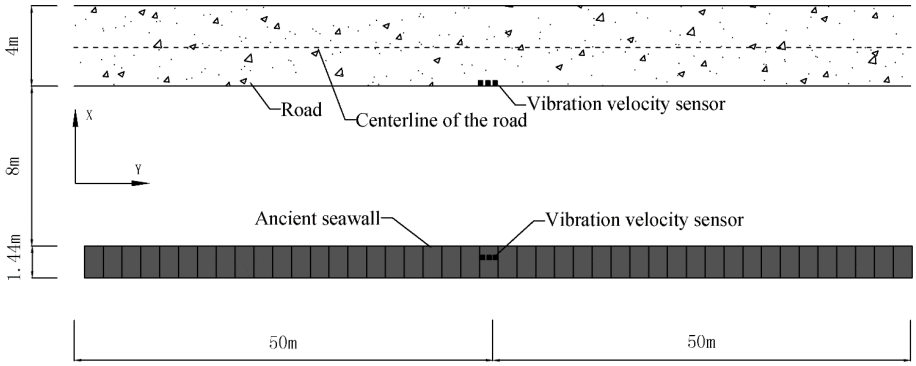

FIGURE 6
Schematic diagram of the vehicle-induced vibration test section plan.

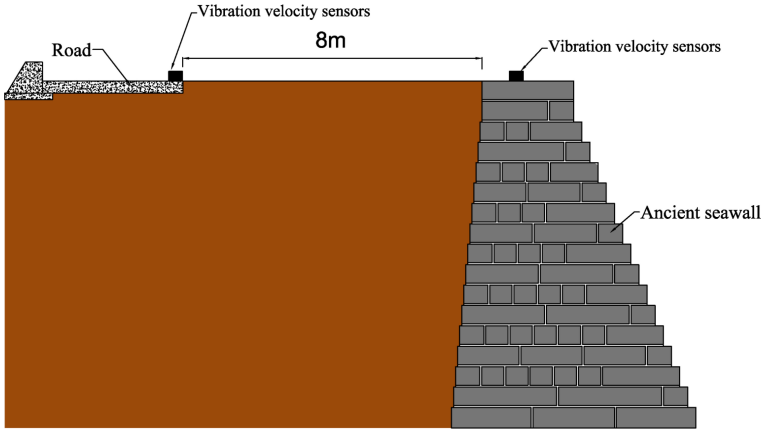

FIGURE 7
Schematic diagram of vehicle-induced vibration test points.

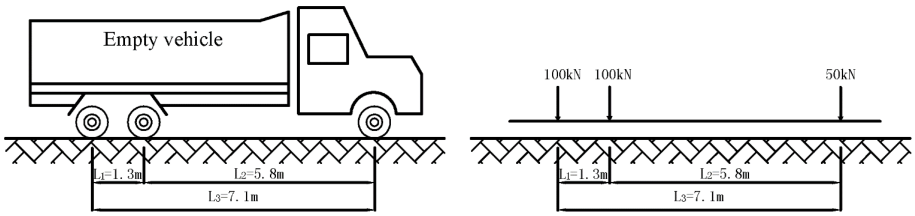

FIGURE 8
Total weight 25t, axle load 10t.

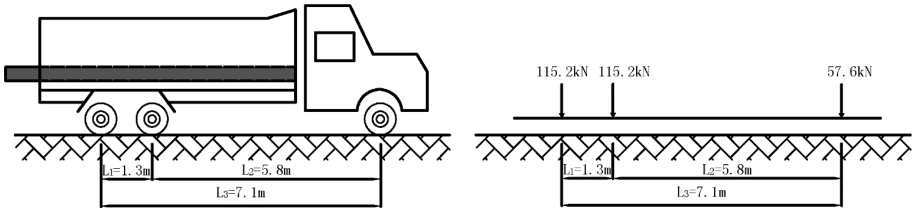

FIGURE 9
Total weight 28.8t, axle load 11.52t.

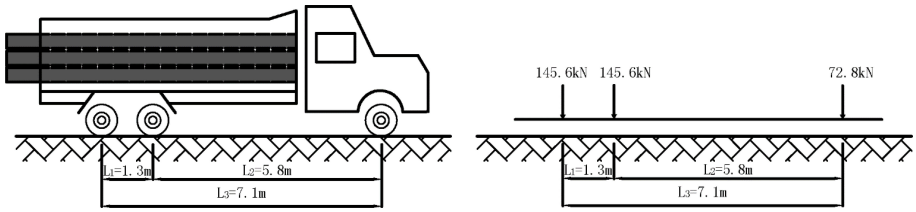

FIGURE 10
Total weight 36.4t, axle load 14.56t.

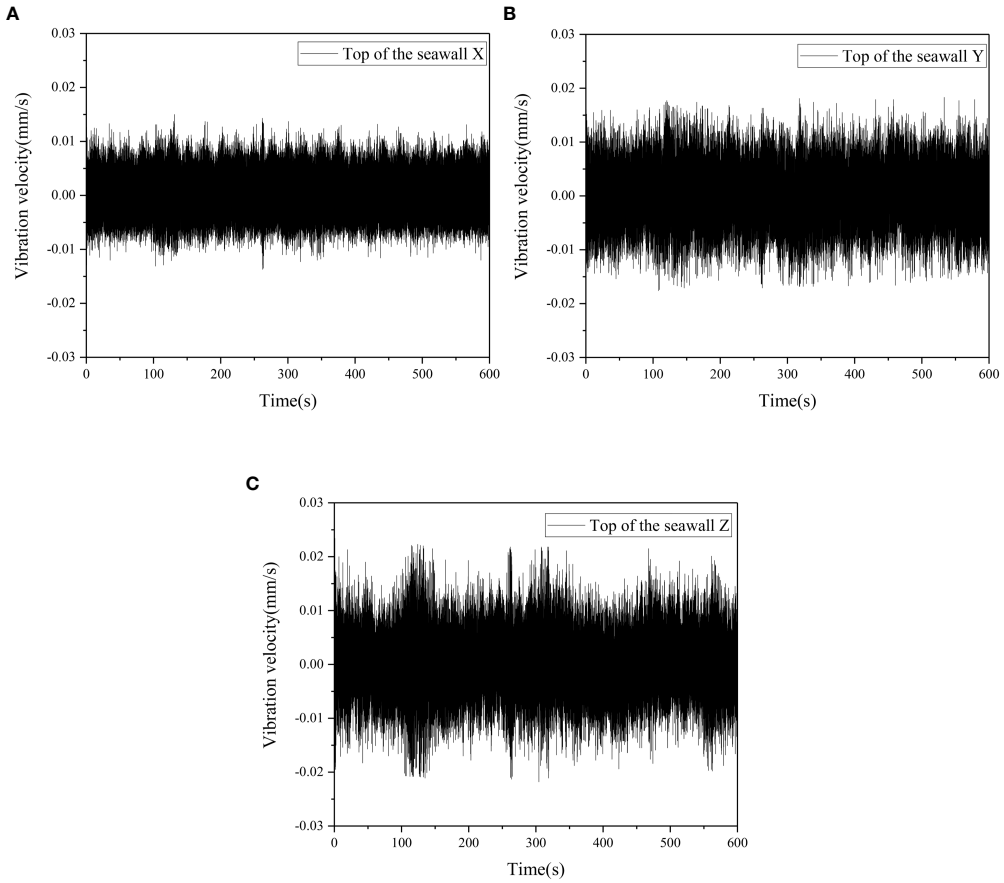

FIGURE 11
Pulsation time-history curves. **(A)** Horizontal direction *X*. **(B)** Horizontal direction *Y*. **(C)** Vertical direction *Z*.

TABLE 2 Peak values of three-directional ambient vibration velocity.

Direction	Peak value of vibration velocity (mm/s)
X	0.0150
Y	0.0183
Z	0.0237

linearly with the increase of axle load. The figure presents the fitting equations between the peak values of the three-directional vibration velocity (V_x, V_y, and V_z) and axle load (W), which can be used to predict the three-directional vibration velocity of the ancient seawall structure under other axle load conditions.

4.1.3 Different vehicle speed conditions

The time history curves of vertical vibration velocity (Z) and horizontal vibration velocity (X, Y) of the ancient seawall under different vehicle speed conditions are shown in Figure 14. As seen in the figure, the three-directional vibration velocity of the ancient seawall increases as the vehicle approaches, with the vertical direction showing the most significant increase. As the vehicle speed increases, the three-directional vibration velocity of the ancient seawall structure also increases. The peak values of the three-directional vibration velocity of the ancient seawall structure under different vehicle speed conditions are shown in Table 4. As can be seen from the table, the vertical direction (Z-axis) is the

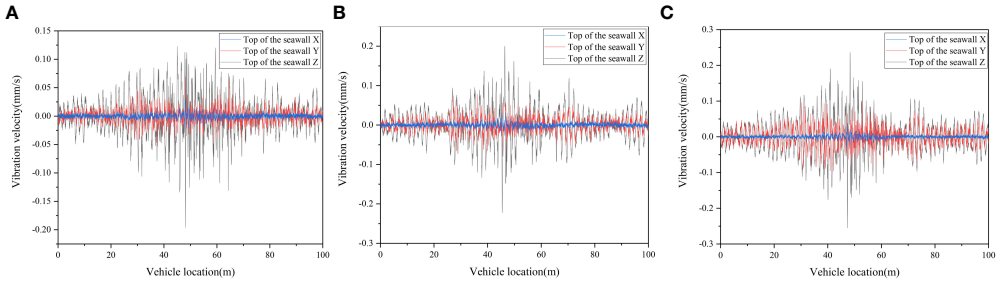

FIGURE 12
Time-domain curves of forced vibrations in ancient seawall structure under different axle load conditions. **(A)** Axle load 10t. **(B)** Axle load 11.52t. **(C)** Axle load 14.56t.

TABLE 3 Peak values of three-directional vibration velocity in ancient seawall under different axle load conditions.

Direction	Axle load		
	10t	11.52t	14.56t
X	0.0293	0.0313	0.0350
Y	0.0688	0.0778	0.0957
Z	0.1959	0.2224	0.2548

dominant direction of vehicle-induced vibration for the ancient seawall, with the peak vibration velocity reaching 7.88 and 2.52 times the horizontal *X* (cross-dike direction) and *Y* directions (along-dike direction), respectively.

As shown in Figure 15, the peak values of the three-directional vibration velocity of the ancient seawall structure basically increase linearly with the increase of vehicle speed. The figure presents the fitting equations between the peak values of the vibration velocity (V_x, V_y, and V_z) and vehicle speed (C), which can be used to predict the three-directional vibration velocity of the ancient seawall structure under other vehicle speed conditions.

From the above analysis, it can be concluded that the vibration response of the ancient seawall caused by vehicle passage is significantly larger than the pulsation response of the ancient seawall in its natural vibration state. Therefore, the vibration impact of vehicle passage on the ancient seawall heritage site cannot be ignored. When a vehicle passes, the three-directional vibration velocity of the ancient seawall structure increases, with the vertical direction being the dominant direction of vehicle-induced vibration and the vibration velocity being much larger than the horizontal direction. The peak vibration velocity of the ancient seawall caused by different vehicle speed conditions is larger than that caused by different axle load conditions, indicating that the ancient seawall vibration is more sensitive to vehicle speed.

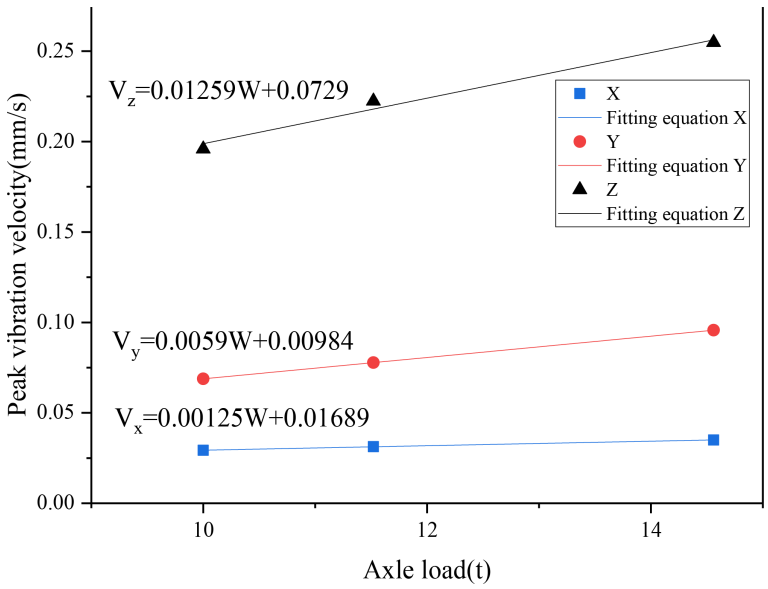

FIGURE 13
Fitting curves of peak three-directional vibration velocity in ancient seawall with respect to axle load changes.

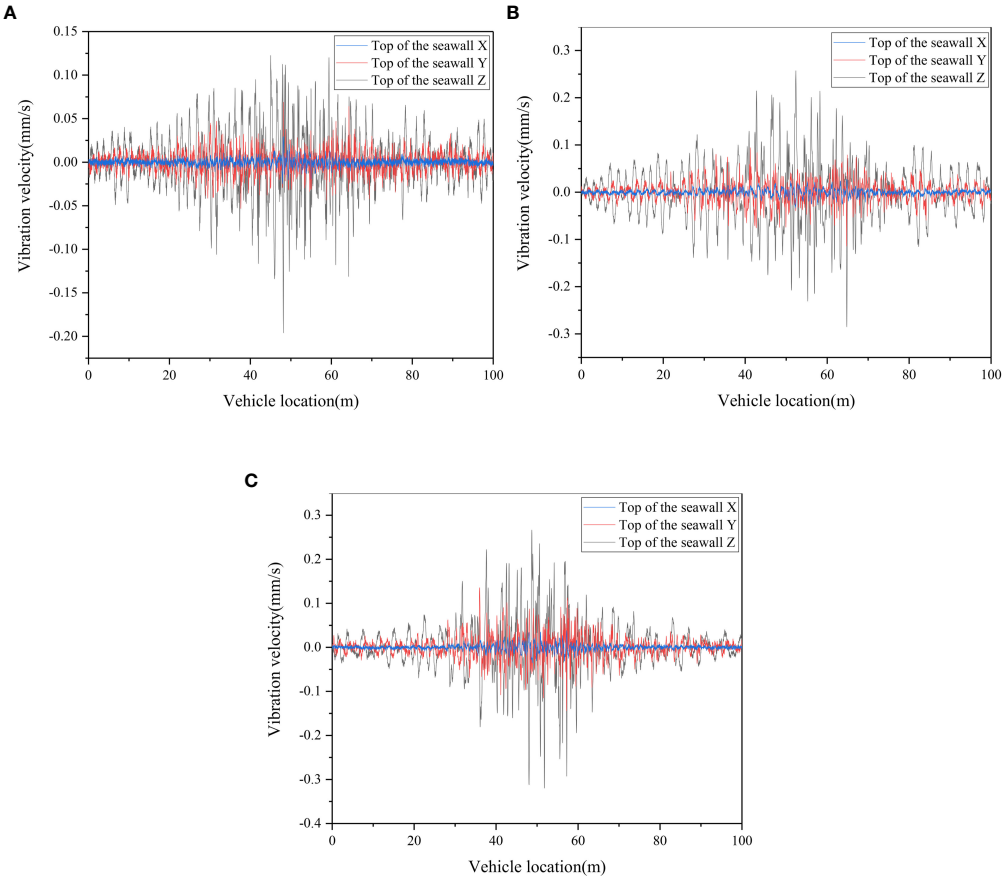

FIGURE 14
Forced vibration time history curves of ancient seawall under different vehicle speed conditions. **(A)** 20km/h. **(B)** 40km/h. **(C)** 60km/h.

TABLE 4 Peak three-directional vibration velocities of ancient seawall under different vehicle speed conditions.

Direction	Vehicle velocity		
	20km/h	40km/h	60km/h
X	0.0293	0.0333	0.0381
Y	0.0688	0.1143	0.1443
Z	0.1959	0.2850	0.3196

4.2 Frequency domain results

The pulsation results were subjected to a spectral analysis to obtain the pulsation spectrum curve shown in Figure 16. It can be seen that the pulsation frequencies of the ancient seawall in the horizontal *Y*-direction (along-dike) and vertical *Z*-direction are concentrated within 5 Hz, while the dominant frequency band of the horizontal *X*-direction pulsation is 0-15 Hz. The three-directional pulsations of the ancient seawall exhibit peaks near 3 Hz and 10Hz, indicating that 3 Hz is the first-order characteristic frequency of the ancient seawall, while 10 Hz is a higher-order characteristic frequency.

By selecting the axle load of 10 t and vehicle speed of 20 km/h condition and performing a spectral analysis on the time-domain results of the ancient seawall vibration, the typical spectrum curve of vehicle-induced vibration of the ancient seawall is obtained, as shown in Figure 17. As can be seen from the figure, the three-directional vehicle-induced vibrations of the ancient seawall are mainly concentrated within the 0-30 Hz frequency band, with high-frequency vibrations experiencing significant attenuation, and three-directional vibrations above 50 Hz are almost zero.

As the vehicle axles pass through the measuring point in sequence, they form a moving axle periodic excitation effect on the measuring point, with an excitation frequency of $f = C/L$, where L is the axle spacing. For the tri-axle loaded vehicle shown in Figure 8, there are three cases of axle spacing L, namely $L_1 = 1.3$ m, $L_2 = 5.8$ m, and $L_3 = 7.1$ m. The moving axle load excitation frequencies for different vehicle speeds are shown in Table 5.

As can be seen from Table 5, the moving axle load excitation frequencies f_1 and f_2 at $C = 20$ km/h are 4.27 Hz and 0.96 Hz, respectively. The contributions of moving axle periodic excitation frequency nf_1 (where n is a positive integer) can be seen in Figure 17, as indicated by the vertical lines at f_1, $2f_1$, and $3f_1$. It should be noted that Figure 17 does not show peaks exactly at nf_1, but rather on either side of it, which is the Doppler effect of the moving load. For example, the three-directional vibrations in

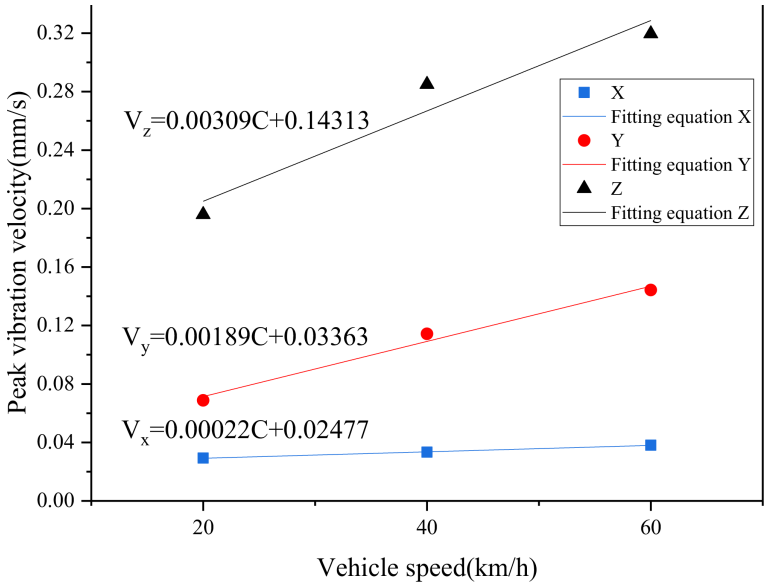

FIGURE 15
Fitting curves of peak three-directional vibration velocity in ancient seawall with respect to vehicle speed changes.

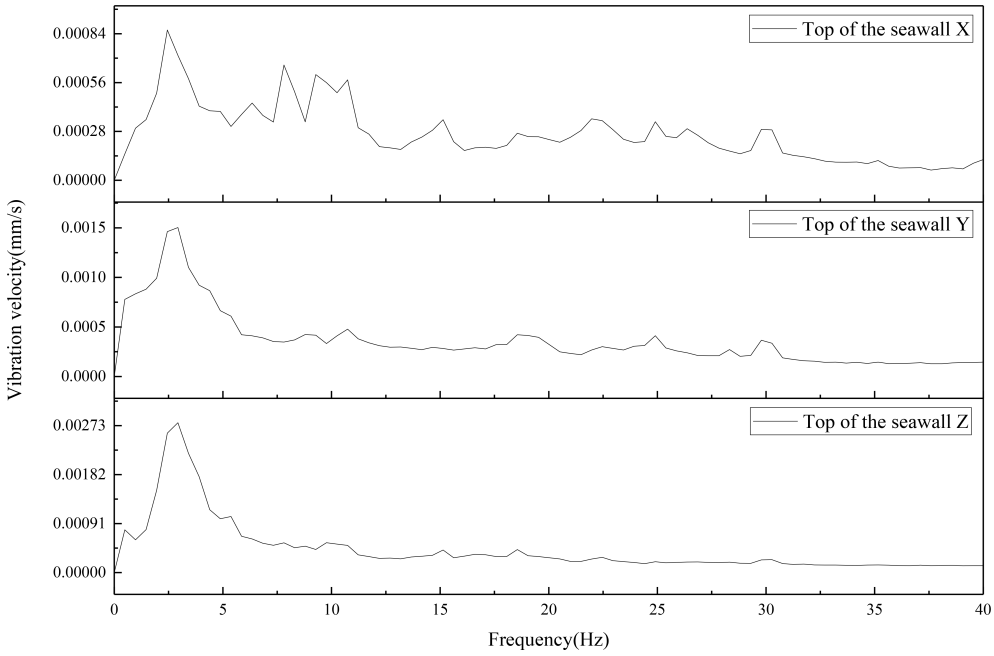

FIGURE 16
Ancient seawall pulsation spectrum curve.

Figure 17 exhibit peaks at 3.90 Hz to the left of f_1 and 4.39 Hz to the right. In addition, Figure 17 clearly shows the contributions of moving axle periodic excitation frequency nf_2, as indicated by the short vertical lines. In contrast to moving axle periodic excitation frequencies nf_1 and nf_2, the contribution of nf_3 is not evident, which may be due to the fact that this frequency is contributed by axles 1 and 3 of the loaded vehicle, which are furthest apart, making it difficult to cause periodic excitation.

Compared with conventional time-domain extreme value analysis and spectral curves, the 1/3 octave analysis can present the root mean square values of vibration signals in each frequency band, thus better characterizing the frequency and energy

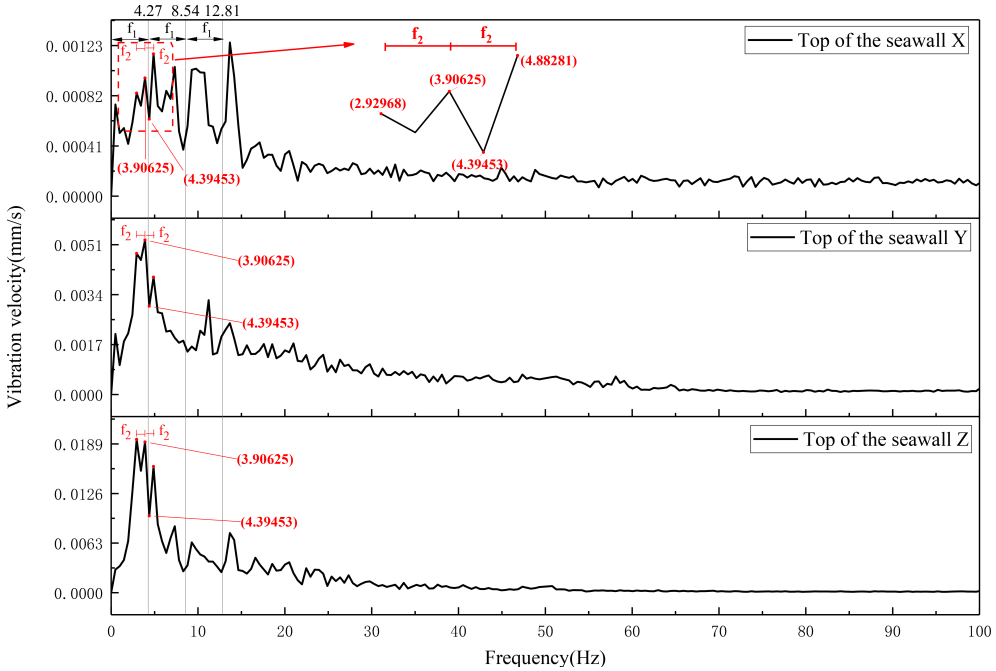

FIGURE 17
Typical frequency spectrum curve of vehicle-induced vibration in ancient seawall.

TABLE 5 Vehicle moving axle load excitation frequency *f*.

Vehicle velocity *C* (km/h)	$f_1=C/L_1$(Hz)	$f_2=C/L_2$(Hz)	$f_3=C/L_3$(Hz)
20	4.27	0.96	0.78
40	8.55	1.92	1.56
60	12.82	2.87	2.35

distribution characteristics of the vibration signal. According to the national standard (GB/T 3241-2010, 2010), the 0-100 Hz frequency range is divided into 21 frequency bands. The center frequencies of each band are as follows: 1, 1.25, 1.6, 2, 2.5, 3.15, 4, 5, 6.3, 8, 10, 12.5, 16, 20, 25, 31.5, 40, 50, 63, 80, and 100 Hz. The upper and lower limits of each frequency band are determined by multiplying and dividing the center frequency by the factor $2^{1/6}$, respectively.

4.2.1 One-third octave results for different axle load conditions

An analysis of the time domain results of forced vibrations under different axle load conditions using the 1/3 octave method is conducted, and the results are shown in Figure 18. It can be observed from the figure that the distribution pattern of the 1/3 octave band of the three-directional vibrations of the ancient seawall is not significantly affected by the changes in axle load. The peak values of the three-directional vibrations under different axle load conditions appear in both 3.15 Hz and 10 Hz frequency bands. The peak values of the horizontal *X*-directional vibration in these two frequency bands are similar, but the peak values of the vertical *Z*-direction and horizontal *Y*-direction vibrations at 3.15 Hz are noticeably higher than those in the 10 Hz band. Relative to the 3.15 Hz peak frequency band, the peak frequency band near 10 Hz is broader, essentially encompassing 8 Hz, 10 Hz, 12.5 Hz, and 16 Hz frequency bands. As previously mentioned, the characteristic frequencies of the ancient seawall are 3 Hz and 10 Hz, and by combining the data from Table 5, it can be concluded that the peak values in the 3.15 Hz and 10 Hz bands are caused by the resonance between the vehicle moving axle load excitation frequency and the characteristic frequency of the ancient seawall. For example, the peak in the 3.15 Hz band is rendered by coincidence of the excitation frequency nf2(n=3) and the first characteristic frequency of seawall (i.e. 3Hz).

The stress and deformation behaviors of brick material exhibit a significant frequency dependence (Lacanna et al., 2016), and existing vibration standards (GB 6722-2014, 2015) stipulate different vibration velocity limits according to different frequencies. In general, the higher the frequency, the higher the allowable vibration velocity. Therefore, it is necessary to derive a peak vibration velocity prediction formula for the dominant vibration frequency band of the ancient seawall. As shown in Figure 19, a fitting is conducted for the dominant frequency band (3.15 Hz) in the dominant direction (vertical *Z*-direction) of the structure induced by vehicle vibrations. The figure presents the fitting

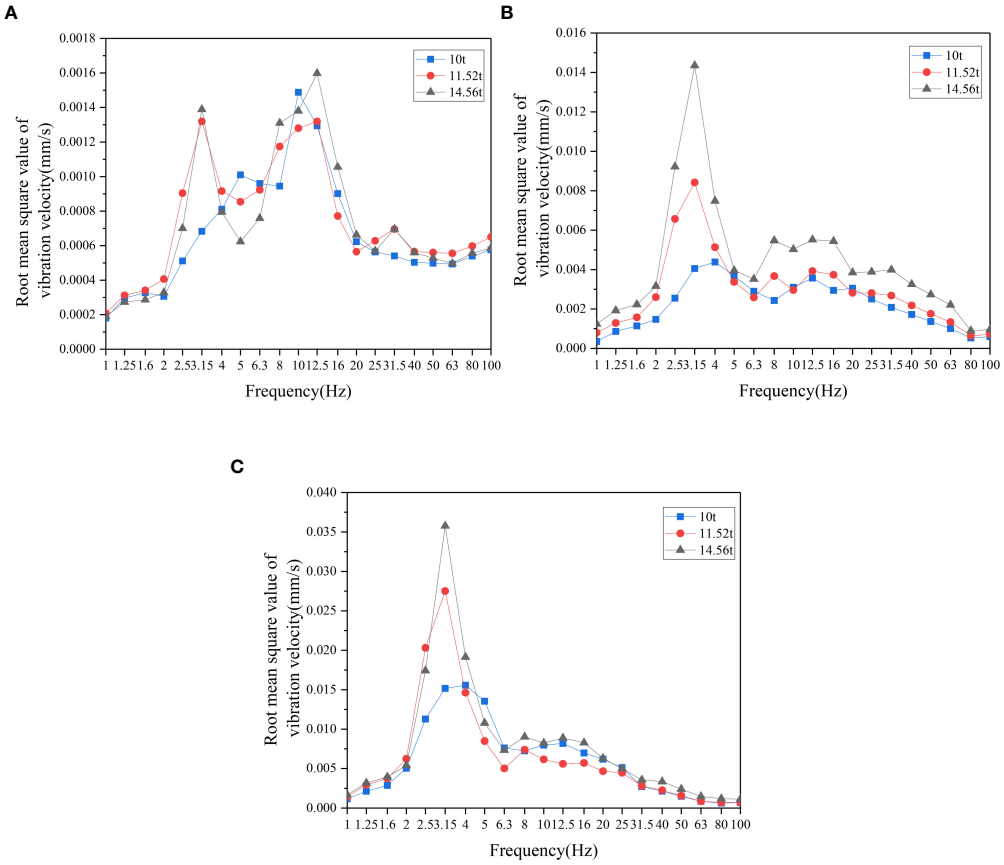

FIGURE 18
Forced vibration one-third octave curves of ancient seawall structure under different axle load conditions. **(A)** Horizontal direction *X*. **(B)** Horizontal direction *Y*. **(C)** Vertical direction *Z*.

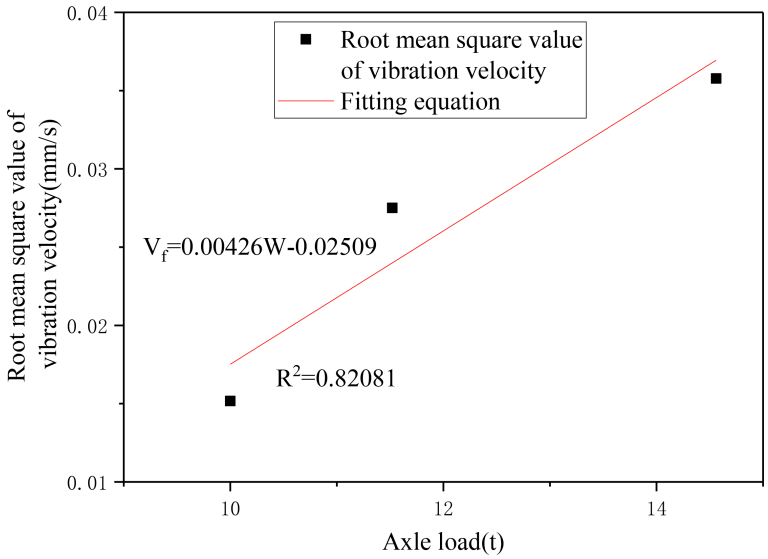

FIGURE 19
Fitting curve of the root mean square value of vertical vibration in the 3.15 Hz frequency band in ancient seawall with respect to axle load changes.

relationship between the root mean square value of vibration velocity (V_f) and axle load (W), which can be used to predict the root mean square value of vibration velocity in the vertical Z-direction of the ancient seawall structure at the 3.15 Hz frequency band under other axle load conditions.

4.2.2 One-third octave results for different vehicle speed conditions

An analysis of the time domain results of forced vibrations under different vehicle speed conditions using the 1/3 octave method is conducted, and the results are shown in Figure 20. As can be observed from the figure, the distribution pattern of the 1/3 octave band of the three-directional vibrations of the ancient seawall generally shifts to the right as the vehicle speed increases. The peak values of the three-directional vibrations under different vehicle speed conditions are mainly concentrated in the 0-10 Hz frequency band. In combination with Table 5, it can be seen that the vehicle moving axle load excitation frequencies (f_1) are 4.27 Hz, 8.55 Hz, and 12.82 Hz, as indicated by the vertical lines in Figure 20. Due to the Doppler effect of the moving load, peak values appear on both sides of f_1 in the 1/3 octave spectra for all three vehicle speed conditions.

Based on the above analysis, it can be concluded that the characteristic frequencies of the ancient seawall are 3 Hz and 10 Hz, and the overall change in the vibration response of the ancient seawall structure caused by vehicle passage behind the embankment is the same, with a general downward trend as the frequency increases. The three-directional vehicle-induced vibrations of the ancient seawall structure are mainly concentrated within the 0-30 Hz frequency band, with the high-frequency vibrations significantly attenuated and the three-directional vibrations virtually zero for frequencies greater than 50 Hz.

5 Analysis and discussion

The ancient seawall is a national-level protected site, and according to the current standard "Technical specifications for protection of historic buildings against man-made vibration ", considering the structure type, materials used, protection level, and the propagation speed of elastic waves in the ancient seawall structure, the allowable vibration limit value for the ancient seawall structure is 0.25 mm/s.

As can be seen from Tables 3, 4, the vertical vibration velocity peak values of the ancient seawall structure under the conditions of an axle

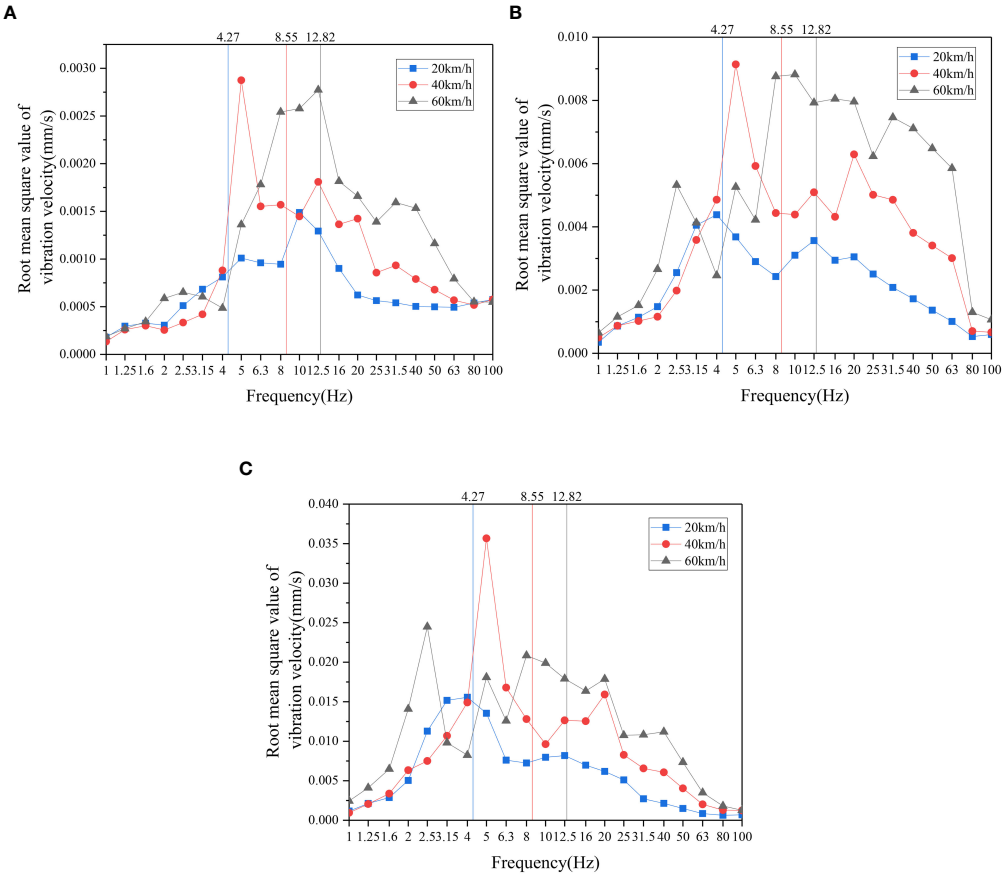

FIGURE 20
Forced vibration one-third octave curves of ancient seawall structure under different vehicle speed conditions. **(A)** Horizontal direction *X*. **(B)** Horizontal direction *Y*. **(C)** Vertical direction *Z*.

TABLE 6 Speed limits for different loading conditions of triaxial loaded vehicles.

Condition	Axle load (t)	Speed limit [C] (km/h)
Empty load	10	34
One sheet pile	11.52	24
Two sheet pile	13.04	20
Three sheet pile	14.56	15

load of 14.56 t and vehicle speeds of 40 km/h and 60 km/h would exceed the aforementioned allowable vibration limit value of 0.25 mm/s. Comparing the sensitivity of the ancient seawall structure's vibrations to vehicle speed and axle load, it can be concluded that controlling the speed of construction vehicles is an effective measure to reduce the vibration response of the ancient seawall. Specifically, based on the fitting curves from Figures 13 and 15, Table 6 presents the speed limits for tri-axle trucks under empty load and towing 1-3 sheet piles, ensuring the vibration safety of the ancient seawall cultural relics.

6 Conclusion

In this study, we conducted field measurements of the ancient seawall's vibrations and the vibration response of the ancient seawall under different construction vehicle speeds and loads. The test results were analyzed in terms of time-domain extremes and frequency-domain characteristics. The characteristic frequencies of the ancient seawall were investigated, leading to the following conclusions:

1. The vibration measurements showed that vehicle traffic primarily induced vertical vibrations in the ancient seawall structure.
2. The characteristic frequencies of the ancient seawall were 3 Hz and 10 Hz, and three-directional vibrations induced by vehicles were mainly concentrated in the 0-30 Hz frequency range. High-frequency vibrations exhibited severe attenuation, with three-directional vibrations virtually zero above 50 Hz.
3. Comparing the allowable vibration limits specified in the "Technical specifications for protection of historic buildings against man-made vibration, " it was evident that the vertical vibration velocity peaks of the ancient seawall structure induced by a 14.56-ton axle load and vehicle speeds of 40 km/h and 60 km/h exceeded the allowable vibration speed limits, posing risks to the structural integrity of the ancient seawall.
4. Empirical relationships between the time-domain maximum vibrations of the ancient seawall and axle load and vehicle speed were established based on the measurement results. Using the allowable vibration speeds proposed in the "Technical specifications for protection of historic buildings against man-made vibration " as limiting values, the maximum vehicle speeds under different load conditions for allowable vibration limits were calculated as follows: unloaded vehicles should not exceed 34 km/h, vehicles carrying one pile (3.8 t) should not exceed 24 km/h, vehicles carrying two piles (7.6 t) should not exceed 20 km/h, and vehicles carrying three piles (11.4 t) should not exceed 15 km/h.

Data availability statement

The original contributions presented in the study are included in the article/Supplementary Material. Further inquiries can be directed to the corresponding author.

Author contributions

Conceptualisation: LS, SZ and LZ. Methodology: XT, MH and LS. Formal analysis: LZ and XT. Writing—original draft preparation: LS, SZ, MH and XT. Data curation: SZ and MH. Writing—review and editing: LS, MH and LZ. All authors have read and agreed to the published version of the manuscript. All authors contributed to the article and approved the submitted version.

Funding

This study was supported by 2021 Zhejiang Provincial Water Resources Department Science and Technology Plan Project (RB2123).

Conflict of interest

Authors XT, MH, and LZ was employed by Huadong Engineering Corporation Limited.

The remaining authors declare that the research was conducted in the absence of any commercial or financial relationships that could be construed as a potential conflict of interest.

Publisher's note

References

Alan, S., and Caliskan, M. (2017). "Prediction of ground-borne vibrations on historical structures due to tram traffic in antalya, Turkey," in *Proceedings of Meetings on Acoustics*, Honolulu, Hawaii. (Acoustical Society of America), 065007. doi: 10.1121/2.0000555

Aras, F., Krstevska, L., Altay, G., and Tashkov, L. (2011). Experimental and numerical modal analyses of a historical masonry palace. *Construction Building Mater.* 25, 81–91. doi: 10.1016/j.conbuildmat.2010.06.054

Cai, C., Gao, L., He, X., Zou, Y., Yu, K., and Wu, D. (2021). The surface wave attenuation zone of periodic composite in-filled trenches and its isolation performance in train-induced ground vibration isolation. *Comput. Geotech.* 139, 104421. doi: 10.1016/j.compgeo.2021.104421

Chen, J., Geng, J., Gao, G., Luo, W., Liu, Y., and Li, K. (2022). Mitigation of subway-induced low-frequency vibrations using a wave impeding block. *Transportation Geotech.* 37, 100862. doi: 10.1016/j.trgeo.2022.100862

Cheng, G., Shan, Y., and Zhou, X. (2022). "Influence of metro vehicle operation on adjacent high-speed railway bridge pier," in *Advances in transportation geotechnics IV, lecture notes in civil engineering*. Eds. E. Tutumluer, S. Nazarian, I. Al-Qadi and I. I. A. Qamhia (Cham: Springer International Publishing), 963–974. doi: 10.1007/978-3-030-77238-3_72

Crispino, M. (2001). Measurement and prediction of traffic-induced vibrations in a heritage building. *J. Sound Vib.* 246 (2), 319–335. doi: 10.1006/jsvi.2001.3648

De Angelis, A., Lourenço, P. B., Sica, S., and Pecce, M. R. (2022). Influence of the ground on the structural identification of a bell-tower by ambient vibration testing. *Soil Dynamics Earthquake Eng.* 155, 107102. doi: 10.1016/j.soildyn.2021.107102

Fan, F., Chen, J., and Wang, J. (2018). Protection of historical buildings in metro line construction: a case study in shanghai, China. *J. Shanghai Jiaotong Univ. (Sci.)* 23, 490–504. doi: 10.1007/s12204-017-1883-8

GB/T 3241-2010. (2010). *Electroacoustics-octave-band and fractional-octave-band filters* (Beijing: Chinese Standards Press).

GB/T 50452-2008. (2008). *Technical specifications for protection of historic buildings against man-made vibration* (Beijing: China Architecture & Building Press).

GB 6722-2014. (2015). *The national standards compilation group of people's republic of China* (Beijing: Chinese Standard Press).

Gentile, C., and Saisi, A. (2007). Ambient vibration testing of historic masonry towers for structural identification and damage assessment. *Construction Building Mater.* 21, 1311–1321. doi: 10.1016/j.conbuildmat.2006.01.007

Hinzen, K.-G. (2014). Subway-induced vibrations in cologne cathedral. *Seismol. Res. Lett.* 85, 631–638. doi: 10.1785/0220140003

Jiang, Y., Wang, J., Fang, Y., Qi, C., and He, C. (2012). "Analysis of impact of shield tunnel construction on xi'an bell tower in loess strata, in: ICPTT 2012," in *ICPTT 2012: Better Pipeline Infrastructure for a Better Life*, Wuhan, China. (American Society of Civil Engineers), 1574–1584. doi: 10.1061/9780784412619.160

Lacanna, G., Ripepe, M., Marchetti, E., Coli, M., and Garzonio, C. A. (2016). Dynamic response of the baptistery of San Giovanni in Florence, Italy, based on ambient vibration test. *J. Cultural Heritage* 20, 632–640. doi: 10.1016/j.culher.2016.02.007

Li, M., Ma, M., Cao, Z., Xia, Q., and Liu, W. (2021). Dynamic response analysis of train-induced vibration impact on the probhutaratna pagoda in Beijing. *Earthq. Eng. Eng. Vib.* 20, 223–243. doi: 10.1007/s11803-021-2016-9

Ma, M., Cao, Y., Sun, X., and Liu, W. (2018). "Prediction of metro train-induced vibrations on a historic building: the case of the round city and chengguang hall in Beijing," in *Recent developments in railway track and transportation engineering, sustainable civil infrastructures*. Eds. J. Pombo and G. Jing (Cham: Springer International Publishing), 133–141.

Ma, M., Liu, W., Qian, C., Deng, G., and Li, Y. (2016). Study of the train-induced vibration impact on a historic bell tower above two spatially overlapping metro lines. *Soil Dynamics Earthquake Eng.* 81, 58–74. doi: 10.1016/j.soildyn.2015.11.007

Ma, M., Markine, V., Liu, W., Yuan, Y., and Zhang, F. (2011). Metro train-induced vibrations on historic buildings in chengdu, China. *J. Zhejiang Univ. Sci. A.* 12, 782–793. doi: 10.1631/jzus.A1100088

Meng, Z., Chang, Y., Song, L., and Yuan, J. (2009). "The effects of micro-vibration excited by traffic vehicles on xi'an bell tower, in: international conference on transportation engineering 2009," in *International Conference on Transportation Engineering 2009, Southwest Jiaotong University*, Chengdu, China. (American Society of Civil Engineers), 37–42. doi: 10.1061/41039(345)7

Pal Roy, P., Sawmliana, C., and Singh, R. K. (2016). Safety concerns of ancient temple due to blasting in adjacent mines. *Geotech. Geol. Eng.* 34, 901–909. doi: 10.1007/s10706-016-0013-y

Sadeghi, J., and Esmaeili, M. H. (2017). Safe distance of cultural and historical buildings from subway lines. *Soil Dynamics Earthquake Eng.* 96, 89–103. doi: 10.1016/j.soildyn.2017.02.008

Vogiatzis, C. (2000). 'Vibration at buildings of high cultural value from tbm operation at athens metro line: akademia - syntagma." in *Inter-noise and noise-con congress and conference proceedings*. (Institute of Noise Control Engineering).

Wang, H., Zhang, C., Jiang, J., Huang, W., Guo, D., and Sheng, T. (2022). Vibration characteristics and isolation in vibration-sensitive areas under moving vehicle load. *Soil Dynamics Earthquake Eng.* 153, 107077. doi: 10.1016/j.soildyn.2021.107077

Watts, G. R. (1992). The generation and propagation of vibration in various soils produced by the dynamic loading of road pavements. *J. Sound Vibration* 156, 191–206. doi: 10.1016/0022-460X(92)90692-Q

Xin, Y., Li, X., and Wang, J. (2019). "Risk analysis of the impact of metro construction activities on cultural relics," in *Proceedings of the Sixth Symposium of Risk Analysis and Risk Management in Western China (WRARM 2019)*, Kunming, China. (Atlantis Press), doi: 10.2991/wrarm-19.2019.39

Xiong, J., Si, J., and Zheng, Y. (2020). Analysis of controlled blasting for Large-span tunnel passing beneath cultural relics building. *IOP Conf. Ser.: Mater. Sci. Eng.* 741, 12105. doi: 10.1088/1757-899X/741/1/012105

Yang, W., Yuan, R., and Wang, J. (2018). Vibration induced by subway trains: open-trench mitigation analysis in the time and frequency domains. *Shock Vibration* 2018, 1–16. doi: 10.1155/2018/1879392

Zhao, T. F., Meng, Z. B., Jin, J., and Li, X. F. (2013). Dynamic response analysis of xi'an bell tower timber structure under the metro-vibration load of line 6. *AMM* 353–356, 1718–1723. doi: 10.4028/www.scientific.net/AMM.353-356.1718

frontiers | Frontiers in Marine Science

TYPE Original Research
PUBLISHED 20 July 2023
DOI 10.3389/fmars.2023.1213820

OPEN ACCESS

EDITED BY
Zhen Guo,
Zhejiang University, China

REVIEWED BY
Guoxiong Mei,
Guangxi University, China
Alfrendo Satyanaga,
Nazarbayev University, Kazakhstan

*CORRESPONDENCE
Zili He
hezili77@zjut.edu.cn

RECEIVED 28 April 2023
ACCEPTED 03 July 2023
PUBLISHED 20 July 2023

CITATION
Cai J, He Z, Xu B and Yu M (2023) The effect of PVD layout on the consolidation characteristics of dredged slurry under vacuum preloading.
Front. Mar. Sci. 10:1213820.
doi: 10.3389/fmars.2023.1213820

The effect of PVD layout on the consolidation characteristics of dredged slurry under vacuum preloading

Jing Cai[1], Zili He[2]*, Bin Xu[2] and Mengfei Yu[2]

[1]Institute of Underground Space, Zhejiang University of Technology Engineering Design Group Co., Ltd, Hangzhou, China, [2]College of Civil Engineering, Zhejiang University of Technology, Hangzhou, China

Vacuum preloading coupled with prefabricated vertical drains (PVDs) has been widely used to improve the property of the dredged slurry. However, the effect of PVD layout on slurry consolidation characteristics remains poorly understood. This study conducted two vacuum preloading model tests—with single and dual PVDs. Particle image velocimetry (PIV) was used to directly observe the slurry displacements and strain paths. The test results revealed that the slurry consolidation characteristics were similar under different PVD layouts in the early stage of vacuum preloading. However, in the mid-stage, the effect of dual PVDs led to a significant reduction and increased dispersion of the slurry horizontal displacement. This, in turn, resulted in a thinner clogging zone and a subsequent decrease in vacuum pressure loss. Consequently, the slurry near the PVDs experienced an extended period of consolidation deformation. During the later stage, the single PVD model test exhibited a distinct zone of both vertical and horizontal compression in the slurry, while under dual PVDs, the slurry primarily underwent vertical compression and horizontal extension. The study also provided the relationship between the clogging zone thickness and time, which provided a reference for theoretical consolidation calculations.

KEYWORDS

vacuum preloading, dredged slurry, particle image velocimetry, deformation, clogging

1 Introduction

The technique of vacuum preloading combined with prefabricated vertical drains (PVDs) was invented by Kjellman. It is one of the most common methods for treating hydraulic landfill and *in-situ* marine soils (Mesri and Khan, 2012; Cai et al., 2016; Cai et al., 2017; Geng and Yu, 2017; Wang et al., 2017a; Cai et al., 2018; Fang et al., 2019; Ni and Geng, 2022; Zhang et al., 2022). There is usually significant settlement and inward lateral displacement with this method (Chai et al., 2005; Robinson et al., 2012; Chai et al., 2020; Sun et al., 2022a; Sun et al., 2022b). Many studies have reported the displacement of slurry during the vacuum preloading process. Sun et al. (2022b) reported that the horizontal

displacement of slurry elements increases first and then decreases along the radial direction. Also, the slurry elements near the PVD exhibit horizontal extension prior to compression during the improvement of high-water-content slurry. Chai et al. (2020) found less settlement near the PVD in single-PVD model tests. Yao et al. (2023) observed the displacement of dredged slurry during air-boost vacuum preloading and indicated the pressurization induces soil cracking, thereby facilitating the consolidation of dredged slurry. Feng et al. (2022) monitored the surface settlement of the soil under air-boosted vacuum preloading and proposed a ground settlement prediction empirical formula based on a 2D continuum FE analysis. Wang et al. (2019) pointed out that the horizontal displacement of the soil at the midpoint between the two PVDs is zero. Pan et al. (2020) found that slurries near the PVD and in the far field are dominated by radial and vertical consolidation, respectively. These studies mainly focus on the soil deformation under vacuum preloading by means of model tests, finite element and *in-situ* tests, and the soil displacement patterns near the PVD or at the boundary of the consolidation zone are obtained. Since the soil displacement depends on the stress state (Chai et al., 2005), the deformation characteristics are also affected by the PVD layout. However, owing to a lack of data on the displacement and strain profile of slurry under different PVD layouts during consolidation, the effect of PVD layout on slurry deformation characteristics under vacuum preloading remains poorly understood.

In addition to the uncertainty regarding the effect of PVD layout on deformation characteristics, there is also a lack of research on the effect of PVD layout on the clogging zone. Numerous laboratory and *in-situ* tests have reported a low-permeability clogging zone occurred near the PVD during the vacuum preloading treating the dredged slurry, which demonstrates the prevention of vacuum pressure propagation as well as a slowing of pore water pressure dissipation, resulting in inadequate improvement (Tang et al., 2010; Bao et al., 2014; Deng et al., 2019; Sun et al., 2020; Xu et al., 2020; Wu et al., 2022). Many studies discussed the formation of soil columns and also proposed methods such as pretreating the slurry (Wang et al., 2017a; Wang et al., 2017b; Sun et al., 2022c), step vacuum preloading (Fang et al., 2019), and reducing PVD spacing (Tang et al., 2010; Wu et al., 2021) to reduce the clogging. In addition, Fang et al. (2019); Zhou et al. (2021); Sun et al. (2022a); Sun et al. (2022b), and Shen (2018) used particle size distribution, soil sample water content distribution, vane shear strength along the radial direction and particle image velocimetry (PIV) technology to determine the thickness of the clogging zone to be 40–100 mm under a single-PVD model test. As the formation of the clogging zone is the result of the accumulation of soil particles near PVD (Sun et al., 2022a; Sun et al., 2022b), with the gradual transfer of vacuum pressure from PVD to far field during consolidation, the effect of PVD layout on the displacement of soil particles will further impact the formation of the clogging zone. Compared with the extensive studies focused on the thickness of the clogging zone, few studies have investigated the clogging zone development, especially the development under different PVD layouts. Determining the development characteristics and differences in the slurry clogging zone under different PVD layouts can further improve the understanding of clogging zone development and provide a reference for developing consolidation theory that considers clogging zones.

In the past decade, particle image velocimetry (PIV), which is a non-intrusive method, has played an important role in experimental geomechanics. It can obtain the displacement of the soil as well as the strain paths occurring throughout the improvement process. Compared to traditional displacement measurement methods, PIV offers higher accuracy and the advantage of full-field measurement (White et al., 2003; White and Bolton, 2004; Wang et al., 2021). With the advancement of photography and algorithms, PIV technology has been more widely used in geotechnical tests, such as vacuum preloading model tests (Jiang et al., 2020; Sun et al., 2022a; Sun et al., 2022b), cone penetration tests (White and Bolton, 2004; Arshad et al., 2014) and undrained cyclic torsional shear tests (Zhao et al., 2020). These cases rely on an artificial texture when modelling fine-grained soils, which provides the basis for this research.

In this study, two laboratory model tests were carried out to investigate the effect of PVD layout on the consolidation characteristics of dredged slurry under vacuum preloading. The displacement field and strain profile during the improvement process were visualized using PIV technology. The effect of PVD layout on consolidation characteristics was investigated by combining PIV analysis with monitoring information, such as pore water pressure dissipation and water discharged mass data. The results provide a reference for developing consolidation theory that considers the clogging zone.

2 Experimental materials and methods

2.1 Testing materials

The dredged slurry used in this study was taken from a construction site in Dongtou District, Wenzhou City, Zhejiang Province, China. The properties of the slurry sample are listed in Table 1. The liquid and plastic limits of the slurry were 53% and 32%, respectively. The particle size distribution of the slurry is shown in Figure 1.

As the variation in pixel intensity is crucial in PIV analysis (White et al., 2003; Stanier and White, 2013; Stanier et al., 2016), tracer particles must be used to create artificial textures when performing geotechnical tests on fine-grained soils of uniform color (Take and Bolton, 2011; Kim et al., 2017). Black-dyed sand was used as tracer particles in this PIV analysis (Bauer et al., 2016; Kwak et al., 2020; Wang et al., 2021), which has been proven a good representativeness (>93%) in the movement of particles within the slurry (Wang et al., 2021). Since the tracer particles were randomly

TABLE 1 Index properties of slurry sample.

Initial water content, w_0 (%)	Plastic limit, w_P (%)	Liquid limit, w_L (%)	D_{50} (mm)	Specific gravity
113	32	53	5	2.68

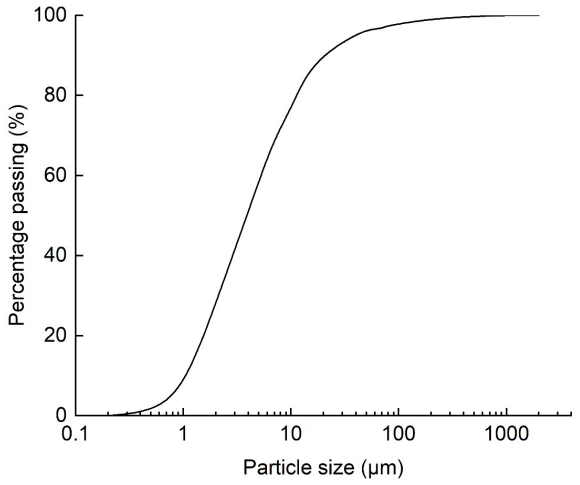

FIGURE 1
Particle size distribution of the slurry sample.

sprayed on the contact of the Perspex sheet and slurry sample, they had little effect on the slurry improvement process due to their small amount and high permeability (Wang et al., 2019). Moreover, as the PIV algorithm (Stanier et al., 2016) used in this study will update the new 'reference' image during the calculation process when the correlation coefficient for one of the subsets contravenes user-defined thresholds. Thus, a small amount of the tracer particles mixed into the slurry during the consolidation has no significant influence on the results.

The integral PVD used in this study had dimensions of 100 ± 3 mm (width) × 4 mm (thickness) × 310 mm (height). The tensile strength of the PVD was >2 kN/10 cm, the equivalent pore diameter was 75 μm, and the permeability coefficient was > 5×10^{-3} cm/s.

2.2 Testing apparatus

The testing apparatus consists of three parts: a model testing box, a vacuum system, and a data and image acquisition system.

As shown in Figure 2, a cuboid aluminium model testing box with an internal dimension of 870 mm (length) × 160 mm (width) × 620 mm (height) was made for the laboratory tests. Silicon grease was smeared onto the inner wall of the case to reduce the friction between the soil and the model walls (Sun et al., 2022b). The front wall of the testing box consisted of a Perspex window with a thickness of 45 mm, in which control points for optimizing the photogrammetric transformation parameters were set (White et al., 2003). To minimize friction between the Perspex window and slurry sample, the window was polished and then flanged to the testing box (Sun et al., 2022b). The top of the box was sealed with a polyvinyl chloride (PVC) membrane to ensure airtightness during vacuum preloading. The PVD was attached to the Perspex sheet and fixed to a custom-made iron bracket to prevent bending during the tests. Model tests with a single PVD and dual PVDs were carried out to compare the effects of PVD layout under vacuum preloading. In *in-situ* practice, the PVDs layout patterns commonly follow a square or triangular arrangement, with spacing ranging from 0.6–1.5 m (Chu et al., 2000; Tang and Shang, 2000; Bergado et al., 2002; Wang et al., 2019). Thus, the dual PVDs model test with a spacing of 0.6 m was conducted. The single-PVD model test was used to simulate the slurry under a large spacing between PVDs. The PVDs were connected to the vacuum system *via* a vacuum tube and geosynthetic cap. As shown in Figures 2C, D, the slurry displacements were tracked by PIV through observation windows 1 (OW1) and 2 (OW2; dimensions 300 × 180 mm) in the Perspex sheet on the right side of the PVD.

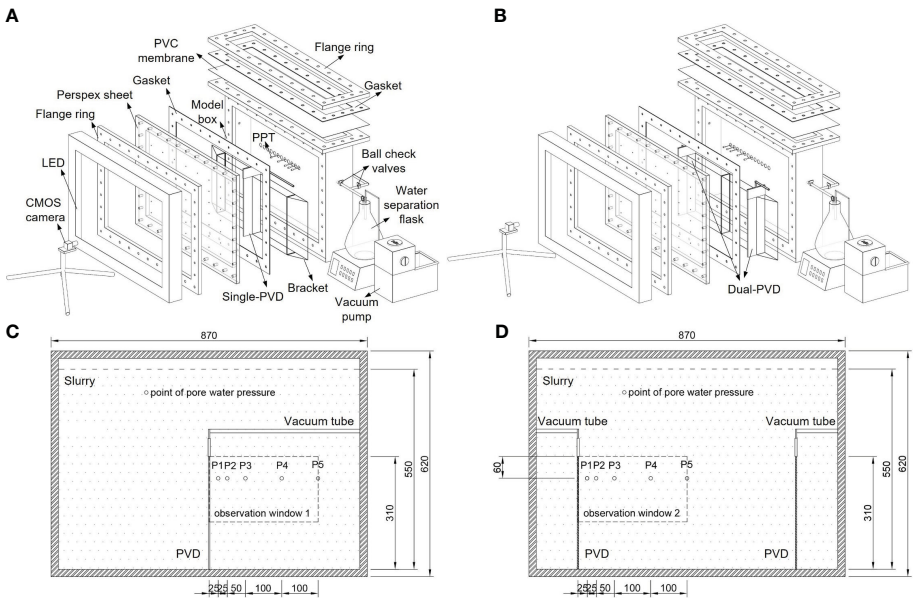

FIGURE 2
Testing apparatus. Exploded views of the **(A)** single-PVD and **(B)** dual-PVD model tests; schematic diagrams of the **(C)** single-PVD and **(D)** dual-PVD- model tests.

As shown in Figures 2A, B, the vacuum system was mainly composed of a vacuum pump, water separation bottle and vacuum tubes. The water separation bottle separated the airflow from the water flow. The water separation bottle was connected to the vacuum pump by vacuum tubes to apply vacuum pressure. Based on the *in-situ* applications of vacuum preloading tests, the 80 kPa vacuum pressure was adopted as the design value for the model test.

The data and image acquisition system consisted of five pore water pressure transducers (PPTs), an electronic scale, a light emitting diode (LED) light source, and a complementary metal oxide semiconductor (CMOS) camera. As shown in Figures 2C, D, the PPTs (P1–P5) were fixed at positions 25, 50, 100, 200, and 300 mm away from the PVD and 60 mm from the top of the PVD to record the variation in pore water pressure along the horizontal direction during the tests. The electronic scale was placed at the bottom of the water separation bottle to record the water discharged mass during vacuum preloading. The CMOS camera (18 megapixels) was placed on the front side of the model testing box to record the slurry sample's displacement during consolidation. The LED light source was placed between the box and camera to illuminate the observation windows. Figure 3 shows a typical captured photo demonstrating that the tracer particles can be distinguished from the light-gray slurry, ensuring the PIV analysis. In the PIV analysis, the photographs were divided into thousands of slurry elements (shown in Figure 3) for correlation calculation (White et al., 2003).

2.3 Testing procedure

The primary procedures of the test are as follows, more details of the operation of the PIV test are given in Sun et al. (2022b):

(i) Check the airtightness of the test apparatus. (ii) Spray tracer particles onto the Perspex sheet using a powder spray ball. (iii) Connect the PVD to the geosynthetic cap and seal the connection to reduce vacuum pressure loss. (iv) Fix the PVDs on a custom-made iron bracket, which was then fixed to the bottom of the testing box. (v) Connect the geosynthetic cap, water separation bottle and vacuum pump through the vacuum tube and seal each interface with clamps to reduce vacuum pressure loss. (vi) Install the PPTs and Perspex sheet into the testing box. (vii) Place slurry into the model case slowly and place one layer of PVC membrane on top of the dredged slurry. Seal the model testing box using a flange connection. (viii) Adjust the camera and light source in front of the model testing box and take 1 image each minute. (ix) Switch on the vacuum pump and record the pore water pressure and water discharge. (x) Stop the vacuum preloading test after 340 h, when the pore water pressure no longer decreases, and the water discharged mass remains stable.

3 Test results

3.1 Discharged water

Figure 4 shows the variations in water discharged mass (m) and water mass discharged rate (q) versus consolidation time (t) for the single PVD model test (test C1) and the dual PVDs model test (test C2). Based on the m curves in Figure 3, it can be observed that the increased PVD resulted in a higher m for test C2, with m values of 15.94 kg at t=340 h, which is approximately 24% higher than test C1. Furthermore, due to the increased PVD in test C2, the q was significantly higher than test C1 at t=0 h, with q=0.237 kg/h and 0.637 kg/h for test C1 and C2, respectively. Notably, q tended to be

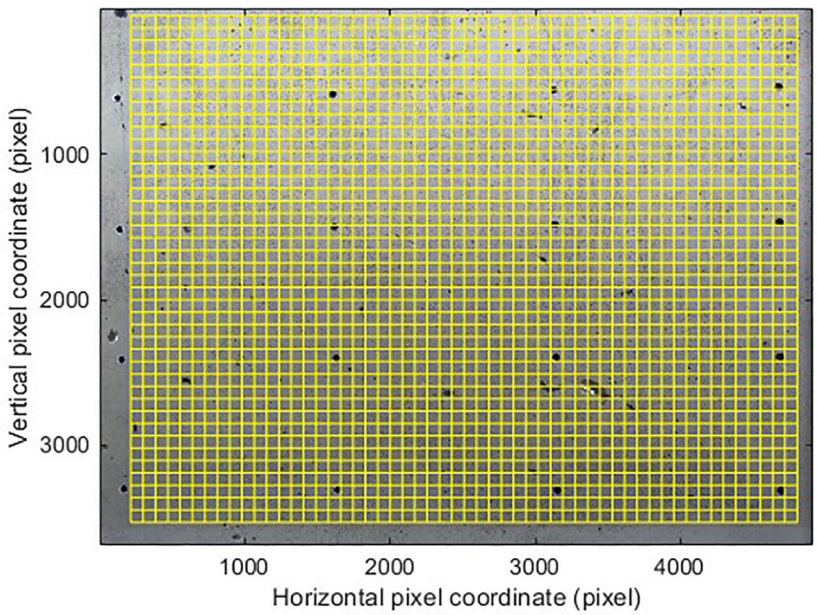

FIGURE 3
Typical captured photo and PIV mesh.

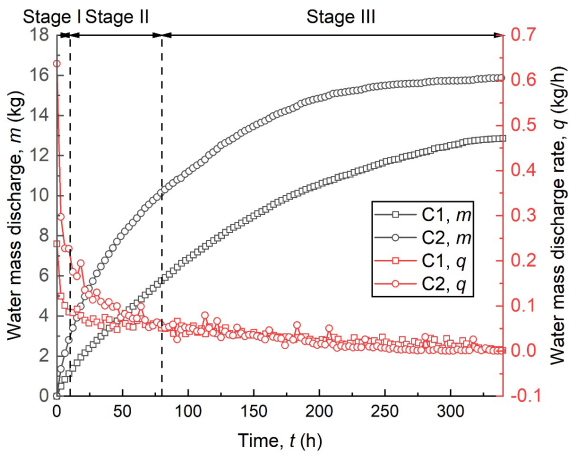

FIGURE 4
The curves of water discharged versus time.

the same at 80 h in both tests, which means that the clogging stabilized. Based on the q curves, the consolidation process can be divided into three stages: Stage I (0–10 h), where clogging developed rapidly, resulting in a rapid decrease in q. In stage II (10–80 h), the formation velocity of the clogging was relatively slow, resulting in q decreasing slowly. In stage III (80–340 h), the clogging remained stable and q was similar in both tests.

3.2 Pore water pressure dissipation

Figure 5 shows the pore water pressure (U) dissipation law, in which Figures 5A, B show how U dissipated with consolidation time at different positions, with the three stages defined above marked with dashed lines. Figure 5C plots the U distribution along the horizontal direction at the end of each stage.

As shown in Figure 5, the U dissipation rate at P1 (25 mm away from the PVD, x=25 mm) was much faster than that at other positions within stage I. Since the vacuum pressure did not propagate to the far field, the U in test C2 at P1 was not affected by the right PVD, thus resulting in a similar lateral distribution of U within stage I (see Figure 5C). In stage II, the U at P2 (x=50 mm) decreased significantly as the vacuum pressure was transmitted to the far field. Notably, as shown in Figure 5C, the U dissipation in test C2 was greater than that in test C1 within stage II, and test C1 had a higher vacuum pressure loss (i.e., the slope of the curve) from P1 to P2. This indicates that the adjacent PVD enhanced the consolidation efficiency of dredged slurry, reducing the clogging between P1 and P2. Within stage III, U dissipated further, and the U dissipation curves at P3, P4 and P5 (100, 200 and 300 mm away from the PVD, respectively) were approximated in both tests. As shown in Figure 5C, at t=340 h in C2, the U dissipation decreased slowly along the lateral direction and the uneven consolidation phenomenon was reduced, while in C1, the U dissipation at P1–P2 were significantly greater than those at P3–P5. This indicates that

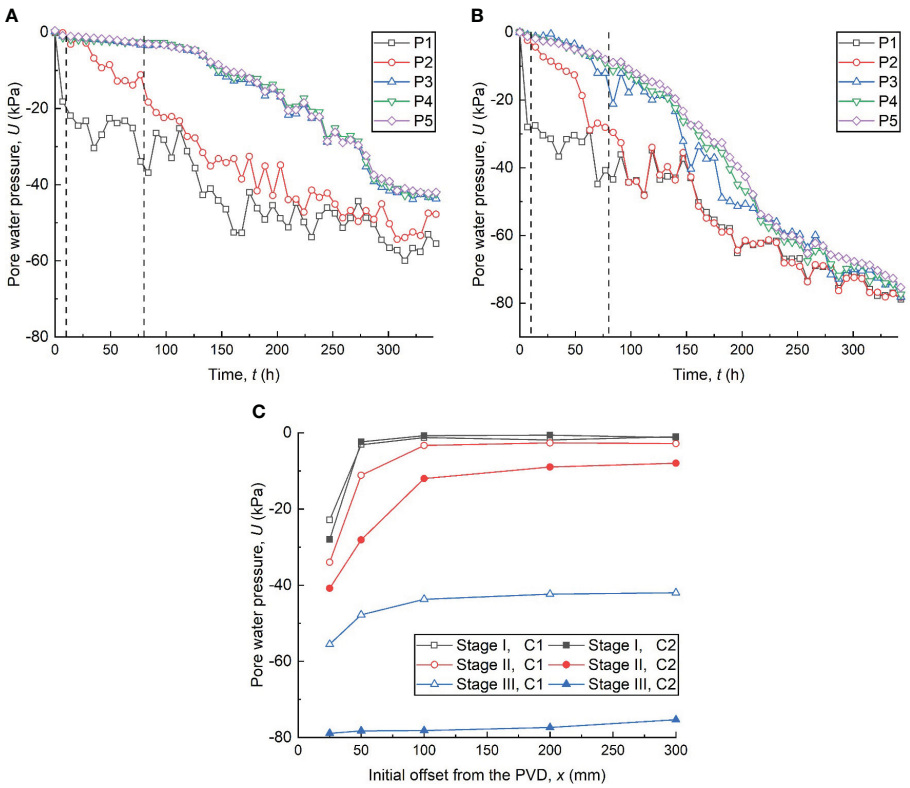

FIGURE 5
Curves of pore water pressure dissipation versus time in **(A)** single-PVD and **(B)** dual-PVD model tests; and **(C)** pore water pressure distribution along the horizontal direction.

the effect of an adjacent PVD can relieve the vacuum pressure loss near the PVD during stage III, thus improving the vacuum preloading effect.

3.3 Horizontal displacement of slurry elements

The horizontal and vertical displacements of each slurry element were calculated, respectively. Figure 6 shows the horizontal displacement (d_x) field of the slurry during the three stages, where the negative d_x represents the slurry move toward to the PVD. Due to the significant settlement of the slurry during the consolidation, some elements defined in the PIV technique move outside the calculation field while some undefined elements move in the calculation field, resulting in a blank area.

As shown in Figures 6A, B, the d_x fields in the range of x=0–225 mm of the two tests were roughly the same in stage I. Based on the vacuum pressure transition characteristics, the displacement field can be divided into two zones by the d_x. Zone I is a consolidated zone where the slurry has been consolidated, and the d_x=-2–0 mm. Zone II is a transitional zone, where the $|d_x|$>2 mm. It is worth noting that in test C2, a horizontal displacement contour with d_x=0 mm appeared in the range of x=250–300 mm, while the slurry still moved toward the PVD at the same position in test C1. This is because the vacuum pressure from the two PVDs in C2 reached equilibrium at x=250–300 mm. This finding is consistent with the test results reported by Wang et al. (2019), which indicated that the d_x in the midpoint between two PVDs is zero. The difference between this study and Wang et al. (2019) may be attributed to the difference in vacuum pressure loss in the two PVDs. Figures 6C, D show the variations in d_x for the two tests in stage II. In stage II, as

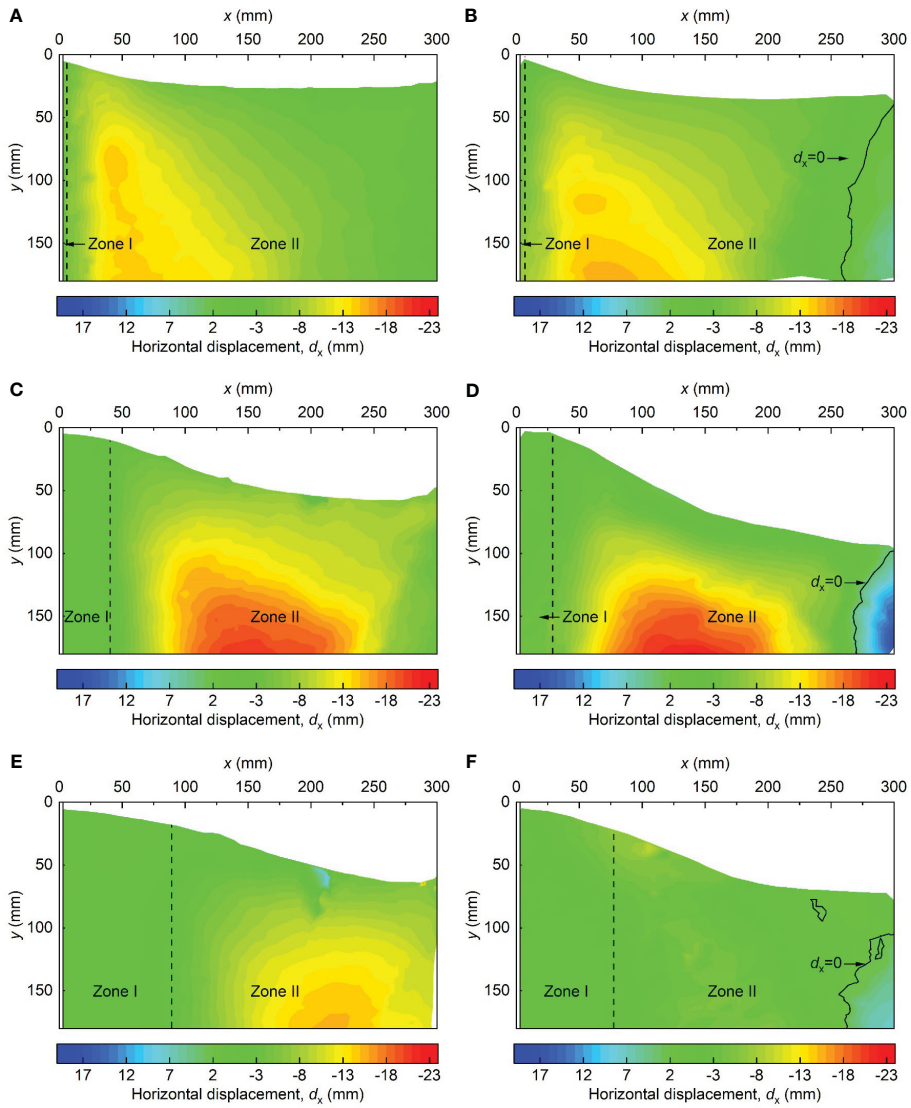

FIGURE 6
Horizontal displacement fields of dredged slurry in different tests at different times: **(A)** C1, 0–10 h; **(B)** C2, 0–10 h; **(C)** C1, 10–80 h; **(D)** C2, 10–80 h; **(E)** C1, 80–340 h; and **(F)** C2, 80–340 h.

the vacuum pressure propagated further in the slurry, the d_x of the far-field slurry increased further, and the maximum horizontal displacement moved away from the PVD. It is worth noting that zone I was further enlarged in stage II, and the width of zone I was larger in test C1 than in test C2. As reported by Sun et al. (2022a); Sun et al. (2022b), the dredged slurry near the PVD rapidly moves towards the PVDs under the vacuum pressure gradient, resulting in the formation of a clogging zone. A larger Zone I indicates a thicker thickness of the clogging zone, which implies that the adjacent PVD can effectively reduce the thickness of the clogging zone around the PVD, thereby reducing vacuum pressure loss and improving the consolidation efficiency of the dredged slurry (as shown in Figure 5). Figures 6E, F show the variations in d_x for both tests in stage III. Within stage III, the vacuum pressure loss due to the clogging zone caused a significant decrease in d_x. Furthermore, in test C2, the decrease in d_x of the slurry is also due to the horizontal vacuum stress offset by the vacuum pressure transmitted from the right PVD.

To further compare the differences in d_x between the two tests, the mean horizontal displacement ($\bar{d}_x$) distributions of the slurry within each stage were calculated. Figure 7 shows the $\bar{d}_x$ with error bars representing ± 1 standard deviation in each stage.

As shown in Figure 7A, since the vacuum pressure transmitting from the right PVD did not reach x=0–225 mm, the $\bar{d}_x$ distribution and standard deviation of the slurry in this range were approximately the same in stage I. Within x=225–300 mm, the vacuum pressures from the two PVDs canceled each other out, resulting in a slightly larger standard deviation of d_x in test C2 than in C1, indicating a more scattered d_x of the dredged slurry. In addition, the slopes of each curve reflect the degree of lateral strain experienced by the slurry element. The positive slope indicates that the element was compressed horizontally, while the negative slope signifies the element was under extension. And the higher negative slope in x=225–300 mm means the slurry underwent a larger extension (see below). As shown in Figure 7B, the $\bar{d}_x$ of C1 was larger than that of C1 in x=0–75 mm, and the $\bar{d}_x$ of C2 was much smaller than that of C1 in x=75–263 mm. The larger $\bar{d}_x$ of C2 in x=0–75 mm indicates that higher consolidation effect during this stage. Furthermore, as the vacuum pressure transmitted from the PVD was partially canceled by the vacuum pressure from the adjacent PVD, it is noteworthy that the d_x distribution of the slurry in C2 was more scattered, especially in x=75–263 mm. In Figure 7C, the $\bar{d}_x$ and standard deviation in x=0–114 mm in test C2 was larger than in C1, indicating that the slurry near the left PVD in test C2 was further consolidated. In addition, the $\bar{d}_x$ in x=114–300 mm was much greater in test C1 than in C2 in stage III. Differing from stage II, the d_x in C1 was more discrete, which can be explained by the vacuum stress from the right PVD acting on the slurry element having stabilized, leading to a lower and more uniform d_x value.

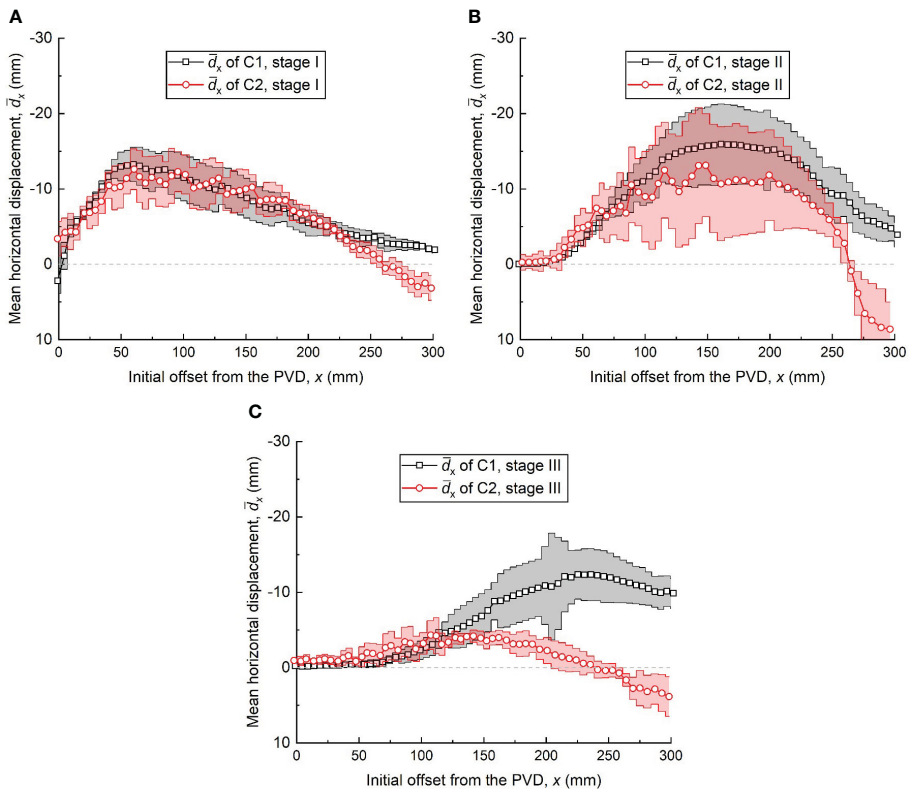

FIGURE 7
Horizontal displacement distributions at stages: **(A)** 0–10 h, stage I, **(B)** 10–80 h, stage II and **(c)** 80–340 h, stage III (mean ± 1 standard deviation).

3.4 Vertical displacement of slurry elements

Figure 8 shows the vertical displacement (d_y) of the displacement vector of dredged slurry within the three stages. A positive d_y value represents vertical settlement of the slurry. As shown in Figures 8A, B, a non-uniform settlement was observed near the PVD, characterized by smaller d_y near the PVD and larger d_y in the far field. Moreover, owing to the limited propagation of vacuum pressure, d_y of test C1 demonstrates an initial increase followed by a subsequent decrease along the x. Additionally, in test C2, the slurry vertical settlement superimposed in the far field, resulting in a "W"-shaped distribution of d_y contour lines. Figures 8C, D show the d_y fields of the slurry during stage II in the two tests. In stage II, the d_y was developed toward the far field and downward. In addition, the d_y of the slurry corresponding to C2 was superimposed by the effect of the two PVDs, resulting in d_y being much larger than that of C1. Figures 8E, F show the d_y field in stage III corresponding to C1 and C2. In stage III, d_y was significantly reduced due to the stabilization of clogging, which also reduced the difference in d_y between the two tests.

Similarly, the mean vertical displacements ($\bar{d}_y$) and standard deviations of the vertical displacements of the slurry along the horizontal direction within each stage were calculated. As shown in Figure 9A, the $\bar{d}_y$ near the PVD (x≈0 mm) corresponding to tests C1 and C2 were approximated. Since the vacuum pressure did not propagate to the far field, the slurry element underwent the same stress state, resulting in similar standard deviations in $\bar{d}_y$ in tests C1 and C2. As shown in Figure 9B, in the range of x=0–28 mm, the slurry in test C1 trended to be stable, whereas the slurry in C2 still underwent a small settlement. As vacuum pressure propagated to the far field, the $\bar{d}_y$ difference between the two tests increased further. In addition, $\bar{d}_y$ in test C1 decreased at x=220–300 mm, which indicates that the vacuum pressure was significantly reduced.

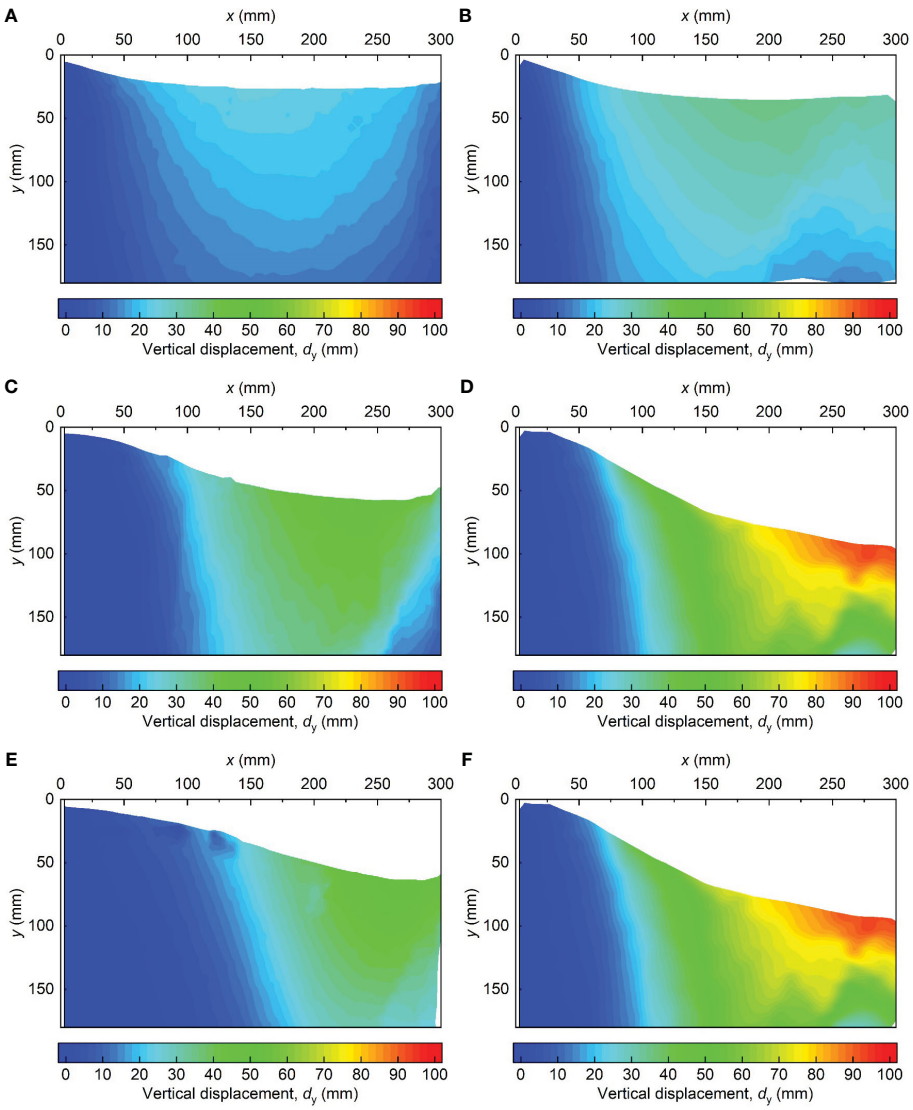

FIGURE 8
Vertical displacement fields of dredged slurry in the different tests at different stages: **(A)** C1, 0–10 h; **(B)** C2, 0–10 h; **(C)** C1, 10–80 h; **(D)** C2, 10–80 h; **(E)** C1, 80–340 h; and **(F)** C2, 80–340 h.

Moreover, the standard deviation in $\bar{d}_y$ in stage II was greater in test C2 than in C1. This is because the vertical non-uniform vacuum stress applied to the slurry element between the two PVDs made d_y of the slurry more discrete. Figure 9C shows the $\bar{d}_y$ distributions of two tests in stage III. The differences in the $\bar{d}_y$ and standard deviation in both tests were reduced due to the loss of vacuum pressure. As dual PVDs reduce the clogging zone near the PVD, the slurry near the PVD further settled.

3.5 Strain profile of slurry elements

The GeoPIV-RG algorithm (Stanier et al., 2016) was adopted to convert the horizontal and vertical displacements to horizontal strain and vertical strain, respectively. Natural strains were used, as is conventional for large-strain behavior with positive compression (White and Bolton, 2004; Stanier et al., 2016).

Figure 10 shows the mean horizontal strain ($\bar{\epsilon}_x$) profiles of the three stages in the two tests. Within stage I, the slurry elements near the PVD (x=0–28 mm) underwent severe horizontal compression ($\bar{\epsilon}_x$ ≈19%). In the range of x=0–50 mm, the horizontal vacuum stress acting on the slurry element was greater than the stress of the element maintaining the at-rest state, which led to the slurry being compressed horizontally. As the vacuum pressure attenuated along the lateral direction, $\bar{\epsilon}_x$ gradually decreased to 0 and was converted to horizontal extension. Within x=0–225 mm, the $\bar{\epsilon}_x$ distribution was approximately the same for both tests. The horizontal extension strain of C2 was greater than that of C1 in the x=225–300 mm range due to the effect of the two PVDs. In stage II, as the slurry elements near the PVD consolidated in stage I rapidly, the $\bar{\epsilon}_x$ in x=0–28 mm were low. In addition, the $\bar{\epsilon}_x$ of test C2 in this range was larger than that in test C1, indicating a longer consolidation stage of slurry near the PVD. As the horizontal vacuum stress transmitted from the PVD was partially cancelled, the $\bar{\epsilon}_x$ values in the range of x=28–100 mm were less than those in test C1. In stage III, the horizontal compression range in C1 increased further to x≈225 mm, while that in C2 was only x=0–115 mm, and the $\bar{\epsilon}_x$ of test C2 in the range was only about 3%.

Figure 11 shows the mean vertical strain ($\bar{\epsilon}_y$) profiles of during the three stages in the two tests. In stage I, $\bar{\epsilon}_y$ was about zero at x=0 mm and gradually increased with x. In test C2, $\bar{\epsilon}_y$ was greater than in C1 due to the effect of the two PVDs. In stage III, the slurry elements in the far field compressed further vertically under the vertical vacuum stress, and $\bar{\epsilon}_y$ was much greater than in stage I. In stage III, $\bar{\epsilon}_y$ was slightly reduced compared with stage II. Compared with the $\bar{\epsilon}_x$ values, it can be inferred that the slurry in test C2 was mainly compressed vertically in stage III.

To compare the degree of uneven consolidation of slurry along the horizontal direction under different PVD layout, the volume strains of slurry elements at each stage in tests C1 and C2 were calculated, and the mean volume strains ($\bar{\epsilon}_{vol}$) are shown in Figure 12. As shown in Figure 12A, slurry in both tests C1 and C2 experienced rapid compression near the PVD (x=0–28 mm), with $\bar{\epsilon}_{vol}$ ≈19%. In the range of x=28–300 mm, the $\bar{\epsilon}_{vol}$ of slurry

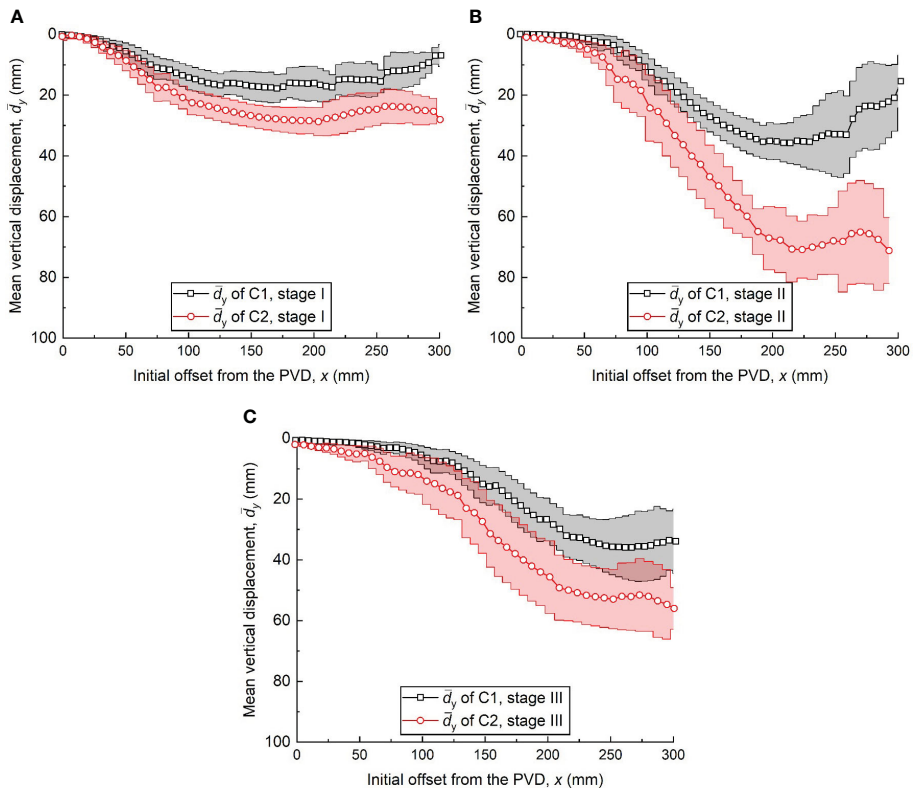

FIGURE 9
Vertical displacement distributions at different stages: **(A)** 0-10 h, stage I **(B)** 10-80 h, stage II and **(C)** 80-340 h, stage III (mean ± 1 standard deviation).

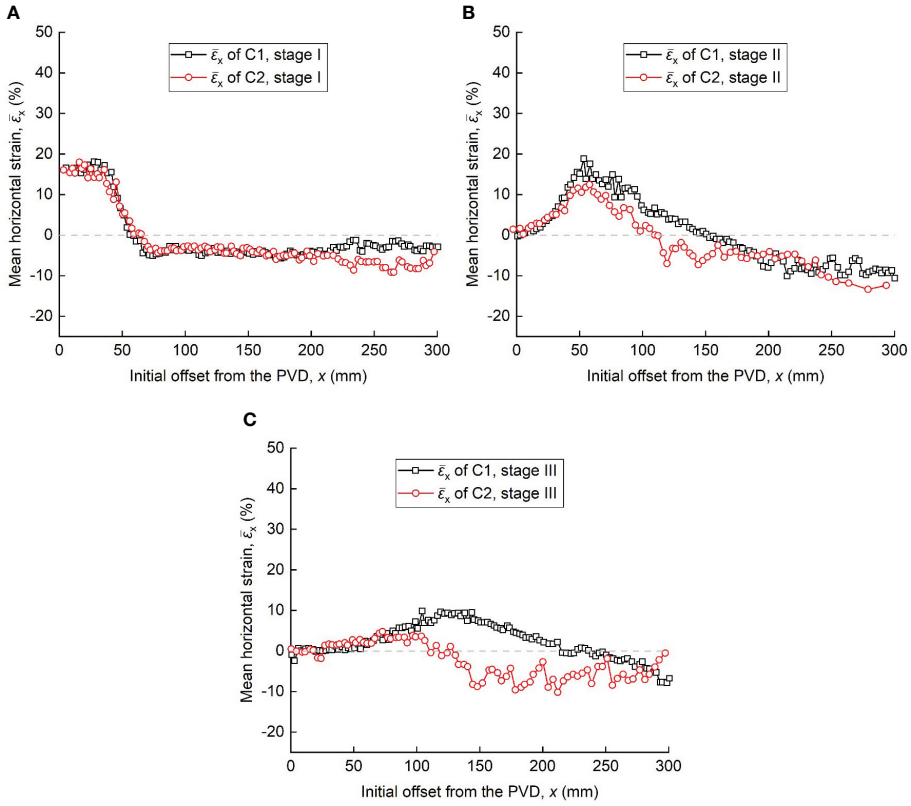

FIGURE 10
Mean horizontal strains distributions at different stages: **(A)** 0–10 h, stage I, **(B)** 10–80 h, stage II and **(C)** 80–340 h, stage III.

element in tests C1 and C2 was relatively similar. This is attributed to the fact that the vacuum pressure was not transmitted to the far field within this range, resulting in minimal stress difference among the slurry elements. Figure 12B indicates that during stage II, slurry units within the range of x=100–300 mm experienced greater volume compression strains under the influence of dual PVDs, leading to larger dissipation of pore water pressure within this range (as shown in Figure 5C). As shown in Figure 12C, the $\bar{\varepsilon}_{vol}$ of slurry element in test C2 were greater than those in test C1. This implies that under the influence of dual PVDs, slurry elements in test C2 underwent greater volume compression after the stabilization of the clogging zone, with compression mainly occurring vertically (as shown in Figure 11C). This indicates that test C2 achieved better consolidation effects for the slurry.

3.6 Clogging zone development

The clogging zone has been widely reported (Tang et al., 2010; Bao et al., 2014; Xu et al., 2020; Sun et al., 2022a). The development of clogging zone thickness in the presence of one or two PVDs was investigated. As mentioned above, the formation of clogging zone was related to the horizontal displacement of the slurry. As per (Sun et al., 2022b), a contour representing zero horizontal strain was defined as the boundary of the clogging zone. The average thickness of the clogging zone over the whole field was used to characterize the thickness versus time.

Figure 13 shows the variation in clogging zone thickness (R) with consolidation time. In stage I, R was roughly the same in both tests. In early stage II (t=10–25 h), the clogging zone thicknesses were approximately equal because the vacuum pressure from the right PVD did not transfer to the observation field. When the vacuum pressure was transmitted to the far field, the horizontal vacuum pressure applied to the slurry elements was offset by the vacuum pressure transmitted from the right PVD, making R greater in test C1 than in C2 at 20–80 h. Since the development of clogging zone thickness stabilized at about 140 h, in which the water discharge rate and the pore water pressure dissipation rate tend to a constant, the later variations in R are not shown in Figure 11. The fitted curves are listed below:

$$R = 105.25 \times (1 - e^{-0.043t}) \quad (1)$$

$$R = 79.87 \times (1 - e^{-0.081t}) \quad (2)$$

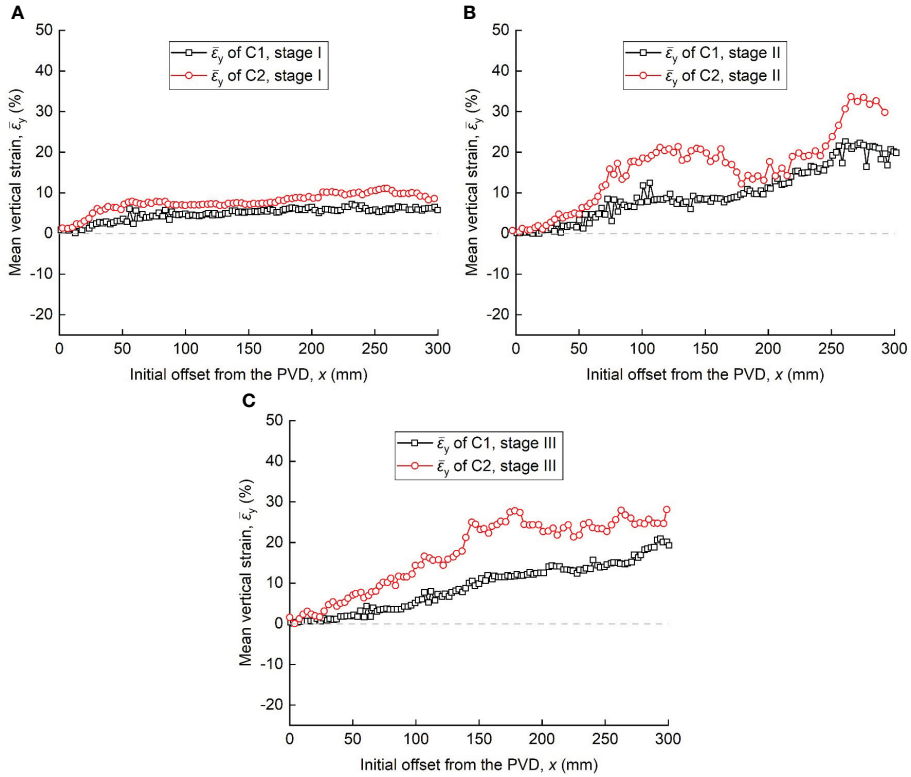

FIGURE 11
Mean vertical strains distribution at different stages: **(A)** 0–10 h, stage I, **(B)** 10–80 h, stage II and **(C)** 80–340 h, stage III.

4 Discussion

4.1 Consolidation characteristics under different PVD layout

The two tests revealed different consolidation characteristics under different PVD layout. These are summarized as follows:

In stage I, the slurry near the PVD was rapidly consolidated by horizontal compression under vacuum pressure. Since the vacuum pressure transmitted from the right PVD did not reach this vicinity, the dual PVD had less influence on the consolidation of the slurry near the PVD in this stage. Thus, there was a similar pore pressure dissipation distribution (Figure 5). Besides, the accumulation of vertical vacuum stress and the offset of horizontal vacuum stress led to a larger vertical displacement and strain in the far-field slurry under the dual PVD condition.

In stage II, as the vacuum pressure in test C2 was transmitted from one PVD to the other PVD, the vacuum stresses between the two PVDs were superimposed in the vertical direction, while they offset each other in the horizontal direction. This resulted in a further reduction in the horizontal migration of slurry in test C2 during stage II, reducing the clogging and the thickness of clogging zone in this test. As a result, the slurry near the PVD further consolidated during this stage II, leading to larger pore water pressure dissipation of slurry.

In stage III, the slurry deformation became gradually stabilized and the displacement and strain were much smaller than in stage II, resulting in slow rates of water drainage and pore water pressure dissipation (Figures 4 and 5). The consolidation patterns of the slurry exhibit certain differences during stage III. In test C1, the displacement field of the slurry can be divided into two zones: a zone near the PVD characterized by horizontal compression and vertical compression, and a far-field zone characterized by vertical compression and horizontal compression. On the other hand, in test C2, the deformation pattern of the slurry is predominantly characterized by vertical compression and horizontal stretching, with only a small amount of horizontal compression strain observed near the PVD. Furthermore, the less vacuum pressure loss in test C2 resulted in higher volume compression of the slurry, thereby enhancing the consolidation effect of the slurry.

4.2 Potential application

This paper provided equations describing the relationship between clogging zone thickness and time that can be used in consolidation calculations that consider the clogging effect. As indicated by Liu et al. (2021) the thickness of the clogging zone is vital important in calculating the consolidation process of dredged slurries improved by vacuum preloading. It can thus make the calculation more practical when considering the gradual increase in the radius of the clogging zone. A direct and accessible method can be used for applying the equation in consolidation calculation, in which the effective zone around a PVD can be divided into a

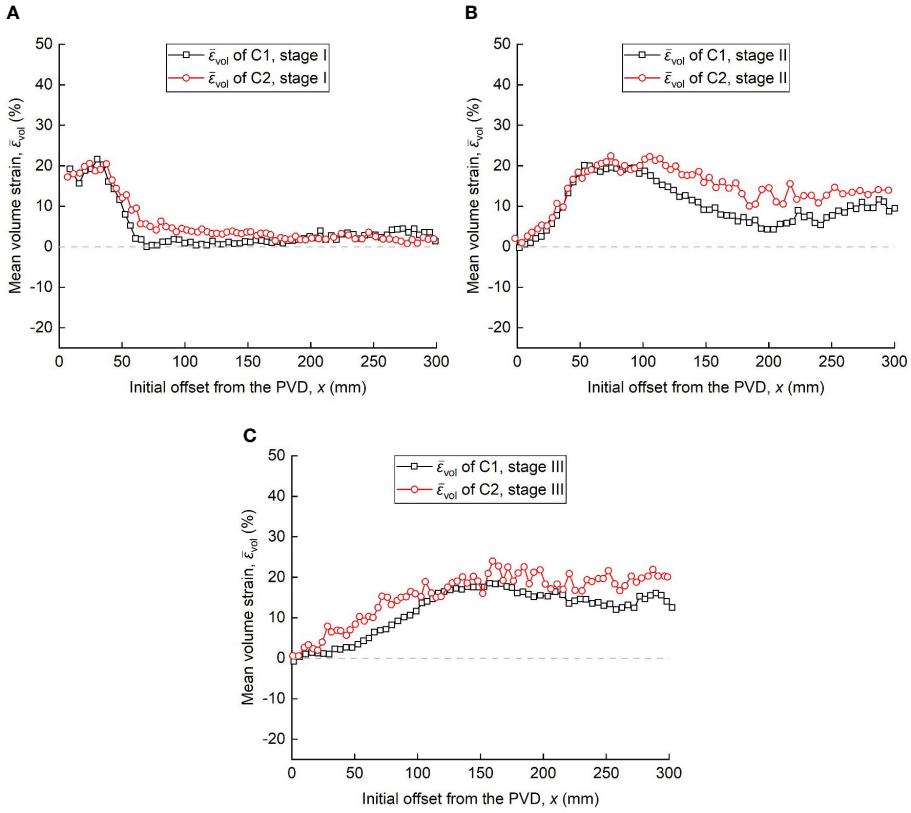

FIGURE 12
Mean volume strains distribution at different stages: **(A)** 0–10 h, stage I, **(B)** 10–80 h, stage II and **(C)** 80–340 h, stage III.

clogging zone and a normal zone in the consolidation model. As shown by Eq. (1) or (2), the radius of the clogging zone can be assumed as a function of time with other basic assumptions in the large or small strain consolidation theory reserved.

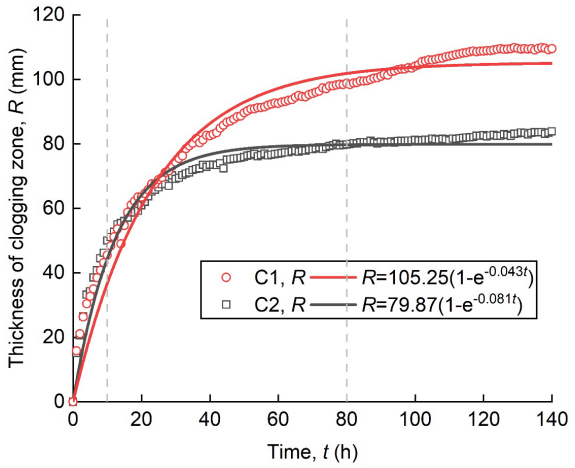

FIGURE 13
Average clogging zone thickness versus time.

5 Conclusions

This study investigated the effect of PVD layout on the characteristics of dredged slurry deformation under vacuum preloading. Two vacuum preloading model tests were carried out —with single and dual PVDs. The PIV technology was used to observe the displacement and strain profile of dredged slurry during consolidation. The test results offer the following conclusions:

1. Due to the vacuum stresses transmitted from the two PVDs offset each other in the horizontal direction, the horizontal displacement of slurry significantly decreased and became more dispersed in the mid-stage of vacuum preloading, resulting in a thinner clogging zone, thereby reducing vacuum pressure loss, which in turn improved the dissipation efficiency of pore water pressure.
2. In the case of dual PVDs, the slurry near the PVD underwent a longer period of consolidation deformation, and the consolidation pattern of the slurry was primarily characterized by vertical compression and horizontal extension during the later stages of vacuum preloading. In the case of a single PVD, there is a distinct zone where

the slurry experienced both vertical and horizontal compression deformation in the later stages.

3. The development of the clogging zone during the initial stage of vacuum preloading was similar under different PVD layouts. In the later stages of consolidation, the growth rate of the clogging zone was slow in two PVDs case. A relationship between the thickness of the clogging zone and time is proposed, providing a reference for theoretical consolidation calculations considering the clogging zone.

Data availability statement

The raw data supporting the conclusions of this article will be made available by the authors, without undue reservation.

Author contributions

JC contributed to conception and design of the study. ZH, and BX conducted the model test. ZH performed the analysis. ZH wrote the first draft of the manuscript. BX, and MY wrote sections of the manuscript. All authors contributed to manuscript revision, read, and approved the submitted version.

Conflict of interest

Author JC was employed by the company Zhejiang University of Technology Engineering Design Group Co.,Ltd.

The authors declare that the research was conducted in the absence of any commercial or financial relationships that could be construed as a potential conflict of interest.

Publisher's note

References

Arshad, M. I., Tehrani, F. S., Prezzi, M., and Salgado, R. (2014). Experimental study of cone penetration in silica sand using digital image correlation. *Géotechnique* 64 (7), 551–569. doi: 10.1680/geot.13.P.179

Bao, S., Lou, Y., Dong, Z., Mo, H., Chen, P., and Zhou, R. (2014). Causes and countermeasures for vacuum consolidation failure of newly-dredged mud foundation. *Chin. J. Geotechnical Eng.* 36 (7), 1350–1359. doi: 10.11779/CJGE201407020

Bauer, J., Kempfert, H.-G., and Reul, O. (2016). Lateral pressure on piles due to horizontal soil movement. *Int. J. Phys. Model. Geotechnics* 16 (4), 173–184. doi: 10.1680/jphmg.15.00005

Bergado, D. T., Balasubramaniam, A., Fannin, R. J., and Holtz, R. D. (2002). Prefabricated vertical drains (PVDs) in soft Bangkok clay: a case study of the new Bangkok international airport project. *Can. Geotechnical J.* 39 (2), 304–315. doi: 10.1007/s40891-021-00339-x

Cai, Y., Qiao, H., Wang, J., Geng, X., Wang, P., and Cai, Y. (2017). Experimental tests on effect of deformed prefabricated vertical drains in dredged soil on consolidation *via* vacuum preloading. *Eng. Geology* 222, 10–19. doi: 10.1016/j.enggeo.2017.03.020

Cai, Y. Q., Wang, J., Ma, J., Wang, P., and Fu, H. (2016). A new method to improve the effectiveness of vacuum preloading on the consolidation of dredged fill in wenzhou. *Japanese Geotechnical Soc. Special Publ.* 2 (51), 1794–1797. doi: 10.3208/jgssp.TC217-05

Cai, Y., Xie, Z., Wang, J., Wang, P., and Geng, X. (2018). New approach of vacuum preloading with booster prefabricated vertical drains (PVDs) to improve deep marine clay strata. *Can. Geotechnical J.* 55 (10), 1359–1371. doi: 10.1139/cgj-2017-0412

Chai, J. C., Carter, J. P., and Hayashi, S. (2005). Ground deformation induced by vacuum consolidation. *J. Geotechnical Geoenvironmental Eng.* 131 (12), 1552–1561. doi: 10.1061/(Asce)1090-0241(2005)131:12(1552

Chai, J.-c., Fu, H.-t., Wang, J., and Shen, S.-L. (2020). Behaviour of a PVD unit cell under vacuum pressure and a new method for consolidation analysis. *Comput. Geotechnics* 120. doi: 10.1016/j.compgeo.2019.103415

Chu, J., Yan, S. W., and Yang, H. (2000). Soil improvement by the vacuum preloading method for an oil storage station. *Géotechnique* 50 (6), 625–632. doi: 10.1680/geot.2000.50.6.625

Deng, Y., Liu, L., Cui, Y.-J., Feng, Q., Chen, X., and He, N. (2019). Colloid effect on clogging mechanism of hydraulic reclamation mud improved by vacuum preloading. *Can. Geotechnical J.* 56 (5), 611–620. doi: 10.1139/cgj-2017-0635

Fang, Y., Guo, L., and Huang, J. (2019). Mechanism test on inhomogeneity of dredged fill during vacuum preloading consolidation. *Mar. Georesources Geotechnology* 37 (8), 1007–1017. doi: 10.1080/1064119x.2018.1522398

Feng, S., Lei, H., and Lin, C. (2022). Analysis of ground deformation development and settlement prediction by air-boosted vacuum preloading. *J. Rock Mechanics Geotechnical Eng.* 14 (1), 272–288. doi: 10.1016/j.jrmge.2021.05.006

Geng, X., and Yu, H. S. (2017). A large-strain radial consolidation theory for soft clays improved by vertical drains. *Géotechnique* 67 (11), 1020–1028. doi: 10.1680/jgeot.15.T.013

Jiang, H., Wu, Y., Kong, G., and Li, J. (2020). Transparent soil model test of vacuum preloading method on ultra-soft soil and formation mechanism of "soil pile". *J. Harbin Inst. Technol.* 52, 33–40. doi: 10.11918 /201809039

Kim, J., Woo, S. I., and Chung, C.-K. (2017). Assessment of non-uniform deformation during consolidation with lateral drainage using particle image velocimetry (PIV). *KSCE J. Civil Eng.* 22 (2), 520–531. doi: 10.1007/s12205-017-0707-6

Kwak,, Park,, Kim,, Chung,, and Baek, (2020). Shear band characterization of clayey soils with particle image velocimetry. *Appl. Sci.* 10 (3), 1139. doi: 10.3390/app10031139

Liu, S. J., Cai, Y. Q., Sun, H. L., Geng, X. Y., Shi, L., and Pan, X. D. (2021). Consolidation considering clogging effect under uneven strain assumption. *Int. J. Geomechanics* 21 (1), 12. doi: 10.1061/(asce)gm.1943-5622.0001898

Mesri, G., and Khan, A. Q. (2012). Ground improvement using vacuum loading together with vertical drains. *J. Geotechnical Geoenvironmental Eng.* 138 (6), 680–689. doi: 10.1061/(asce)gt.1943-5606.0000640

Ni, J., and Geng, X.-Y. (2022). Radial consolidation of prefabricated vertical drain-reinforced soft clays under cyclic loading. *Transportation Geotechnics* 37, 100840. doi: 10.1016/j.trgeo.2022.100840

Pan, X., Zhou, L., Sun, H., Cai, Y., Shi, L., and Yuan, Z. (2020). Vacuum preloading test for high moisture content slurry using particle image velocimetry. *J. ZheJiang Univ. (Engineering Science)* 54 (6), 1078–1085. doi: 10.3785/j.issn.1008-973X.2020.06.004

Robinson, R. G., Indraratna, B., and Rujikiatkamjorn, C. (2012). Final state of soils under vacuum preloading. *Can. Geotechnical J.* 49 (6), 729–739. doi: 10.1139/t2012-024

Shen, J. (2018). Laboratory model test of vacuum preloading on dredged clays at high initial water content. *Nanjing China: Southeast Univ.*

Stanier, S. A., Blaber, J., Take, W. A., and White, D. J. (2016). Improved image-based deformation measurement for geotechnical applications. *Can. Geotechnical J.* 53 (5), 727–739. doi: 10.1139/cgj-2015-0253

Stanier, S. A., and White, D. J. (2013). Improved image-based deformation measurement in the centrifuge environment. *Geotechnical Testing J.* 36 (6), 915–928. doi: 10.1520/gtj20130044

Sun, H.-l., He, Z.-l., Geng, X.-y., Shen, M.-f., Cai, Y.-q., Wu, J., et al. (2022a). Formation mechanism of clogging of dredge slurry under vacuum preloading visualized using digital image technology. *Can. Geotechnical J.* 59 (7), 1292–1298. doi: 10.1139/cgj-2021-0341

Sun, H.-l., He, Z.-l., Pan, K., Lu, J.-l., Pan, X.-d., Shi, L., et al. (2022b). Consolidation mechanism of high-water-content slurry during vacuum preloading with prefabricated vertical drains. *Can. Geotechnical J.* 59 (8), 1373–1385. doi: 10.1139/cgj-2021-0248

Sun, H. L., Weng, Z. Q., Geng, X. Y., Shen, M. F., Pan, X. D., Shi, L., et al. (2022c). Experimental study on the effects of particle grading on lime-treated slurry with vacuum preloading. *Mar. Georesources Geotechnology* 40 (7), 869–881. doi: 10.1080/1064119x.2021.1946626

Sun, H.-l., Weng, Z.-q., Liu, S.-j., Geng, X.-y., Pan, X.-d., Cai, Y.-q., et al. (2020). Compression and consolidation behaviors of lime-treated dredging slurry under vacuum pressure. *Eng. Geology* 270, 105573. doi: 10.1016/j.enggeo.2020.105573

Take, W. A., and Bolton, M. D. (2011). Seasonal ratcheting and softening in clay slopes, leading to first-time failure. *Géotechnique* 61 (9), 757–769. doi: 10.1680/geot.9.P.125

Tang, T., Huang, J., Guan, Y., Chen, H., and Cheng, W. (2010). Experimental study on dredged fill sludge improved by vacuum preloading. *Port Waterway Eng.* 4, 115–122. doi: 10.16233/j.cnki.issn1002-4972.2010.04.027

Tang, M., and Shang, J. Q. (2000). Vacuum preloading consolidation of yaoqiang airport runway. *Géotechnique* 50 (6), 613–623. doi: 10.1680/geot.2000.50.6.613

Wang, J., Cai, Y., Ni, J., Geng, X., and Xu, F. (2017a). Effect of sand on the vacuum consolidation of dredged slurry. *Mar. Georesources Geotechnology* 36 (2), 238–244. doi: 10.1080/1064119x.2017.1304473

Wang, J., Fu, Z., Yu, Y., Wang, G., Shi, L., Yuan, Z., et al. (2021). Numerical investigating on representativeness of tracers in PIV model test of dredged slurry treated by vacuum preloading. *Appl. Sci.* 11 (20), 9715. doi: 10.3390/app11209715

Wang, P., Han, Y., Wang, J., Cai, Y., and Geng, X. (2019). Deformation characteristics of soil between prefabricated vertical drains under vacuum preloading. *Geotextiles Geomembranes* 47 (6), 798–802. doi: 10.1016/j.geotexmem.2019.103493

Wang, J., Ni, J., Cai, Y., Fu, H., and Wang, P. (2017b). Combination of vacuum preloading and lime treatment for improvement of dredged fill. *Eng. Geology* 227, 149–158. doi: 10.1016/j.enggeo.2017.02.013

White, D. J., and Bolton, M. D. (2004). Displacement and strain paths during plane-strain model pile installation in sand. *Géotechnique* 54 (6), 375–397. doi: 10.1680/geot.2004.54.6.375

White, D. J., Take, W. A., and Bolton, M. D. (2003). Soil deformation measurement using particle image velocimetry (PIV) and photogrammetry. *Géotechnique* 53 (7), 619–631. doi: 10.1680/geot.2003.53.7.619

Wu, Y.-j., Li, J.-p., Lu, Y.-T., Zhang, X.-d., Le, T. H., and Chau, N. X. Q. (2021). The influence of drainage spacing on the deformation characteristics of transparent ultrasoft soil. *Int. J. Geosynthetics Ground Eng.* 7 (4), 99. doi: 10.1007/s40891-021-00343-1

Wu, Y. J., Zhou, R., Lu, Y. T., Zhang, X. D., Zhang, H. Q., and Tran, Q. C. (2022). Experimental study of PVD-improved dredged soil with vacuum preloading and air pressure. *Geotextiles Geomembranes* 50 (4), 668–676. doi: 10.1016/j.geotexmem.2022.03.008

Xu, B.-H., He, N., Jiang, Y.-B., Zhou, Y.-Z., and Zhan, X.-J. (2020). Experimental study on the clogging effect of dredged fill surrounding the PVD under vacuum preloading. *Geotextiles Geomembranes* 48 (5), 614–624. doi: 10.1016/j.geotexmem.2020.03.007

Yao, K., Cheng, D., Sheng, J., Shi, L., Hu, L., and Yu, Y. (2023). Real-time behaviour of dredged slurry treated by air-booster vacuum consolidation. *Appl. Sci.* 13 (6), 3550. doi: 10.3390/ app13063550

Zhang, H., Geng, X.-y., Sun, H.-l., Deng, Y.-f., Liu, S.-j., and Cai, Y.-q. (2022). Consolidation theory of slurry dewatered by permeable geotextile tube with distributed prefabricated drains. *Can. Geotechnical J.* 60 (2), 213–229. doi: 10.1139/cgj-2022-0083

Zhao, C., Koseki, J., and Liu, W. (2020). Local deformation behaviour of saturated silica sand during undrained cyclic torsional shear tests using image analysis. *Géotechnique* 70 (7), 621–629. doi: 10.1680/jgeot.18.T.017

Zhou, Y., Wang, P., Shi, L., Cai, Y., and Wang, J. (2021). Analytical solution on vacuum consolidation of dredged slurry considering clogging effects. *Geotextiles Geomembranes* 49 (3), 842–851. doi: 10.1016/j.geotexmem.2020.12.013

frontiers | Frontiers in Marine Science

TYPE Original Research
PUBLISHED 26 September 2023
DOI 10.3389/fmars.2023.1270286

OPEN ACCESS

EDITED BY
Zefeng Zhou,
Norwegian Geotechnical Institute (NGI), Norway

REVIEWED BY
Xiantao Zhang,
Shanghai Jiao Tong University, China
Lifen Chen,
Dalian University of Technology, China

*CORRESPONDENCE
Zhenguo Gao
zhenguo.gao@just.edu.cn

RECEIVED 31 July 2023
ACCEPTED 05 September 2023
PUBLISHED 26 September 2023

CITATION
Gao Z, Li Z, Niu J, Yin Q and Liu K (2023) Application of nonlinear stiffness mechanism on energy harvesting from vortex-induced vibrations. *Front. Mar. Sci.* 10:1270286. doi: 10.3389/fmars.2023.1270286

Application of nonlinear stiffness mechanism on energy harvesting from vortex-induced vibrations

Zhenguo Gao*, Zhifu Li, Jianjie Niu, Qilin Yin and Kun Liu

School of Naval Architecture & Ocean Engineering, Jiangsu University of Science and Technology, Zhenjiang, Jiangsu, China

This study investigates the potential of vortex-induced vibration (VIV) as a renewable energy source, achieved when fluid flow interacts with a bluff body, inducing self-sustained oscillations through vortex shedding in the wake. While VIV research has traditionally focused on understanding its mechanisms and mitigating detrimental effects, interest in VIV energy harvesting has surged as a means to convert marine hydrokinetic (MHK) energy into usable electrical power. The nonlinear effects of two linear oblique springs on VIV energy harvesting are explored using the wake oscillator model, encompassing bistable and Duffing hardening stiffness. The study examines the response and energy harvesting performance while considering the impact of undeformed spring length, structural damping, and initial conditions on VIV energy conversion. Findings show that nonlinear stiffness application in the VIV system can broaden the synchronization bandwidth or reduce the VIV initiation flow speed. Bistable stiffness may broaden the synchronization velocity range, while Duffing hardening stiffness efficiently reduces the VIV initiation speed with small energy harvesting loss. Combining both stiffness types with appropriate control strategies presents a promising approach for achieving a broad synchronization VIV bandwidth and low initiation flow speed. Key parameters, such as the nondimensional parameter defining spring system obliquity and the ratio between undeformed spring length and cylinder diameter, significantly influence VIV response and energy harvesting. Moreover, optimal structural damping is vital to maximize energy harvesting efficiency, and understanding and controlling initial conditions are crucial for optimizing VIV synchronization bandwidth and energy harvesting efficiency for both bistable and Duffing hardening stiffness. This study provides valuable insights into VIV system dynamics and energy conversion potential with nonlinear springs, offering promising avenues for enhancing energy harvesting efficiency and inspiring further applications of nonlinear effects in VIV energy converters.

KEYWORDS

vortex-induced vibration energy converter, nonlinear stiffness, bistable, Duffing hardening, wake oscillator model

1 Introduction

Vortex-induced vibration (VIV), which occurs when a fluid flow interacts with a bluff body, induces self-sustained oscillations resulting from the periodic shedding of vortices in the wake. Due to the adverse consequences of VIV including fatigue damage and compromised integrity of structures in many engineering disciplines such as ocean, civil and aerospace engineering, extensive research efforts have been dedicated to comprehending the underlying mechanisms of VIV (Sarpkaya, 2004; Williamson and Govardhan, 2008; Bearman, 2011) and developing strategies to mitigate its detrimental effects on engineering structures (Zhu et al., 2015; Gao et al., 2021). However, in recent years, the increasing demand for renewable energy sources has fueled the recognition of the potential for VIV to be harnessed as a valuable source of renewable energy. The marine hydrokinetic (MHK) energy, which is abundant in steady current flows, such as those in rivers, tides, and ocean currents have sparked significant interest in exploring the concept of VIV energy harvesting, which aims to convert the MHK energy to usable electrical energy through VIV (Bernitsas, 2016). The concept of VIV-based energy converter was earlier proposed by (Bernitsas et al., 2008) and the first vortex induced vibration for aquatic clean energy (VIVACE) converter was developed and following generations of VIVACE converters are continuously developed (Kim et al., 2021).

The efficiency of the VIV energy converter depends on the lock-in region, where synchronization occurs when the vortex shedding frequency is close to the natural period of the structure. When the incoming flow velocity is out of the lock-in region, the amplitude decreases sharply, leading to reduced energy conversion efficiency or even complete energy loss (Wang et al., 2020; Lv et al., 2021). Thus, broadening the operating bandwidth becomes a key factor in enhancing the power capture efficiency. Equally crucial is the VIV initiation speed, which significantly impacts the VIV energy converter's design. A low-speed VIV initiation with broad synchronization bandwidth can substantially improve the converter's efficiency and scalability in practical applications. Numerous studies have explored diverse aspects of the VIV energy converter to enhance power capture efficiency. For instance, Azadeh-Ranjbar et al. (2018) investigated the influence of the cylinder's aspect ratio on the response of the VIV, finding increasing the aspect ratio amplifies the cylinder's amplitude and expands the lock-in frequency region of VIV. Zhang et al. (2017) examined the impact of the bluff body cross sections on VIV energy harvesting in tandem arrangements and concluded that the Cir-Tria prism has better performance on energy harvesting. Chang et al. (2011) applied passive turbulence control through selectively distributed surface roughness to enhance the VIV's synchronization range and amplitude. In addition to investigating the influence of the cylinder parameters, systemic parameters of the VIV setup have attracted attentions as well. Sun et al. (2016) studied the effect of mass-ratio, damping and stiffness on optimal hydrokinetic energy conversion of a rough cylinder, discovering that increasing the spring stiffness can shift the VIV synchronization range to higher flow velocity region. Further, Sun et al. (2018) introduced adaptive piecewise-linear springs in the hydrokinetic energy converter, revealing that the nonlinear springs can lower the VIV initiation speed and improve the energy harvesting efficiency.

In addition to the nonlinearity based on the piecewise-linear springs, the nonlinearity from the bistable or Duffing hardening springs can be a potential way to improve the energy harvesting efficiency (Ramlan et al., 2010). By selecting suitable spring nonlinearity, the theoretical energy harvester can achieve high performance across a significantly broader range of Reynolds numbers compared to a conventional system (Mackowski and Williamson, 2013). The bistable springs were applied in a VIV system by Huynh and Tjahjowidodo (2017) and experiments shown that the chaotic vibrations may occur, control strategy may be needed to prevent the VIV energy converter operating in chaotic regions (Huynh et al., 2018). Recently, the lock-in regime for VIV of a cylinder attached to a bistable spring was investigated by Badhurshah et al. (2019) with an Equilibrium Constraint approach proposed and compared to the wake oscillator model. While these studies have enhanced our understanding of the bistable VIV system's mechanism, a successful implementation of bistable springs in the VIV energy converter remains to be explored.

In the present study, the effect of nonlinearity, specifically from the nonlinear springs composed of two linear oblique springs, on the VIV energy harvesting is investigated. The nonlinearity effect includes not only the bistable effect but also the Duffing hardening effect as both effects can be easily achieved by the setup of two linear oblique springs. Through the wake oscillator model, the VIV response and the energy harvesting efficiency are examined, while the influence of the undeformed spring length, structural damping and initial condition on the VIV energy harvesting has been evaluated as well.

The rest of the paper is organized as follows. Following this introduction, the VIV energy harvesting model is presented in Section 2, including the wake oscillator model, nonlinear spring system and the state space model for solving the governing equations. In Section 3, the energy harvesting performance and dynamic responses for the VIV system with nonlinear springs are analyzed. In Section 4, the influence of undeformed spring length, structural damping and initial condition on the VIV energy harness is investigated. Finally, the conclusions are drawn in Section 5.

2 VIV modelling for energy harvesting

This section presents the governing equations for VIV modelling based on the wake oscillator model and introduces the numerical simulation method for solving the coupled equations between the VIV structure and the wake oscillator utilizing the state space model. The reliability of numerical model is verified by comparing it with the experimental results with the same parameters.

2.1 Governing equations for VIV based on wake oscillator model

A typical VIV system with linear springs is illustrated in Figure 1A. The system comprises a circular cylinder equipped with two sets of linear springs and dampers positioned at both ends. Under the influence of a steady current, the cylinder experiences oscillatory motion, which is constrained exclusively in the y direction. This oscillation converts the MHK energy to mechanical energy of the cylinder. Through the implementation of the power take-off system, the mechanical energy is further converted to electricity. In the present analysis, the power take-off system is simplified by considering it as a damping element incorporated into the structure. Moreover, we assume that the structural damping solely arises from the presence of the power take-off system.

The wake oscillator model, which was proposed by Facchinetti et al. (2004) and subsequently refined by Farshidianfar and Dolatabadi (2013), is employed to simulate the fluid dynamics. This model enables the simulation of the intricate fluid-structure interactions inherent in the VIV phenomenon. The coupling equations between the structure and the wake oscillator are expressed as follows:

$$\left(m_s+\frac{1}{4}\pi C_a\rho D^2\right)\ddot{y}+\left[r_s+\gamma\left(\frac{2\pi \mathrm{St}U}{D}\right)\rho D^2\right]\dot{y}+F(y)=\frac{1}{4}\rho U^2 D C_{L0} q \tag{1}$$

$$\ddot{q}+\epsilon\left(\frac{2\pi \mathrm{St}U}{D}\right)(1-\beta q^2+\lambda q^4)\dot{q}+\left(\frac{2\pi \mathrm{St}U}{D}\right)^2 q=\frac{A}{D}\ddot{y} \tag{2}$$

where m_s is the structural mass of the cylinder per unit length; $C_a\rho D^2\pi/4$ is the fluid added mass, in which C_a is the added mass coefficient, D is the cylinder diameter and ρ is the water density; r_s is the structural damping; γ is the stall parameter, which is given as $\gamma = C_d/(4\pi \mathrm{St})$ where C_d denotes the drag coefficient; St is the Strouhal number; U is the current velocity; $F(y)$ is the restoring force from the spring system; C_{L0} is the reference lift coefficient; q is the wake variable; ϵ is the coefficient of nonlinearity for the wake oscillator; β and λ are the damping coefficients of the second-order and the fourth-order term over ϵ, respectively; A is the force coefficient for the coupling of the wake oscillator.

2.2 Nonlinear spring system

For nonlinear spring system as shown in Figure 1B, the two identical springs of undeformed lengths l_0 with the stiffness of $k/2$ connect a lumped mass to a surrounding frame of span $2d$. It is assumed that the displacements of the mass are in a vertical direction, i.e., along the y-axis only.

$$F(y)=ky\left[1-l_0/\sqrt{y^2+d^2}\right] \tag{3}$$

Define the spring system obliquity as $\alpha = d/l_0$, the non-dimensional force can be written as

$$F^*(y^*)=\left(1-\frac{1}{\sqrt{y^{*2}+\alpha^2}}\right)y^* \tag{4}$$

where $F^*(y^*) = F(y)/(kl_0)$, $y^* = y/l_0$. For the present setup, $\alpha > 0$. When $\alpha < 1$, i.e., $l_0 > d$, the mass cannot be easily maintained in the central configuration, i.e., the zero-displacement position, $y = 0$, is not stable, while the two symmetric stable positions are adjacent to the central unstable state. Thus, it is a bistable system. When $\alpha \geq 1$, i.e., $l_0 \leq d$, the nonlinear system can be seen as a Duffing hardening system (Wang and Harne, 2017), the mass will come to rest at the zero-displacement position, $y = 0$, and it is a monstable system.

The dimensional potential energy of the nonlinear spring system is determined by

$$E^*(y^*)=\left(\sqrt{y^{*2}+\alpha^2}-1\right)^2 \tag{5}$$

where $E^*(y^*) = E(y)/(0.5kl_0^2)$.

The nondimensional equivalent stiffness of the nonlinear spring system is given as

$$\frac{dF^*(y^*)}{dy^*}=1-\frac{\alpha^2}{(y^{*2}+\alpha^2)^{3/2}} \tag{6}$$

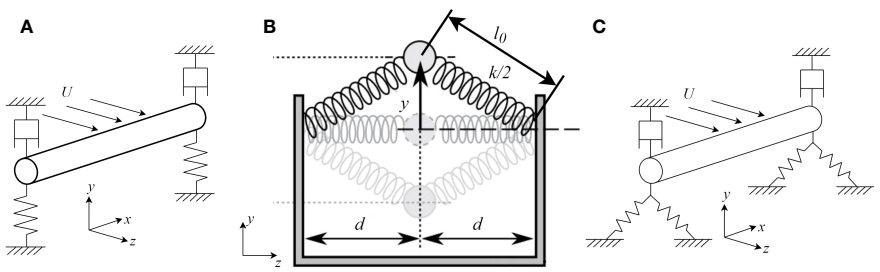

FIGURE 1
Schematic of **(A)** a VIV energy harvester with linear springs (Huynh and Tjahjowidodo, 2017), **(B)** a nonlinear spring system (Wang and Harne, 2017), and **(C)** a VIV energy harvester with nonlinear springs.

The nondimensional force-displacement curves for different α values are demonstrated in Figure 2A, illustrating the nonlinear characteristics of the system. Notably, a distinct jump in the resultant force from the two springs is observed as the mass passes through the symmetric stable positions. It is seen that the smaller value of α results in sharper jumps. Combining the nondimensional equivalent stiffness curves shown in Figure 2B, it is evident that the system exhibits negative stiffness within the regions between the two stable positions when $\alpha < 1$. Furthermore, absolute value of the equivalent stiffness at the central position increases as α value decreases. Conversely, when $\alpha > 1$, the equivalent stiffness becomes positive, signifying a transition to a monostable system. For the potential energy depicted in Figure 2C, two potential energy wells are apparent and an energy peak exists at the central unstable position when $\alpha < 1$. Smaller values of α correspond to higher central energy peaks, which results in increased difficulty for the mass to cross the central position and form inter-well oscillation. As α increases, the central energy peaks diminish. When $\alpha > 1$, the central energy peak vanishes entirely, indicating a monstable configuration.

2.3 State space model for solving governing equations

A state space model is adopted to solve the coupled equations of the structure and the wake oscillator. Define the following state vector:

$$x = [x_1, x_2, x_3, x_4]^{\mathrm{T}} = [y, \dot{y}, q, \dot{q}]^{\mathrm{T}} \tag{7}$$

For the VIV energy converter with a linear spring system as shown in Figure 1A, $F(y) = ky$, the governing equations (Eqs. (1) and (2)) can be written in a state-space form as:

$$\begin{aligned}
\dot{x}_1 &= x_2 \\
\dot{x}_2 &= \left\{\tfrac{1}{4}\rho U^2 D C_{L0} x_3 - [r_s + \gamma(\tfrac{2\pi \mathrm{St} U}{D})\rho D^2]x_2 - kx_1\right\}\left(\tfrac{4}{4m_s + \pi C_M \rho D^2}\right) \\
\dot{x}_3 &= x_4 \\
\dot{x}_4 &= \tfrac{A}{D}\left\{\tfrac{1}{4}\rho U^2 D C_{L0} x_3 - [r_s + \gamma(\tfrac{2\pi \mathrm{St} U}{D})\rho D^2]x_2 - kx_1\right\}\left(\tfrac{4}{4m_s + \pi C_M \rho D^2}\right) \\
&\quad - \epsilon(\tfrac{2\pi \mathrm{St} U}{D})(1 - \beta x_3^2 + \lambda x_3^4)x_4 - \left(\tfrac{2\pi \mathrm{St} U}{D}\right)^2 x_3
\end{aligned} \tag{8}$$

For the VIV energy converter with a nonlinear spring system as shown in Figure 1C, $F(y) = ky\{1 - [(y/l_0)^2 + \alpha^2]^{-1/2}\}$, Eqs. (1) and (2) are rewritten in a state-space form as:

$$\begin{aligned}
\dot{x}_1 &= x_2 \\
\dot{x}_2 &= \left\{\tfrac{1}{4}\rho U^2 D C_{L0} x_3 - [r_s + \gamma(\tfrac{2\pi \mathrm{St} U}{D})\rho D^2]x_2 - k\left[1 - \tfrac{1}{\sqrt{(x_1/l_0)^2 + \alpha^2}}\right]\right\}\left(\tfrac{4}{4m_s + \pi C_M \rho D^2}\right) \\
\dot{x}_3 &= x_4 \\
\dot{x}_4 &= \tfrac{A}{D}\left\{\tfrac{1}{4}\rho U^2 D C_{L0} x_3 - [r_s + \gamma(\tfrac{2\pi \mathrm{St} U}{D})\rho D^2]x_2 - k\left[1 - \tfrac{1}{\sqrt{(x_1/l_0)^2 + \alpha^2}}\right]\right\}\left(\tfrac{4}{4m_s + \pi C_M \rho D^2}\right) \\
&\quad - \epsilon(\tfrac{2\pi \mathrm{St} U}{D})(1 - \beta x_3^2 + \lambda x_3^4)x_4 - \left(\tfrac{2\pi \mathrm{St} U}{D}\right)^2 x_3
\end{aligned} \tag{9}$$

Based on the state space model, the displacement and velocity of the VIV system with linear and nonlinear spring systems can be numerically achieved for discrete time by solving Eqs. (8) and (9) using the 4$^{\mathrm{th}}$ order Runge-Kutta method. By obtaining the cylinder velocity, the time-averaged power harvested by the VIV system can be determined. For the sake of analysis simplification, the harnessed power per unit cylinder length is calculated based on the damping component r_s, which is given as:

$$P = \frac{r_s}{t_2 - t_1}\int_{t_1}^{t_2} \dot{y}^2 dt \tag{10}$$

where t_1 and t_2 are the starting and ending time for the power generation, respectively. In the present analysis, t_1 is selected as 1000s to avoid the initial transient effect from the numerical simulation and t_2 is selected to be 10000s.

The power conversion efficiency is defined as:

$$\eta(\%) = \frac{P}{P_{\mathrm{fluid}} \times \text{ Betz limit}} \times 100 \tag{11}$$

where the Betz limit serves as a commonly employed metric for assessing the power efficiency of wind turbines. It represents the theoretical upper bound of power efficiency (59.26%) that can be attained by any energy converter extracting power from an open flow (Kim et al., 2021);

P_{fluid} is the power in a fluid flowing through the area swept by the cylinder with unit length, which is define as:

$$P_{\mathrm{fluid}} = \frac{1}{2}\rho U^3 (2A_m + D) \tag{12}$$

where A_m is the motion amplitude of the cylinder.

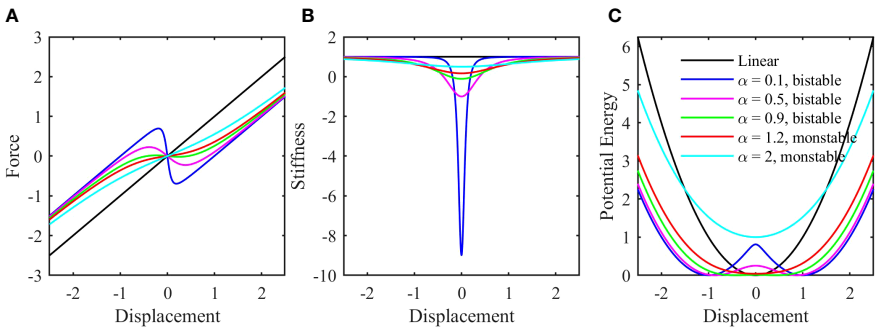

FIGURE 2
The characteristics of the nonlinear spring system with different α values: **(A)** The force-displacement curve; **(B)** The equivalent stiffness; **(C)** The potential energy.

2.4 Model parameters and verification of numerical model

The parameters of the VIV structure and the wake oscillator model are listed in Table 1. In the present study, the circular cylinder is assumed to be 1.0 m long.

To verify the numerical model, typical parameters of a VIV system presented by Khalak and Williamson (1999), i.e., $m^* = m_s/(0.25\pi\rho D^2) = 10.1$, $\xi = r_s/2\sqrt{k(m_s + 0.25\pi\rho D^2)} = 0.00129$, are used. In the experiments conducted by Khalak and Williamson (1999), a rigid cylinder was elastically mounted with linear springs, and its transverse oscillations were measured across a range of reduced velocities, considering both low and high mass-damping conditions. Though the parameters selected in the present study may not represent an optimistic design for a VIV energy harvester, they serve well for the verification of the numerical model since the primary objective of this study is to investigate the influence of nonlinear springs on the VIV system.

The nondimensional motion amplitude is plotted against the reduced velocity in Figure 3, where the reduced velocity, U_r, is defined as $U_r = U/(f_n D)$, with f_n is representing the natural frequency of the VIV system. The comparison between the numerical model results and the experimental data reveals a good agreement for the VIV upper branch measured points. However, it should be noted that the lower branch from the experiments cannot be accurately captured by the wake oscillator employed in this study. This limitation stems from the wake oscillator model's half-empirical nature, which involves fixed empirical parameters to simplify the intricate fluid-structure interaction. Thus, the inherent inability of the wake oscillator model to capture certain nonlinear behaviors, including the response seen in the lower branch, should be recognized (Han et al., 2023). Given that the primary focus of this study is to investigate the impact of nonlinear stiffness on the maximum responses of the VIV system, the omission of the upper-lower-branch transition in VIV can be considered reasonable. While the model may not fully capture the entire range of VIV behavior, it remains suitable for examining the specific objective of assessing the influence of nonlinear stiffness.

TABLE 1 Parameters of the VIV structure and the wake oscillator model.

VIV structure		Wake oscillator model	
Parameters	Values	Parameters	Values
D	0.5 m	C_a	1.0
m_s	1983.13 kg	C_d	2.3
k	42.16 kN/m	St	0.2
r_s	2.473 Ns/m	C_{L0}	0.3
		A	12
		ϵ	0.3
		β	0.0625
		λ	0.0005
		ρ	1000 kg/m^3

3 Energy harvesting performance and dynamic responses for VIV system with nonlinear springs

In this section, the energy harvesting performance and the dynamic responses of the VIV system with linear and nonlinear springs are investigated. In the numerical simulations, the structural damping ratio is selected as ξ= 0.0129, which corresponds to a damping coefficient of r_s=24.73 N/s. The remaining parameters are kept consistent with those used in the verification case. For the nonlinear springs, the length of the undeformed spring is l_0= 0.5 m, resulting a nondimensional undeformed spring length of l_0/D= 1.0. The α value varies from 0.1 to 2.0 to study the dynamic characteristics of the nonlinear system.

3.1 Energy harvesting performance

The harnessed power and the power conversion efficiency of the VIV system with nonlinear springs are presented in Figure 4, alongside the corresponding values obtained from the VIV system with linear springs. This comparison is conducted to showcase the energy harvesting performance of the VIV system, considering various α values associated with the nonlinear springs.

As shown in Figure 4A, the harnessed power by the VIV system with linear springs come from current velocity range from 1.5 m/s to 2.2 m/s, indicating the VIV harvesting device works only in this current velocity region. With the nonlinear springs utilized in the VIV system, the velocity range where the fluid energy can be harvested expands or shifts. For small α values (say 0.1 and 0.3) of the nonlinear springs, the range of the current velocity amenable to power extraction expand to both the larger and smaller velocity regions. Additionally, the averaged power peak shifts towards the lower velocity region, accompanied by a reduction of the peak magnitude.

Continuing with increasing α values (e.g., 0.5 and 0.7), the velocity range favorable for energy harvesting gradually shifts towards to lower velocity regions gradually and the power peak becomes flatter and lower. When the α approaches 0.9, the range of velocities suitable for power extraction shifts to a significantly lower region, spanning from 0.7m/s to 0.9 m/s, which is considerably lower than the range observed with linear springs. As α surpasses 1.0 (e.g., 1.2 and 2.0), the velocity range at which the VIV system operates effectively reverts back to the large velocity region with increasing α values and the peak power increases again.

In Figure 4B, it is as expected that the power harness efficiency, which is derived from the averaged power, exhibits a similar expansion or shift of the velocity range as observed Figure 4A. However, our attention is drawn to the peaks of the power harness efficiency curves. While the averaged power peaks obtained from the nonlinear springs with different α values consistently remain lower than those from the linear springs, the efficiency peak shows a distinct trend.

For small α values (e.g., 0.1 – 0.5), the efficiency peak undergoes minimal change as α increases, despite the decrease in peak power. This behavior can be attributed to the shift towards lower current velocity regions, where the fluid power flowing through the VIV device decreases due to the reduced velocity. As α continues to

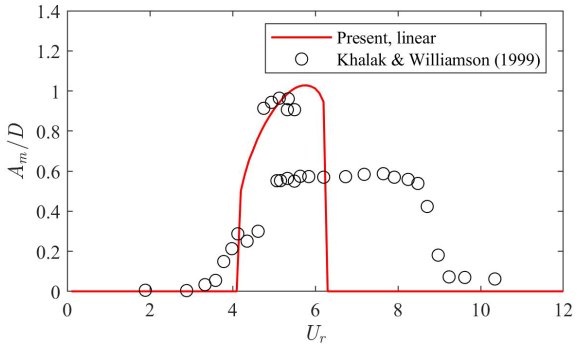

FIGURE 3
Verification of the numerical model with linear spring system.

increase while remaining smaller than 1.0, the efficiency peak gradually diminishes. However, when α exceeds 1.0, an interesting observation emerges: the efficiency peak experiences a sharp increase, even though the working velocity remains low (as seen in the curve with α = 1.2). Further increasing α results in a decrease in the efficiency peak but still larger than that from the linear springs.

It is seen that the utilization of bistable stiffness, characterized by small α values (0.1 – 0.5), demonstrates the capability to expand the working velocity range for energy harvesting without compromising the efficiency, in comparison to the VIV system equipped with linear springs. However, it is important to note that bistable stiffness with larger α values (> 0.5) leads to a decrease in energy harness efficiency, despite enabling the utilization of the lower current velocity range. On the other hand, when the nonlinear spring system becomes monstable (α > 1.0), a favorable shifting of the current velocity range can still be achieved, accompanied by a significant increase in the energy harness efficiency beyond what the linear springs system can achieve.

3.2 Dynamic responses of VIV system with nonlinear springs

To investigate the underlying reasons for the power harvesting performance of the VIV system, a comprehensive analysis of the motion characteristics is conducted and presented in Figures 5–9. Figure 5 specifically focuses on the VIV system equipped with linear springs, revealing the presence of regular motion in the displacement and velocity time histories (see Figures 5A, B). Moreover, the phase portrait shown in Figure 5C illustrates the formation of elliptical trajectories. Power spectral density analysis in Figure 5D further confirms the occurrence of synchronization between the fluid represented by the wake oscillator and the circular cylinder, with the cylinder's response predominantly exhibiting a single frequency.

Figure 6 illustrates the dynamic responses of the VIV system equipped with nonlinear springs with a value of α= 0.1. The displacement and velocity time histories displayed in Figures 6A, B showcase the cylinder's oscillation around the equilibrium position at y = 0.5, indicating an intra-well oscillation due to presence of the bistable stiffness. This observation is further substantiated by the phase portrait in Figure 6C, where the centre of the elliptical trajectory aligns with a displacement of 0.5 m. In addition, the symmetry observed in the phase portrait indicates the intra-well oscillation of the cylinder closely resembles that of a linear system. This can be explained by examining the equivalent stiffness curves shown in Figure 2B. Specifically, for the case α= 0.1, the curve demonstrates a narrow region of highly negative stiffness. However, outside this region, the equivalent stiffness at the stable equilibrium tends to be linear. Consequently, when the cylinder undergoes intra-well oscillations with small amplitudes, it remains within the linear stiffness region and does not enter the nonlinear regime. Notably, Figure 6D reveals the persistence of synchronization between the fluid and the circular cylinder as evidenced by the alignment of the frequency peaks between the structure and the wake oscillator. The dominated frequency of the structure motion is the lowest frequency peak, and the displacement and velocity time histories appear regular though some minor higher frequency peaks are observed in the power spectral density curve of the cylinder.

Upon increasing α to 0.5 for the nonlinear springs, the dynamic responses of the VIV system are presented in Figure 7 Notably, the steady oscillation of the cylinder remains intra-well. However, a distinct change can be seen in the displacement and velocity time histories depicted in Figures 7A, B, where asymmetry in the crests

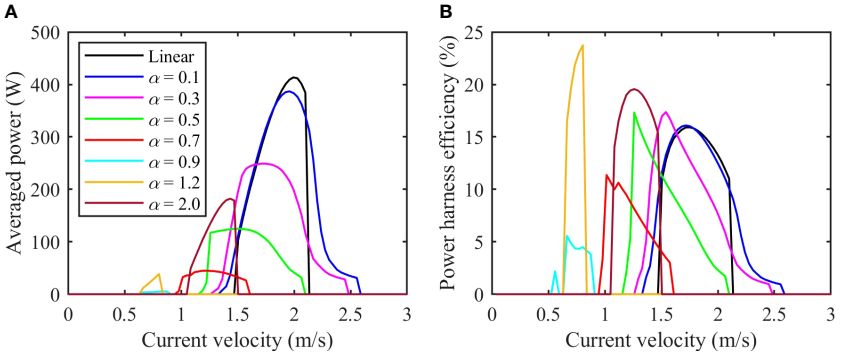

FIGURE 4
The power **(A)** and power efficiency **(B)** harvested by the VIV system with nonlinear spring stiffness l_0/D = 1.0, y_0 = 0, where y_0 is the initial displacement of the cylinder).

10.3389/fmars.2023.1270286

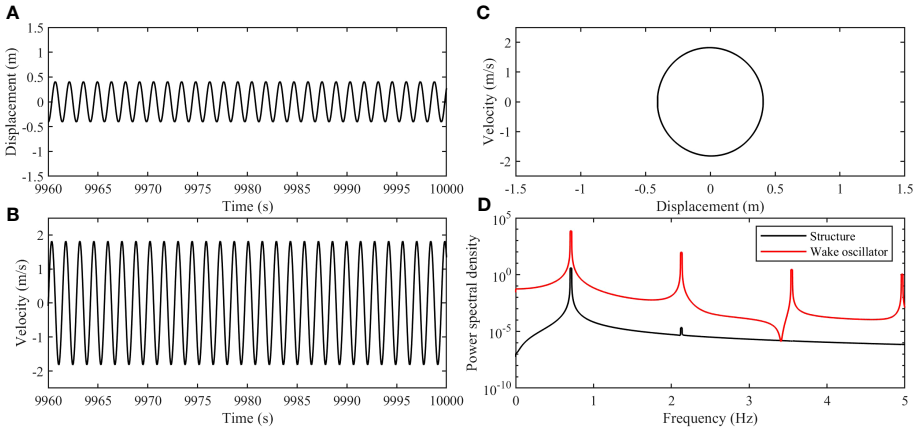

FIGURE 5
The dynamic responses of the cylinder with linear springs (y_0 = 0, U = 2.0 m/s): **(A)** The displacement time history; **(B)** The velocity time history; **(C)** The phase portrait from the displacement and the velocity; **(D)** Power spectral density of the displacement for the cylinder and the wake oscillator.

and troughs is evident, unlike the case of α= 0.1. This asymmetry is further manifested in the phase portrait shown in Figure 7C, which resembles the shape of a water droplet. The emergence of this asymmetry can be attributed to the increased α value, which expands the nonlinear stiffness region, as illustrated in Figure 2B. During an oscillation period, the cylinder traverses both the linear stiffness region, which lies far from the central position and the nonlinear negative stiffness region near the central position y = 0 without crossing it. Consequently, an asymmetric oscillation pattern is formed around the stable equilibrium position. Moreover, Figure 7D confirms the synchronization between the cylinder and the wake oscillator, reinforcing the influence of the fluid on the cylinder's response.

As α further increases to 0.9 for the nonlinear springs, the cylinder demonstrates distinct dynamic responses, as depicted in Figure 8 Notably, the displacement and velocity time histories in Figures 8A, B exhibit irregular features, and the cylinder crosses the central position y = 0, indicating the occurrence of inter-well oscillation. This behavior can be attributed to the significant reduction of the potential barrier at the central position as α reaches 0.9, facilitating the cylinder's movement across the central position and the formation of the inter-well oscillation. However, Figure 8C reveals that the phase portrait fails to form a closed shape, indicating the emergency of chaotic oscillations in the cylinder's motion. Moreover, the power spectral density curves depicted in Figure 8D confirm the absence of synchronization between the cylinder and the wake oscillator, as no dominating frequency peak is observed in the cylinder motion. These findings suggest that the cylinder undergoes chaotic motion under the influence of the nonlinear springs with α= 0.9.

The subsequent increase of α to 1.2 signifies the transition of the VIV system with nonlinear spring system to a monstable state. This monstable characteristic is evident in the dynamic responses of the cylinder, as depicted in Figure 9 Notably, the displacement and velocity time histories displayed in Figures 9A, B exhibit steady regular shapes with a mean displacement of 0, indicative of a stable oscillatory behavior. Furthermore, Figure 9C demonstrates the

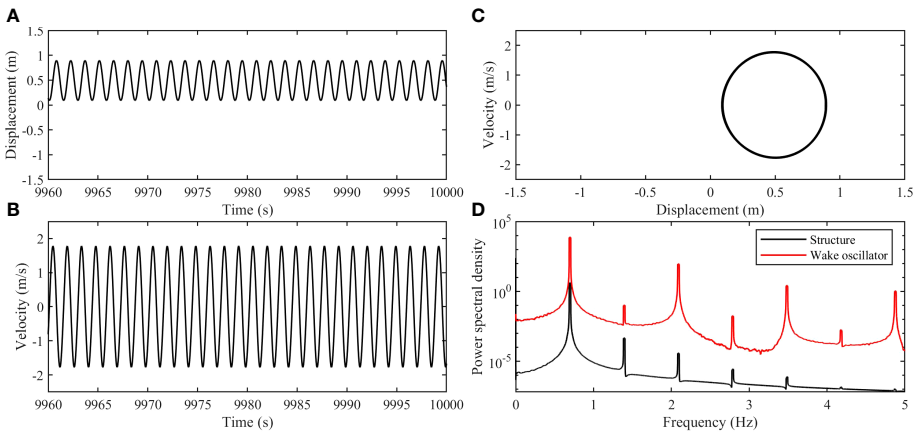

FIGURE 6
The dynamic responses of the cylinder with α = 0.1 (l_0/D = 1.0, y_0 = 0, U = 1.9 m/s): **(A)** The displacement time history; **(B)** The velocity time history; **(C)** The phase portrait from the displacement and the velocity; **(D)** Power spectral density of the displacement for the cylinder and the wake oscillator.

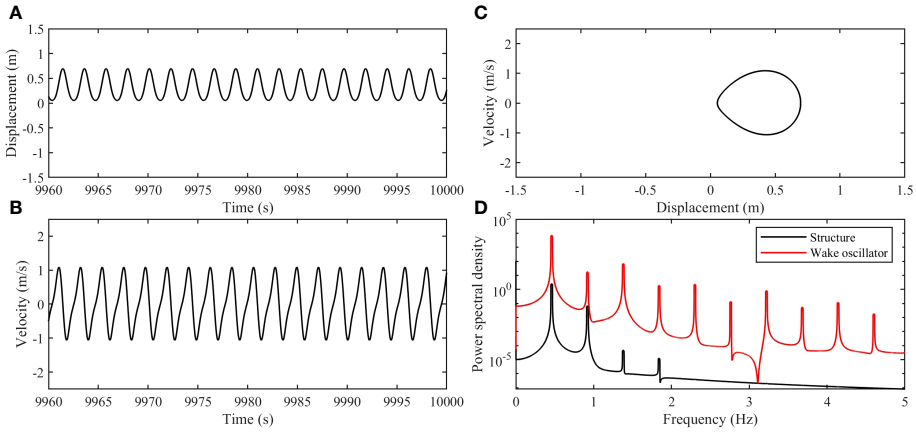

FIGURE 7
The dynamic responses of the cylinder with α = 0.5 (l_0/D = 1.0, y_0 = 0, U = 1.3 m/s): **(A)** The displacement time history; **(B)** The velocity time history; **(C)** The phase portrait from the displacement and the velocity; **(D)** Power spectral density of the displacement for the cylinder and the wake oscillator.

formation of an elliptical trajectory in the phase portrait, further confirming the monstable nature of the system. Additionally, the synchronization between the cylinder and the wake oscillator is observed, as evidenced by the power density curves presented in Figure 9D. These findings illustrate the distinct dynamic responses of the VIV system with nonlinear springs in the monostable regime, characterized by stable oscillations and synchronization with the wake oscillator.

4 Key parameters for VIV system with nonlinear springs

4.1 Nondimensional undeformed spring length

While the nondimensional parameter α determines the dynamic characteristics of the nonlinear spring system itself, the nondimensional undeformed spring length, which is the ratio between the dimensional undeformed spring length to the cylinder diameter, may influence the dynamic responses of the cylinder when the nonlinear springs are coupled to the VIV system. This nondimensional parameter serves as an indicator of the compatibility between the nonlinear springs and the VIV system.

To investigate this influence, four cases with different nondimensional undeformed spring length ratios (0.6, 1.0, 2.0 and 5.0) are considered while the other parameters are kept unchanged from Section 3. The value of α for all three cases is from 0.1 to 2.0. Figure 10 illustrates the power conversion efficiency for each case. It is observed that for bistable nonlinear spring system, varying the l_0/D values has a significant impact on the power conversion efficiency magnitude while the range of current velocities that can be harvested is not remarkably changed. For example, when α= 0.1, the power efficiency peaks of the case with l_0/D= 0.6 demonstrate a significant drop compared to those of cases with l_0/D= 1.0, 2.0 and 5.0. For cases with α= 0.5, a remarkable

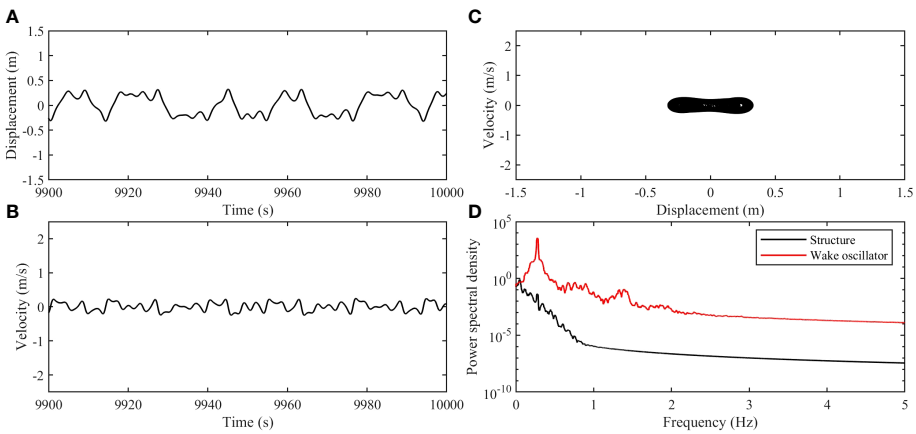

FIGURE 8
The dynamic responses of the cylinder with α = 0.9 (l_0/D = 1.0, y_0 = 0, U = 0.7 m/s): **(A)** The displacement time history; **(B)** The velocity time history; **(C)** The phase portrait from the displacement and the velocity; **(D)** Power spectral density of the displacement for the cylinder and the wake oscillator.

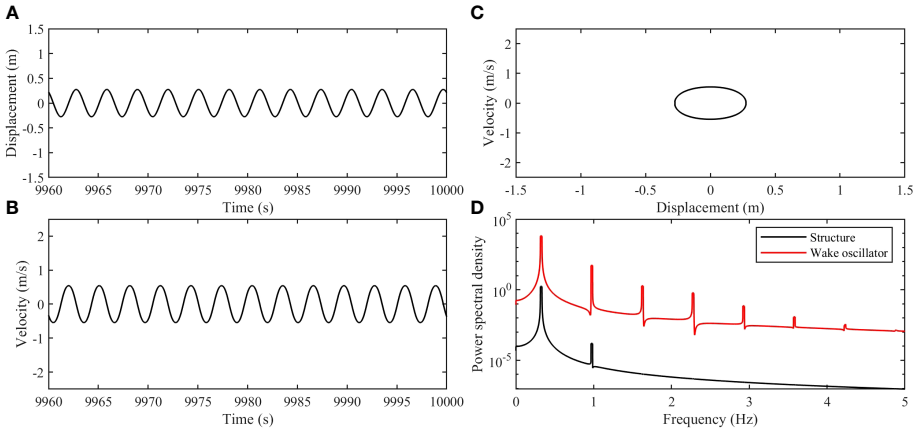

FIGURE 9
The dynamic responses of the cylinder with α = 1.2 (l_0/D = 1.0, y_0 = 0, U = 0.8 m/s): **(A)** The displacement time history; **(B)** The velocity time history; **(C)** The phase portrait from the displacement and the velocity; **(D)** Power spectral density of the displacement for the cylinder and the wake oscillator.

increase of the power conversion efficiency is observed when the l_0/D value increases from 0.6 to 5. On the other hand, for the monstable nonlinear spring system (i.e., α= 1.2 and 2), the influence of different l_0/D values is relatively small.

The dynamic responses of the cylinder for cases with different l_0/D values are examined, as depicted in Figures 11 and 12. For cases with α= 0.1, the displacement time histories for the cases with l_0/D= 1.0, 2.0 and 5.0 exhibit intra-well oscillations, with the equilibrium positions shift farther away from the central position (y= 0) as l_0/D increases. However, in the case with l_0/D= 0.6, the cylinder displacement shows a combination of inter-well and intra-well oscillations. The phase portrait curves of l_0/D= 1.0, 2.0 and 5.0 show similar closed shapes with different center locations, indicating the regular oscillations with different equilibrium positions. In contrast, the phase portrait curve for l_0/D= 0.6 demonstrates that the cylinder motions tend to be chaotic. For cases with α= 0.5 as shown in Figure 12, all the four cases with different l_0/D values show stable intra-well oscillations, and motion amplitude increases with the increasing l_0/D value. The equilibrium position shifts further away from the central position (y= 0) as the l_0/D value increases as well.

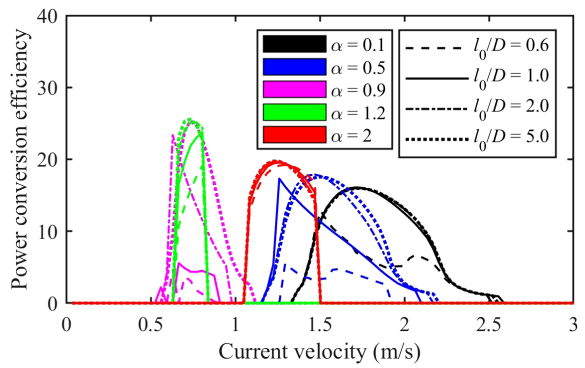

FIGURE 10
The power conversion efficiency of the VIV energy converter equipped with nonlinear springs with different l_0/D values.

4.2 Structural damping

The structural damping, which is assumed from the power take off system only in the present study, is a key design parameter in the VIV energy harvesting device. Small structural damping may lead to suboptimal energy conversion efficiency from the mechanical energy to electricity, while excessive structural damping may impede cylinder motions, resulting in reduced energy conversion efficiency from the fluid energy to mechanical energy.

The influence of the structural damping on the power conversion efficiency is investigated by varying the damping ratio ξ while all the other parameters in the simulations are kept the same with those from Section 3. The power conversion efficiency curves are shown in Figure 13. It is evident that if the damping ratio is small, i.e., ξ= 0.0013, the power conversion efficiency is very low for all the α values, indicating that the bottle-neck of the VIV system is on the damping ratio. When ξ increases from 0.0013 to 0.013, the power conversion efficiency increases significantly for all the α values, though the different increase magnitudes are observed for different α values. A further increase of the ξ value from 0.013 to 0.13 demonstrate distinct influences on the power conversion efficiency for different α values. For small α values, i.e., 0.1 and 0.5, a further remarkable increase of the power conversion efficiency is observed, while for α values of 0.9, 1.2 and 2.0, the cylinder motions are suppressed due to the increased damping ratios. Thus, striking the right balance in structural damping is essential for achieving optimal energy conversion efficiency in the design of VIV energy harvesting device.

4.3 Initial conditions

The sensitivity of dynamic responses to the initial conditions is well-documented in bistable system (Wang and Harne, 2017). In the context of this study, where the bistable springs are coupled with the wake oscillator model representing the fluid, it is essential to investigate where the coupled VIV system with bistable springs retains sensitivity to the initial conditions.

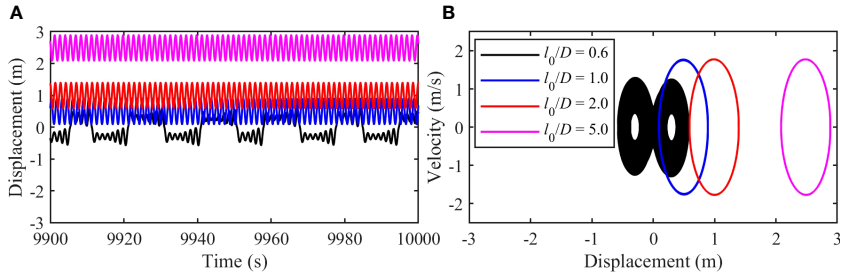

FIGURE 11
The dynamic responses of the cylinder with different l_0/D values (α = 0.1, y_0 = 0, U = 1.89 m/s): **(A)** The displacement time history; **(B)** The phase portrait from the displacement and the velocity.

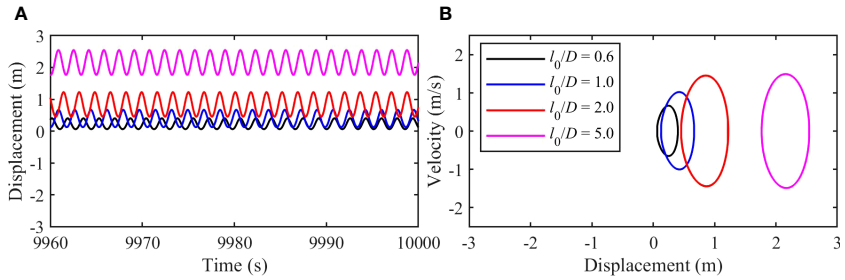

FIGURE 12
The dynamic responses of the cylinder with different l_0/D values (α = 0.5, y_0 = 0, U = 1.65 m/s): **(A)** The displacement time history; **(B)** The phase portrait from the displacement and the velocity.

The impact of different initial conditions on the power conversion efficiency is analysed by investigating various scenarios, as depicted in Figure 14. The results reveal that the initial displacements of the cylinder play a role in determining the range of current velocities that the VIV system can effectively utilize, particularly affecting the maximum current velocity that can be harnessed. In the case of α= 0.1, which indicates the system is bistable, the utilizable current velocity range experiences a slight initial increase, followed by a decrease with higher initial displacements. Conversely, for the system with α= 2.0, the maximum utilizable current velocity initially increases with higher initial displacements, but eventually becomes bounded. Both bistable and monostable nonlinear VIV systems are influenced by the initial conditions, with the primary impact being on the range of utilizable flow velocities, as certain initial conditions may prevent the VIV system from being excited.

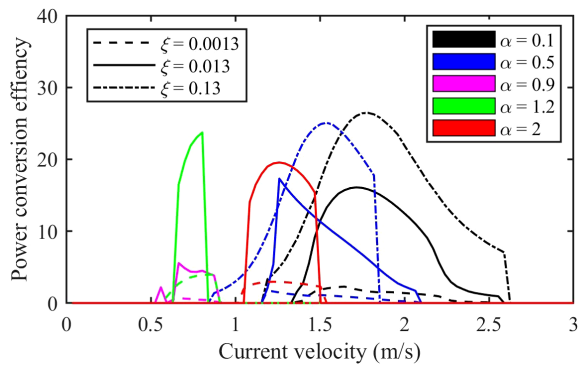

FIGURE 13
The power conversion efficiency of the VIV energy converter equipped with nonlinear springs with different damping ratios.

5 Conclusions

The nonlinear effect from two linear oblique springs on the VIV energy harvesting is investigated based on the wake oscillator model. The bistable stiffness and the Duffing hardening stiffness are both considered and their effects on the system's response and energy harvesting performance are studied. Notably, the application of nonlinear stiffness in the VIV system shows promising outcomes in terms of expanding the synchronization bandwidth of VIV or lowering the VIV initiation flow speed.

The bistable stiffness with small α values demonstrates a capacity to broaden the synchronization velocity range, while large α values lower the VIV initiation flow speed. However, the VIV response under bistable stiffness with large α values tends to become chaotic. In contrast, the system with Duffing hardening stiffness exhibits a monstable behavior and proves more efficient in lowering the VIV initiation flow speed without significant energy harvesting efficiency loss. This may enlighten the combination of the bistable stiffness and Duffing hardening stiffness in a single VIV

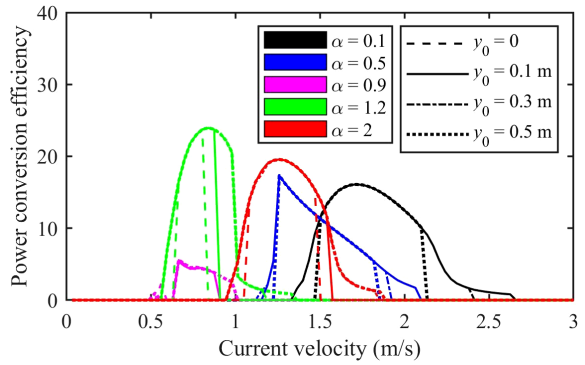

FIGURE 14
The power conversion efficiency of the VIV energy converter equipped with nonlinear springs with different initial conditions.

setup with two oblique springs by employing appropriate control strategies to adjust α values, thus achieving a broad synchronization VIV bandwidth with a low initiation flow speed.

For the nonlinear spring system composed of two linear oblique springs, the nondimensional parameter α, which defines the obliquity of the spring system in undeformed state, is a key parameter influencing the nonlinearity. When this nonlinear spring system is applied in a VIV system, the ration between the undeformed spring length to the cylinder diameter serves as an essential indicator of the compatibility between the nonlinear springs and the VIV system. Both parameters significantly influence the VIV response and energy harvesting performance, calling for careful consideration in the design and optimization process.

Regarding structural damping, which is assumed to be all from the PTO system, it is evident that small damping results in larger VIV response but lower power conversion efficiency. Conversely, higher structural damping may lead to smaller VIV motion amplitudes. The optimal structural damping is a key factor to achieve the highest energy harvesting efficiency from VIV.

Lastly, the initial condition of the VIV is found to exert a considerable influence on the VIV response and corresponding energy harvesting, regardless of whether bistable or Duffing hardening stiffness is at play. Understanding and controlling the initial condition can thus contribute significantly to optimizing the VIV synchronization bandwidth and energy harvesting performance.

It's important to recognize that the introduction of nonlinearities can also introduce complexities, such as the potential for chaotic behavior within the VIV system. As a result, optimizing the performance of a nonlinear VIV system demands intricate design strategies, significantly more involved than those applied in linear systems. Moreover, the implementation of nonlinear VIV systems might necessitate more sophisticated control mechanisms to sustain optimal working conditions. Thus, further studies on the optimization and control of the VIV energy harvesting with nonlinear springs are needed.

Data availability statement

The raw data supporting the conclusions of this article will be made available by the authors, without undue reservation.

Author contributions

ZG: Conceptualization, Formal Analysis, Software, Writing – original draft. ZL: Funding acquisition, Writing – review & editing. JN: Data curation, Methodology, Writing – review & editing. QY: Visualization, Writing – review & editing. KL: Project administration, Writing – review & editing.

Funding

The author(s) declare financial support was received for the research, authorship, and/or publication of this article. This research is supported by the National Natural Science Foundation of China (Grant No. 52271279 and Grant No. 52071162) and the Research Start-Up Funds of Jiangsu University of Science and Technology (Grant No. 1012932104).

Conflict of interest

The authors declare that the research was conducted in the absence of any commercial or financial relationships that could be construed as a potential conflict of interest.

Publisher's note

All claims expressed in this article are solely those of the authors and do not necessarily represent those of their affiliated organizations, or those of the publisher, the editors and the reviewers. Any product that may be evaluated in this article, or claim that may be made by its manufacturer, is not guaranteed or endorsed by the publisher.

References

Azadeh-Ranjbar, V., Elvin, N., and Andreopoulos, Y. (2018). Vortex-induced vibration of finite-length circular cylinders with spanwise free-ends: Broadening the lock-in envelope. *Phys. Fluids* 30, 105104. doi: 10.1063/1.5042774

Badhurshah, R., Bhardwaj, R., and Bhattacharya, A. (2019). Lock-in regimes for Vortex-Induced Vibrations of a cylinder attached to a bistable spring. *J. Fluids Struct.* 91, 102697. doi: 10.1016/j.jfluidstructs.2019.102697

Bearman, P. W. (2011). Circular cylinder wakes and vortex-induced vibrations. *J. Fluids Struct.* 27, 648–658. doi: 10.1016/j.jfluidstructs.2011.03.021

Bernitsas, M. M. (2016). *Harvesting energy by flow included motions BT - springer handbook of ocean engineering*. Eds. M. R. Dhanak and N. I. Xiros (Cham: Springer International Publishing). doi: 10.1007/978-3-319-16649-0_47

Bernitsas, M. M., Raghavan, K., Ben-Simon, Y., and Garcia, E. M. H. (2008). VIVACE (Vortex induced vibration aquatic clean energy): A new concept in generation of clean and renewable energy from fluid flow. *J. Offshore Mech. Arct. Eng.* 130. doi: 10.1115/1.2957913

Chang, C.-C., Ajith Kumar, R., and Bernitsas, M. M. (2011). VIV and galloping of single circular cylinder with surface roughness at 3.0×104≤Re≤1.2×105. *Ocean Eng.* 38, 1713–1732. doi: 10.1016/j.oceaneng.2011.07.013

Facchinetti, M. L., de Langre, E., and Biolley, F. (2004). Coupling of structure and wake oscillators in vortex-induced vibrations. *J. Fluids Struct.* 19, 123–140. doi: 10.1016/j.jfluidstructs.2003.12.004

Farshidianfar, A., and Dolatabadi, N. (2013). Modified higher-order wake oscillator model for vortex-induced vibration of circular cylinders. *Acta Mech.* 224, 1441–1456. doi: 10.1007/s00707-013-0819-0

Gao, Z., Efthymiou, M., Cheng, L., Zhou, T., Minguez, M., and Zhao, W. (2021). Towards a model of hydrodynamic damping for a circular cylinder with helical strakes at low KC. *Mar. Struct.* 78, 103025. doi: 10.1016/j.marstruc.2021.103025

Han, P., Langre, E., Thompson, M. C., and Hourigan, K. (2023). *Vortex-induced vibration forever even with high structural damping*. (Cambridge University Press: The Journal of Fluid Mechanics). 962, 1–16. doi: 10.1017/jfm.2023.268

Huynh, B. H., and Tjahjowidodo, T. (2017). Experimental chaotic quantification in bistable vortex induced vibration systems. *Mech. Syst. Signal Process.* 85, 1005–1019. doi: 10.1016/j.ymssp.2016.09.025

Huynh, B. H., Tjahjowidodo, T., Zhong, Z. W., Wang, Y., and Srikanth, N. (2018). Design and experiment of controlled bistable vortex induced vibration energy harvesting systems operating in chaotic regions. *Mech. Syst. Signal Process.* 98, 1097–1115. doi: 10.1016/j.ymssp.2017.06.002

Khalak, A., and Williamson, C. H. K. (1999). Motions, forces and mode transitions in vortex-induced vibrations at low mass-damping. *J. Fluids Struct.* 13, 813–851. doi: 10.1006/jfls.1999.0236

Kim, E. S., Sun, H., Park, H., Shin, S., Chae, E. J., Ouderkirk, R., et al. (2021). Development of an alternating lift converter utilizing flow-induced oscillations to harness horizontal hydrokinetic energy. *Renew. Sustain. Energy Rev.* 145, 111094. doi: 10.1016/j.rser.2021.111094

Lv, Y., Sun, L., Bernitsas, M. M., and Sun, H. (2021). A comprehensive review of nonlinear oscillators in hydrokinetic energy harnessing using flow-induced vibrations. *Renew. Sustain. Energy Rev.* 150, 111388. doi: 10.1016/j.rser.2021.111388

Mackowski, A. W., and Williamson, C. H. K. (2013). An experimental investigation of vortex-induced vibration with nonlinear restoring forces. *Phys. Fluids* 25. doi: 10.1063/1.4819082

Ramlan, R., Brennan, M. J., Mace, B. R., and Kovacic, I. (2010). Potential benefits of a non-linear stiffness in an energy harvesting device. *Nonlinear Dyn.* 59, 545–558. doi: 10.1007/s11071-009-9561-5

Sarpkaya, T. (2004). A critical review of the intrinsic nature of vortex-induced vibrations. *J. Fluids Struct.* 19, 389–447. doi: 10.1016/j.jfluidstructs.2004.02.005

Sun, H., Kim, E. S., Nowakowski, G., Mauer, E., and Bernitsas, M. M. (2016). Effect of mass-ratio, damping, and stiffness on optimal hydrokinetic energy conversion of a single, rough cylinder in flow induced motions. *Renew. Energy* 99, 936–959. doi: 10.1016/j.renene.2016.07.024

Sun, H., Ma, C., and Bernitsas, M. M. (2018). Hydrokinetic power conversion using Flow Induced Vibrations with nonlinear (adaptive piecewise-linear) springs. *Energy* 143, 1085–1106. doi: 10.1016/j.energy.2017.10.140

Wang, J., Geng, L., Ding, L., Zhu, H., and Yurchenko, D. (2020). The state-of-the-art review on energy harvesting from flow-induced vibrations. *Appl. Energy* 267, 114902. doi: 10.1016/j.apenergy.2020.114902

Wang, K. W., and Harne, R. L. (2017). *Harnessing bistable structural dynamics: for vibration control, energy harvesting and sensing* (Hoboken, New Jersey: John Wiley & Sons).

Williamson, C. H. K., and Govardhan, R. (2008). A brief review of recent results in vortex-induced vibrations. *J. Wind Eng. Ind. Aerodyn.* 96, 713–735. doi: 10.1016/j.jweia.2007.06.019

Zhang, B., Song, B., Mao, Z., Tian, W., and Li, B. (2017). Numerical investigation on VIV energy harvesting of bluff bodies with different cross sections in tandem arrangement. *Energy* 133, 723–736. doi: 10.1016/j.energy.2017.05.051

Zhu, H., Yao, J., Ma, Y., Zhao, H., and Tang, Y. (2015). Simultaneous CFD evaluation of VIV suppression using smaller control cylinders. *J. Fluids Struct.* 57, 66–80. doi: 10.1016/j.jfluidstructs.2015.05.011

frontiers | Frontiers in Marine Science

TYPE Original Research
PUBLISHED 09 November 2023
DOI 10.3389/fmars.2023.1270428

OPEN ACCESS

EDITED BY
Shengjie Rui,
Norwegian Geotechnical Institute (NGI), Norway

REVIEWED BY
Lysel Garavelli,
Pacific Northwest National Laboratory (DOE), United States
Kanmin Shen,
PowerChina Huadong Engineering Corporation Limited, China
Hang Xu,
Zhejiang University, China, in collaboration with reviewer KS

*CORRESPONDENCE
Jezella I. Peraza
jezper@uw.edu

RECEIVED 31 July 2023
ACCEPTED 23 October 2023
PUBLISHED 09 November 2023

CITATION
Peraza JI and Horne JK (2023) Quantifying conditional probabilities of fish-turbine encounters and impacts.
Front. Mar. Sci. 10:1270428.
doi: 10.3389/fmars.2023.1270428

Quantifying conditional probabilities of fish-turbine encounters and impacts

Jezella I. Peraza* and John K. Horne

Fisheries Acoustic Research Laboratory, University of Washington, School of Aquatic and Fishery Sciences, Seattle, WA, United States

Tidal turbines are one source of marine renewable energy but development of tidal power is hampered by uncertainties in fish-turbine interaction impacts. Current knowledge gaps exist in efforts to quantify risks, as empirical data and modeling studies have characterized components of fish approach and interaction with turbines, but a comprehensive model that quantifies conditional occurrence probabilities of fish approaching and then interacting with a turbine in sequential steps is lacking. We combined empirical acoustic density measurements of Pacific herring (*Clupea pallasii*) and when data limited, published probabilities in an impact probability model that includes approach, entrainment, interactions, and avoidance of fish with axial or cross-flow tidal turbines. Interaction impacts include fish collisions with stationary turbine components, blade strikes by rotating blades, and/or a collision followed by a blade strike. Impact probabilities for collision followed by a blade strike were lowest with estimates ranging from 0.0000242 to 0.0678, and highest for blade strike ranging from 0.000261 to 0.40. Maximum probabilities occurred for a cross-flow turbine at night with no active or passive avoidance. Estimates were lowest when probabilities were conditional on sequential events, and when active and passive avoidance was included for an axial-flow turbine during the day. As expected, conditional probabilities were typically lower than analogous independent events and literature values. Estimating impact probabilities for Pacific herring in Admiralty Inlet, Washington, United States for two device types illustrates utilization of existing data and simultaneously identifies data gaps needed to fully calculate empirical-based probabilities for any site-species combination.

KEYWORDS

collision risk, empirical modeling, encounter, environmental impact, fish, hydrokinetic turbines, marine renewable energy, tidal energy

1 Introduction

Tidal turbines are a potential Marine Renewable Energy (MRE) source that can be deployed in high flow current regions (Pelc and Fujita, 2002). Tidal energy technology has been deployed but widespread adoption is hampered, in part, by concerns of aquatic animal impacts (Copping and Hemery, 2020). Primary concerns include collisions with stationary

turbine components and/or strikes from rotating blades that could inhibit growth or affect survival of fish, seabirds, or marine mammals (Hemery et al., 2021). Knowledge gaps and inadequate empirical data on animal-device interactions necessitate obtaining, quantifying, and interpreting physical and biological data that can be used to discern the influence of animal-turbine encounters (e.g., Copping and Hemery, 2020), collisions (e.g., Müller et al., 2023), and blade strikes (e.g., Castro-Santos and Haro, 2015; Courtney et al., 2022). Unverified perceptions of mortality from animal-device interactions can impede development of monitoring regulations for tidal turbine sites. Comprehensive baseline and post-installation monitoring data on animal-tidal device interactions are not available, resulting in uncertainty among regulators who are cautious when permitting full-scale MRE sites (Copping et al., 2020a).

Encounter and collision rates between aquatic animals and tidal turbines are not well quantified due to limited opportunities and appropriate technologies to observe, measure, and characterize interactions (Fox et al., 2018; Courtney et al., 2022; Bender et al., 2023). Worldwide, there have been few (Copping et al., 2021) acoustic and optical technologies deployed to monitor tidal energy sites (e.g., Williamson et al., 2017; Staines et al., 2022). Even though stationary acoustic multibeam and multi-frequency echosounders are available, their deployment is often limited due to operational constraints including limited detection of weaker targets (Williamson et al., 2017). An approach that supplements empirical measures when animal behavior and hydrodynamic data are limited is the use of models to estimate the probability of animal-device interactions (Buenau et al., 2022). These studies include fish swimming trajectories during approach (Shen et al., 2016) or interaction (e.g., Viehman and Zydlewski, 2015; Bevelhimer et al., 2017) with tidal turbines. There remains a need for a comprehensive model that quantifies probabilities as fish approach and potentially interact with a hydrokinetic turbine.

To fully estimate potential encounter and interaction risks that influence MRE monitoring requirements and operational regulations, additional risk factors should be incorporated into a conditional, encounter-impact probability model. Current empirical observations and many encounter models lack active and passive avoidance behaviors of fish as they approach and interact with a device. Collision with stationary components of a device is another factor that is not commonly separated from blade strikes in published models. Collisions with stationary structures (Müller et al., 2023) could disorient fish (Courtney et al., 2022) and potentially lead to a blade strike.

This study develops a conditional probabilistic model that quantifies encounter and interactions of fish with tidal turbines. The encounter-impact model estimates probabilities of approach, encounter, collision with stationary components, blade strike by rotating blades, and sequential collision and blade strike using acoustic data from Admiralty Inlet, Washington, United States, and literature values when empirical data are lacking. Existing data gaps are identified along with appropriate next steps for model application. This encounter-impact model is designed to be generic and can be applied to any potential tidal energy project site.

2 Methods

2.1 Model description

The encounter-impact model computes occurrence probabilities for individual model components, and conditional probabilities of fish approaching and potentially interacting with a tidal turbine in sequential steps (Figure 1).

The approach phase quantifies when an animal enters the vicinity of an MRE device and includes the model domain, zone of influence, and estimates of active or passive avoidance. The model domain is comprised of the study area and estimates the probability of whether a fish is present within a site. If fish are present, then the domain model component is assigned a probability value of 1 (Table 1). As an empirical analog, Shen et al. (2016) used mobile hydroacoustics to track fish approaching a cross-flow tidal turbine and observed responses to a turbine by fish, measured using change in swimming direction, at distances over a hundred meters (Shen et al., 2016). We define the zone of influence

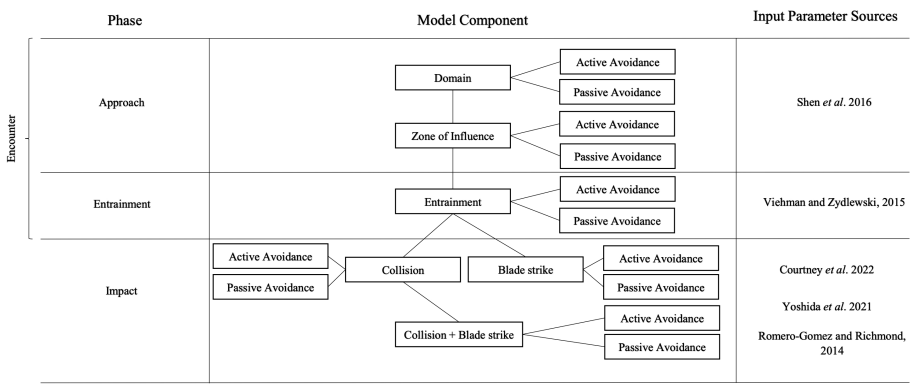

FIGURE 1
A schematic of the empirical encounter-impact probability model. The left column identifies the model phase, the center column details model components, and the right column identifies literature used to extract parameter values that are used in corresponding model components.

TABLE 1 Probability equations for each component of the encounter-impact model.

Model component	Probability equation
Domain	P(Domain) = [1, 0]
Zone of Influence	P(Zone of Influence) = 1 * P(1 – Avoid)
Entrainment	P(Entrainment) = P(Zone of Influence) * P(1 – Avoid | Zone of Influence)
Collision	P(Collision) = P(Entrainment) * P(Collision | Entrainment)
Blade strike	P(Blade strike) = P(Entrainment) * P(Blade strike | Entrainment)
Collision and Blade strike	P(Collision and Blade strike) = P(Entrainment) * [P (Collision) * P(Blade strike | Collision)]
Overall Impact	P(Overall Impact) = {1 * P(1 – Avoid) * [P(Zone of Influence) * P(1 – Avoid | Zone of Influence)] * [P (Entrainment) * P(Collision | Entrainment)]} + {1 * P(1 – Avoid) * [P(Zone of Influence) * P(1 – Avoid | Zone of Influence)] * [P(Entrainment) * P(Blade strike | Entrainment)]} + {1 * P(1 – Avoid) * [P(Zone of Influence) * P(1 – Avoid | Zone of Influence)] * [P(Entrainment) * (P(Collision) * P (Blade strike | Collision))]} *Simplified:* P(Overall Impact) = P(Collision) + P(Blade strike) + P(Collision and Blade strike)

as the reaction distance between an animal and the turbine. In this model, the zone of influence is set to Shen et al.'s (2016) 140 m upstream from an axial or cross-flow tidal turbine (Figures 2A, B). A vertical height of 25 m above the seafloor is used to represent approximately twice the vertical footprint of a proposed turbine in Admiralty Inlet (Jacques, 2014) and is within Shen et al.'s (2016) range of water depths (25 m at low tide to 32 m at high tide) at their study site. The probability of being within the zone of influence is dependent on the device's shape and size, water depth, range of tidal current speeds, and fish swimming ability. The probability of being in the zone of influence is defined as the probability of a fish being within the domain multiplied by the complement of an individual avoiding the device (Table 1).

Entrainment occurs when a fish is within the area adjacent to the device, normal to the device face. If an animal continues its current trajectory with no avoidance, it will collide with the turbine base or enter the turbine. The turbine base and entry area are half the vertical height of the turbine (Figures 2A, B). Areal dimensions of the cross-flow turbine base and turbine entrance are both 30 m by 10 m. Areal dimensions of the axial-flow turbine base and turbine entrance are 5 m by 10 m. The probability of entrainment is defined as the probability of a fish being within the zone of influence multiplied by the probability of 1 minus avoiding the device given that the individual is within the zone of influence (Table 1). Avoidance calculations are detailed below.

Interactions between a fish and a tidal turbine are composed of collisions and/or blade strikes. We define collision as physical contact between an animal and the turbine base or a non-moving device component (e.g., Müller et al., 2023). We define blade strike as contact between an animal and a rotating blade (e.g., Castro-Santos and Haro, 2015; Courtney et al., 2022). In the model, collision and blade strike are treated as potential sequential events, where fish can collide with a turbine support structure and then be struck by a rotating blade. There is inconsistent use of these terms in the literature. A singular term, collision (e.g., Copping and Hemery, 2020), has been used to describe interactions between an animal and a device. However, the terms collision and strike have also been used interchangeably when characterizing interactions between animals and turbine blades (e.g., Hammar et al., 2013; Yoshida et al., 2020; Yoshida et al., 2021), and omitting animal contact with stationary turbine structures. This may not be a trivial oversight as turbine dimensions can exceed 15 to 20 m in length and width (cf. Viehman and Zydlewski, 2015; Shen et al., 2016; Courtney et al., 2022), which provides large surface areas for fish to collide with a turbine base or non-rotating structures when avoidance is not possible.

Impact is defined as one or more interactions between a fish and a device through collision and/or blade strike (e.g., Yoshida et al., 2021; Courtney et al., 2022). Since blade strike constitutes the greatest risk to fish and are a concern among researchers and regulators (Copping et al., 2020a), experimental and field data are used to calculate probability estimates, with published values emphasizing blade strikes. In cases where empirical data are lacking, the impact phase of the model incorporates laboratory and simulation model data (Romero-Gomez and Richmond, 2014) that align with our encounter-impact collision and blade strike model components.

Impact probabilities are calculated for each model subcomponent and overall potential impact (Table 1). All impact probabilities also depend on whether an animal is present within the entrainment area. The occurrence probability of collision with a turbine is calculated as the probability of entrainment multiplied by the probability of collision given that a fish is entrained. The probability of blade strike is defined as the probability of entrainment multiplied by the probability of a blade strike given that a fish has entered the device. Lastly, the probability of collision and blade strike is defined as the probability of entrainment, multiplied by the probability of collision, multiplied by the probability of blade strike given that a fish collided with the device. The overall probability of impact is calculated as the sum of the three potential interaction events: collision, blade strike, and collision and blade strike.

All phases of the encounter-impact model include active and passive avoidance (Figure 1). Avoidance is defined as a change in a fish's trajectory in response to tidal devices. In behavioral studies, fish have been shown to actively avoid predation and navigate around obstacles, even at long distances (e.g., Utne, 1997; Muirhead and Sprules, 2003; Zhang et al., 2017; Berry et al., 2019; Bender et al., 2023; Müller et al., 2023). Tidal flow speeds often surpass fish swimming capabilities (cf. Okubo, 1987; He, 1993), potentially leading to passive transport through the water and passage around or through MRE devices. Therefore, the definition of avoidance is expanded to a fish's response and movement away

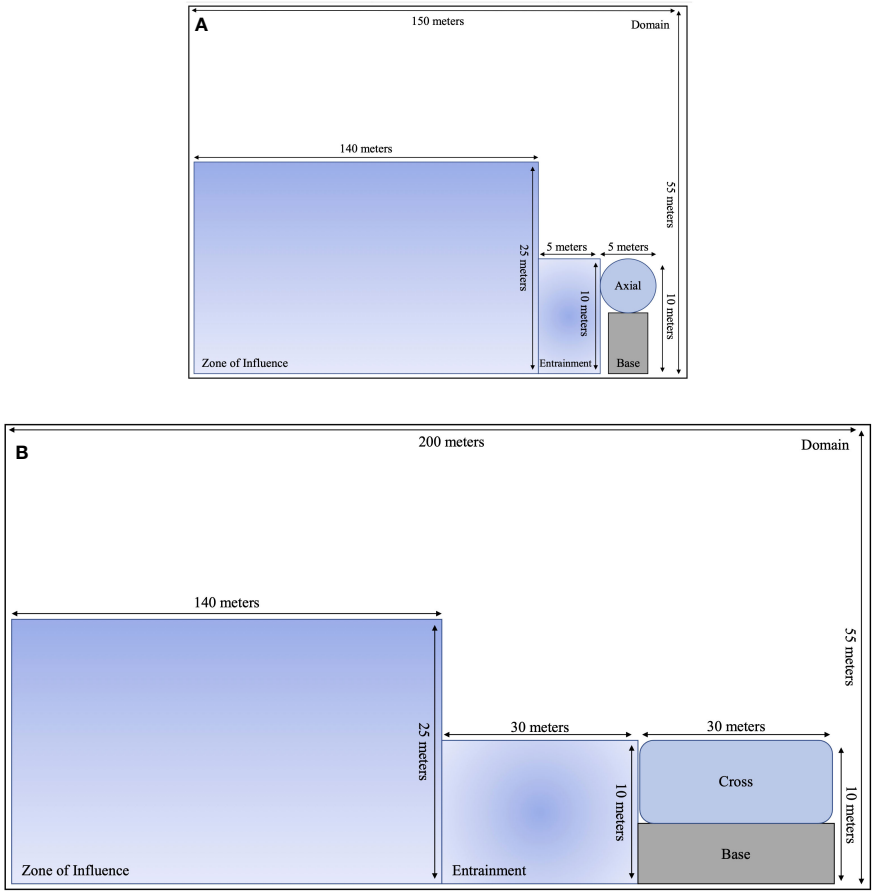

FIGURE 2
A two-dimensional schematic showing dimensions of the encounter-impact model components for **(A)** axial and **(B)** cross-flow turbines.

from a device and/or its avoidance due to hydrodynamic forces (Copping and Hemery, 2020). We define the threshold between active and passive avoidance using the ratio of swimming capability to tidal flow. Average Pacific herring *(Clupea pallasii)* fork length from Admiralty Inlet net samples is used to estimate swimming speed using Okubo's (1987) locomotion equation:

$$S_S = 2.69 \cdot L^{0.86} \quad (1)$$

where S_s is swimming speed (ms^{-1}), and L is fish length (m). Active locomotion is assumed when the ratio of swimming speed to tidal flow is greater than 1 body length per second (bls^{-1}) (He, 1993). Passive locomotion occurs when the tidal speed exceeds 1 bls^{-1}, in this study 0.155 ms^{-1}.

2.2 Tidal turbine dimensions

For this study, representative axial and cross-flow tidal turbine devices are used in calculations of encounter and impact probabilities. Tidal turbine dimensions used are based on an axial-flow Verdant Power Kinetic Hydropower System (KHPS) (Bevelhimer et al., 2017) (Figure 2A) and a cross-flow Ocean Renewable Power Company (ORPC) TidGen Power System (Shen et al., 2016) (Figure 2B). Verdant Power KHPS turbine characteristics include a three-bladed, single-rotor turbine. The height of the device is approximately 10 m, with a rotor-swept area of 5 m in diameter, defining an area of 5 m by 10 m. The TidGen device is 31.2 m long and 9.5 m high with foils (i.e., rotating blades) 6.7 - 9.5 m above the seafloor, defining an area of 30 m by 10 m.

2.3 Empirical data description

Data used to estimate occurrence probabilities were collected in 2011 (Horne et al., 2013) at a site in Admiralty Inlet, Puget Sound, Washington chosen by the Snohomish Public Utility District for potential deployment of two Open Hydro (https://www.emec.org.uk/about-us/our-tidal-clients/open-hydro/) turbines. The proposed site is approximately 750 m off Admiralty Head at a depth of 55 m mean tide height. Data were collected using a Simrad EK-60 echosounder operating at 120 kHz, an autonomous bottom-deployed 1MHz Nortek AWAC acoustic doppler current profiler (ADCP), and a midwater trawl deployed from a mobile surface vessel. Acoustic and fish surveys were conducted from May 2 to May 13 and June 3 to June 14, 2011, during day and night for a

combined total transect length of 28 km (Jacques, 2014). 324 parallel transects (0.7 to 1.5 km long) extending northwest and southeast of the proposed turbine location, were spaced 0.5 km apart (see Horne et al., 2013 for survey details). The ADCP, deployed from May 9 until June 10, 2011, collected concurrent tide state and tidal velocity measurements for 12 minutes every two hours (Jacques, 2014).

A Marinovich midwater trawl, a 6 m x 6 m box trawl fished with 4.6 m x 6.5 m steel V-doors, was used to capture samples to quantify species composition and length-frequencies of the fish community. Among captured species, Pacific herring represented 32% of the total catch by number. In this study, all acoustic backscatter is attributed to Pacific herring in acoustic density calculations. The average length of Pacific herring caught in the midwater trawl was 0.155 m and is used in all acoustic and swimming speed calculations. Given analogous fish lengths and time of year, the target strength conversion equation for Pacific herring from Thomas et al. (2002): $26.2 \cdot \log10(L_{cm})$ - 72.5 is used to transform acoustic-derived densities (m^2 m^{-3}) to fish densities (fish m^{-2}).

2.4 Factors contributing to model component probabilities

Since no turbine was deployed during data collection, the Admiralty Inlet dataset provides the flexibility to analyze acoustic fish densities and distributions using multiple turbine types and light regimes represented by time of day. To observe how acoustic densities varied with light fluctuations, probabilities of occurrence for each model component during day and night are calculated for each turbine type. Fish densities are estimated by dividing each surveyed transect in horizontal 140 m, 30 m, or 5 m bins (corresponding to turbine type, Figures 2A, B) and then grouping bins to match the size of each model component. This approach also ensures that each bin along every transect can be used as a location for sequential model components or a device.

Probability estimates in the encounter-impact model are also influenced by active and passive avoidance. The zone of influence in the model uses three avoidance scenarios in probability estimates. The first scenario assumes fish are unable to avoid the turbine within the zone of influence. In the second scenario, fish can avoid the turbine within the zone of influence using active and passive avoidance. Active avoidance rates are estimated from the Admiralty Inlet dataset by discounting abundance estimates of fish within model components by Shen et al.'s (2016) avoidance rate of 0.372. Passive avoidance rates are estimated by tabulating fish observations swimming around or above model components, assuming that avoidance will occur to the side or above a device. The proportion of time passive avoidance occurs is determined by the tidal cycle – when tidal flow speeds surpass fish swimming speeds. The third scenario uses Shen et al.'s (2016) active avoidance rate of 0.372 without incorporating passive avoidance. When an avoidance rate from Admiralty Inlet or Shen et al. (2016) is incorporated into the model, estimates of fish impact are calculated using conditional probabilities from sequential model components. This approach evaluates a fish's ability to avoid a device across model components and provides insight into the likelihood of impact for each model phase and overall encounters with tidal turbines. Conversely, when an avoidance rate is not included, calculated impact probabilities are not dependent on sequential model components and analogous to rates in published studies.

2.5 Estimating empirical probabilities

Occurrence of fish during day and night is determined by enumerating acoustic abundance estimates detected within bins along each mobile survey transect, aligned with areas of each model component (Figures 2A, B). Abundances along binned cells are summed to estimate total abundance for each transect. Probabilities of occurrence for each model component are determined by dividing the number of fish detected within each cell of each model component by total fish abundance.

Since no fish-turbine interaction measurements are available from Admiralty Inlet, encounter and impact published values are used in model calculations. At this time, there are no published probability estimates of collisions between fish and stationary tidal structures or collisions followed by blade strikes. Collision probabilities are estimated by calculating the complement of published blade strike probabilities and discounting by length-dependent swimming speed and time of day avoidance rates published in Viehman and Zydlewski (2015).

Blade strike probabilities are taken from field measurements (Courtney et al., 2022), laboratory experiments (Yoshida et al., 2021), and calculated using a blade-strike model (Romero-Gomez and Richmond, 2014):

$$P(strike) = \frac{nNL\cos(\alpha)}{U} \quad (2)$$

where $P(strike)$ is the probability of a blade strike, n is the number of blades, N is a fixed rotation rate [i.e., 0.357 s^{-1} for a cross-flow turbine (Viehman and Zydlewski, 2015) and 0.667 s^{-1} for an axial-flow turbine (Bevelhimer et al., 2017)], L is fish length (m), α represents the fish approach angle perpendicular to the blade plane ($\alpha = 0$), and U is tidal velocity (ms^{-1}). Blade strike probabilities are estimated using Equation (2) for tidal velocities observed in Admiralty Inlet that ranged from 1.0 ms^{-1} to 3.0 ms^{-1} (Horne et al., 2013) in increments of 0.2 ms^{-1}. Incremental changes in tidal velocities depict the progression of a tidal cycle, yielding a range of strike probabilities in response to periodic flow conditions. The encounter-impact model also uses blade strike rates from Courtney et al. (2022) (0.13) and Yoshida et al. (2021) (0.02 – 0.05) in blade strike calculations. Inclusion of these rates in the blade strike model component compensates for limited data availability and introduces a range of probability estimates that incorporate turbine design, time of day, and device avoidance.

The sequential occurrence probability of collision and blade strike is determined by multiplying collision and published blade strike probability estimates. Probabilities of collision, blade strike, and collision and blade strike are discounted by avoidance rates in model calculations. Overall impact

probabilities are calculated by summing estimated probabilities of each impact subcomponent (Table 1).

3 Results

Probabilities of occurrence for each component of the encounter-impact model are influenced by turbine type, time of day, and avoidance. Probabilities of occurrence for the zone of influence range between 0.0636 to 0.0649 for both turbine types (Tables S1A–D, Supplementary Material). Entrainment probabilities range between 0.00245 to 0.0408 for an axial-flow turbine (Tables S1A, B, Supplementary Material) and 0.0118 to 0.0408 for a cross-flow turbine (Tables S1C, D, Supplementary Material). Probabilities of impact depend on occurrences of collision, blade strike, or sequential collision and blade strike. Collision probabilities between fish and tidal devices span three orders of magnitude from 0.000364 to 0.324 for both turbine types, with similar probabilities of blade strike ranging between 0.000261 to 0.40 for both turbine types (Tables S1A–D, Supplementary Material). As expected, probabilities of collision and blade strike are lower than either single event impact, ranging between 0.0000242 to 0.0678 for both turbine types (Tables S1A–D, Supplementary Material). Overall impact probabilities, a summation of subcomponents, for the two turbine types are nearly identical ranging between 0.00110 to 0.666 for an axial-flow turbine and 0.00110 to 0.689 for a cross-flow turbine (Table 2).

When comparing occurrence probabilities for each model component, estimates are higher at night than during the day for both turbine types averaging between 0.00194 to 0.100 (Tables S1A–D, Supplementary Material). Blade strike occurrence probabilities are the only model component that have higher average probabilities during the day than at night, with an average 0.00238 difference for the axial-flow turbine (Tables S1A, B, Supplementary Material), and an average 0.00237 difference for the cross-flow turbine (Tables S1C, D, Supplementary Material). When comparing overall impact probabilities in light regimes, probabilities are higher at night than during the day for both turbine types, with probability variations ranging over three orders of magnitude (Table 2). Turbine design influences impact probabilities, with an axial-flow turbine exhibiting the lowest risk of impact across factors and avoidance scenarios (Table 2).

As expected, probabilities of occurrence for each model component are higher when no avoidance is included and model components are not conditioned on preceding events in model calculations (Tables S1A–D, Supplementary Material). Probabilities of occurrence are lowest when Admiralty Inlet avoidance rates are applied, reflecting the inclusion of conditional probabilities in model calculations. Probabilities of occurrence for the zone of influence are similar across all avoidance scenarios for both turbine types ranging between 0.0636 and 0.0649 (Tables S1A–D, Supplementary Material). Probabilities of occurrence for entrainment are higher when Shen et al.'s 2016 avoidance rate (0.0408) is applied to the model for both turbine types (Tables S1B, D, Supplementary Material). Probabilities of impact are highest by two to three orders of magnitude when no avoidance is included for a cross-flow turbine (Table 2). Collision probabilities (0.324), blade strike probabilities (0.40), and sequential collision and blade strike probabilities (0.0678) are all highest for both turbine types when subcomponents are modeled with no avoidance (Tables S1A–D, Supplementary Material). Minimum and maximum probability values are similar between subcomponents and overall impact estimates, with larger values occurring when no avoidance is applied and lowest when avoidance rates from Admiralty Inlet were used in model calculations (Table 2).

Conditional probability estimates from this study are both lower and higher than other published values (Table 3). Shen et al. (2016) and Bangley et al. (2022) observed order of magnitude higher probabilities of fish approach and encounter with a tidal turbine than average approach estimates in this study. Similarly, Viehman and Zydlewski (2015) report order of magnitude higher average probabilities of entrainment at night with a 0.290 probability estimate difference between day and night calculations. Band et al. (2016) observed order of magnitude higher probabilities of collision for Harbor seals with turbine rotors when

TABLE 2 Impact probability estimates for axial and cross-flow turbines for avoidance scenarios using alternate blade strike probability estimates.

		Axial-Flow Turbine		Cross-Flow Turbine	
Avoidance scenario	Blade strike probability estimate	Day	Night	Day	Night
No avoidance	Courtney et al., 2022	0.172	0.455	0.172	0.455
	Yoshida et al., 2021	0.0928	0.353	0.0928	0.353
	Romero-Gomez and Richmond, 2014	0.436 - 0.175	0.666 - 0.171	0.337 - 0.138	0.689 - 0.423
Admiralty Inlet avoidance	Courtney et al., 2022	0.00204	0.00541	0.00204	0.00541
	Yoshida et al., 2021	0.00110	0.00419	0.00110	0.00419
	Romero-Gomez and Richmond, 2014	0.00515 - 0.00206	0.00805 - 0.00545	0.00907 - 0.00191	0.0176 - 0.00529
Shen et al. (2016) avoidance	Courtney et al., 2022	0.00687	0.0185	0.00687	0.0185
	Yoshida et al., 2021	0.00370	0.0144	0.00370	0.0143
	Romero-Gomez and Richmond, 2014	0.0164 - 0.00699	0.0276 - 0.0187	0.0304 - 0.00647	0.0357 - 0.0181

TABLE 3 Comparison of average occurrence probabilities for each phase of the encounter-impact model to published literature values.

Encounter-Impact Model Phase	Encounter-Impact Model Probabilities		Literature Model Phase	Literature Results		Literature Source	Literature Focal Species
	Day	Night		Day	Night		
Approach	0.0636	0.0649		0.432		Shen et al., 2016	Unidentified
				0.150 – 0.400		Bangley et al., 2022	Striped bass
Entrainment	0.0200	0.0203		0.0432	0.333	Viehman and Zydlewski, 2015	Unidentified
	0.0200	0.0203		0.154		Bevelhimer et al., 2017	Unidentified
Collision	0.0126	0.0982	Collision	0.306		Band et al., 2016	Harbor seal
Blade strike	0.0567	0.0543	Encounter	0.000212		Wilson et al., 2006	Pacific herring
Collision and Blade strike	0.00243	0.0126	Encounter	0.000363		Wilson et al., 2006	Harbor porpoise

compared to results of this study. In contrast, Wilson et al.'s (2006) non-conditional encounter probabilities for Pacific herring were two orders of magnitude lower than those estimated in this study.

Regardless of the combination of factors, probabilities of fish-turbine encounters and impact range from a minimum of 0.0000242 to a maximum of 0.324. Overall impacts ranged from a minimum of 0.00110 to a maximum of 0.689. Probability values are particularly low when conditioned on fish occurring within a turbine's zone of influence, where subsequent entrainment may lead to an impact. All highest probability values occur at night with no avoidance in calculations for a cross-flow turbine.

4 Discussion

Occurrence probability estimates of fish-turbine interactions are influenced by model component, device surface area, and turbine design. The concept of a zone of influence, demonstrated by Shen et al. (2016) and Grippo et al. (2020), represents a large range in which fish can respond to turbine presence. Larger turbine designs, exemplified by the 30 m by 10 m silhouette of the ORPC TidGen cross-flow turbine, also present a large surface area for potential collisions and interactions with a device. The cross-flow turbine is approximately six times longer than the Verdant Power KHPS axial-flow turbine. Greater cross-flow impact probability estimates and congruent empirical blade strike estimates from Courtney et al. (2022) demonstrate high probabilities of entrainment and collision associated with cross-flow turbines, attributable to the large size of the device. Design characteristics of turbines also affect the entrainment model component, as entrainment dimensions scale with turbine size.

Light and dark cycles have limited influence on empirical data-based variations in occurrence and impact probabilities. A slight increase in probability values is observed for model estimates based on night empirical data compared to those sampled during the day. Fish behavior in light and dark conditions provides insight on fish-turbine detection distances where field (Viehman and Zydlewski, 2015; Viehman et al., 2015; Williamson et al., 2019) and experimental (Yoshida et al., 2021) studies found that light intensity affects fish distribution in the presence of MRE devices. Williamson et al. (2019) observed a 2.63 times greater increase in fish aggregation rates around turbine structures at night compared to day, supporting previous studies that show greater probabilities of turbine entry for fish at night (Viehman and Zydlewski, 2015). Viehman et al. (2015) reported that fish are more evenly distributed at night, even at dynamic tidal turbine sites, demonstrating the persistence of fish in dark conditions where turbines are present.

Variations in model component and impact probability estimates are contingent on turbine type, light conditions, avoidance scenarios, and blade strike probabilities. Occurrence probabilities for the zone of influence are unaffected by avoidance scenarios, with slight elevation in nighttime estimates, as probabilities are directly extracted from the Admiralty Inlet empirical data that had no turbine present at the site. Probabilities of entrainment modeled with no avoidance are similar or an order of magnitude lower for the smaller axial-flow turbine compared to the cross-flow turbine. Analogous encounter rate studies (Bangley et al., 2022; Sanderson et al., 2023) using acoustic telemetry tags found encounter rate probabilities an order of magnitude higher compared to the conditional encounter probability estimates. Impact probabilities in model scenarios with no avoidance (e.g., Wilson et al., 2006) result in higher values by one to two orders of magnitude compared to impact subcomponents that include avoidance. It is worth noting that fish-turbine encounter probabilities reported by Wilson et al. (2006) are based on Pacific herring but are not conditional and do not

incorporate active or passive avoidance. Comparing blade strike probabilities derived from literature values, Yoshida et al.'s (2021) probabilities result in the lowest overall impact probability estimates when combined with an avoidance scenario. These lower probability values are attributed to a lower turbine blade rotational speed to fish swimming speed ratio, resulting in greater avoidance and lower blade strike rates. In contrast, impact probabilities are highest when using blade strike probabilities from the Romero-Gomez and Richmond (2014) blade strike model that does not include fish avoidance, despite model probabilities decreasing as flow speeds increase. In combination, our probability estimates demonstrate that avoidance is an important factor influencing impact probability estimates, both as a scenario within the conditional model and experimentally with fish and a turbine present.

Additional empirical data are needed to quantify collision rates with stationary structures and blade strikes. Data that track individual fish through turbine encounters supports probability estimates of avoidance, collision with turbine structures, and the combination of collision followed by blade strike. Long-range fish trajectory data can be used to quantify active and passive turbine avoidance behaviors through each step of a sequential encounter model and be used in conditional probability of occurrence calculations. The lack of collision and sequential collision and blade strike data or suitable published values necessitated modification of blade strike rates for model subcomponent calculations. Parameter values for these impact subcomponents are derived by multiplying blade strike probabilities from the literature using Shen et al.'s (2016) avoidance rate of 0.372. The use of published blade strike probabilities in calculation of collision probability estimates may have increased collision probabilities. To illustrate by example, Courtney et al. (2022) observed greater blade strike occurrences compared to other studies that found no blade strikes in natural environments (e.g., Hammar et al., 2013; Viehman and Zydlewski, 2015; Shen et al., 2016; Bevelhimer et al., 2017 Romero-Gomez and Richmond's, 2014) blade-strike model, parameterized for Pacific herring in Admiralty Inlet, does not include avoidance, which increased blade strike estimates compared to field (Hammar et al., 2013; Courtney et al., 2022; Bender et al., 2023) and experimental (Zhang et al., 2017; Berry et al., 2019; Yoshida et al., 2020; Yoshida et al., 2021; Müller et al., 2023) studies. Probabilities calculated using blade strike rates from Courtney et al. (2022) and Romero-Gomez and Richmond (2014) resulted in overall impact probability values that range one to two orders of magnitude higher than estimates derived from Yoshida et al.'s (2021) blade strike estimates. The lack of data or published probability values for collisions and blade strikes, that also include avoidance rates, illustrate a current knowledge gap. Availability of animal-turbine interaction datasets facilitates validation of probability estimates and will allow resource managers to quantify injury and mortality of aquatic animals including species of special status such as the threatened Puget Sound Chinook salmon (*Oncorhynchus tshawytscha*) (Hall et al., 2018).

Empirical data from a demonstration tidal turbine site are used in this study but sample conditions may affect probability estimates. For example, fish densities derived from the Admiralty Inlet acoustic dataset are categorized as Pacific herring. Representing a mixed fish community by a single species in the conversion of acoustic backscatter measurements to density and abundance estimates is potentially biased, but any biases in the data are assumed constant and low. Pacific herring are used to represent pelagic, schooling fish that are common constituents of any fish community at a MRE site. The encounter-impact model does not explicitly include diel vertical migration, a factor that may affect probability estimates (e.g., Rossington and Benson, 2020), but did include day and night periods to reflect differences in vertical distributions. We did not include crepuscular changes in vertical distributions, which represent brief periods (<3% total) during a 24-hour cycle. Williamson et al. (2019) examined day/night fish aggregation vertical distributions in proximity to turbine structures and observed lower school heights at night compared to those during the day, suggesting that vertical migration can potentially influence probability estimates for specific times during a day, but also emphasizing our limited understanding of fish behavior in proximity of tidal devices. At the time of data collection there were no hydrokinetic devices deployed in Admiralty Inlet. Fish density data used in probability calculations lack information on fish-turbine interactions, necessitating the use of published avoidance, collision, and blade strike values. The absence of a turbine at the data collection site also precludes the ability to measure indirect or delayed impacts of animal-device interactions. Indirect or delayed impact examples include hydraulic shear stress (Hammar et al., 2015) and/or barotrauma (Copping et al., 2020b) that may lead to additional fish injury and/or mortality. Conditional probability values are calculated using empirical acoustic transect data along sequential steps in the encounter-impact model. The data serve as a series of spatiotemporal snapshots of fish distributions but do not explicitly include individual fish trajectories as they pass through a model domain.

The encounter-impact model provides a robust framework for estimating impact probabilities for both individual fish and specific turbines. The model is not structured to estimate encounter or impact probabilities for fish populations or for arrays of tidal turbines. Models such as Hammar et al.'s (2015) population collision risk model and the Exposure Time Population Model (ETPM) from Grant et al. (2014) estimate impacts of animal-tidal turbine interactions on populations encountering and interacting with a device. Hammar et al.'s (2015) model incorporates a component for tidal turbine array passage and co-occurrence, depicting fish approaching and being at the same depth as rotor blades during turbine operation. This component is used to estimate probabilities of a fish population passing through a tidal turbine array and potentially encountering rotor-swept areas of any turbine within the site. The ETPM estimates collision risk for diving birds interacting with MRE devices by evaluating mortality rates that would lead to population-level impacts, which could be adapted to estimate fish and aquatic mammal interaction and mortality rates. The challenge remains to scale high resolution, individual animal-device interactions to populations or species in a single model that accurately estimates impacts of MRE arrays on aquatic communities.

Our model combines analyses of empirical data from Admiralty Inlet with literature values to estimate probabilities of device encounters and impacts on fish. Numeric models can also be used to estimate values for unknown variables such as fish approach and

turbine interaction that identify data gaps in the MRE research portfolio (Buenau et al., 2022). An alternate approach to address challenges associated with incomplete empirical data is agent-based modeling. Agent-based models represent populations using individual agents (i.e., organisms) containing unique traits and interact with other agents and their environment (DeAngelis and Mooij, 2005). Within a specified domain, agent-based models are initialized with parameter values and behavioral rules (e.g., aggregation, avoidance) formulated using field observations, existing datasets, or published values (Murphy et al., 2020). When applied to MRE, agent-based models can include individual and aggregative behaviors in response to hydrokinetic devices (e.g., Goodwin et al., 2004) that are then used to quantify impact probabilities for individuals (e.g., Rossington and Benson, 2020) or populations (Hammar et al., 2015). The combination of empirical data with numerical models is a formidable tool to assess fish interactions with MRE devices and is essential for informed regulatory decision-making, conservation strategies, and sustainable development of the MRE blue economy.

5 Conclusion

MRE is an applied science and engineering field that requires foundational and operational understanding through increased research and environmental monitoring. One area of uncertainty is characterizing fish avoidance behaviors, including reaction distances to MRE devices. This knowledge gap hinders permitting/consenting and subsequent development of MRE projects worldwide. To facilitate progress from demonstration projects to commercial-scale sites, it is essential to implement effective risk management strategies, comprehensive environmental monitoring, and regulatory frameworks that provide clear standards for operation of all MRE sectors including tidal energy (Inger et al., 2009). The encounter-impact empirical model in this study estimates probabilities of occurrence for sequential stages of fish interactions with tidal turbines and can be adapted for any species, location, and device. The comprehensive yet flexible structure of this model serves as a starting point to quantify encounter and impact risks and to further discussion on impact uncertainty.

Data availability statement

The raw data supporting the conclusions of this article will be made available by the authors, without undue reservation.

Ethics statement

Only remotely sensed, acoustic data were collected in the original study by the University of Washington. Species composition and length data from net catches were originally collected by and under the authority of the Washington State Department of Fish and Wildlife (WDFW). We received data that were used to choose the type species and calculate an average length for conversion of acoustic backscatter (i.e., reflected energy) measurements to fish density and abundance estimates.

Author contributions

JP: Conceptualization, Data curation, Formal Analysis, Investigation, Methodology, Software, Visualization, Writing – original draft, Writing – review & editing. JH: Conceptualization, Funding acquisition, Investigation, Methodology, Project administration, Resources, Supervision, Validation, Writing – review & editing.

Funding

The author(s) declare financial support was received for the research, authorship, and/or publication of this article. This work was supported by a Department of Energy grant (DE-EE-0006816.0000) to the ALFA project with additional financial support of a Graduate Fellowship from the School of Aquatic and Fishery Sciences, University of Washington, Seattle, Washington. This publication is partially funded by the Cooperative Institute for Climate, Ocean, & Ecosystem Studies (CICOES) under NOAA Cooperative Agreement NA20OAR4320271, Contribution No. 2023-1300.

Acknowledgments

We thank the captain and crew of the RV Centennial along with the science crew who collected and processed the Admiralty Inlet acoustic and fish catch data: Dale Jacques, Sandra Parker-Stetter, Hannah Linder, and Jennifer Nomura.

Conflict of interest

The authors declare that the research was conducted in the absence of any commercial or financial relationships that could be construed as a potential conflict of interest.

Publisher's note

Supplementary material

The Supplementary Material for this article can be found online at: https://www.frontiersin.org/articles/10.3389/fmars.2023.1270428/full#supplementary-material

References

Band, B., Sparling, C., Thompson, D., Onoufriou, J., San Martin, E., and West, N. (2016). Refining estimates of collision risk for harbour seals and tidal turbines. *Scott. Mar. Freshwater Sci.* 7 (17), 123. doi: 10.7489/1786-1

Bangley, C. W., Hasselman, D. J., Flemming, J. M., Whoriskey, F. G., Culina, J., Enders, L., et al. (2022). Modeling the probability of overlap between marine fish distributions and marine renewable energy infrastructure using acoustic telemetry data. *Front. Mar. Sci.* 9. doi: 10.3389/fmars.2022.851757

Bender, A., Langhamer, O., Francisco, F., Forslund, J., Hammar, L., Sundberg, J., et al. (2023). Imaging-sonar observations of salmonid interactions with a vertical axis instream turbine. *River Res. Appl.* 39 (8), 1578–1589. doi: 10.1002/rra.4171

Berry, M., Sundberg, J., and Francisco, F. (2019). Salmonid response to a vertical axis hydrokinetic turbine in a stream aquarium. In 13th European Wave and Tidal Energy Conference (EWTEC).

Bevelhimer, M., Scherelis, C., Colby, J., and Adonizio, M. A. (2017). Hydroacoustic assessment of behavioral responses by fish passing near an operating tidal turbine in the east river, new york'. *Trans. Am. Fisheries Soc.* 146 (5), 1028–1042. doi: 10.1080/00028487.2017.1339637

Buenau, K. E., Garavelli, L., Hemery, L. G., and García Medina, G. (2022). A review of modeling approaches for understanding and monitoring the environmental effects of marine renewable energy. *J. Mar. Sci. Eng.* 10 (1), 94. doi: 10.3390/jmse10010094

Castro-Santos, T., and Haro, A. (2015). Survival and behavioral effects of exposure to a hydrokinetic turbine on juvenile atlantic salmon and adult american shad. *Estuaries Coasts* 38 (1), 203–214. doi: 10.1007/s12237-013-9680-6

Copping, A. E., Freeman, M. C., Gorton, A. M., and Hemery, L. G. (2020a). Risk retirement—Decreasing uncertainty and informing consenting processes for marine renewable energy development. *J. Mar. Sci. Eng.* 8 (3), 172. doi: 10.3390/jmse8030172

Copping, A., and Hemery, L. (2020). OES-environmental 2020 state of the Science report: Environmental effects of marine renewable energy development around the world. Report for ocean energy systems (OES). PNNL–29976, 1632878. doi: 10.2172/1632878

Copping, A., Hemery, L., Overhus, D., Garavelli, L., Freeman, M., Whiting, J., et al. (2020b). Potential environmental effects of marine renewable energy development-the state of the science. *J. Mar. Sci. Eng.* 8 (11), 879–897. doi: 10.3390/jmse8110879

Copping, A. E., Hemery, L. G., Viehman, H., Seitz, A. C., Staines, G. J., and Hasselman, D. J. (2021). 'Are fish in danger? A review of environmental effects of marine renewable energy on fishes'. *Biol. Conserv.* 262, 109297. doi: 10.1016/j.biocon.2021.109297

Courtney, M. B., Flanigan, A. J., Hostetter, M., and Seitz, A. C. (2022). Characterizing sockeye salmon smolt interactions with a hydrokinetic turbine in the kvichak river, alaska. *North Am. J. Fisheries Manage.* 42 (4), 1054–1065. doi: 10.1002/nafm.10806

DeAngelis, D. L., and Mooij, W. M. (2005). Individual-based modeling of ecological and evolutionary processes. *Annu. Rev. Ecology Evolution Systematics* 36, 147–168. doi: 10.1146/annurev.ecolsys.36.102003.152644

Fox, C. J., Benjamins, S., Masden, E. A., and Miller, R. (2018). Challenges and opportunities in monitoring the impacts of tidal-stream energy devices on marine vertebrates. *Renewable Sustain. Energy Rev.* 81, 1926–1938. doi: 10.1016/j.rser.2017.06.004

Goodwin, R. A., Anderson, J. J., and Nestler, J. M. (2004). 'Decoding 3-d movement patterns of fish in response to hydrodynamics and water quality for forecast simulation', in Hydroinformatics. *World Sci. Publishing Company* 2, 254–261. doi: 10.1142/9789812702838_0031

Grant, M. C., Trinder, M., and Harding, N. J. (2014). "A diving bird collision risk assessment framework for tidal turbines," in *Scottish natural heritage commissioned report no. 773*. Available at: https://tethys.pnnl.gov/sites/default/files/publications/SNH-2014.pdf.

Grippo, M., Zydlewski, G., Shen, H., and Goodwin, R. A. (2020). Behavioral responses of fish to a current-based hydrokinetic turbine under mutliple operational conditions. *Environ. Monit. Assess.* 192 (10), 645. doi: 10.1007/s10661-020-08596-5

Hall, J. E., Greene, C. M., Stefankiv, O., Anderson, J. H., Timpane-Padgham, B., Beechie, T. J., et al. (2018). 'Large river habitat complexity and productivity of Puget Sound Chinook salmon. *PloS One* 13 (11), e0205127. doi: 10.1371/journal.pone.0205127

Hammar, L., Andersson, S., Eggertsen, L., Haglund, J., Gullström, M., Ehnberg, J., et al. (2013). Hydrokinetic turbine effects on fish swimming behaviour. *PloS One* 8 (12), e84141. doi: 10.1371/journal.pone.0084141

Hammar, L., Eggertsen, L., Andersson, S., Ehnberg, J., Arvidsson, R., Gullström, M., et al. (2015). A probabilistic model for hydrokinetic turbine collision risks: exploring impacts on fish. *PloS One* 10 (3), e0117756. doi: 10.1371/journal.pone.0117756

He, (1993). Swimming speeds of marine fish in relation to fishing gears. *ICES Mar. Sci. Symp* 196, 183–189.

Hemery, L. G., Copping, A. E., and Overhus, D. M. (2021). Biological consequences of marine energy development on marine animals. *Energies* 14 (24), 8460. doi: 10.3390/en14248460

Horne, J. K., Jacques, D. A., Parker-Stetter, S. L., Linder, H. L., and Nomura, J. M. (2013). *Evaluating Acoustic Technologies to Monitor Aquatic Organisms at Renewable Energy Sites Final Report* (U.S. Dept. of the Interior, Bureau of Ocean Energy Management. BOEM), 2014–2057. Available at: https://espis.boem.gov/final%20reports/5415.pdf.

Inger, R., Attrill, M. J., Bearhop, S., Broderick, A. C., James Grecian, W., Hodgson, D. J., et al. (2009). Marine renewable energy: potential benefits to biodiversity? An urgent call for research. *J. Appl. Ecol.* 46 (6), 1145–1153. doi: 10.1111/j.1365-2664.2009.01697.x

Jacques, D. A. (2014) *Describing and Comparing Variability of Fish and Macrozooplankton Density at Marine Hydrokinetic Energy Sites*. Available at: https://digital.lib.washington.edu:443/researchworks/handle/1773/27479.

Muirhead, J., and Sprules, W. G. (2003). Reaction distance of Bythotrephes longimanus, encounter rate and index of prey risk for Harp Lake, Ontario. *Freshw. Biol.* 48 (1), 135–146. doi: 10.1046/j.1365-2427.2003.00986.x

Müller, S., Muhawenimana, V., Sonnino-Sorisio, G., Wilson, C. A. M. E., Cable, J., and Ouro, (2023). 'Fish response to the presence of hydrokinetic turbines as a sustainable energy solution'. *Sci. Rep.* 13 (1), 7459. doi: 10.1038/s41598-023-33000-w

Murphy, K. J., Ciuti, S., and Kane, A. (2020). An introduction to agent-based models as an accessible surrogate to field-based research and teaching. *Ecol. Evol.* 10 (22), 12482–12498. doi: 10.1002/ece3.6848

Okubo, A. (1987). *Lecture notes in biomathematics, no. 71* (New York: Springer-Verlag).

Pelc, R., and Fujita, R. M. (2002). Renewable energy from the ocean. *Mar. Policy* 26 (6), 471–479. doi: 10.1016/S0308-597X(02)00045-3

Romero-Gomez,, and Richmond, M. C. (2014). Simulating blade-strike on fish passing through marine hydrokinetic turbines. *Renewable Energy* 71, 401–413. doi: 10.1016/j.renene.2014.05.051

Rossington, K., and Benson, T. (2020). An agent-based model to predict fish collisions with tidal stream turbines. *Renewable Energy* 151, 1220–1229. doi: 10.1016/j.renene.2019.11.127

Sanderson, B. G., Bangley, C. W., McGarry, L., and Hasselman, D. J. (2023). Measuring detection efficiency of high-residency acoustic signals for estimating probability of fish–turbine encounter in a fast-flowing tidal passage'. *J. Mar. Sci. Eng.* 11 (6), 1172. doi: 10.3390/jmse11061172

Shen, H., Zydlewski, G. B., Viehman, H. A., and Staines, G. (2016). Estimating the probability of fish encountering a marine hydrokinetic device. *Renewable Energy* 97, 746–756. doi: 10.1016/j.renene.2016.06.026

Staines, G. J., Mueller, R. P., Seitz, A. C., Evans, M. D., O'Byrne, P. W., and Wosnik, M. (2022). Capabilities of an acoustic camera to inform fish collision risk with current energy converter turbines. *J. Mar. Sci. Eng.* 10 (4), 483. doi: 10.3390/jmse10040483

Thomas, G. L., Kirsch, J., and Thorne, R. E. (2002). *Ex situ* target strength measurements of pacific herring and pacific sand lance. *North Am. J. Fisheries Manage.* 22 (4), 1136–1145. doi: 10.1577/1548-8675(2002)022<1136:ESTSMO>2.0.CO;2

Utne, A. C. W. (1997). The effect of turbidity and illumination on the reaction distance and search time of the marine planktivore Gobiusculus flavescens. *J. Fish Biol.* 50 (5), 926–938. doi: 10.1111/j.1095-8649.1997.tb01619.x

Viehman, H. A., and Zydlewski, G. B. (2015). Fish interactions with a commercial-scale tidal energy device in the natural environment. *Estuaries Coasts* 38 (1), 241–252. doi: 10.1007/s12237-014-9767-8

Viehman, H. A., Zydlewski, G. B., McCleave, J. D., and Staines, G. J. (2015). Using hydroacoustics to understand fish presence and vertical distribution in a tidally dynamic region targeted for energy extraction. *Estuaries Coasts* 38 (1), 215–226. doi: 10.1007/s12237-014-9776-7

Williamson, B. J., Fraser, S., Blondel, P., Bell, P. S., Waggitt, J. J., and Scott, B. E. (2017). Multisensor acoustic tracking of fish and seabird behavior around tidal turbine structures in scotland. *IEEE J. Oceanic Eng.* 42 (4), 948–965. doi: 10.1109/JOE.2016.2637179

Williamson, B., Fraser, S., Williamson, L., Nikora, V., and Scott, B. (2019). Predictable changes in fish school characteristics due to a tidal turbine support structure. *Renewable Energy* 141, 1092–1102. doi: 10.1016/j.renene.2019.04.065

Wilson, B., Batty, R., Daunt, F., and Carter, C. (2006). "Collision risks between marine renewable energy devices and mammals, fish and diving birds," in *Report to the scottish executive*. Available at: https://tethys.pnnl.gov/publications/collision-risks-between-marine-renewable-energy-devices-mammals-fish-diving-birds.

Yoshida, T., Furuichi, D., Williamson, B. J., Zhou, J., Dong, S., Li, Q., et al. (2021). Experimental study of fish behavior near a tidal turbine model under dark conditions. *J. Mar. Sci. Technol* 27, 541–548. doi: 10.1007/s00773-021-00850-w

Yoshida, T., Zhou, J., Park, S., Muto, H., and Kitazawa, D. (2020). 'Use of a model turbine to investigate the high striking risk of fish with tidal and oceanic current turbine blades under slow rotational speed'. *Sustain. Energy Technol. Assessments* 37, 100634. doi: 10.1016/j.seta.2020.100634

Zhang, J., Kitazawa, D., Taya, S., and Mizukami, Y. (2017). Impact assessment of marine current turbines on fish behavior using an experimental approach based on the similarity law. *J. Mar. Sci. Technol.* 22 (2), 219–230. doi: 10.1007/s00773-016-0405-y

frontiers | Frontiers in Marine Science

TYPE Original Research
PUBLISHED 09 April 2024
DOI 10.3389/fmars.2024.1372676

OPEN ACCESS

EDITED BY
Zhenkui Wang,
Zhejiang University, China

REVIEWED BY
Xipeng Wang,
Hangzhou City University, China
Yang Qu,
Beijing University of Technology, China

*CORRESPONDENCE
Sunwei Li
li.sunwei@sz.tsinghua.edu.cn

RECEIVED 18 January 2024
ACCEPTED 20 March 2024
PUBLISHED 09 April 2024

CITATION
Feng Y, Li S and Chen D (2024) Tensioned flexible riser vibrations under wave excitation, an investigation on the scale effect.
Front. Mar. Sci. 11:1372676.
doi: 10.3389/fmars.2024.1372676

Tensioned flexible riser vibrations under wave excitation, an investigation on the scale effect

Yunli Feng[1], Sunwei Li[2*] and Daoyi Chen[2,3]

[1]School of Naval Architecture and Marinetime, Zhejiang Ocean University, Zhoushan, China, [2]Institute for Ocean Engineering, Shenzhen International Graduate School, Tsinghua University, Shenzhen, China, [3]School of Environment, Tsinghua University, Beijing, China

In order to study the scale effect in wave-structure interactions and the role that structure-related parameters (tension T or bending stiffness EI) plays, riser model tests under regular waves were conducted using the model with multiple geometric scales (1:15, 1:12 and 1:9) in a wave basin. The riser model used is a novel structural design combing the outer polyvinyl chloride pipe with the core steel rod which could be simplified as a cantilever beam. Different initial tension T acting on the riser are tested by adjusting the slotted weight. The results show that the amplitude varies in a cubic fashion with the distance from the fixed end. In addition, the influence of the wave period and top tension T on the amplitude are investigated, which ultimately leads to a dimensionless number $\pi_1 = KC_d \cdot TL^2/EI$ where KC is the classical Keulegan–Carpenter number (KC), EI shows the bending stiffness of the riser model and L gives the pipe length. With the KC number revised to take the distance from the fixed end into the calculation, this parameter provides a good measure in estimating the amplitudes of the riser vibrations induced by the waves.

KEYWORDS

gravity wave, scale effect, wave-induced vibration, similarity theory, fluid-structure interaction

1 Introduction

The exploitation of offshore oil and gas resources is gradually shifted from shallow waters (<125m) to deep sea areas (125m~1500m) and ultra deep sea areas (>1500m) (Manning, 2016). The riser system which connects the floating offshore platform with underwater equipment hence plays a significant role. The dynamics of the marine riser not only shows the reliability of engineering projects installed offshore, but also impacts the marine hydrodynamic environment and ecosystems as the riser interacts with seawater and presents the condition for the near-surface marine biology. Changes in the hydrodynamic environment, such as wave and current characteristics, can alter the migration, diffusion,

and transformation patterns of marine pollutants. More importantly, once the marine riser is damaged, it will cause serious environmental pollution. For example, the Diamond Offshore's marine riser connection failed during operations on April 22, 2002; Discoverer Enterprise drilling vessel's riser ruptured in the Gulf of Mexico in 2003, leading to significant economic loss and environmental damages (Chang et al., 2018).

According to DNV-RP-F204 concerning the riser fatigue estimations, there are three main sources of riser fatigue failures: 1) waves, 2) low frequency motion, and 3) vortex-induced vibrations (VIV). Comparing to the fatigue damages induced by waves, the vibrations of risers under the influences of low-frequency motion of the platforms and vortices have been studied extensively (Jauvtis and Williamson, 2004; Zhang et al., 2020; Gao et al., 2021). Discovers made in such studies have been taken into consideration in the structural design. The vibrations and structural responses of the riser system under waves, on the other hand, are seldom investigated. British Petroleum, for example, monitored the full-scale drilling riser's response during a drilling campaign in the Gulf of Mexico between 13th April and 11th July in 2007 (Joseph et al., 2017). The acceleration spectrum shows the excitation is from VIV, drilling string rotation and wave induced motion. The measured peak frequency is 0.0866 Hz which is identified to be the response frequency of VIV, but it also falls in the typical wave frequency range. In addition, Huang et al. (2022) discussed a variety of models all revealing the significant wave induced vibrations of TTR and SCR. Liang et al. (2023) compared the wave-induced fatigue and VIV-induced fatigue of a free-hanging riser numerically. Luo (2022) studied the fatigue characteristics of subsea wellhead connector considering the action of riser wave-induced vibrations. Consequently, the structural design of the riser preventing the wave-induced vibrations is not as thorough as the designs concerning the VIV. The further study is significant on the underlying mechanisms of the wave-induced vibrations and could advance our understanding of the fluid-structure interactions and help better develop and utilize the ocean.

Due to the unacceptable cost for the full-scale experiment, the investigation on the riser vibration mainly relies on the scaled-down experiment. For example, Lee and Allen tested two scaled top-tensioned, flexible cylindrical structures' VIV (Lee and Allen, 2010). Zhang et al. cut off the anchor chain connecting to the drilling platform to dynamically simulate the structural behavior of an anchor chain (Zhang et al., 2007). The cut-off model ensures the static similarity and avoids unrealistically small scaled-down experiment. Ren et al. conducted the SCR's VIV experiment with a complex geometry in ocean basin (Ren et al., 2020). Although these experiments reveal important features for the vibrations of risers induced by environmental loading, the scale effect could deteriorate the results when they are used to reveal the behavior of the full-scale riser.

In order to unveil the scale effect in the scaled-down experiments of riser vibrations, efforts have been continuously made. For instance, Li (2013) and Zhou and Huang (2013) used the commercial numerical tools of SHEAR7 and ANSYS-CFX to simulate the VIV of a riser at the full-scale and of its geometrically scaled-down models. Bearman et al. (2001) and Ren et al. (2011), in addition, designed a series of scaled-down experiments following the Froude similarity theory and fluid-structure interaction theory to investigate the VIV of risers. Lee and Allen (2010) conducted two flexible risers' VIV tests mainly to investigate the effects of the top tension and structural stiffness on response. The previous studies disclosed the importance of the Reynolds number similarity and structural property similarity in designing the scaled-down experiment for the VIV of risers. In fact, it is found that the similarity of fluid-structure interaction parameters, such as the mass ratio, plays a crucial role in designing riser vibraation experiments within a certain range of Reynolds numbers.

Although a number of studies have already been devoted to reveal the scale effect for the VIV of risers, it is rarely investigated for wave-induced vibrations with neither numerical simulations nor laboratory experiments. The conclusions drawn from the VIV's experiments, on the other hand, are not applicable for the wave-induced vibration since

1) The Froude number similarity, which is verified not that important in the VIV of risers, could play a significant role in the wave-induced vibrations;
2) The common fluid-structure interaction parameters, such as mass ratio, may be not as influential in the wave-induced vibration as in the VIV;
3) The viscosity of the fluid, which is the key in determining the amplitudes and frequencies of VIV could be ignored in the wave kinematics, and hence in wave-induced vibrations.

Consequently, the structural design of the riser preventing the wave-induced vibrations is not as thorough as the designs concerning the VIV.

In the literature effect from wave is often treated as a static force calculated by Morison's equation or other wave theory. While wave-induced vibrations are mostly coupled with water flow. To the authors' best knowledge there is no separate analysis of the dynamic effect of waves on risers, and the scale effects.herein is still an open topic and should be systematically investigated. It is postulated that the structural parameters, together with the wave kinematics, are important in determining the wave-induced vibrations of a riser, and hence should be paid attention to when designing the scale-down experiments. In detail, the present study preliminarily investigates the scale effect of the riser vibrates under excitation of waves using the carefully designed wave-basin tests on the riser models with different geometric scales. After introduction, section 2 presents the design of the scaled riser models under investigation, the description of the wave test basin and facilities, experimental set up and the method of data analysis. Experimental results are discussed in section 3. Conclusions are drawn in section 4.

2 Experimental setup and procedure

A truncated model of a riser, at three different geometric scales, is placed in the wave-basin and its vibrations under the excitation of waves with different kinematics are measured. From the measurements of riser model vibrations, the scale effect of the

wave-induced vibration is investigated, which focused on the influences of wave kinematics and structural properties of the riser model. This sections briefly reviews the similarity theories in describing the wave-induced vibration and articulates the set-ups and procedures to conduct the wave-basin tests for riser models at different geometric scales.

2.1 Similarity theory

Since the cost associate with an experiment of risers at the full-scale is unacceptably high, the academic investigations focusing on the dynamic features of wave-induced riser vibrations mainly relies on the scaled-down experiments. Given that the scaled-down experiments are commonly used to reveal dynamic behavior of complex systems, similarity theories have been developed for the design of them. Ideally, both the dynamic characteristics at the fluid side and the structure side should be similar for the prototype and the model. The perfectly scaled-down experiment, however, does not exist due to the absence of proper materials at both the fluid and structure sides. Consequently, the dominate dynamic features in the full-scale system should be identified, and corresponding similarity theory is developed for the design of the scaled-down experiments.

In the scaled-down experiment for the offshore structures, the Reynolds and Froude Number similarity theories are usually employed. It is widely acknowledged that Reynolds similarity is highly difficult to satisfy in the experiment. In the field of ocean engineering, the Froude similarity is most widely followed through adjust the geometry of the model and the velocity of the flow. When the wave dynamics is of concern, the Keulegan-Carpenter (KC) number similarity is also important as it reveals the periodic nature of the wave excitation. Froude similarity is applied in the current work. Table 1 provides the conversion of physical quantities between model and prototype. The ratio of seawater to freshwater density is γ ($\gamma = 1.025$).

With regards to the wave-induced vibration of risers, it is expected that both the parameters in association with the KC number similarity and the fluid-structure interaction should play a role. In detail, it is postulated that the periodic nature of the wave excitation and the natural frequencies of the riser are both important in determining the dynamic responses of the riser under waves. In addition to the frequencies, the magnitudes of hydrodynamic forces and the structural properties of the riser together determine the amplitude of the vibration. Since there is no commonly acknowledged similarity theory to guide this kind of experiments, it is beneficial to reveal the relative importance of parameters for wave kinematics and structural properties, which could lead to discoveries of novel dimensionless number describing the dynamic responses of risers under the wave excitation.

2.2 Riser model

In order to investigate the scale effect for the riser vibrating under waves, a series of wave-basin tests were conducted and reported in the present study. In fact, riser models at different geometric scales were tested, which reveals the connections of frequencies and amplitudes of riser vibrations with wave kinematics and its structural properties. As revealed by Lee and Allen (2010), the axial and lateral stiffness, in the combination with the top tension, determines the dynamic features of the riser vibration under periodic excitation. So it is reasonable to ignore the axial stiffness of the riser as it seldom influences the structural responses of a riser in the range of wave elevations. Consequently, the top tension and the bending stiffness are focused in the design of the riser model in the present study.

The riser model employed is scaled down from a real riser used by China National Offshore Oil Corporation (CNOOC) in a project installed in the South China Sea. The major structural parameters of the riser at the full-scale is summarized in Table 2. Considering the restrictions of the wave-basin dimensions, the geometric scales for the design of the riser model are specified as 1:9, 1:12 and 1:15.

It is apparent that the geometrically perfect scaled-down of the real riser would lead to an unrealistic model with extremely thin ring as the cross-section. In fact, the riser model corresponding to the scale of 1:9 shows a thickness of 3.5 mm. Consequently, a novel approach to manufacture the riser model is suggested in the present study. Because the geometric and structural similarity are most important in the manufacturing process, it is designed that the outer diameter and the bending stiffness are preferentially scaled-down. This is achieved by the combination of round steel and polyvinyl chloride (PVC) pipes. In order to eliminate the additional stiffness brought about by the PVC tubes, they are disconnected along the whole length.

In fact, the scaled-down model is manufactured as follows. a) the fully-threaded steel rod with desired diameters is selected and truncated to be the core of the riser model, and to present the desired bending stiffness; b) PVC tube segments, with the outer diameters determined from the geometric scale, are manufactured; 3) the PVC tube segments placed onto the lateral supports of the core steel rod are assembled along the core steel rod using water-proof glue; d) the assembled PVC tube is sealed at both ends to have a water-tight riser model. Figure 1 shows the components, i.e., the

TABLE 1 Scaling criterion of physical quantities between model and prototype.

Quantity	Symbol	Conversion coefficient	Quantity	Symbol	Conversion coefficient
Length	L_p/L_m	λ	Period	T_p/T_m	$\lambda^{1/2}$
Area	A_p/A_m	λ^2	Mass	M_p/M_m	$\gamma\lambda^3$
Volume	V_p/V_m	λ^3	Force	F_p/F_m	$\gamma\lambda^3$
Inertia	I_p/I_m	λ^4	Young's modulus	E_p/E_m	$\gamma\lambda$

TABLE 2 Geometric and structural characteristics of the CNOOC riser at the full-scale.

Outer diameter (mm)	457
Thickness (mm)	31.8
EI of the Pipe (Nm^2)	2×10^8
Mass (kg)	6×10^6
Length (m)	1800
Material	API PSL2 X65 Carbon Steel

steel core rod and the outer PVC tube segments, used to manufacture the riser model at different geometric scales.

To obtain the desired bending stiffness, the deflection of the assembled riser model is accurately measured in the mechanic laboratory using a three-point bending machine to apply the load. Supplementary Figure 1 shows the sketch for the bending test and the photo showing the site.

In addition to the bending stiffness, the top tension also influences the dynamic behavior of the riser. In fact, it is suggested that the dimensionless parameter of TL^2/EI determines the behavior of the riser, in which T is the initial tension, L is the length of the riser and EI, in general, shows the bending stiffness. While TL^2 larger than EI indicates string-like behavior of the riser, $TL^2/EI<1$ implies that it is a beam-like structure. Consequently, three different slotted weights—47, 95, and 143 kg—are connected to the riser model at the geometric scale of 1:9 to evaluate the influence of top tension on wave-induced vibrations. Given the riser models are at three different geometric scales and three slotted weights are connected to the riser model at the scale of 1:9, six different riser models are under investigation. Table 3 summarizes the structural properties of them. For the sake of brevity, these models at the scales of 1:15, 1:12 and 1:9 are labeled as Small, Medium and Large model respectively. The value of slotted weights is appended to those label for further clarification.

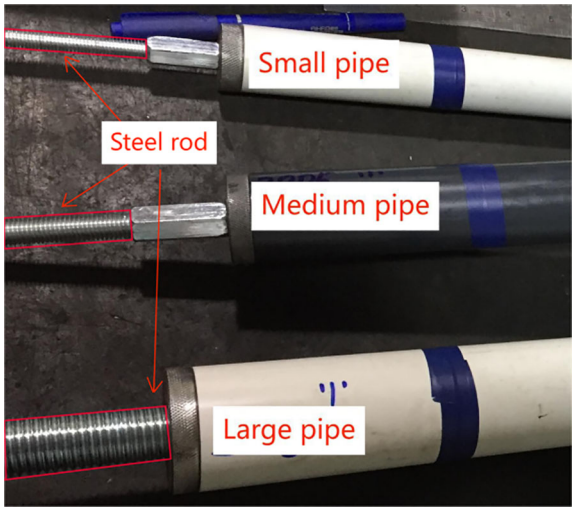

FIGURE 1
Comparison of riser models at different geometric scales.

2.3 Experiment facilities

The riser models at different geometric scales are tested in the wave basin in the Shenzhen International Graduated School, Tsinghua University. In fact, the vibrations of the riser models under the regular waves with different kinematic characteristics were employed in the present study to investigate the wave-induced vibration.

In fact, the wave basin is 25m long, 8m wide and filled with water up to 5m shown in Supplementary Figure 2. In other words, the water depth of it is 5m. It is equipped with a flap wave maker and a wind tunnel at one end. While the regular waves are generated by the wave maker, the wind tunnel is turned off in the present experiment to eliminate the influence of winds on the vibration of riser models. The riser model is installed at the bottom of the trailer and placed in the middle of the basin. Given the diameters of the riser models and the location of their installation, the wall proximity effect are negligible. The maximum wave height generated in the basin is 0.75m. However, the wave heights are in the range of 0.1m~0.5m in the present study to avoid the stability issue for higher wave heights. Opposite to the wave maker, there is a absorbing beach at the end of the basin.

The trailer is controlled to positioned at the horizontal center of the basin and is fixed at the predefined location throughout the experiment, which provides a fixed boundary condition for the model. At the top end of the model, a force sensor is attached to measure the top tension during the experiment. At the lower end, a specifically designed frame is used to host the slotted weights. It is noted that the frame only restricts the horizontal movement of the slotted wight. The layout of the riser model is shown in Figure 2. Supplementary Figure 3 shows the apparatus connected to both ends of the riser model.

In order to measure the dynamic responses of the riser model under waves, a series of strain gauges are attached along its axial direction. Since the dynamic responses near the free surface is of concern, the strain gauges are placed denser close to the free surface. More specifically, there are 6 gauges along the axis of the riser model, and their locations are shown in Figure 3. It is noted that the gauges are placed in pair to measure the strains for both the upstream and downstream directions. While the gauge P1 is located above the free surface, P2-P6 gauges are underwater. In fact, the gauge P1 is installed 0.75m beneath the top of the riser model, and is 0.35m above the still water. The signals of the gauges are sent to the central computer via the M3841 collection system as shown in Supplementary Figure 4. In addition, a series of wave elevation sensors are installed before the riser model to verify the wave load conditions. The specifications of the measuring equipment are summarized in Supplementary Table 1.

2.4 Experimental produces and wave load cases

During the wave-basin test, the riser could be regarded as a cantilever beam. In fact, it is essentially a truncated model, in which the influence of remaining riser occupying the water down to the

TABLE 3 Key parameters of the scaled riser model.

	Small	Medium	Large0	Large47	Large95	Large143
Scale Ratio	1:15	1:12	1:9	1:9	1:9	1:9
Outer Diameter of the PVC Pipe/mm	32	40	50	50	50	50
Diameter of the Steel Rod/mm	10	12	24	24	24	24
Measured *EI* of the Pipe/Nm^2	107	118	1937	1937	1937	1937
Total Mass/kg	7.6	10.6	28.8	28.8	28.8	28.8
Slotted Weight/kg	0	0	0	47	95	143
Pipe Length/m	6	6	6	6	6	6
Initial Tension/N	99.7	145.4	186.7	579.2	1092.6	1565.5
TL^2/EI	33.5	44.2	3.5	10.8	20.3	29.0

seabed is ignored. At first, it is practically impossible to model the entire riser system as the riser in the real project is around 1800 meters long. Secondly, the wave-induced vibration is understandably only observed near the free surface. Therefore, a truncated model is fabricated in the present study. And the remaining part of the riser in fact provides the restriction for the motion of the truncated model. Considering the extensive length of the it, it is reasonable to assume it hardly restricts the dynamic responses of the model under the waves. Therefore, the model is regarded as a cantilever beam, and the restriction of the remaining riser part is simply ignored.

The general procedures to conduct the wave basin experiments are as follows: a) the core rod is manufactured according to the desired geometric scale and the strain gauges are attached to the rod at the prescribed locations; b) The core rod is connected to the outer PVC tube segments to prepare the riser model at different geometric scales; c) A three-dimensional force sensor is installed at the end of the trailer, and the interface is designed to connect with the riser model at its top end; d) The riser model, together with the desired slotted weight, is hoisted and installed onto the trailer (Figure 4); Meanwhile, the base frame is placed to the bottom of the wave basin; The riser model is then carefully moved by the trailer to the predefined position with the slotted weight perfectly hosted by the base frame; e) The wires connecting the strain gauges and the force sensor are sealed inside the outer PVC tube segments and dredged out to collect the signals to the central computer; f) The wave maker is activated to generate the regular waves and the measurements of the strains and top tensions are accumulated.

With regards to the kinematics of waves, the heights and periods of regular waves were varied to provide different load cases. In fact, different wave kinematics are adopted for riser at different geometric scales. For the Small riser model, the wave height ranges from 0.1m to 0.4m and the wave periods ranges from 0.7s to 2.0s. For the Medium riser model, the wave height varies in the range of 0.12m-0.45m, and the wave period varies in the range of 0.79s to 2.07s. The wave heights and periods both increase in the test corresponding to the Large riser model to ranges of 0.15m-0.56m and 0.84s-2.24s. The details of the load cases employed are illustrated in the Table 4; Supplementary Tables 2, 3. All the waves are seen as deep-water waves. During the test, the wave parameters are controlled by the wave-making system.

2.5 Data analysis

Strains of the riser model are the main measurement accumulated in the wave-basin test. Given the strains at various positions along the riser model are measured, the dynamic displacements are discerned via modal analysis. In addition, it is well known, from the VIV experiments, that the dynamic responses of a riser may couple with the tension to present a complex fluid-structure interaction phenomenon, in which the simple modal

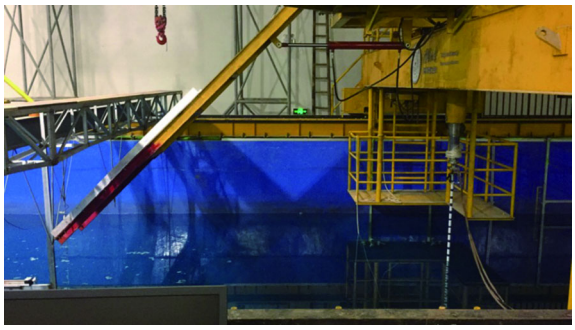

FIGURE 2
Layout of the riser model in the wave basin.

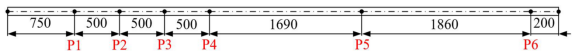

FIGURE 3
Schematic diagram of strain gauge arrangement (unit: mm).

analysis linking the strains and dynamic displacements of a riser is no longer applicable. Consequently, the strain gauges are arranged symmetrically about the axis of the riser in the wave-incident direction to evaluate the influence of vibrations on the tension, and in turn on the strains of a riser.

2.5.1 Strain acquisition

Since it is reported, in the literature concerning the VIV, that the vibration could induce periodic variations in tension, which ultimately influences the dynamic responses of the riser, the strains measured symmetrically about the neutral axis in the wave-basin are employed to eliminate the influence of tensions. In detail, the strains measured across the neutral axis of the riser show the variation of the neutral position of the riser model, which indirectly reveals the deformation characteristics of the riser.

Figure 5 shows a segment of strain time history measured at the position of P5 under the load case of #13 corresponding to the Large143 model. It is observed from the figure that the two strain time serials are equal in value and opposite in the sign, and the averages of the strains in the opposite directions is acceptably close to zero. Such an feature implies that the riser model under investigation in the wave-basin test is in the pure bending state, in which the shear does not play a dominate role. In other words, the strain measurements corresponding to the upstream face of the riser in the wave-incident direction contain all the information required to estimate the dynamic displacements, and therefore only those measured at the upstream face are used for subsequent processing and discussion.

2.5.2 Modal analysis

The strains measured at the upstream face are used to infer the vibration response of the riser via modal analysis (Equations 1–6) as demonstrated by Gao et al. (2015). In detail, it is assumed that there

FIGURE 4
Hoisting of the riser model.

are n-th modes participating in the dynamic response of the riser, and the displacement at a given location along the riser axis is obtained through a linear superposition of the participated modes. In other words, the displacement along the axis of a riser model is expressed as:

$$x(z,t) = \sum_{i=1}^{n} \phi_i(z) h_i(t) \tag{1}$$

where $x(z,t)$ is the displacement of a riser in the wave-incident direction;z shows the vertical coordinates of the location; t is the time; φ_i is the shape of i-th mode participating in vibration; n is the highest mode order considered in the modal analysis; h_i is the i-th mode contributing coefficient, i.e., the contribution of the i-th mode to the total displacement response of the system. The relationship between the displacement and curvature $\kappa(z, t)$ shows:

$$\kappa(z,t) = \frac{\mathrm{d}^2 x}{\mathrm{d}z^2} = \sum_{i=1}^{n} \phi_i^{''}(z) h_i(t). \tag{2}$$

From the structural dynamics of a cantilever beam, its mode shapes are,

$$\phi_i(z) = A_1[\cos a_i z - \cosh a_i z - \frac{\cos a_i L + \cosh a_i L}{\sin a_i L + \sinh a_i L}(\sin a_i z - \sinh a_i z)] \tag{3}$$

where A_1 and a_i are undetermined constants. Then the curvature corresponding to the selected mode shape is given by

$$\phi_i^{''}(z) = a_i^2 A_1[-\cos a_i z - \cosh a_i z - \frac{\cos a_i L + \cosh a_i L}{\sin a_i L + \sinh a_i L}(-\sin a_i z - \sinh a_i z)] \tag{4}$$

According to classic structural dynamics (Liu et al., 2005), the first four solutions of aL are 1.875, 4.964, 7.855 and 10.996, respectively.

Considering the relationship between curvature and strain ϵ:

$$\kappa(z,t) = \frac{\varepsilon(z,t)}{R} \tag{5}$$

where R is the diameter of steel rod, it is derived that

$$\varepsilon(z,t) = \kappa(z,t) \cdot R = \sum_{i=1}^{n} \phi_i^{''}(z) h_i(t) \cdot R = \sum_{i=1}^{n} \phi_i^{''}(z) e_i(t), \tag{6}$$

in which $e_i(t)$ is the i-th mode contribution coefficient to the total strain. The relationship between displacement and strain can then be obtained combing the relationships shown in Equations (7):

$$\begin{pmatrix} \varepsilon(z_1,t_1)\varepsilon(z_1,t_2)\cdots\varepsilon(z_1,t_{Nt}) \\ \varepsilon(z_2,t_1)\varepsilon(z_2,t_2)\cdots\varepsilon(z_2,t_{Nt}) \\ \cdot \\ \cdot \\ \cdot \\ \varepsilon(z_N,t_1)\varepsilon(z_N,t_2)\cdots\varepsilon(z_N,t_{Nt}) \end{pmatrix} = \begin{pmatrix} \phi_1^{''}(z_1)\phi_2^{''}(z_2)\cdots\phi_n^{''}(z_N) \\ \phi_1^{''}(z_2)\phi_2^{''}(z_2)\cdots\phi_n^{''}(z_N) \\ \cdot \\ \cdot \\ \cdot \\ \phi_1^{''}(z_1)\phi_2^{''}(z_2)\cdots\phi_n^{''}(z_N) \end{pmatrix} \begin{pmatrix} e_1(t_1)e_1(t_2)\cdots e_1(t_{Nt}) \\ e_2(t_1)e_2(t_2)\cdots e_2(t_{Nt}) \\ \cdot \\ \cdot \\ \cdot \\ e_n(t_1)e_n(t_2)\cdots e_n(t_{Nt}) \end{pmatrix} \tag{7}$$

With the help of the measurements of strains taken, the contribution coefficients of the modes participated in the dynamic responses of the riser model are determined, which in turn leads to the estimates of the displacements given the known mode shape. Figure 6A shows the time history of the contribution coefficients of

TABLE 4 Regular wave height and period for Small pipe model test.

#	Height H/m	Period T/s	Frequency f/Hz	Froude No.	KC No.
1	0.10	0.70	1.40	0.64	9.82
2	0.10	0.90	1.11	0.39	9.82
3	0.10	1.00	1.00	0.31	9.82
4	0.10	1.20	0.83	0.22	9.82
5	0.10	1.50	0.67	0.14	9.82
6	0.10	1.80	0.56	0.10	9.82
7	0.20	1.02	0.98	1.21	19.64
8	0.20	1.20	0.83	0.87	19.64
9	0.20	1.50	0.67	0.56	19.64
10	0.20	1.80	0.56	0.39	19.64
11	0.20	2.00	0.50	0.31	19.64
12	0.30	2.00	0.50	0.71	29.45
13	0.40	2.00	0.50	1.26	39.27

the first four modes corresponding to the riser model at the geometric scale of 1:15 under the load case of #1. The coefficients are around -6×10^{-6} ~ 1×10^{-5}、-8×10^{-6} ~ 7×10^{-6} 、-9×10^{-7} ~ $1\times10^{-6}$and -9×10^{-7} ~ 7×10^{-7}, respectively. Therefore, the first two order modes are considered dominant the vibration of the riser model. The sum of the energies corresponding to the first three modes reaches 95% (Figure 6B). Consequently, it is sufficient to estimate the vibration of the riser model considering the first three participating modes.

3 Results and discussions

Including the riser models at different geometric scales and slotted weights applied at the end, there are 6 different models tested in the wave basin. For each of them, 13 different load cases are applied, which is named as #1 through #13. Using the measurements of strains, the dynamic responses, mainly the vibration frequency and amplitudes, are analyzed to reveal the scale effect of risers vibrated in waves.

3.1 Spectrum of the displacement

With the help of the measurements of strains at different location along the riser model, the time histories of displacements at corresponding locations are obtained, which are used to show the spectral characteristics of the vibrations through Fourier transformations.

Figure 7 depicts the vibration spectra at different sampling points for the Large0 model under the load condition of #12 (see

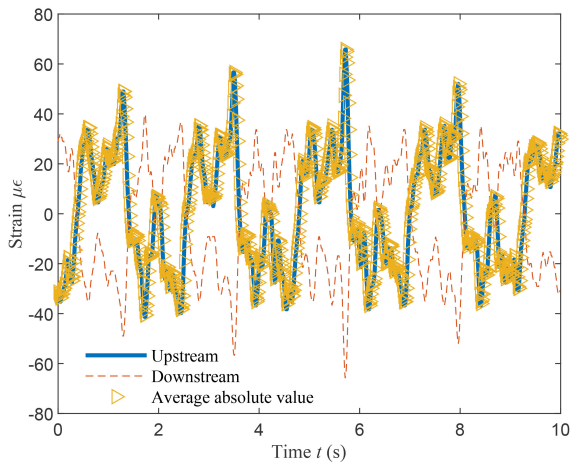

FIGURE 5
Strain time history for Large143 pipe under condition #13.

10.3389/fmars.2024.1372676

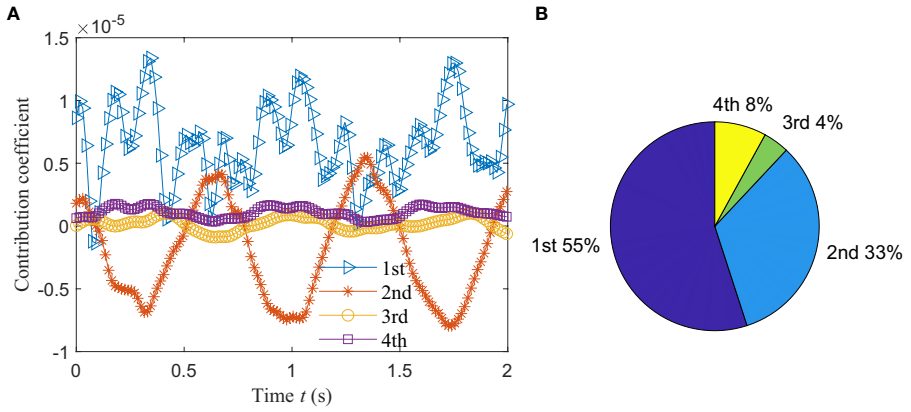

FIGURE 6
Contribution coefficients of the first four modes: **(A)** Temporal variation; **(B)** Percentages.

Supplementary Table 3). It is revealed from the figure that the vibration of the riser model is fairly periodic with a dominant frequency equaling to the frequency of the wave excitation. In some cases, the secondary vibration frequency, which is twice as the wave excitation frequency, cannot be ignored.

In addition to the spectral characteristics, the time histories of the displacements also leads to the estimates of the vibration amplitudes. Figure 8 shows the root-mean square of displacements normalized by the diameter of the riser models under the excitation of the load case of #1. It is noted that the first point showing a vertical coordinate of 0.35m is above the still water surface, and the other five points are well below the water surface even in the wave condition. As expected, Figure 8 shows that the vibration amplitude for all the riser model under investigation

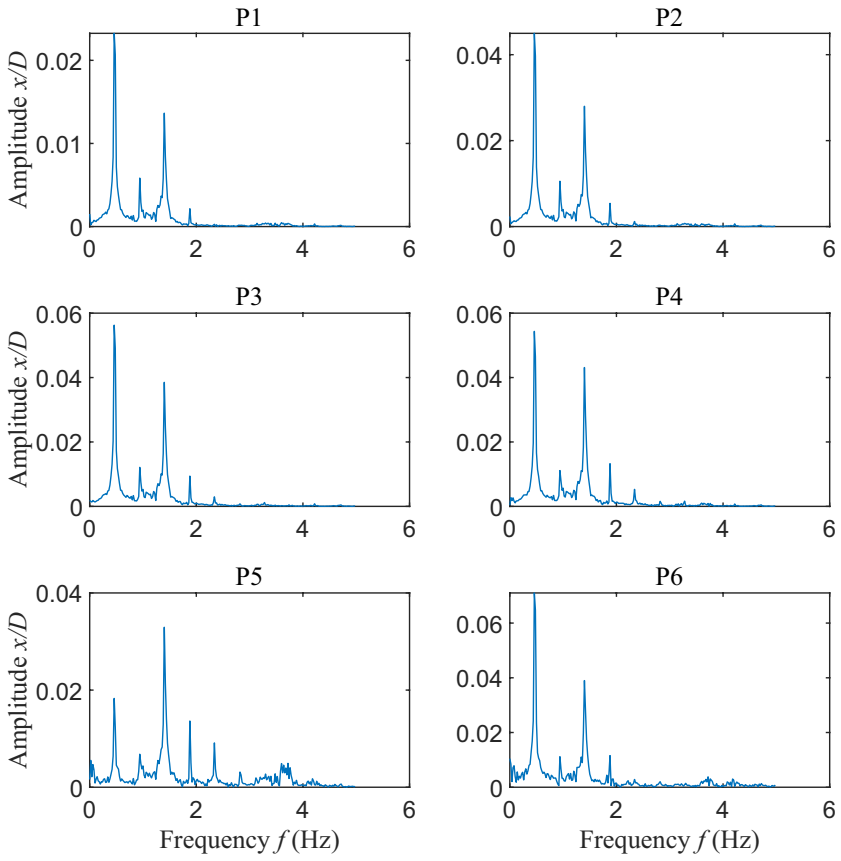

FIGURE 7
Spectrum for Large0 pipe (*Fr*=0.70, *KC*=25.13).

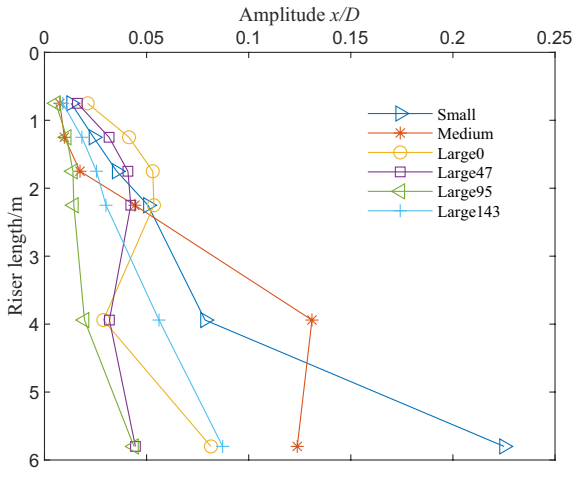

FIGURE 8
Amplitude along with the risers.

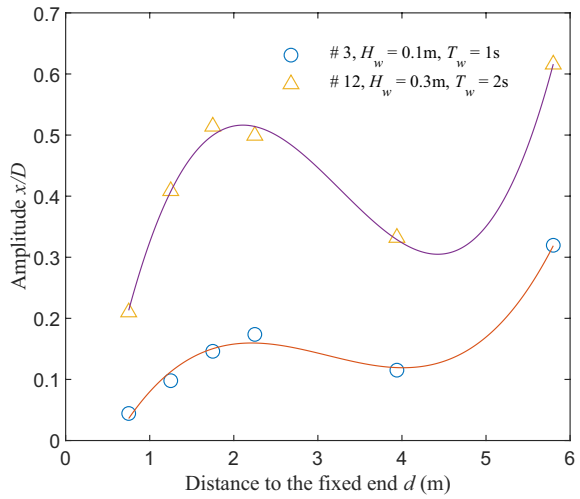

FIGURE 9
Amplitude with the distance to the fixed end.

increases downwards. Such a finding substantiates that the experiment configuration discloses the dynamic responses of a cantilever beam under the excitation of waves.

3.2 Vibration amplitude along the riser model

According to the structural dynamic theory concerning the cantilever beam, it is postulated that the vibration amplitudes of the riser model is related to the distance from the fixed end of the riser model in a nearly cubic fashion. In fact, when the excitation of waves is modeled as external loads mainly applied within a narrow band near the water surface, the deformation of the riser model can be satisfactorily described as a cubic function of the distance from the fixed end. Figure 9 shows the variation of the vibration amplitude of the Small model with the distance from the fixed end under the load cases of #3 and #12. The cubic functions calculated by fitting the measured vibration amplitudes are also included here. It is noted that the vibration amplitude is defined as the standard deviations of the time series of displacements obtained from the wave basin test.

The agreement shown in Figure 9 between the vibration amplitudes and the fitted cubic function indicates that amplitudes of wave-induced vibration beneath the water surface can be satisfactorily estimated via the wave-induced vibrations observed near the water surface. The coefficients of the fitting function differ due to their wave height and period. As the wave height period increases, the corresponding absolute value of the coefficient also increases.

3.3 Vibration amplitude with scale ratio

In the present study, both geometry similarity of the pipe and wave load similarity are considered following the Froude criterion. Froude number for each wave load case (#1 ~ #11) corresponding to different pipes is approximately equal. Figure 10 compares the nondimensional amplitude for these eleven load cases with different scale ratios. Theoretically each curve with the same Froude number should be a horizontal line. It is shown that dimensionless amplitude decreases with scale ratio almost linearly for case #1, #2, #4 and #7; while for the other group the curve shows a hill shape. Apparently, the straight lines occur when the wave height and period are both small in these cases nonlinearities are not that intense. Vibrations are influenced mainly by the magnitude of the wave forces. Also, it should be mentioned that the bending stiffness can not be exactly scaled down. In fact, it is smaller than its theoretical value, which makes the vibration frequency near the natural frequency for Medium model causing a larger amplitude, i.e. the hill-like curves. In the later case, the nonlinearity increases with the wave hydrodynamics and the structural characteristics start to play the dominant roles. Therefore, these results indicate a greater impact of structural properties of the riser than fluid characteristics given nonlinear enhancement of waves.

3.4 Influence of wave periods

As in the VIVs, it is concerned that the resonance occurred in the wave-induced vibration could bring significant damages to the riser. Therefore, it is interesting to reveal the connections between the amplitudes and the wave periods. Figure 11 shows the variation of the wave-induced vibration amplitudes with the wave period for the riser models without slotted weights, i.e. the Small, Medium and Large0 models. Since it is shown that the vibration amplitudes of the entire riser model can be well represented by the those near the water surface, these amplitudes shown here all corresponds to the sampling point of P2. It is noted that the load cases are in association with different wave heights. While the wave heights in the load cases of #1~6 are 0.1m, the wave heights in the load cases of #7~11 are 0.2m.

It is shown from the figure that vibration amplitudes first increase with the wave periods and then decreases with a peak

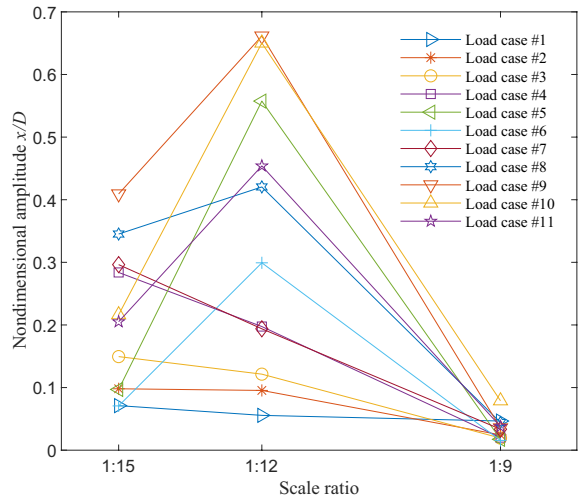

FIGURE 10
Vibration amplitude x/D with different scale ratios.

appeared in the middle. The only exception is found for the Large model in the load case with the wave height of 0.1m, and can be explained as the wave excitation is not strong enough to induce the resonance. Other curves shown in Figure 11, on the other hand, contain a resonance peak illustrate the importance of wave periods in describing the wave-induced vibration. To be more specific, the natural frequencies of different riser models are calculated and compared to the wave periods corresponding to the resonance peaks. In detail, the natural frequencies of the riser model are estimated (Equation 8) according to Lee and Allen (2010) as

$$f_n = \frac{n^2\pi}{2L^2}\sqrt{\frac{EI}{m}\left(1+\frac{TL^2}{n^2\pi^2 EI}\right)}\ ,$$

$$T_n = 2\pi/f_n, n = 1, 2, 3\ldots, \quad (8)$$

where n is the selected mode number, f_n and T_n are the nth natural frequency or period of the riser model, m and L are the mass

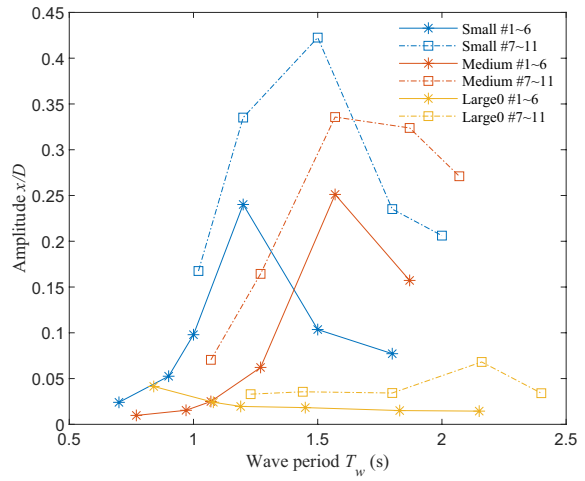

FIGURE 11
Variation of amplitude with wave period for different pipes: # 1~6, H_w = 0.1m; # 7~11, H_w = 0.2m.

TABLE 5 Wave periods with peaks and natural periods of different model.

Riser Model	Wave period with peaks (s)	Natural period (s)
Small	1.2 & 1.5	1.1 (2nd)
Medium	1.57 & 1.57	1.2 (2nd)
Large0	0.84 &2.16	0.7 (2nd) & 2.3 (1st)

and the length of the riser model; EI shows the bending stiffness and T is the initial tension. Table 5 compares the periods corresponding to the resonance peak shown in Figure 11 with the natural frequencies of the corresponding riser model. For the Small model, the resonance peaks are observed at T_w = 1.2s (H_w = 0.1m) and 1.5s (H_w = 0.2m), which is near the second natural period of this pipe (T_n = 1.1s). For the Large0 model, the frequencies corresponding to the resonance peaks are 0.84s (H_w = 0.1m) and 2.16s (H_w = 0.2m), which agrees with the corresponding first and second order natural frequencies.

3.5 Influence of the top tension

As revealed in Figure 11 and Table 5, the resonance occurs when the periods of the wave excitation are close to the natural periods of the riser model. Since the natural frequency is related to not only the bending stiffness, but also the tension when the riser behaves as a string, it is reasonable to suggest that the wave-induced vibrations is influenced by the top tensions applied to the model.

Figure 12 depicts the time history of the fluctuating tension, strain and non-dimensional vibration displacement and their corresponding spectrum for Small pipe at Load case #1. The second column in the figure is the initial part of the first column to present a close look on the vibration curves. It's shown that top tension, strain and displacement are nearly in phase and there is no hysteresis among them. In addition, the dominant frequency corresponding to tensions, strains and vibrations are the same (~1.4 Hz) in this specific case. Such simultaneous measurements of top tension and vibration under the excitation of waves indicate that waves cause the variation in the tension with no lag comparing to the dynamic vibration of the riser model.

Figure 13 shows the variation of the amplitude with the initial tension at sampling point P2 corresponding to the models with different slotted weights, i.e., the Large0 model to Large143 model. Six curves correspond to the first six wave load cases (see Table 4; Supplementary Tables 2, 3). It is observed from the figure that the amplitudes of wave-induced vibration decrease with the top tension monotonically with a rebound at Load case #1, #2 and #4. It maybe because the second order natural period of the Large143 model is close to these wave periods.

3.6 Influence of the $KC_d{\cdot}TL^2/EI$ on amplitude

From the investigation on the amplitudes of vibrations under the influences of the distance from the fixed end, the wave period

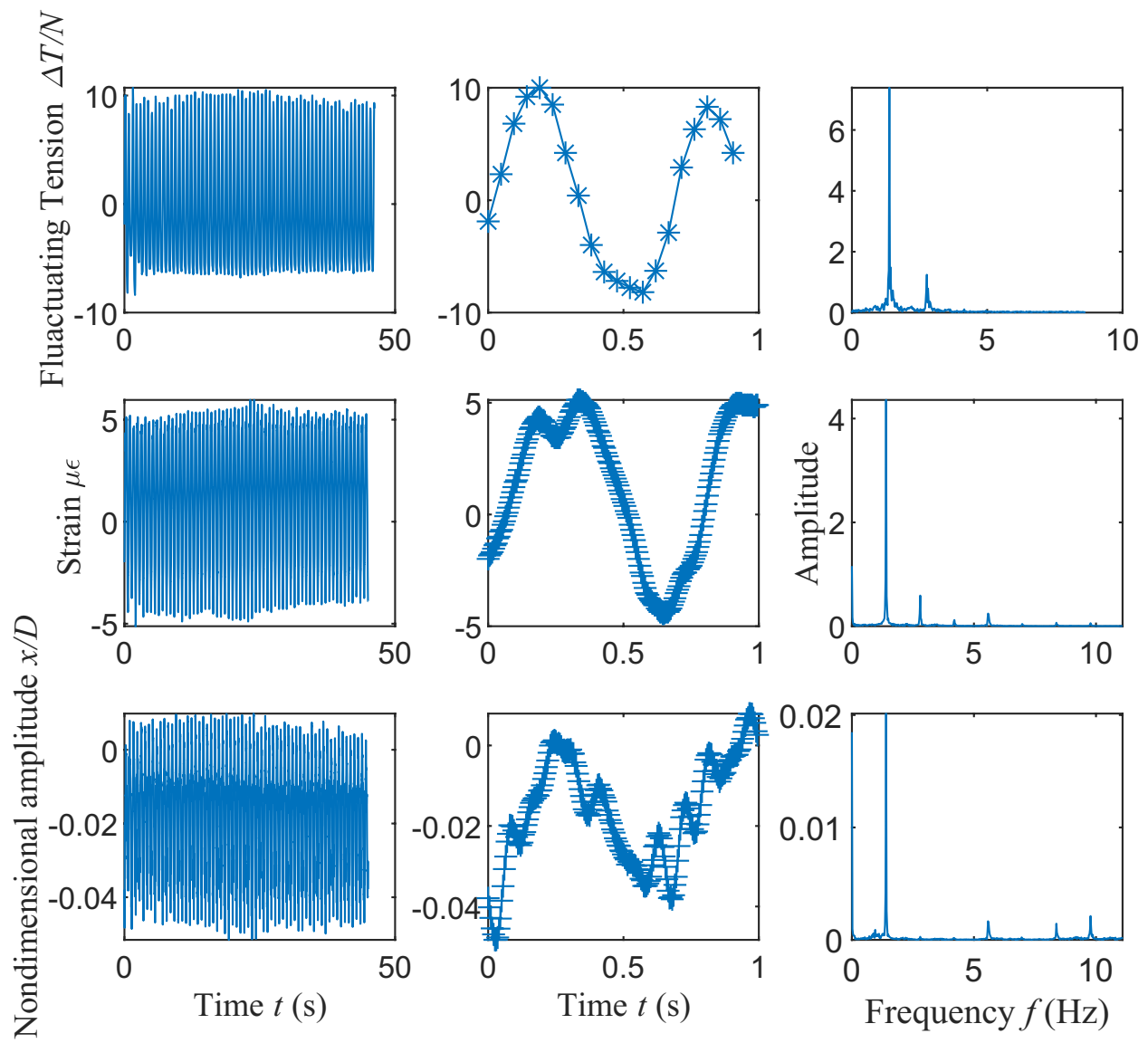

FIGURE 12
Time history and spectrum of fluctuating tension, strain and dimensionless displacement (Small pipe, Load case #1).

and the initial tensions applied to the riser model, it is suggested that the estimate of the vibration amplitude should take into consideration wave periods and structural properties of the riser model. In addition, it is common knowledge that the wave-induced vibration amplitude is in connection with the wave height, i.e., the strength of external loading, and the bending stiffness of the riser model. Consequently, it is attempted, based on the measurements of the wave-basin experiment, to suggest a dimensionless parameter to estimate the vibration amplitude of risers.

In fluid dynamics, the *KC* number is an important dimensionless parameter ($KC = UT/L_c$) that characterizes the periodic wave forces acing on offshore platforms. By definition, the *KC* number quantifies the relative importance of resistance over inertial forces on blunt bodies in oscillating flows. The present study revised the *KC* number to indicate the general strength of the wave loads in a distance of x from the fixed end of the riser model. In other words, the present study suggests that the distance from the fixed end (x) replaces the characteristic length of the bluff body (L_c) to deliver a KC_d number.

In structural dynamics, TL^2/EI is widely used to measure the relative importance of two different mechanism contributed to the total structural stiffness of a riser (Ren et al., 2020). In detail, TL^2 shows the stiffness resulted from the string-like behaviour, and EI gives the stiffness of beam-like behaviour. Such a dimensionless parameter is hence borrowed in the present study to show the overall stiffness and to imply the natural frequencies of the riser.

Combing the revised KC_d number and the dimensionless parameter of TL^2/EI, the present study suggests a new dimensionless number π_1 ($\pi_1 = KC_d \cdot TL^2/EI$), which comprehensively takes the wave and structure into account, to estimate the amplitude of wave-induced vibrations. Figure 14 shows the amplitude normalized by the cubic of the distance x at sampling

10.3389/fmars.2024.1372676

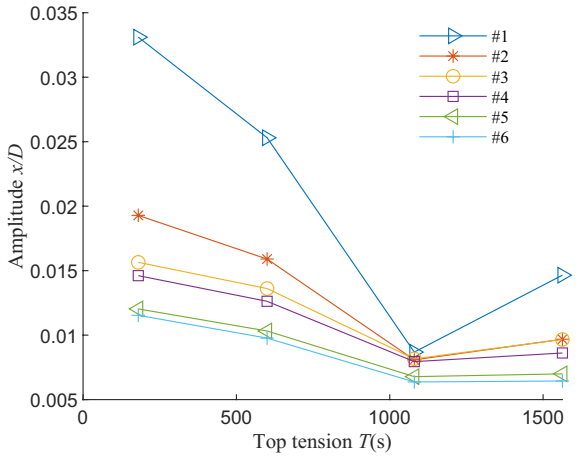

FIGURE 13
Variation of amplitude with the initial top tension.

points P1 to P6 as a function of π_1 for six models. It is concluded that the normalized amplitude collapse into a single curve described by a function of π_1. The amplitudes at the sample point P1 agree with the global trend but their magnitude are one order larger than the value at P2 to P6. There are two ways this could be interpreted. The first one is this P1 is above the water surface which leads to different loading and vibration. The other one is near the fixed end where the boundary condition has primary effect. So the conclusion here predicting wave-induced vibrations is not applicable to the sampling point which is above the water surface or near the boundary ($x/L < 0.2$). That is the limitation of the proposed dimensionless parameter. While it is suitable to describe the wave-induced vibration for those underwater and away from the boundary ($x/L > 0.2$).

It is discerned from the figure that the normalized vibration amplitudes monotonically increase with the dimensionless parameter of π_1. In fact, it is found that the normalized amplitude marginally increases when π_1 is below 10, and the increase is significantly expanded when $\pi_1 > 10$. From such an observation, it is suggested that further studies can be conducted separately for the wave-induced vibration of risers corresponding to the regime of $\pi_1 < 10$ and $\pi_1 > 10$.

3.7 Dominant vibration frequency

Figure 15 shows the dominant vibration frequency reduced by wave incidence frequency between different sampling points of each pipe. It's obvious from the figure that the dominant frequency of the vibration agrees, in most cases, the wave incident frequency. In certain cases, the dominant frequency of vibration is 2, 3, 5, or 6 times the wave frequency. In Figure 15C, the dominant frequency of Large0 pipe under conditions # 4 and # 8 ~ #9 is twice the wave frequency; while it is threefold under conditions # 10~# 13 and fivefold (0.51Hz vs 2.49Hz) under conditions # 13 for the Small pipe. It should be noted that different sampling points have different frequency component at the same load case. P5 and P6 usually have higher dominant frequency and more spectral components. The generation of the multi-frequency is related to the higher-order

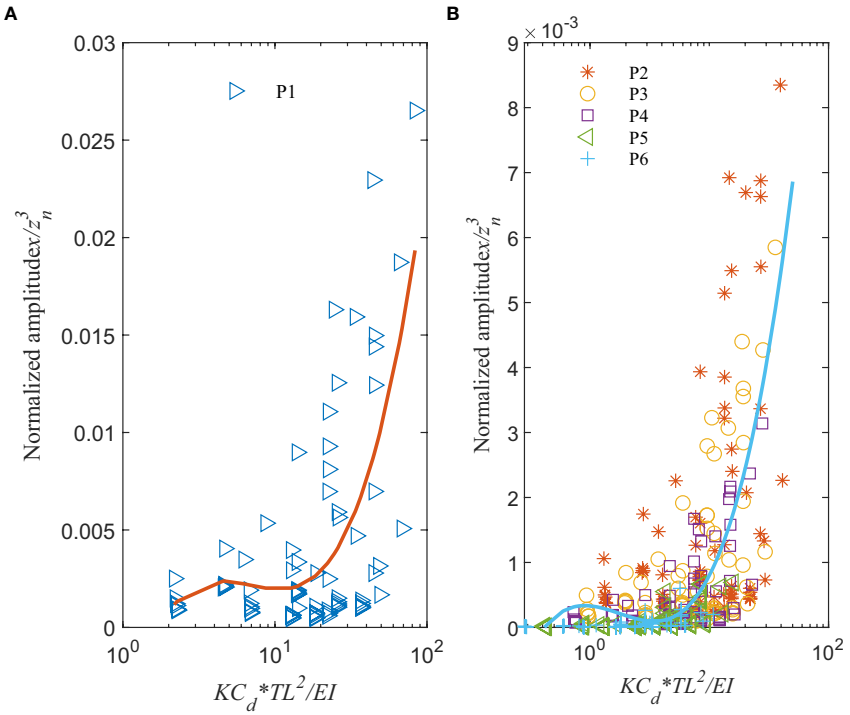

FIGURE 14
Variation of normalized amplitude with KC_d*TL^2/EI for six pipes: **(A)** P1; **(B)** P2~P6.

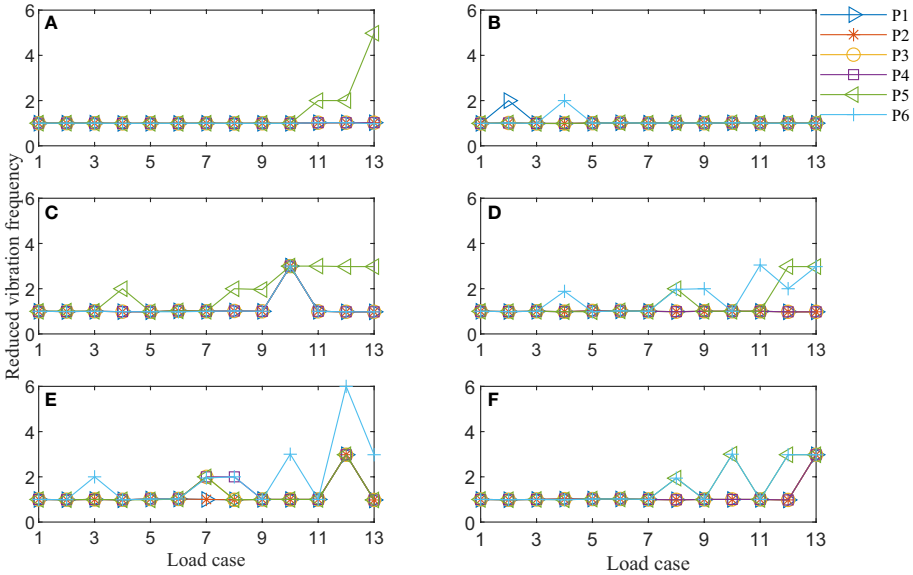

FIGURE 15
Dominant frequency at different sampling points normalized by wave frequency: **(A)** Small; **(B)** Medium; **(C)** Large0; **(D)** Large47; **(E)** Large95; **(F)** Large143.

components generated by waves passing through a cylinder. The displacement at the lower end of the pipe to be delayed compared to the displacement at the upper end. The lower end of the riser has not yet returned to its equilibrium position Thus, the displacement at the lower end is excited by the superposition of multiple waves.

4 Conclusion

Multiple scaled riser model tests under regular waves were conducted in a wave basin to study the scale effect of riser in waves. Considering that the hydrodynamic geometries and the structural stiffness are the most influential factors in determining the dynamic responses of a riser under the excitation of waves, the present study offers a novel design of the scaled-down model of risers combing the disconnected PVC tubes with steel core rod.

Using the novel riser models, a series of wave-basin tests were carried out with different wave kinematics and riser models at different geometric scales. The results show that the vibration amplitude of the riser model is a cubic function with the distance x from the fixed end. When the wave height is constant, the amplitude of wave-induced vibrations varies with the wave period showing a resonance peak around the pipe's natural period. Based on the measurement concerning the wave-induced vibrations along the riser model, a dimensionless number $\pi_1 = KC_d \cdot TL^2/EI$ is introduced where L is the pipe length, EI is the bending stiffness, T is the top tension and the characteristic length in the KC number is taken as the distance x. The normalized amplitude of the wave-induced vibration is found increase with this parameter. While the increase of normalized vibration amplitude is only marginal when $\pi_1 < 10$, it significantly expanded when $\pi_1 > 10$.

Data availability statement

The original contributions presented in the study are included in the article/Supplementary Material. Further inquiries can be directed to the corresponding author.

Author contributions

YF: Conceptualization, Data curation, Formal analysis, Investigation, Methodology, Resources, Software, Validation, Visualization, Writing – original draft, Writing – review & editing. SL: Conceptualization, Funding acquisition, Investigation, Methodology, Project administration, Supervision, Visualization, Writing – review & editing. DC: Conceptualization, Funding acquisition, Project administration, Supervision, Writing – review & editing.

Funding

The author(s) declare financial support was received for the research, authorship, and/or publication of this article. The work described in this article was supported by the grants from Guangdong Basic and Applied Basic Research Foundation (Project No. 2022B1515130006). The authors acknowledge the support from the Tsinghua Shenzhen International Graduate School - Shenzhen Pengrui Young Faculty Program of Shenzhen Pengrui Foundation. The numerical computations reported in the

manuscript were partially performed at the Hefei Advanced Computing Center.

Acknowledgments

We would like to thank the reviewers of this manuscript for their helpful and insightful comments.

Conflict of interest

The authors declare that the research was conducted in the absence of any commercial or financial relationships that could be construed as a potential conflict of interest.

Publisher's note

Supplementary material

The Supplementary Material for this article can be found online at: https://www.frontiersin.org/articles/10.3389/fmars.2024.1372676/full#supplementary-material

References

Bearman, P., Johanning, L., and Owen, J. (2001). Large scale laboratory experiments on vortex-induced vibration, 20th International Conference on Offshore Mechanics and Arctic Engineering (Rio de Janeiro, Brazil: ASME).

Chang, Y., Wu, X., Chen, G., Ye, J., Chen, B., Xu, L., et al. (2018). "Comprehensive risk assessment of deepwater drilling riser using fuzzy Petri net model," Transactions of The Institution of Chemical Engineers. *Process Saf. Environ. Protection Part B* 117, 483. doi: 10.1016/j.psep.2018.05.021

Gao, D., Deng, Z., Yang, W., and Chen, W. (2021). Review of the excitation mechanism and aerodynamic flow control of vortex-induced vibration of the main girder for long-span bridges: A vortex-dynamics approach. *J. Fluids Structures* 105. doi: 10.1016/j.jfluidstructs.2021.103348

Gao, Y., Fu, S., Cao, J., and Chen, Y. (2015). "Experimental study on response performance of VIV of a flexible riser with helical strakes," in *Chinese Ocean Engineering Society*, vol. 29, 673.

Huang, W. P., Wu, X. M., Liu, J., and Bai, X. L. (2022). *Dynamics of Deepwater Riser: Theory and Method* (Shanghai, China: Shanghai Jiao Tong University Press). doi: 10.1007/978-981-16-2888-7

Jauvtis, N., and Williamson, C. H. K. (2004). The effect of two degrees of freedom on vortex-induced vibration at low mass and damping. *J. Fluid Mechanics* 509, 23. doi: 10.1017/S0022112004008778

Joseph, R. S., Wang, J., Ong, M. C., and Jakobsen, J. B. (2017). Vortex-induced vibration (VIV) effects of a drilling riser due to vessel motion. *IOP Conf. Series: Materials Sci. Eng.* 276. doi: 10.1088/1757-899x/276/1/012013

Lee, L., and Allen, D. (2010). Vibration frequency and lock-in bandwidth of tensioned, flexible cylinders experiencing vortex shedding. *J. Fluids Structures* 26, 602. doi: 10.1016/j.jfluidstructs.2010.02.002

Li, M. (2013). *An investigation of scale effects in the vortex-induced vibration model test of of risers* (Shanghai, China: Shanghai Jiao Tong University).

Liang, T., Xu, Y., Fu, S., Ren, H., Zhang, M., and Song, B. (2023). Wave-induced fatigue and VIV-induced fatigue of a free-hanging riser. *J. Vibration Shock* 42, 313. doi: 10.13465/j.cnki. jvs.2023.18.035

Liu, J., Du, X., and Ou, J. (2005). *Structural dynamics* (Beijing: China Machine Press), 164–165.

Luo, W. (2022). *Research on Fatigue Characteristics of Subsea Wellhead Connector Considering the Action of Riser Wave-Induced* (Beijing, China: China University of Petroleum).

Manning, M. (2016). *Offshore oil production in deepwater and ultra-deepwater is increasing* (Washington, DC: U.S. Energy Information Administration).

Ren, T., Fu, S., Li, R., and Yang, J. (2011). Full scale riser Vortex-Induced-Vibration response prediction based on model test. *J. Ship Mechanics* 15, 364.

Ren, T., Xu, Y.-w., Wang, J., Ren, H.-j., Zhang, M.-m., Fu, S.-x., et al. (2020). An experiment study of vortex induced vibration of a steel catenary riser under steady current. *J. Hydrodynamics* 32, 834. doi: 10.1007/s42241-020-0067-4

Zhang, C., Kang, Z., Stoesser, T., Xie, Z., and Massie, L. (2020). Experimental investigation on the VIV of a slender body under the combination of uniform flow and top-end surge. *Ocean Eng.* 216, 108094. doi: 10.1016/j.oceaneng.2020.108094

Zhang, W., Yang, J., Hu, Z., and Xiao, L. (2007). The experimental and numerical analysis for a deep-water semi-submersible platform. *J. Shanghai Jiao Tong Univ.* 41, 1429.

Zhou, Y., and Huang, W. (2013). *Experimental Method for Vortex Induced Vibration of Cylinders Based on Reynolds Similarity* (: China Academic Journal Electronic Publishing House Dalian, China).

Frontiers in Marine Science

Explores ocean-based solutions for emerging global challenges

The third most-cited marine and freshwater biology journal, advancing our understanding of marine systems and addressing global challenges including overfishing, pollution, and climate change.

Discover the latest Research Topics

See more →

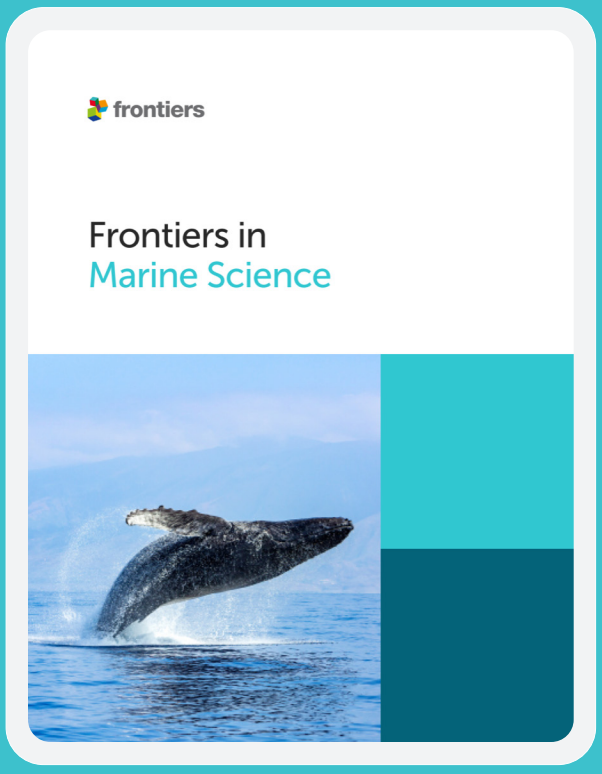

Frontiers

Avenue du Tribunal-Fédéral 34
1005 Lausanne, Switzerland
frontiersin.org

Contact us

+41 (0)21 510 17 00
frontiersin.org/about/contact